School of Electrical and Computer Engineering

Multi-Function Power Electronic Interface for Hybrid Mini-Grid Systems

James Darbyshire

This thesis is presented for the degree of
Doctor of Philosophy
Curtin University of Technology

March 2010

Declaration

To the best of my knowledge and belief this thesis contains no material previously published by any other person except where due acknowledgment has been made.

This thesis contains no material which has been accepted for the award of any other degree or diploma in any university.

Signature: ………………………………………….

Date: ………………………...

Abstract

In the past five years, global interest regarding the development of renewable energy technologies has significantly increased. The conventional electric power generation methods sourced from fossil fuels is now problematic, from both the supply and emission points of view. Fossil fuels are non-renewable limited resources that have taken millions of years to form; eventually they will be exhausted and the current cost of automotive fuel is evidence of them becoming diminished. The carbon dioxide emissions created through the energy conversion process are causing an increase in the overall atmospheric concentrations, which through global warming may have serious consequences for humanity.

Natural sources of energy production can be derived from the Sun through the use of solar and wind generation methods. Converting these sources to electricity requires the technology of power electronics, the central area of research for this dissertation. Solar energy can most easily be harnessed through the photo-electric effect which creates DC electricity. However, the majority of electric loads and transmission require AC electricity. The inverter is the electronic device required for this power conversion. Wind turbines usually create variable voltage and frequency AC that is rectified to DC and then converted to grid type AC through an inverter.

Voltage source inverters, their topologies and control are investigated within this dissertation. Voltage control methods are adopted for both stand-alone and grid connected techniques where control of active and reactive power is required. Current control techniques in the form of PI and hysteresis are applied to allow novel interfaces between generation sources to be achieved. Accurate control of the power electronics allows an enhancement in the power production from the renewable energy source. The power electronic device of the DC-DC converter, either buck or boost is controlled to allow the renewable resource to operate at its optimum power point. The control aspects and algorithms of these converters are central to this research. The solar algorithms of perturb and observe, and incremental conductance are developed with the latter being more favourable to changing levels of irradiation. The author draws a parallel between rapidly changing solar conditions with normally changing wind

states. This analogy with an understanding of the mechanics of PMSG allows a novel wind MPPT algorithm to be developed which is simulated in PSIM. Methods to analyse the usefulness of the algorithm are developed and general conclusions are drawn.

Another aim central to the research is the efficient combination of renewable energy sources into a single reliable power system. This forms the multi-function aspect of the research. The interconnection of the sources on the AC or DC sides is investigated for both stand-alone and grid connected topologies. A requirement of the stand-alone system is to provide power when no renewable resources are available causing some form of energy storage to be utilised. Conventional batteries are used, causing the VC-VSI to become bi-directional allowing charging. This is simulated in PSIM and demonstrated as part of the Denmark and Eco Beach projects. Many differing topologies of stand alone, grid connected and edge of grid systems are developed, simulated and some are demonstrated.

While investigating the currently used topologies the author invents the novel complimentary hybrid system concept. This idea allows a single inverter to be used to feed energy from either the wind or solar resource. With careful engineering of the PV array and wind turbine characteristics only a small loss of energy is caused, deemed the crossover loss. This original concept is mathematically modelled, simulated and demonstrated with results presented from the Denmark project. The strength of this idea is from the quite complimentary nature of wind and solar resources, for only a small proportion of the year are high solar and strong wind conditions occurring simultaneously.

Compared to a solar resource, the wind resource is much more complicated to model. An analysis of readily available wind source data is presented with a statistical analysis of the scaling methods; a novel box and whiskers plot is used to convey this information. New software is presented to allow a more accurate and digital model of a power curve to be recreated, allowing a more precise annual energy generation calculation. For various wind turbines a capacity factor analysis is presented with its disadvantages explained. To overcome these issues the concepts of economic efficiency and conversion efficiency are explained. These prevent some of the typical methods to enhance the standard capacity factor

expression. The combination of these three methods allows selection of the most suitable wind turbine for a site.

The concept of a mini-grid is an isolated power generation and distribution system, which can have its renewable energy sources, centralised or decentralised. The methods used to coalesce conventional generation with renewable energy technology forms another key piece of this research. A design methodology for the development of a hybrid power system is created with examples used from projects attributed to the author. The harmonising of the renewable energy sources with the conventional generation while providing a stable and robust grid is explained in detail with respect to the generator loading and control. The careful control of the renewable resource output is shown to allow a greater overall penetration of renewable energy into the network while continuing network stability. The concept of frequency shift control is presented, simulated and demonstrated with reference to the Eco Beach project. This project epitomises much of the research that has been presented in this dissertation. It combines centralised and decentralised inverters, with battery storage and the control of diesel generators. An overall controller dictates the optimum times to charge or draw from the battery based upon the local environmental and time of day variables. Finally, the monitoring aspects of this project are representative of a future smart grid where loads may be shed on demand through under frequency or direct control.

Acknowledgements

The last four years has been an amazing and exciting journey. I still look back and wonder what my Professor saw in an ambitious, however naive twenty-four year graduate of Electrical Engineering from the University of Western Australia. I had little knowledge of renewable energy engineering when I began this research. After four years under the guidance of Professor Chem Nayar I was lucky enough to project manage and engineer the largest hybrid renewable energy system ever implemented in Western Australia. Professor Nayar, I would like to thank you for your careful steering of my development for our mutual success. The industry partner Regen Power is a unique and rewarding avenue for research and development.

Being the only child by migratory parents from the UK I have relied and depended upon many friends for guidance, support and encouragement over the last few years. In no particular order I would like to thank Brett Chalmers, Reuven Gordon, Joel Mendelson, Nicholas Blackman, Timothy Anderson, Christina Smolarek, Omar Hafez, Adrian Boeing, Shanil Heart, Matthew Trigg, Greg Cresp and Daniel Wedge. Also, my housemates who have tolerated my angst include Luke Cream, Jason Foo, Estelle Winterflood, James Crowe and Alexander Pitt, thanks guys! I would also like to include a special mention of Emma Jackson who gave me the confidence to start on this process in the first place.

Many people have helped me with various aspects of the work in this thesis. The Curtin University staff and students; Dr Sumedha Rajakaruna, Prof Syed Islam, Mark Fowler, Zibby Cielma, Russell Wilkinson, Roy Mercer and Dedet Raiwan. Some students who have helped me with various aspects of this research include; Timothy Clements, Vlatko Marjanovich, Aileen Wong and Leslie Tan. Many other people have influenced my research and been solid sounding boards for ideas and applications, a few who deserve mention are; Mike Dymond, Jatuporn Sukhumjitpittayotai, Wuthipong Suponathana, Durmus Yildiz, Dave Feeney, Lawrence Borle, Edward Blackley and John Woodland.

Finally, I would like to thank and dedicate this thesis to my mother, Carol Darbyshire. Without her enduring and everlasting love and support I would have given up. She supported me though some tough times while letting me live my own life. Thanks for the constant knowledge of your support even when you aren't sure where I am….

Table of Contents

Table of Figures

Table of Tables

Equations

Symbols

Symbol	Description	Units
A	Wind turbine blade swept area	m^2
c_L	Speed of light	m/s
c	Rayleigh scale parameter	
C	Capacitance	F
C_p	Aerodynamic performance coefficient	
D_{WT}	Diameter of wind turbine	m
D	Day number of year	
E	Energy generated	J
E_{photon}	Energy of an incident photon	J
f	frequency	Hz
$f(\nu)$	Wind probability distribution	
h	Planks' constant	Js
I	Solar irradiance	W/m^2
I	Current by denotation	A
I_L	Light generated current	A
I_O	Output current	A
I_S	PV cell reverse saturation current	A
φ	Earth's angle to elliptical plane	°
k	Rayleigh shape parameter	
k_B	Boltzmann's constant	J/K
λ_{photon}	Wavelength of photon	m
λ	Tip-speed ratio	
Lat	Latitude of the location	°
L_D	Average day length (day time)	hrs
L_S	Average daily sun hours	hrs
L_W	Average wind only time (night time)	hrs
M	Number of strings in PV array	
n	PV cell diode ideality factor	
N	Number of cells in PV array string	
ν_{WIND}	Wind speed	m/s

n_S	Shaft speed	rpm
n	harmonic order	
ν_T	Transition wind speed	m/s
P	Power by denotation	W
q	Charge on a electron	C
R_{WT}	Wind turbine blade radius	m
ρ	Air density	kg/m3
R	Resistor	Ω
R_P	PV cells equivalent parallel resistance	Ω
R_S	PV cells equivalent series resistance	Ω
t	time variable	s
T	PV cell temperature	K
V	Voltage by denotation	V
V_m	Magnitude of a voltage sinusoid	V
ω	Angular rotational speed	rad/s
z	Vertical height	m

Acronyms

AC	Alternating Current
AGM	Absorbed Glass Mat
BoM	Bureau of Meteorology
CAR	Controller Adjustment Rate
CCM	Continuous Current Mode
CC-VSI	Current Controlled Voltage Source Inverter
CRoC	Controller Rate of Change
CSI	Current Source Inverter
CT	Current Transformer
CV	Constant Voltage
DC	Direct Current
DCM	Discontinuous Current Mode
DG	Diesel Generator
GUI	Graphic User Interface
HAWT	Horizontal Axis Wind Turbine
HCCU	Hybrid Control Centre Unit
IC	Incremental Conductance
IM	Increment Magnitude
LC	Inductor Capacitor Filter
LCL	Inductor Capacitor Inductor Filter
LOLP	Loss of Load Probability
NASA	National Aeronautical and Space Administration
MPP	Maximum Power Point
MPPT	Maximum Power Point Tracking
pdf	Probability Density Function
PLL	Phase Lock Loop
PMG	Permanent Magnet Generator
P&O	Perturb & Observe
PoE	Power over Ethernet
PV	Photo-voltaic
PWM	Pulse Width Modulation
SAIDI	System Average Interruption Duration Index

SAIFI	System Average Interruption Frequency Index
SMU	System Monitoring Unit
SOC	State of Charge
SWIS	South West Interconnected System
TSR	Tip Speed Ratio
VAWT	Vertical Axis Wind Turbine
VSI	Voltage Source Inverter
VC-VSI	Voltage Controlled Voltage Source Inverter
VRLA	Valve Regulated Lead Acid
WT	Wind Turbine

1. Introduction

The research presented in this thesis strives to provide a framework for future off-grid and edge of grid electricity generation systems. Four main objectives were defined to justify the research.

These objectives are;

- Develop power electronics and control topologies for stable on-grid and off-grid renewable energy generation systems.
- Maximise the use of the renewable energy sources in electric power systems.
- Increase overall hybrid system efficiencies.
- Decrease the dependence on fossil fuel based energy sources, which consequentially reduces carbon dioxide emissions.

This introductory chapter outlines the reasons and justification for the research area. It discusses the key energy generation sources of the sun and wind and the hybridising of these two sources through the technology of power electronics. The solar section of this chapter briefly introduces the photo-electric effect through the photon/electron interaction with the objective to show the PV cell as a current source. The layout of PV cells into modules, and modules into arrays is presented to allow interconnection into complete systems. For a PV array the continually changing solar irradiation causes the system to not operate at its optimum MPP. The reasons of this and methods to extract the maximum power are presented and used in following chapters. The current state of PV technology is presented and finally the differences and benefits of using fixed or tracking PV arrays is presented.

The wind section of this chapter introduces the energy available in the wind and methods that are used to extract it. Various WTs and their operational characteristics and control are presented with a focus on the smaller types of WTs, which are applied in this thesis. The techniques to mathematically model the wind resource is presented with the use of both Weibull and Rayleigh probability distributions. These mathematical functions are routinely used throughout this work to assess the energy that can be collected in different wind regimes. Finally, an introduction into the reasons behind wind MPPT is discussed as background for further chapters.

The next section of this chapter presents an introduction to the power electronic elements used throughout the dissertation. The three major groups of power electronics used in this dissertation are rectifiers, inverters and dc-dc converters. The mathematics, general operation and design of each of these components are introduced at a level required for the forthcoming chapters

Finally, different methods of interconnecting the generation sources are briefly explained with methods to integrate them into a grid. The methods in which wind, solar and conventional generation sources are coupled together to form stable, robust, renewable based power systems are a central goal of this work.

This introductory and background chapter introduces the key elements that allow the reader to familiarise themselves with the key concepts which are further explored in this dissertation. The thesis' overall layout, the authors' original contribution and publications begin this chapter.

1.1. Thesis Structure

This dissertation is divided into eight chapters.

Chapter one, the introductory chapter provides the justifications for the research and the framework for which the work is presented. The background theory and literature review is contained in this chapter. This thesis draws on the areas of power electronics, solar energy concepts and wind turbine theory. The basic premises of these areas and the key equations used throughout the rest of the work are defined in chapter one.

Chapter two builds the simulation environments for the power electronic blocks that are required to test the work in proceeding chapters. PSIM and Visual Studio C++ are extensively used to create the models and MATLAB and Mathematica are used to complete the statistical analysis and mathematical modelling. Complete models of the VSI, both stand alone and grid connected along with the voltage and current control techniques. The differing current control techniques of PI comparator and hysteresis band control are simulated. The bi-directional nature of the H-bridge is explained as a method to allow battery source charging. Finally, the interfacing of solar PV or wind turbines with inverters is investigated with differing approaches discussed. The current commercialised topologies are presented from key manufacturers with their advantages and disadvantages.

Chapter three presents the methods used to extract maximum power from solar and wind generators. The theory of MPPT is explained, derived and simulated. In order to allow accurate analysis of solar MPPT an accurate mathematical model is developed based upon the Newton-Raphson algorithm. This model is then complied into a dynamic link library based upon a configurable solar array from a standard PV modules data sheet information. The techniques of solar MPPT of P&O and IC are simulated and present the advantages and disadvantages of both systems. An analogy is draw between rapidly changing solar conditions and inclement wind conditions, which allow a novel IC, wind algorithm to be developed. This wind IC MPPT is simulated and analysed allowing an optimal tracking speed to be found.

Chapter four introduces the new concept of the complementary hybrid system and compares this with other traditional interconnection topologies. A PSIM/Visual Studio C++ model is developed to allow comparison of the systems. MATLAB and HOMER are used to create a mathematical model, which will approximate the energy yield from each of the systems based upon a location. The concept of crossover loss for the complementary system is defined and calculated for differing solar and wind resource loadings allowing an optimal system be designed for any location. Experimental results from the Denmark project are presented and analysed. Finally other locations are selected and the most ideal hybrid system topology is defined for each one.

Chapter five presents a statistical analysis of wind resource information to obtain a measure of the validity of satellite data verses ground measured data. The box and whiskers plot is used to display the results of the work. Useful methods to digitalise power curves and create Weibull distributions in Microsoft excel are explained. Finally an analysis of differing commercial small wind turbines is presented. The new concepts of conversion efficiency and economic feasibility are defined and calculated alongside the tradition capacity factor definition to allow a more thorough approach to wind turbine selection criteria.

Chapter six presents methods to integrate solar and wind generation sources into new or existing conventional power plants. The centralised and distributed concepts are explained with methods to control and increase the renewable energy penetration levels. Eight design points are encapsulated into a generalised design methodology for any medium to large scale renewable based power system. Generator loading characteristics are included to allow a comprehensive approach the controller methodology for any such power station. The common and split bus topologies are presented as methods to integrate central inverter systems with battery storage into conventional generation plants. Finally two design examples are presented from projects attributed to the author, following the outlined methodology. The Turf Farm project was not implemented due to financial constraints. The Maldives systems were deployed over three islands in 2007, the system design for the island of Uligam is contained in this chapter.

Chapter seven presents the design, simulation and implementation of the Eco Beach Wilderness Resort project, from which the author was design engineer. This project was commissioned in April 2009 and is currently operating as a high class tourist resort south of Broome, Western Australia. At the time of writing it is the largest hybrid stand alone power system of its type in Australia. The design methodology presented in Chapter six is applied with special focus on the systems controller. A novel frequency shift control is used to limit the distributed renewable sources. PSIM is used to simulate this controller, which is based upon the load, renewable energy available and battery SOC. The systems inverter may operate in four modes of operation which are outlined in chapter seven. The chapter concludes with images from the commissioning of the system.

Chapter eight, the final chapter summarises the work conducted as part of the research for this dissertation. It highlights the key pieces of work, which are influential in the research area, and predicts some possible future areas where progress would be valuable.

1.2. Identification of Original Contribution

The key original aspects of this work are summarised below.

- Development of PSIM PV array model from common PV module parameters (Chapter three)
- Wind MPPT IC algorithm (Chapter three)
- Development of complete WT, power converter and control model in PSIM (Chapter four)
- Wind MPPT IC algorithm (Chapter four)
- Combination wind/solar inverter for grid connected applications, invention, development and testing (Chapter four)
- Combination wind/solar inverter for stand-alone applications (Chapter four)
- Concept of crossover loss for hybrid systems (Chapter four)
- Development of a comprehensive small wind turbine selection process (Chapter five)
- Medium to large hybrid system design methodology (Chapter six)
- Frequency shift to control large hybrid systems (Chapter seven)

1.3. List of Publications

J. Darbyshire, C.V.N., *A Wind and Solar Hybrid System Utilising a Single Grid Connected Inverter* IEEE TRANSACTIONS ON ENERGY CONVERSIONS, 2009. **(currently under revision)**.

J. Darbyshire, C.V.N., *Hybrid wind/solar energy systems for peripheral grid connected areas* Renewable Energy Journal, 2009. **(currently under revision)**.

J. Darbyshire, C.V.N. Modelling, simulation and testing of grid connected small scale wind systems. in Australasian Universities Power Engineering Conference. 2007. Perth.

J. Darbyshire, C.V.N. Modelling, Simulation and testing of grid connected PV system. in Symposium on Power Electronics for Distributed Generation Systems. 2007. Hefei: IEEE.

J. Darbyshire, C.V.N., Modelling, Simulation and testing of grid connected small scale wind systems, in Symposium on Power Electronics for Distributed Generation Systems, L. Chang, Editor. 2007, IEEE: Hefei.

Whaley, D.M.E., G. Soong, W.L. Ertugrul, N. Darbyshire, J. Dehbonei, H. Nayar, C.V. Investigation of a Low-Cost Grid-Connected Inverter for Small-Scale Wind Turbines Based on a Constant-Current Source PM Generator. in IEEE Industrial Electronics, IECON 2006 - 32nd Annual Conference on 2006. Paris, France: IEEE.

1.4. Energy resources for the 21st century

Scientists of the world are collectively concerned that the global demand for energy is increasing at a rate that cannot be matched by supply. The scenario of peak oil, the point where oil demand out paces supply is inevitable, the question is not if, but when this will occur. The world's recent yearn for energy principally comes from the less developed countries of the world striving to expand by using the same methods as more developed countries, principally sourcing energy from inexpensive fossil fuels. A high demand for cheap consumer goods in developed countries has ensured that manufacture in less developed countries with cheap labour has boomed. This combined with the recent availability of credit to finance expansion have caused an advancement of energy use and raw material consumption previously unmatched on our planet. Figure 1-1 shows the relative amounts of fuels used with respect to their energy content, where one million tonne of oil equivalent (Mtoe) is the same as 4,187 terajoules (10^{12}). This research aims to develop methods that allow people to live in ways which are more sustainable in terms of their electric energy consumption. The methodology and technology presented within this dissertation can be applied to any area in the world, and hopefully will be.

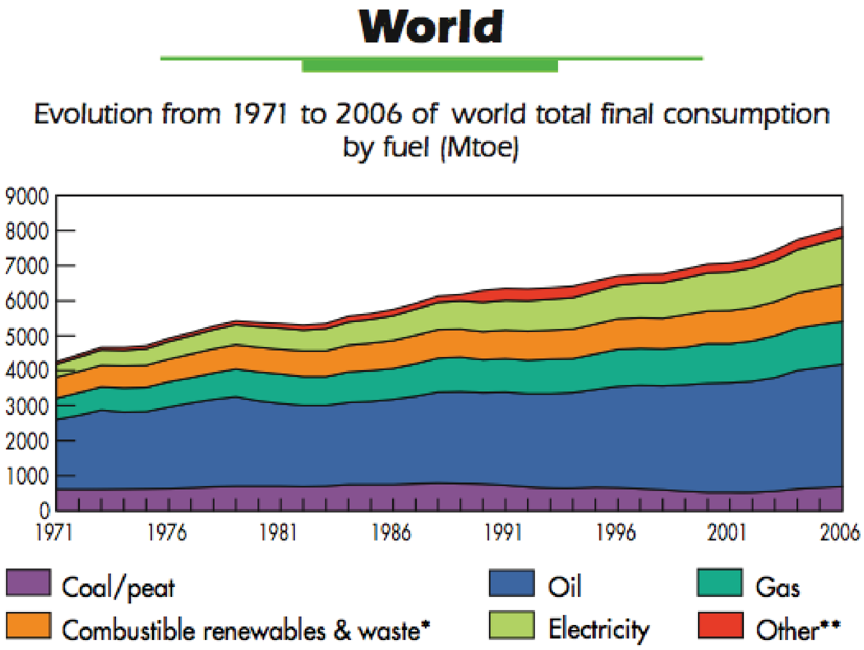

Figure 1-1 : World Total Energy Consumption [1]

The burning of any fossil fuel creates carbon dioxide and other by products such as sulphur dioxide and nitrogen dioxide, which cause acidification of the atmosphere. The effect of an increase in carbon dioxide concentration in the atmosphere is currently being debated around the world. The current consensus seems to be that global temperatures are slightly increasing however the overall effect of this increase remains uncertain. Many industrial processes are also causing other heavy metals to enter the environment with unknown future consequences. A large component of the carbon dioxide emissions are due to electric energy generation and the combining of renewable energy sources to form stable power system will allow us to decrease our dependence on fossil fuel electric generation methods. The research presented in this dissertation provides the future pathway and technology for islanded and fringe of grid electric power systems.

Novel economic market forces may cause a new energy ideology in the form of a cost for carbon dioxide emissions when a fossil fuel is burned. Figure 1-2 shows the current sources of CO_2 emissions based upon fuel. The Kyoto Protocol is an example of a request from the world that we should limit our emissions. At the recent United Nations Climate Change Conference in Bali, the United States was isolated from the rest of world by resisting the requested emissions cuts. By the meetings conclusion, the US had reluctantly agreed to the desired cuts and this has been seen as a fundamental turning point in moving forward [2].

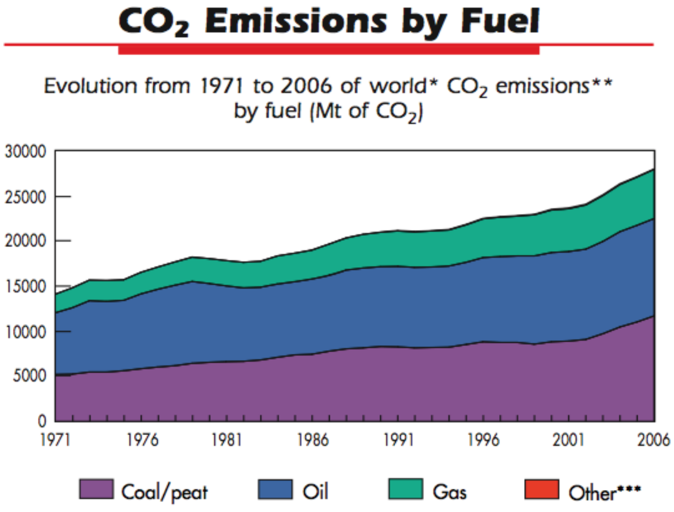

Figure 1-2 : World CO_2 Emissions [1]

As this dissertation is written the major economic markets of the world are under severe financial stress. The economics that underpin much of what generates the capital for businesses and governments to expand is slowing. A centralised approach may eventuate and the environment, energy sustainability and energy efficiency could be major winners among the current turmoil. An example of this is from US car industry has been forced to focus on development on low emission and electric vehicles by the US government of face bankruptcy.

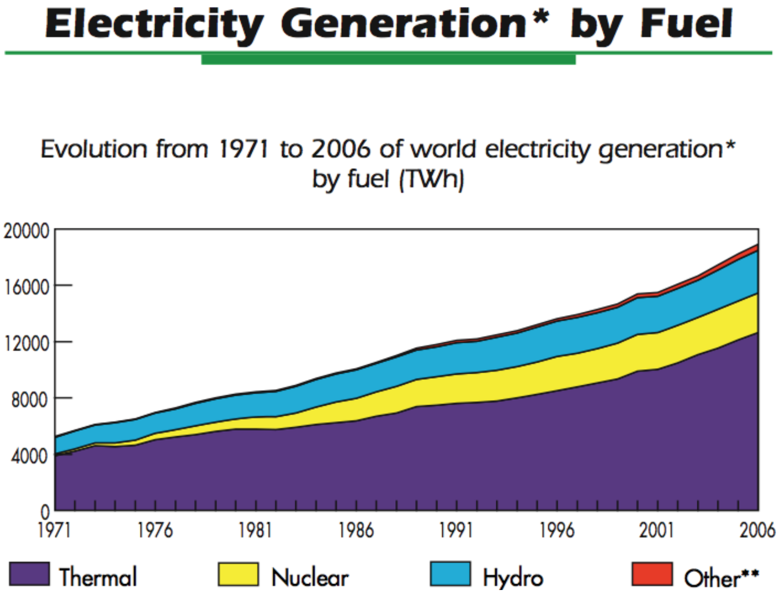

Figure 1-3 : World Electricity Generation [1]

The major uses of energy today are for the generation of electricity and transportation. A breakdown of the fuel sources used to generate electricity is shown in Figure 1-3. A combined approach of reducing overall energy consumption and using more efficient products is required to decrease the net fossil fuel dependence. The recent collaborative approach to removing incandescent lights is an example of increasing electric efficiency. The research presented in this dissertation presents method to reduce the requirements of fossil fuel generation for more sustainable and renewable methods, the electronics and control to successfully extract this free energy are the central focus of this research.

A large proportion of energy is used for transport, current trends in transportation are towards electric vehicles; and many cities already use electric rail networks and trams. The personal vehicle is likely to be replaced by its electric equivalent by 2030 with many hybrid, plug in hybrid and novel fuel vehicles under development. A common rebuttal to electric vehicles is that they merely shift the energy generation requirement onto the electrical grid. It is postulated that large centralised power stations providing energy for our cars seems far healthier and safer option then having noxious emissions and fuels within the city centres. Large-scale power generation for cities will still be provided by coal, gas or nuclear power stations for the foreseeable future, with the majority of the worlds natural hydro resources already exploited[3-5]. However, if we can use these sources for mainly backup purposes and increase the penetration of solar PV, solar thermal, geothermal, wind, wave and tidal energies, we can greatly reduce the requirements on fossil fuels. Methods to allow a greater penetration of renewable energy sources into existing power infrastructure is presented in chapter six.

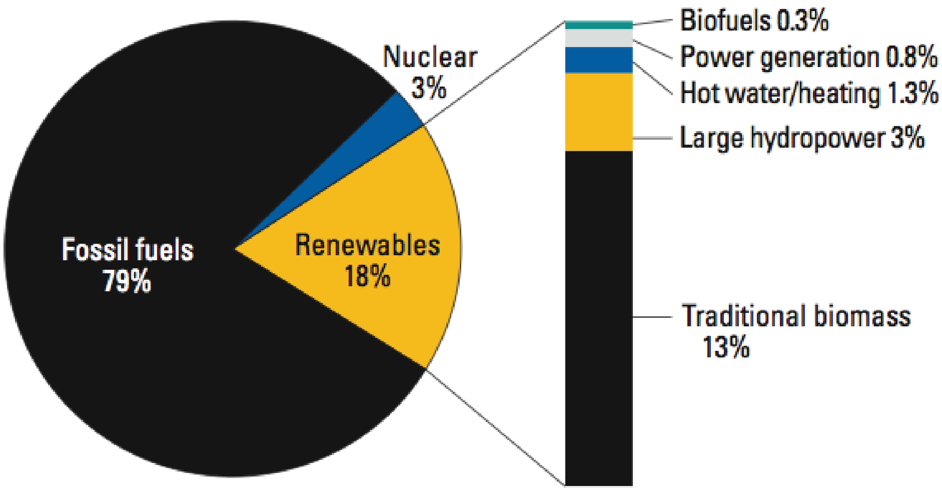

Figure 1-4 : Renewable energy share of global final energy consumption 2006 [6]

The technologies of solar photovoltaic and wind energy generation are mature, proven technologies that will be used within our electricity generation structure in the next century. Large scale wind farms are already prevalent throughout Europe where the electricity grid is well interconnected and can handle fluctuations of power generation. Australia, and specifically Western Australia, has a very dispersed “spider” type grid. Perth’s network is referred to as the South West Interconnected System (SWIS). The lack of system interconnection ensures we have power control problems, which Europe is only beginning to experience as their renewable energy portion approaches 30% penetration. This research addresses the concern of edge of grid power control issues by utilising a power electronic solution while generating excess renewable energy to stabilise the grid [7], this work is presented in chapter four.

The size of Western Australia ensures that many regional towns have stand-alone power generation systems. The majority of these power stations are only fuelled by diesel. This increasing price of diesel and added onus on carbon emissions is continually making these systems less popular and more expensive to operate. This research develops, designs, simulates and tests various hybrid energy system topologies with reference to major projects in which the author was involved. Case studies of the preliminary work for the Maldives “One Hundred Island Project”[8] and Eco Wilderness Resort[9] are presented which is presented in chapters six and seven.

1.5. Hybrid Energy Systems for the Future

There is an abundant level of energy available from renewable methods. The coalescing of solar and wind energy into a reliable power system is fundamental to this research. The key issue is that we, as humans, are not willing to wait for the renewable sources of energy to be available. We require an appliance to turn on whenever we desire, without a thought to the current availability of free renewable energy. The energy production infrastructure currently in place provides an immediate on demand of electricity or gas resources in many countries around the world. So, a requirement of any new installation is to combine with the existing infrastructure in a way that the renewable content of the supply is gradually increased until it is the dominant generation source in the system.

Renewable energy availability and user net load profiles can be considered mutually exclusive, a time will exist when the availability of renewably generated energy cannot match the users load demand. Therefore, the renewable resources of solar and wind cannot be relied upon to produce what is termed “base load” power. This problem ensures that either some sort of energy storage or immediate power generation from a traditional method is always required. The inclusion of some form of energy storage device allows a renewable generator to be treated as base load for a certain proportion of the day. A utility can have knowledge of the SOC of the renewable system for a peak load lopping application.

Due to the unpredictable nature of renewable sources the sizing of the traditional generation method is required to be the same as the peak system load. To date, this requirement has been preventative to the development of renewable technologies penetrating utility networks. A further deterrent to renewable energy sources impacting traditional utility networks is the inefficiency in the process of tradition thermal, coal, oil and gas turbines to produce less then their rated power. A power station operator will prefer to produce a turbine’s maximum power capacity all the time to decrease the net system efficiency loss, and so maximise the profitability of generation. This problem does not assist in promoting the increase in the renewable component into a traditional utility grid. However a large inverter’s efficiency loss at partial load is less affected then that of a conventional generation plant. This research focuses on the connection of renewable sources to the grid and the development of stable hybrid systems, which can operate in both stand-alone and grid connected topologies. The future developments of the power electronics to provide peak lopping or load levelling applications are explored in the final chapter via the Eco Beach project.

The goal of any renewable energy hybrid system is to convert the maximum amount of free energy from natural resources into electricity. The electricity generated can be used in two ways. It can be used to power the load immediately, such as a solar water pumping system, or to feed the energy into the local utility grid. Alternatively it can be stored for long term storage in the form of a battery, or short term in a supercapacitor or flywheel, novel methods allow it to be converted into a different fuel source such as hydrogen through an electrolyse. However, any conversion process inherently causes an efficiency loss, so minimising the conversion steps will increase the overall system efficiency.

Distributed energy generation infers that the energy is generated in various locations across the interconnected grid. A solar or wind source connected to this system is then “grid connected.” The Albany wind farm or BP fuel stations solar arrays are local examples of such systems. If for any reason the voltage or frequency is not within certain permissible limits the generation source will disconnect and the sites electricity supply will also fail. A “stand-alone” system is one that has no interconnection with a utility grid and a local generator or an inverter controls the voltage and frequency. The “edge of grid” system as defined in this dissertation can operate in grid connected or stand-alone operation. While grid connected the local loads can be supplied by either the grid or on site generation capacity. When in stand-alone operation an inverter provides power for the local loads however uses the renewable energy source preferentially over the battery storage. Increasingly sophisticated stand-alone hybrid systems are being developed with multiple renewable sources of energy. In times of meagre renewable energy capability diesel generation is the preferred option. The methodology of utilising this fuel resource when required, while controlling and minimising its usage is developed, simulated and experimental data is presented in chapters four, six and seven.

1.6. Multi-function Power Electronics, the Enabling Technology

Electricity is created in form of a DC or an AC. DC is created at a constant voltage, PV is a source of DC power, and a battery stores energy in this form. Faraday's law states that electricity created by movement of a wire through a magnetic field, which creates an AC. Most traditional sources power generation are AC where some form of turbine is forced to spin a generator to create electricity. WTs and diesel generators both create this form of electricity. AC is more readily used today due to its ability to be increased in voltage easily via a transformer allowing its distribution more efficiently. Power loss through transmission is proportional to the square of the current multiplied by the resistance of the conductor, i^2R, so the higher the transmission voltage the lower current and lower the line losses. Hence, the ability to increase or decrease the voltage in the transmission network is crucial, so this is the dominant method of electricity distribution[10, 11].

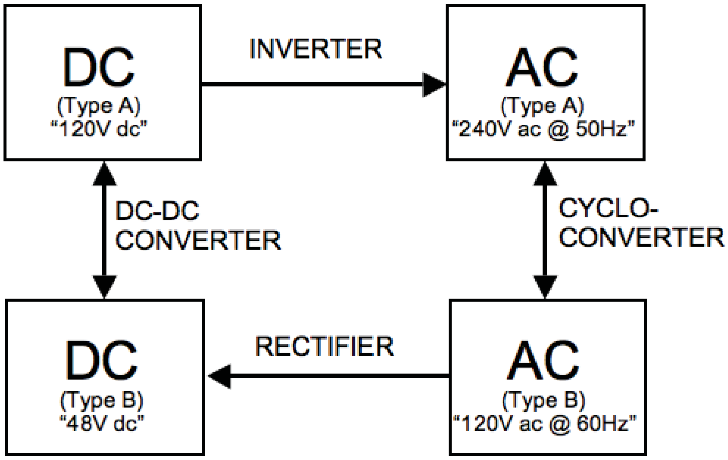

Figure 1-5 : Basic Power Electronic Components

Renewable power systems contain both AC and DC electricity generation sources; storage components are usually DC sources and the transmission of energy to the utility grid is AC [10, 12-17]. The ability to convert electricity between AC and DC and the reverse efficiently is the crux of this research and this area of research is known as power electronics. The basic building blocks of this discipline are the rectifier, DC-DC converter and inverter and cyclo-converter, these four elements allow the conversion of any type to any other type of electricity, Figure 1-5. The multi-function interface aspect of power electronics refers to the different ways by which these components can be coupled and the methods by which they are controlled. The majority of loads to be powered require AC electricity, however the majority of energy storage mechanisms are DC so an inverter is required. The battery however requires to be recharged with DC electricity, so a rectifier is required to perform this function from a generator. Alternatively a DC-DC converter can be used energised from another DC source such as a PV module. Cyclo-converters are not utilised in this research but are useful in interconnecting differing specification AC grids.

The multifunction control aspect refers mainly to the inverter or DC-DC converter control elements. Inverters can be either VSIs or CSIs depending upon the generation source [14, 18, 19]. This research focus's on the control methods of VSIs namely VC-VSIs or CC-VSIs, recently some inverters have the ability to operate in both modes and this will be developed in chapter three and demonstrated in chapter six and seven. Grid connected applications require CC-VSIs and stand-alone applications require VC-VSIs [19-22]. DC-DC converters by definition convert one DC voltage to another. Four main types of DC-DC converters exist; Buck, Boost, Buck-Boost and Cuk. Buck converters generate an output voltage lower magnitude their input voltage, boost converters increase the output voltage, buck-boost can either increase or decrease and Cuk are similar to buck-boost but reverse the polarity. This research confines itself to the buck and boost types and the control methods of these types, typically by providing maximum power point tracking or battery charging methods. Solar PV and wind MPPT require the voltage of the source be controlled in order to extract the maximum power. Battery charging applications require differing methods of control at different SOC; these are usually constant voltage while monitoring the current or constant current while monitoring the voltage [23, 24].

1.7. Hybrid Systems Energy Storage

Any renewable based energy system will, at times, have a discrepancy between the supply and demand of energy. This imposes a requirement of some form of energy storage device within the system. In times of high-energy production, energy can be stored and then drawn upon during times of low renewable resource availability. There is always an inherent loss of energy through any conversion process and minimising this is the key to research in this area. For any system that does not have an auxiliary backup generation source such as a diesel generator a small but quantifiable probability exists that the system will shut down due to an energy resource starvation. This is termed the LOLP[25-28]. If the renewable generation resource is often larger then the load requirement the batteries will be regularly full. Any excess renewable generation at these times will be wasted to prevent damage to the storage device.

The most common energy storage device is the battery, which converts electrical energy into chemical energy (charging) and chemical energy into electrical energy (discharging). Only rechargeable type batteries are useful for hybrid system energy storage. A rechargeable battery relies on a chemical reaction that is reversible. The applying of current to the electrodes and will force the chemicals into one state and they will naturally go back to the opposite state when attached to a load while producing an electrical current. The first rechargeable battery to be invented was the lead acid type in 1859 by Gaston Plante, 150 years later this is still the most readily used battery today. The most serious drawback to the lead acid type is its weight and capacity loss if left uncharged for very long periods of time. This loss is due to the formation of hard lead sulphate deposits on the plates over time causing a decreased plate surface area. Different models of lead acid batteries have been developed over time all relying on the same underlying chemistry. Broadly, they can be divided into gel or liquid electrolyte, open or valve regulated and plated or absorbed glass mat electrodes. The specifications of the cell chosen depend mainly on the specifications of its use. Remote area power systems tend to use one of three types flooded, VRLA-AGM or VRLA-Gel. Flooded cells are used were cost is the deciding factor and continual maintenance to the cells can be provided. AGM cells are used where the battery may be regularly moved however have a lower energy density but a lower self discharge rate compared to flooded and VRLA-Gel. VRLA-Gel type batteries are used in most remote area power systems where maintenance of the cells is difficult and life cycle time needs to be very long. Figure 1-6 outlines the types of lead-acid battery based upon its cycling requirements and rated current ability.

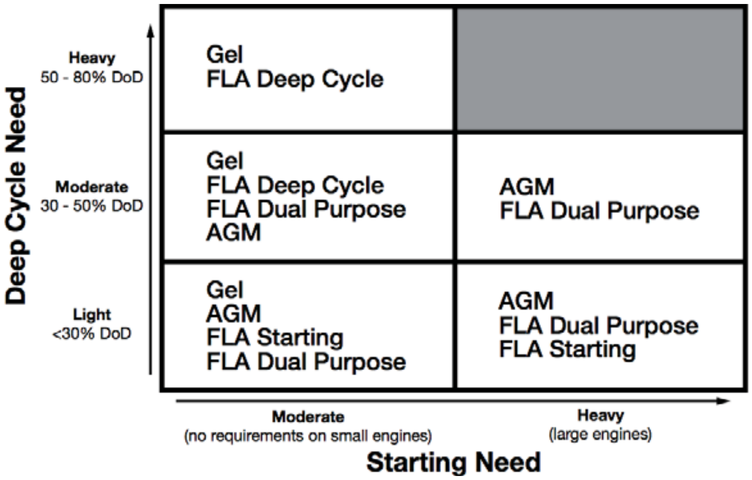

Deep Cycle Need \ Starting Need	Moderate (no requirements on small engines)	Heavy (large engines)
Heavy 50 - 80% DoD	Gel FLA Deep Cycle	▨
Moderate 30 - 50% DoD	Gel FLA Deep Cycle FLA Dual Purpose AGM	AGM FLA Dual Purpose
Light <30% DoD	Gel AGM FLA Starting FLA Dual Purpose	AGM FLA Dual Purpose FLA Starting

Figure 1-6 : Lead Acid Battery Type and Application Matrix [29]

Many other rechargeable batteries have been developed over the last century. The energy density for differing battery types is seen in Figure 1-7. The cost and lifetime of the newer technology batteries is the main reason higher energy capacity batteries have not increased in use over tradition lead-acid types. Currently CSIRO are conducting a trail with a fluid flow Zinc Bromine battery and Vanadium redox batteries have been used on Magnetic Island off Queensland.

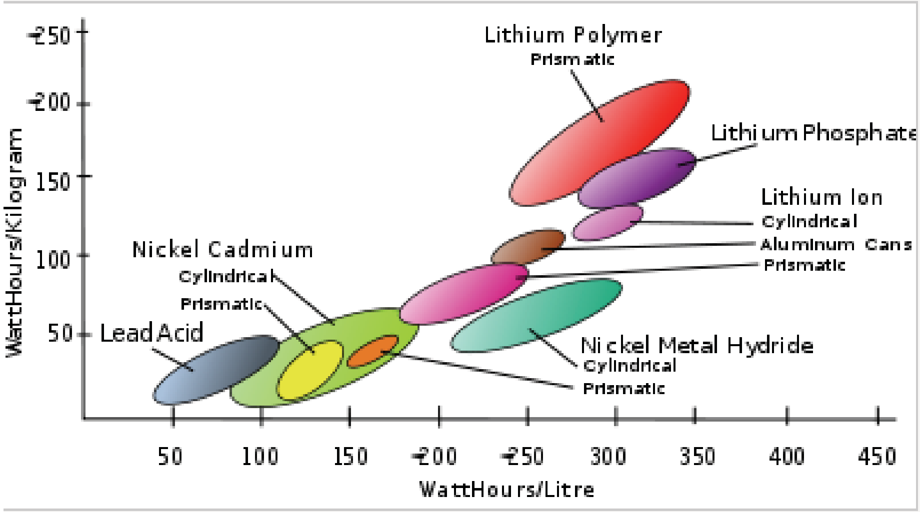

Figure 1-7 : Battery Energy Density

The charging regime of a battery can help determine a hybrid energy systems control strategy. Today, most systems attempt to keep the batteries at a high state of charge and minimise the depth of discharge to increase the overall lifetime of the cells. Chapters six and seven of this dissertation will address the complexities this creates in hybrid system control.

Mechanical methods such as a flywheel have also been successfully implemented for energy storage. A flywheel is a large mass that is rotated at very high speeds. During times of excess energy the flywheel absorbs energy and discharges while the resource energy is low. This method is especially successful for the interim time required for the diesel generator to start, however it includes significant frictional and power electronic losses. Powercorp, a Darwin based power electronics company has successfully integrated this concept in various locations for Verve and Horizon Power [30].

Solar thermal methods to absorb and store energy are also being developed here in Perth by Western Power and Worley Parsons. The concept uses the heat energy from the infrared spectrum of the Sun to melt a metallic salt that retains a high heat capacity. The heated fluid is then stored in a large insulated container, which can be used to create steam through a heat exchanger and power a conventional turbine and electric generator. The ability for the fluid to retain its heat allows the utility to offset the sunlight energy with the utility load, hence a better match of the generation and load profile.

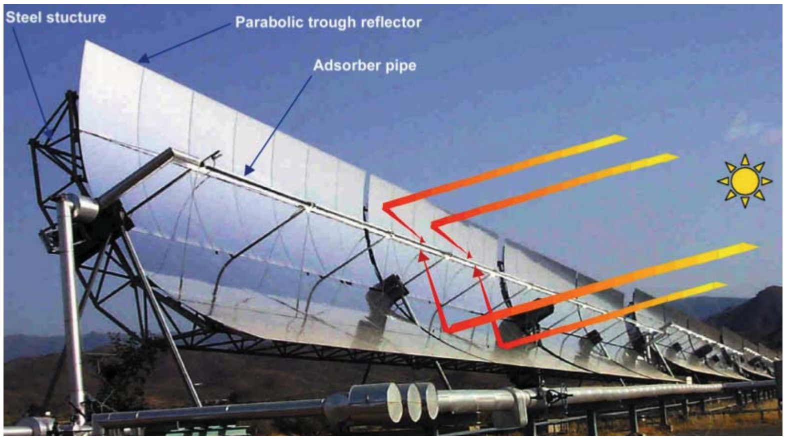

Figure 1-8 : : Solar Thermal Technology [31]

1.8. The Solar Resource

1.8.1. Solar Theory

The sun emits electromagnetic waves of many frequencies, which radiate out in all directions. The total solar power produced by the sun is approximately 3.8x10^{20} MW[32], the Earth receives approximately 1.74x10^{11} MW. Currently, the solar techniques used to harness this energy are solar thermal and solar PV, only the latter is used in this dissertation. Solar thermal techniques utilise the infra-red portion of the spectrum, this is normally concentrated using mirrors to a point which is used to heat a liquid and drive a turbine. Solar PV stems from the photo-electric effect which allows an incident photon with sufficient energy to collide with an electron and excite it into the semiconductors conduction band. Once in the conduction band the electron is free to flow around the circuit as an electrical current. This current is directly proportional to the number of incident photons on the device. The stronger the solar irradiance the more current, and so power the solar cell can produce. This phenomenon determines that the solar cell is a current source by electrical definitions[33, 34].

The photovoltaic cell is similar in construction to the PN junction of a diode. A diode is created be joining two materials with differing work functions, typically one from P-type, hole excess Silicon and one from N-type, electron excess Silicon. The imbalance of static and movable charges creates a void of charge between the materials called a space charge region, this redistribution of charges causes an electrostatic field and hence an electrostatic potential exists between the two layers at the materials junction. This electrostatic potential must be overcome in order to allow the junction to conduct. For a diode this is called the forward bias on voltage.

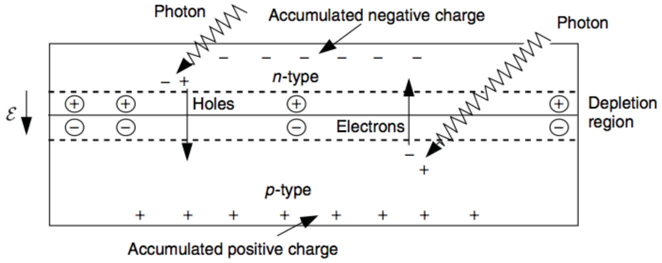

Figure 1-9 : Operation mechanism of a photo voltaic cell [32]

In a solar cell the photons are able to collide with the carriers, and a successful collision results in the creation of an electron hole pair at the junction. The doping and material type allows the energy barrier at the interface to be engineered to create the desired band gap. The energy of an incident photon is described by Plank's equation. From Plank's Equation, Eq 1-1, the minimum frequency, hence minimum energy to surmount the band gap can be calculated.

$$E_{photon} = hf = \frac{hc_L}{\lambda_{photon}}$$

Eq 1-1 : Plank's equation

When a photon transfers sufficient energy to an electron the ideal effect is to have the electron traverse the space charge layer and power the load. A successful photon electron interaction results in a light current. Other less desirable options are that the electron recombines with a hole before flowing across the depletion layer, or the electron loses energy and cannot surmount the energy barrier. The lack of charge in the depletion layer creates a small voltage drop known as the forward bias voltage. This voltage produces a small forward bias current opposing the light current. The combination of these current produces the most simplistic model of the solar cell. This model is developed in chapter three.

Many factors affect the overall efficiency of a solar cell, such as reflectivity of the surface, angle of the incident photon and the quality of the materials as well as the fabrication technique of the pn junction [35]. Currently there are five main types of types of solar cells in use; monocrystalline, polycrystalline, amorphous, Cadmium Telluride and tandem or multi junction cells, their efficiencies in laboratory conditions are shown in Figure 1-10.

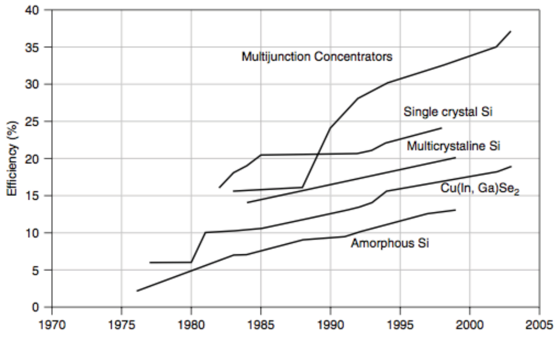

Figure 1-10 : Best laboratory PV cell efficiencies [36]

1.8.2. Solar Array Theory

Individual PV cells are connected in series to form modules. Typical commercial modules contain between 12 and 36 cells all connected in series. Bypass diodes are incorporated into each cell of the module to limit the loss of power if some of the cells are shaded or fail. When these diodes are not included the modules current is limited to that produced by the faulty cell due to the series interconnection. The module as a whole is also usually fitted with a single bypass diode.

A PV array is formed when multiple PV modules are connected together in either series strings or parallel branches or a combination of each. In multiple branch arrays, a situation due to cell degradation or shading can occur where one string will produce more current then another. In this case a blocking diode is required to prevent the back feed of current into the less powerful branch, potentially causing heating or hot spots from resistive loss within the lesser module.

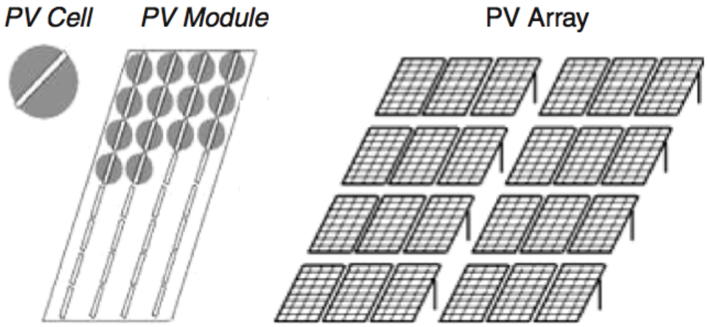

Figure 1-11 : PV configurations

The exact combination of series and parallel interconnections is limited by the power electronic conversion device, load or battery. The number of modules that can be connected in series is limited by the input voltage requirements. A higher DC voltage lowers the i^2R conduction losses by reducing the current but this is unpractical for many loads. Most systems without a power electronic conversion device are paralleled from 12 or 24V nominal PV modules. If the system uses a maximum power point tracking topology, a power electronic conversion device, the highest permissible string voltage with temperature variation allowance should be used to minimise the conduction losses.

1.9. Optimal Power Extraction For Solar Systems

The maximum power operating point for a PV cell, module or array is a function of the insolation, temperature and internal cell parameters. There are two types of PV MPPT; mechanical and electrical. Mechanical tracking attempts to remove the effect of the Sun traversing the sky and the seasonal tilt of the Earth. Electrical tracking ensures the solar panel is operating at its optimal power point as seen in Figure 1-14, this is effected by the changing insolation due to cloud, temperature and PV degradation [37].

Throughout any day the solar irradiation varies with respect to the angle of the panel to the sun and the thickness of the atmosphere, which absorbs a proportion of the sunlight. At the summer equinox at midday the maximum possible insolation would be available to a fixed PV system. Various mechanical tracking arrays have been implemented which rotate the panel orthogonally to the sun as the Earth rotates each day. This is called a single axis tracker. The tilt of the Earth, which creates the seasons, also effects the insolation. A dual axis tracker, which rotates the panel in the North-South direction, also has been previously developed. The cost due to the increase in mechanical complexity has to be traded off against the increased energy yield. Figure 1-12 shows the increase in energy yield from the use of mechanical tracking systems.

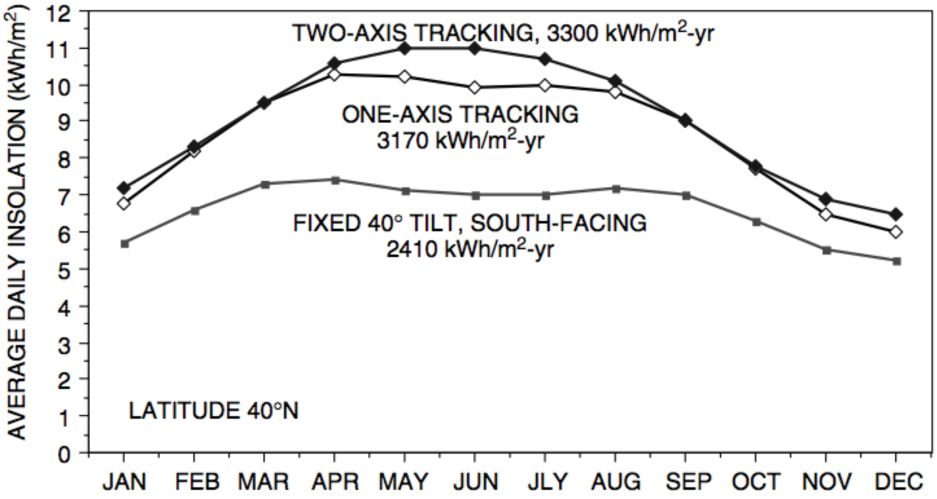

Figure 1-12 : Differences in insolation with and without tracking [32]

The irradiation level on the PV does not greatly affect the power output until the mismatch in angle is greater then 15 degrees, however this photon acceptance angle is different for differing panel types, new CdTe modules have a 25 degree acceptance angle. This observance has determined that for most applications the use of a dual axis tracker is superfluous. A single axis tracker is useful when the power output variance is required to be less then for a fixed array. Many PV power stations implement single axis tracker topologies as they create a more sustained peak daily power profile. Currently a fixed array is preferred for a commercial or residential application. In the southern hemisphere the panels should be angled to face north at an angle equal to the latitude of the location. This ensures the seasonal oscillation will be limited to 11.5 degrees in both directions and the daily peak will correspond to noon when the sun is the closest to directly overhead depending upon the time of year. The effect of an incorrect tilt angle is seen in Figure 1-13

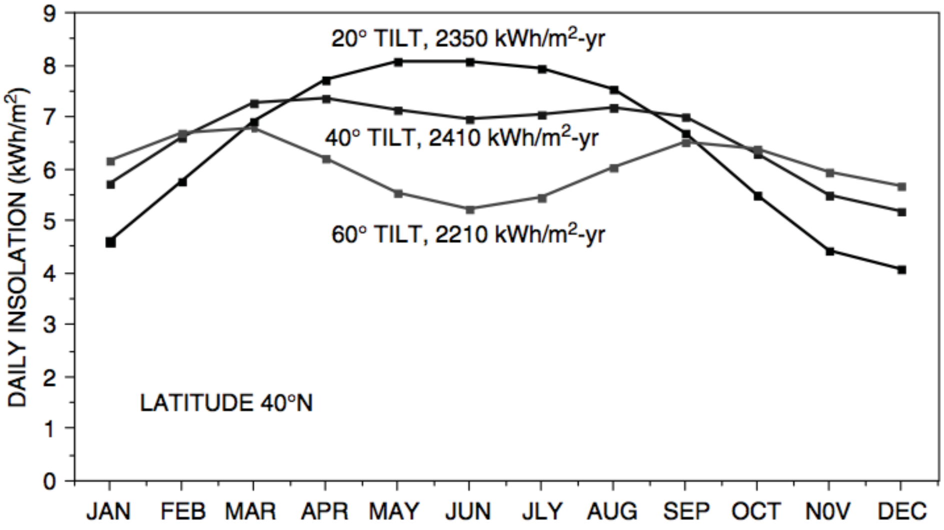

Figure 1-13 : Daily insolation for different tilt angles [32]

Electrical MPPT allows the changing conditions of insolation, temperature and panel degradation to be lumped together. These parameters are expensive or impossible to measure, so a system that can ascertain the MPP irrespective to these variables is required. The PV cell as a current source will produce a certain current based upon the voltage seen across the cell, module or array. A MPPT for a solar system utilises a DC-DC converter that holds the voltage across the panel constant while monitoring the current. The direction and magnitude of the current change allows the converter control and update the voltage imposed across the panel, with a goal of increasing the net power drawn from the panel. Figure 1-14 shows how the MPP voltage changes with differing levels of solar insolation, a closed loop controller which perturbs the voltage and sensors the change in current can continually update the PV arrays MPP allowing the maximum energy to be extracted for the module at all times[38-43]. Various algorithms to achieve this optimum power extraction will be investigated in chapter three.

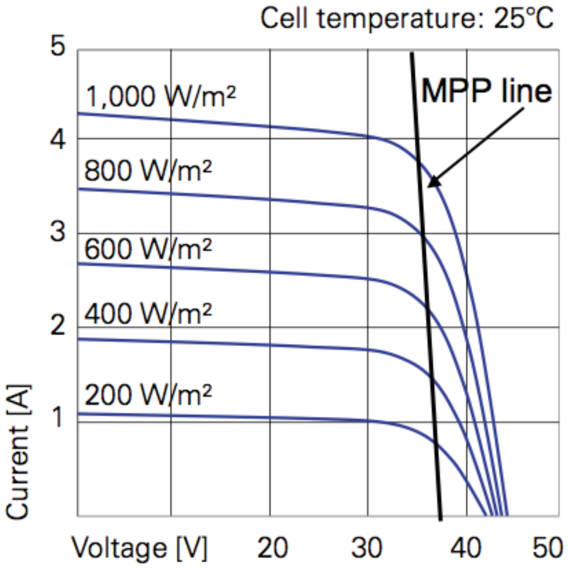

Figure 1-14 : Typical I-V characteristic of a PV panel, Lorentz LA130-24S [44]

1.10. The Wind Resource

The wind resource is a by-product of the heat from the Sun. The heating of sections of the Earth's surface causes low pressure areas while the cooling at night causes higher pressure areas. The wind is simply the moving of air particles from areas of high pressure to areas of low pressure. Humans have harnessed the power from the wind for hundreds of years, the first active use of the wind was to grind grain. Today through the use of electric machines we can create electricity from the movement of air via WTs [45].

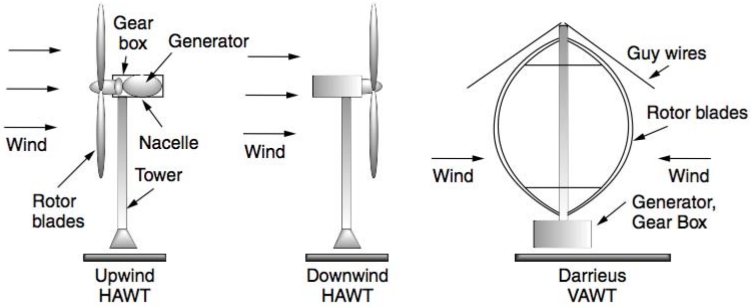

Figure 1-15 : Generic types of electrical WTs

All WTs can be classified as either horizontal or vertical axis machines as seen in Figure 1-15. VAWT have the advantage of generating power from any wind direction. The electric machine is located on the ground, making maintenance much simpler then for the VAWT. However, a major problem of VAWT is the difficulty in controlling the power generated by the machine or for it to tolerate very high wind speeds from storm conditions. A further problem is the inability for the VAWT to generate lift using the Bernoulli effect vastly reducing its efficiency (C_p) as it can only utilise power from the wind in the form of drag [46].

HAWT are more common and are now installed to maximum capacity of 93.864GW at the end of 2007 [47]. The ability to control the pitch of the blade allows faster power control then for the VAWT. This ensures the machine can endure the strongest of winds. The electric machines used within the WT are of different types depending upon the power generation capacity. Smaller machines are generally multi-pole permanent magnet machines, which can operate in a variable speed mode to ensure the maximum extraction of energy. Small and medium size WTs can be standard type induction machines; however their rotation speed is fixed by the grid frequency, and so cannot extract maximum power. The largest commercial WTs are mostly doubly fed induction machines. This type uses a power electronic converter between the rotor and grid, allowing some speed control and enabling maximum power extraction in some wind conditions. Enercon's large WTs utilise a direct drive synchronous machine removing the requirement of a gearbox and increasing the overall efficiency.

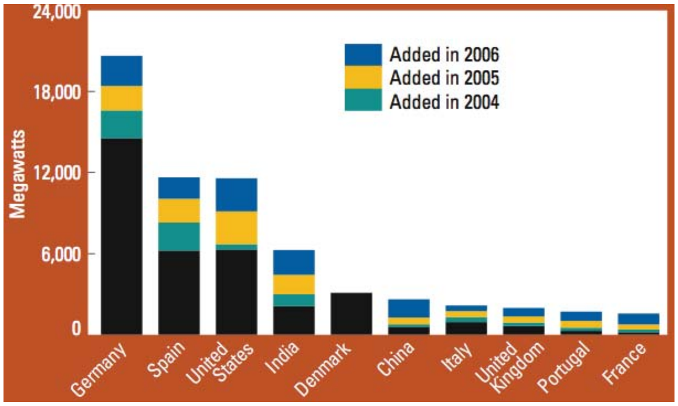

Figure 1-16 : Wind Power Capacity, Top 10 Countries, 2006 [6]

Wind farms, WTs operating together over a small region are most common in Europe, Figure 1-16. Wind power generation is slowly gaining popularity in Australia after initially some strong environmental concerns. The probabilistic nature of wind is generally seen as a drawback to grid integration as they cannot be relied upon to replace conventional generation. However wind farms with multiple WTs can be shown to increase the reliability of the wind resource for certain times of day. The Fremantle Doctor is a common reliable wind seen during the summer months in Perth, Western Australia, it also coincides with the peak summer city energy consumption. Future projects are likely to make use this resource, however the SWIS needs costly upgrades for its implementation. Unfortunately, wind farms cannot be relied upon when calculating the peak generation capacity for a city, although they can directly offset emissions from average energy production.

This research involves the integration of the WT into hybrid energy systems. These applications generally involve one or more small-scale WTs. Consequently the power electronics and control are developed for the PMG type of WTs within this dissertation. Projects involving the integration of WTs into power systems are discussed in chapters through the work.

1.10.1. Extracting Energy from Wind

The extraction of energy from any moving fluid requires the transfer of kinetic energy from the fluid to another object, causing it to move. A force from the fluid is subjected onto the object causing it to move or rotate. In a WT, the blades are forced to rotate around the central nose cone, which is coupled to an electric generator. The amount of energy that can be extracted from the fluid is proportional to the amount that is allowed to pass through or over the object. If all the kinetic energy was extracted then no fluid could flow from the object, conversely if no energy were extracted from the fluid there would be no interaction with the object. The balance of this energy transfer is the aerodynamic power co-efficient of the WT.

Fundamentally, the total mass transfer over the area called the stream tube must be kept constant, Figure 1-17. As the wind velocity at the front the WT decreases the pressure increases, conversely in the wake the turbine the stream tubes area increases so pressure and wind velocity decreases ensuring a balance of the energy. An optimum point exists where a maximum amount of energy can be transferred from the wind to the turbine blades. This maximum limit is called the Betz limit and provides an upper theoretical limit on the efficiency of any WT[45, 48-50]. A proof of this concept is provided as Appendix A1.

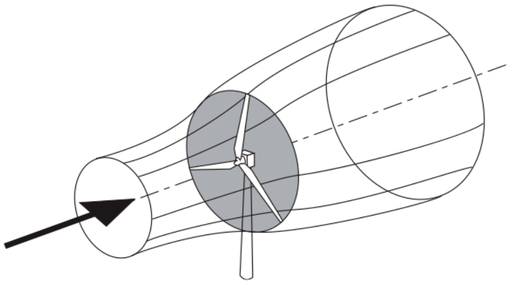

Figure 1-17 : The energy stream-tube for a WT [45]

Kinetic energy is described by:

$$E_K = \frac{1}{2}mv^2 = \frac{1}{2}\rho V^2$$

Eq 1-2 : Kinetic energy in the wind

Therefore the power in a given volume of fluid can be described as:

$$P_W = \frac{1}{2}\rho A v^3$$

Eq 1-3 : Power in the wind

The power transferred to the rotor can never be the same as the power in the wind, the ratio of this loss is known as the power co-efficient (C_p).

$$P_R = C_P P_W = \frac{1}{2} C_P \rho A v^3$$

Eq 1-4 : Power available in the wind

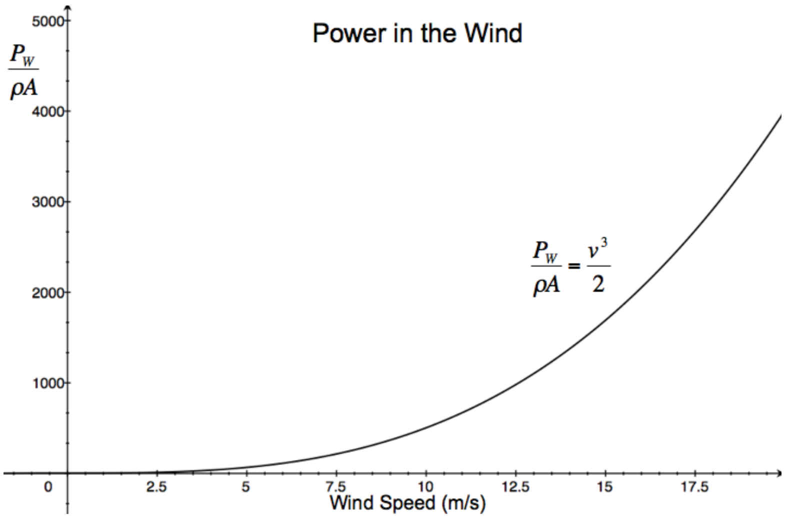

Figure 1-18 : Power in the wind

An ideal WT is designed to operate as close as possible to the Betz limit; this ensures the theoretically maximum power is extracted from the wind. The Betz limit of 59.3% represents the maximum proportion of power, which can be extracted from air. This is also the maximum rotor efficiency. The efficiency of a rotor is proportional to the speed at which it rotates and the velocity of air through the blades. The rate at which the blade cuts the moving air causes a thrust upon the blade, which is seen as a torque upon the generator. If the blade spins to fast not enough force from the moving air is imparted upon the blade, too slow and it begins to stall. The blades design, number of blades and aerodynamic lift which it creates determines the optimal rotational speed for any given wind speed. The relationship between blades tip-speed and wind speed is thus linear. The premise of all MPPT techniques for WTs is to keep the tip-speed ratio constant for differing wind speeds [51-53].

The tip-speed ratio is defined as:

$$TSR = \lambda = \frac{n_s \pi D_{WT}}{60 v_{WIND}} = \frac{\omega R_{WT}}{v_{WIND}}$$

Eq 1-5 : TSR

The TSR is a direct analogy of the aerodynamic lift created by the blades as they rotate, so a normalised bell curve of the performance coefficient can be predicted as the TSR changes. At low values of TSR the WT will stall as insufficient lift is created, higher values will not allow enough air impact on the blade also causing it to stall. WTs with fewer blades require a higher tip speed ratio for their maximum Cp, while turbines which create more thrust per rotation have a lower TSR for their maximum Cp. Figure 1-19 below, shows the tip speed ratio ranges required for the optimal power co-efficient for different WT designs.

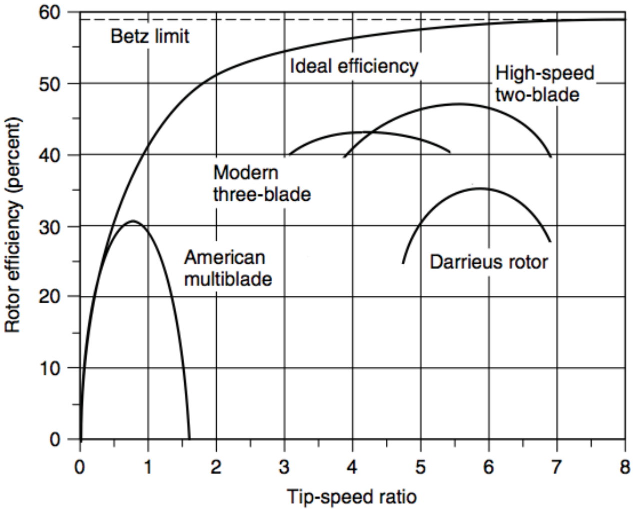

Figure 1-19 : Cp for various types of WTs [32]

Many different papers have empirically created models for the tip speed ratio of various WTs [54]. These are created from measuring the wind speed, rotational frequency and output power from the generator. From these measurements the common C_p-λ plot may be generated for any WT.

$$C_P = \frac{2VI}{\eta_{GEN} \rho A v_{WIND}^3}$$

$$\lambda = \frac{\omega R_{WT}}{v_{WIND}}$$

Eq 1-6 : Cp and TSR relationship

1.10.2. Optimal Power Extraction for Wind Systems

All wind MPPT regimes rely on the premise of maximising the power coefficient of the wind. This is achieved by maintaining the tip speed ratio constant with respect to the wind speed. Sensing the wind speed is notoriously difficult due to turbulence around the turbine or differing wind speed when measured at a different point. For larger WTs the wind speed may not even be constant across the diameter of the blades. This inconsistency in the measurement of the wind speed has promoted development of sensor-less MPPT techniques [50, 55-58].

The same method applies for MPPT whether or not a wind sensor is used. The angular rotational speed of the WT can be seen to be linear with respect to the wind speed, from Eq 1-5, so as the wind speed varies the rotational speed of the WTs blades should be varied accordingly. The TSR can be changed with a power electronic interface, usually a DC-DC converter that can vary the current drawn from the turbine while holding the voltage. Figure 1-20 shows the power map for a typical 20kW WT, the power – wind axes show the normal cubic power relationship until the rated wind speed of approximately 12m/s is attained. The rotor speed axis shows the effect of the WT stalling, or spinning at a lower TSR, which affects the power output. The optimal TSR and hence maximum Cp is seen here at approximately 130rpm.

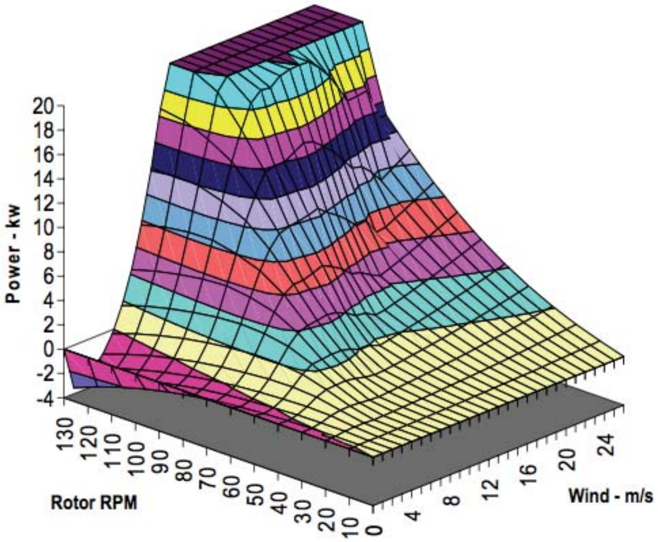

Figure 1-20 : Power map for a 20kW WT [50]

For a typical WT the voltage can be idealised as being proportional to the rotational speed of the WT and the current proportional to the torque or magnetic flux of the machine. If the current drawn for the machine is held constant for an instant in time the voltage or frequency can be sensed. The gradient of this frequency change can be attributed to a change in wind speed. The current reference can consequentially be updated and the process begins again. A closed loop MPPT algorithm can then track the changing wind speed with out using a wind sensor. This will be further investigated in chapter three and a method MPPT is developed.

1.10.3. Control Mechanisms for Wind Turbines

The options to control the power from any WT are limited. All methods involve decreasing the aerodynamic lift created upon the blades which inturn decreases the torque on the generator. These methods are:

- Adjustment of Tip-Speed Ratio
- Blade Pitch Control
- Turbine Yaw Rotation

Most commercial WTs use two or three of these control mechanisms. Variable speed WTs adjust the TSR to extract the maximum amount of available power up until the rated power output of the machine. At this rated power level the electrical generation side of the machine cannot utilise any more energy generated from an increase in wind speed. To limit the loading of the generator the controller deceases the aerodynamic efficiency, or Cp to “spill” the excess energy. This can be done electrically by drawing an excess current from the machine which forces it not to operate at its optimal TSR, which partially stalls the machine causing the power generated to be reduced [45, 59, 60].

The adjustment of the blade angle, with respect to airflow, decreases the force on the blade and hence torque on the generator. Two types of pitch control are used, passive and active. For smaller machines, less the 10kW, passive pitch control is preferred. To implement this, above rated wind speed, mechanical forces on the blades cause them to flex against the wind force reducing the lift, force per blade and hence torque on the machine, other methods counter balance the blade against a spring which will twist the blade with an increasing force. Larger WTs utilise active pitch control, which mechanically through actuators rotate the blades from the optimum angle reducing the force and so torque on the machine. The large doubly-fed megawatt Enercon type machines use this method.

The final method is yaw control, Figure 1-21, which rotates the nacelle out of the direction of the wind. This rapidly decreases the output power and is usually only used for extreme shutdown conditions. The 5kW Westwind WT used as an experimental set up in chapter four has an auto furl function as shown in Figure 1-21

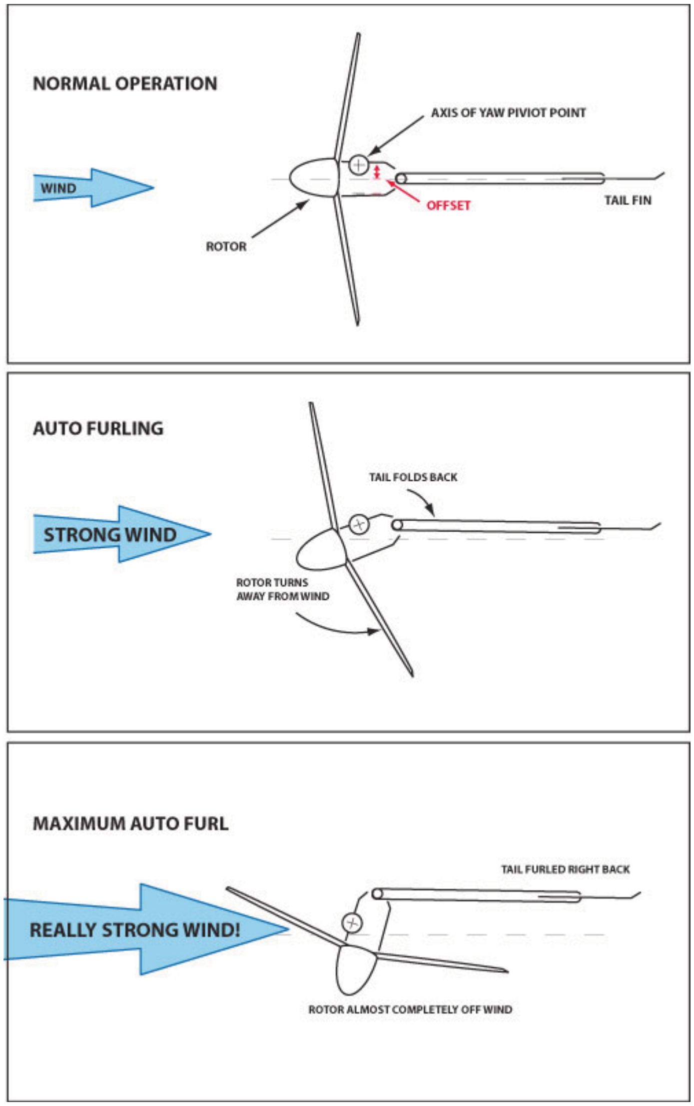

Figure 1-21 : Westwind auto-furl mechanism

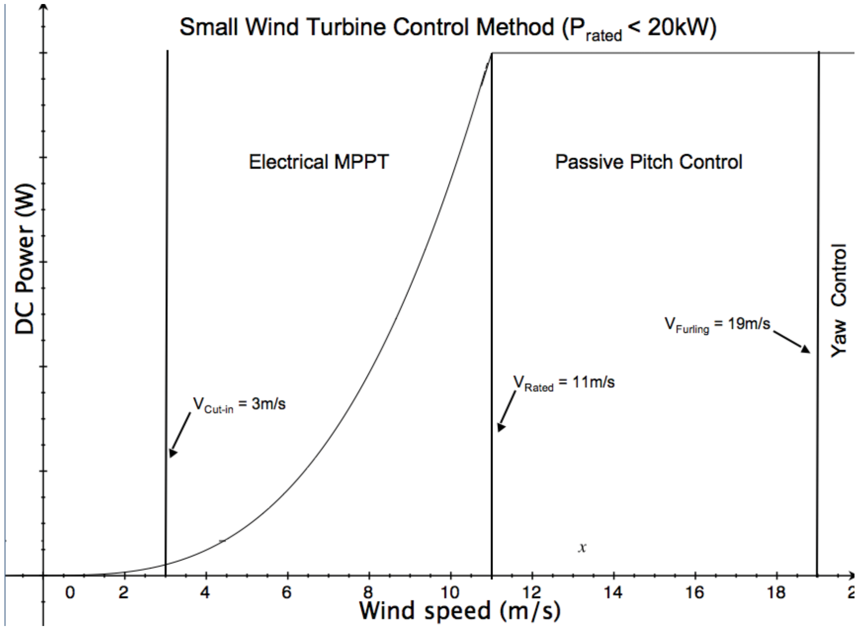

Figure 1-22 : Control methods for small WTs

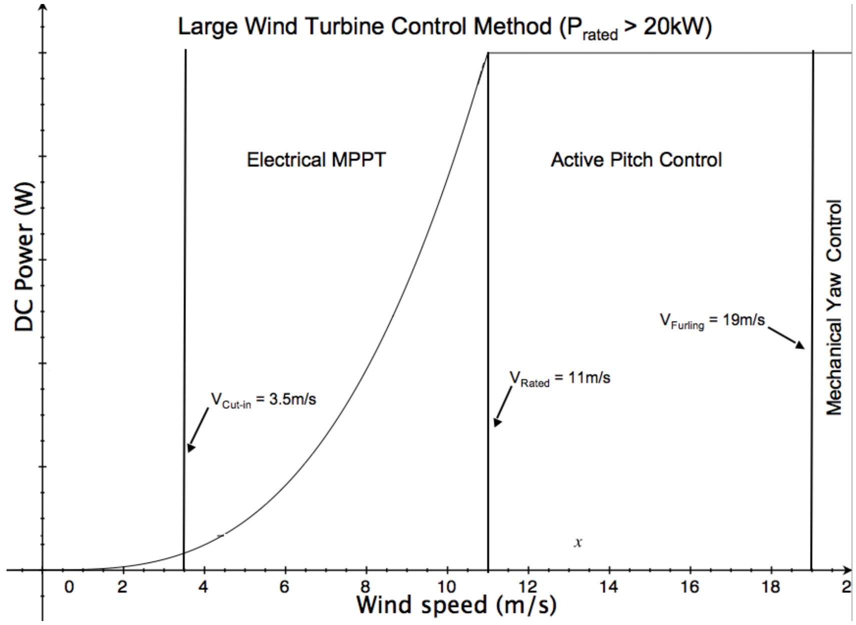

Figure 1-23 : Control methods for large WTs

Figure 1-22 and Figure 1-23 show the different control zones of each class of WTs dependant upon the wind speed. Both types operate essentially in the same way. The major discrepancies are that larger machines rely on mechanical control to limit the power generation through active pitch and yaw control. Larger machines also tend to have higher cut in wind speeds due to the increased frictional inertia of the rotor.

1.10.4. Wind Speed Probability Analysis

The energy that can be extracted from a WT, is dependent upon the amount of available wind at a given site. In order to approximate the energy yield a mathematical model of the wind regime must be created. This model is usually represented by a discrete probability density function which quantises the wind speed into nominally 1 m/s increments, as seen in Figure 1-24. For instance, all wind speeds from 1.5 m/s to 2.5m/s would be lumped into the 2 m/s bin width. This creates a small quantisation error but is acceptable for an annual energy yield approximation. Figure 1-24 shows the wind histogram from the measured wind data from the test site in Denmark, Western Australia. MATLAB is used to obtain the Rayleigh and Weibull probability distribution parameters [61].

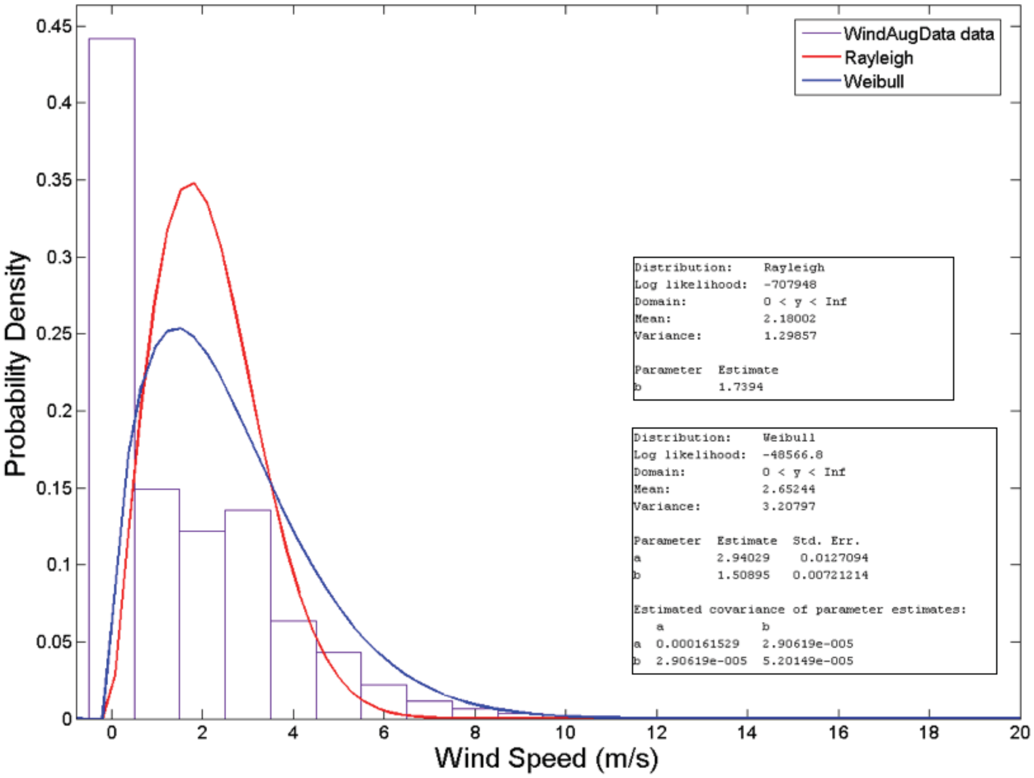

```
Distribution:    Rayleigh
Log likelihood:  -707948
Domain:          0 < y < Inf
Mean:            2.18002
Variance:        1.29857

Parameter  Estimate
b          1.7394
```

```
Distribution:    Weibull
Log likelihood:  -48566.8
Domain:          0 < y < Inf
Mean:            2.65244
Variance:        3.20797

Parameter  Estimate  Std. Err.
a          2.94029    0.0127094
b          1.50895   0.00721214

Estimated covariance of parameter estimates:
   a            b
a  0.000161529  2.90619e-005
b  2.90619e-005 5.20149e-005
```

Figure 1-24 : Denmark august wind histogram

The definition of any probability distribution function is that its area bounded by the curve is equal to one, Eq 1-7.

$$p(0 \le v \le \infty) = \int_{0}^{\infty} f(v)dv = 1$$

Eq 1-7 : Pdf definition

Also, the probability of any wind speed above a certain cut in wind speed can be calculated using, Eq 1-8.

$$p(v_{cut-in} \leq v \leq \infty) = \int_{v_{cut-in}}^{\infty} f(v)dv$$

Eq 1-8 : Pdf integral

There are two types of continuous probability functions that are generally used to approximate the discrete wind model. These are known as the Weibull and Rayleigh probability distribution functions. The Rayleigh is a specific type of Weibull distribution where the shape parameter, k, is fixed. A Weibull distribution takes the form of:

$$f(v) = \frac{k}{c}\left(\frac{v}{c}\right)^{k-1} \exp\left[-\left(\frac{v}{c}\right)^{k}\right]$$

Eq 1-9 : Weibull probability distribution function

Where k is the shape parameter and c is the scale parameter. For most locations where a WT is considered, the site generally exhibits strong continuous winds with a few lulls and occasional extreme conditions. In these locations the probability distribution can be considered to have a relatively evenly distributed wind probability density function. This corresponds to a Weibull function where the shape parameter is set as two. This special Weibull distribution is know as a Rayleigh distribution. The differing Weibull probability density distributions are shown in Figure 1-25.

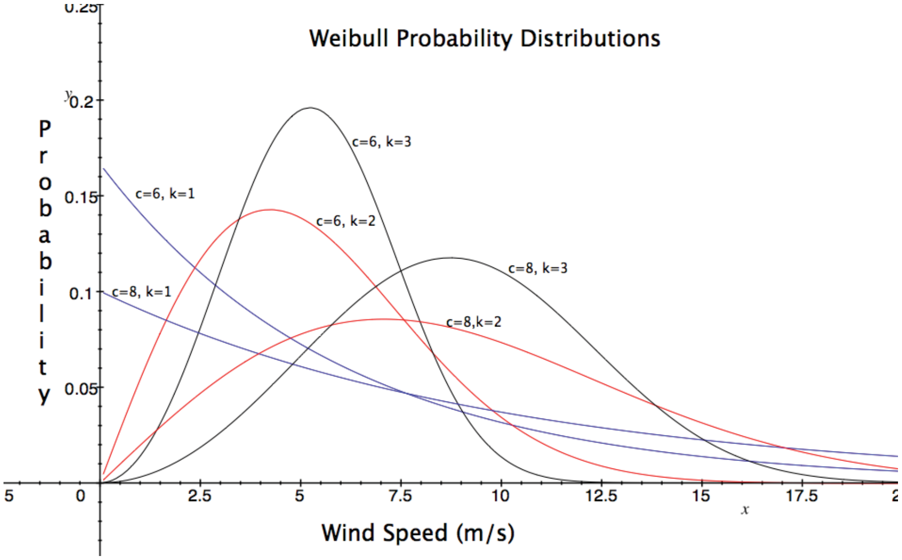

Figure 1-25: Differing Weibull probability distribution functions

The shape parameter for the wind regime at a site is usually between one and three and produces a fairly even bell curve. The scale parameter c is related to the sites average wind speed. This can be approximated quite easily if the Rayleigh distribution is used as seen below.

$$f(v) = \frac{2v}{c^2}\exp\left[-\left(\frac{v}{c}\right)^2\right]$$

$$\bar{v} = \int_0^\infty v \cdot f(v)dv = \int_0^\infty \frac{2v^2}{c^2}\exp\left[-\left(\frac{v}{c}\right)^2\right]dv = \frac{\sqrt{\pi}}{2}c$$

Eq 1-10 : Rayleigh mean definition

Using the Rayleigh approximation of the wind distribution a model can be made based upon only the sites average wind speed. So substituting into Eq 1-10 for c yields.

$$f(v) = \frac{\pi v}{2\bar{v}^2}\exp\left[-\frac{\pi}{4}\left(\frac{v}{\bar{v}}\right)^2\right]$$

Eq 1-11 : Rayleigh pdf definition

If the wind profile can be mapped to a Rayleigh probability distribution function the average power can then be approximated using the following cubed average method FIND REF.

$$\left(v^3\right)_{ave} = \int_0^\infty v^3 \frac{\pi v}{2\bar{v}^2}\exp\left[-\frac{\pi}{4}\left(\frac{v}{\bar{v}}\right)^2\right]dv$$

$$\left(v^3\right)_{ave} = \frac{6}{\pi}\bar{v}^3$$

$$\therefore \bar{P} = \frac{1}{2}\rho A\left(v^3\right)_{ave} = \frac{3}{\pi}\rho A\bar{v}^3$$

Eq 1-12 : Average power using the Rayleigh distribution

1.10.5. Wind Energy Analysis

For a site to be chosen to be the location for a wind turbine or farm the capital cost of the construction must be paid back within a definable period. This requires a prediction of an annual energy production. The basic expression for the calculation of annual energy for a site in kWh is seen in Eq 1-13.

$$E = 8760\int_{0}^{\infty} P(v)f(v).dv$$

Eq 1-13 : Energy generated from wind regime and WT

This expression is difficult to evaluate due to the power changing for each incremental change in wind speed. The most commonly adopted approach is to evaluate the wind probability distribution as a histogram, where each wind speed probability slice is taken as centred on the wind speed. For example, the probability the wind speed is *x* m/s would be given as:

$$P(x - 0.5 \le x \le x + 0.5) = \int_{x-0.5}^{x+0.5} f(v).dv$$

Eq 1-14 : Probability the wind speed lies with a bin width

The power output of the wind turbine at x m/s would then be mapped from the power curve. The total annual energy of this wind slice can then be represented as;

$$E_x = 8760P(x)\int_{x-0.5}^{x+0.5} f(v).dv$$

Eq 1-15 : Energy in a bin width

The summation over the whole probability distribution function in this way yields the total annual energy produced by the wind turbine.

$$E = 8760\sum_{n=\infty}^{n=1} P(n)\int_{n-0.5}^{n+0.5} f(v).dv$$

Eq 1-16 : Total generated energy across all bin widths

Typically methods to evaluate this expression utilise a computer speadsheet analysis. This method computes the most accurate energy production prediction. A further increasingly accurate modelling can be calculated by decreasing the wind speed bin width, set as 1m/s in Eq 1-14. However increasing accurate modelling may not be effective due to the measuring error in recording and modelling the wind speed probability distribution.

Due to the inaccuracies of any modelling to an error in wind modelling a simplistic but common approach is to calculate the average energy in the wind and assume an efficiency factor for the wind turbine.

$$E_{WT,annual} = 8760\eta_{WT}\overline{P} \approx 8365\eta_{WT}\rho A\bar{v}^3$$

Eq 1-17 : Annual energy using Rayleigh approximation

An efficiency factor of 0.3 is commonly used. Expression Eq 1-17 allows the annual energy production to be predicted from only the wind turbine average efficiency and the average wind speed data, assuming the site conforms to a Rayleigh distribution.

The wind energy available at the grid is then calculated by factoring the efficiency losses of the power electronic components.

$$E_{grid} = E_{WT,annual}\eta_{dc-dc}\eta_{inv}$$

Eq 1-18 : Energy available to the utility

1.10.6. Capacity Factor

The capacity factor is a convenient, dimensionless quantity, which directly allows the feasibility of any site to be easily considered. A site is considered excellent if the capacity factor is greater then 50%. The definition of the capacity factor is the proportion of energy produced in a year with respect to what the WT could produce at rated power over a year [32, 45].

$$CF = \frac{\text{Actual Annual Energy Production}}{\text{Total Rated Energy Production}} = \frac{\text{Energy Produced}}{8760 \times \mathrm{P_R}}$$

Eq 1-19 : Definition of capacity factor

The capacity factor will be utilised in chapters five and six in the analysis, sizing and suitability of hybrid systems.

1.10.7. Approximating Wind Speed at Differing Heights

The turbulence in the laminar flow of the air generally decreases with increasing height due to fewer land features disturbing the air. As a result of this a WT will produce more power the higher it can be situated, as the power is proportional to the cube of the wind speed, a small increase in height can cause a large increase in average energy output. A common approximation for the increase in wind speed from a change in height is given by Eq 1-20. A problem with transposing the height for a site from measured data is the Weibull parameters also vary with height. This produces an error in the overall energy analysis [49].

Currently, two main methods are used to determine the hub height wind speed with respect to the measured reference level [49, 62]. The method commonly used in for WT energy analysis in North America is seen below in Eq 1-20.

$$v = v_o \left(\frac{z}{z_o} \right)^{\alpha}$$

Eq 1-20 : North American height correction method [32]

The value of α varies with the roughness factor of the terrain surrounding the site. Common values of this parameter are seen in Table 1-I.

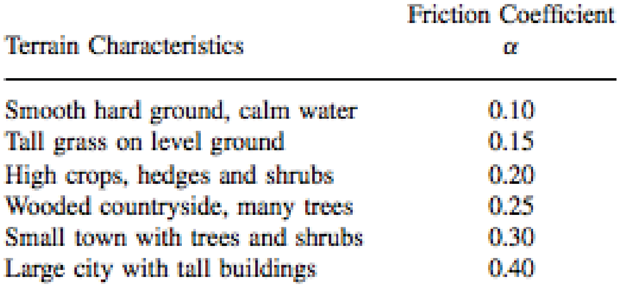

Terrain Characteristics	Friction Coefficient α
Smooth hard ground, calm water	0.10
Tall grass on level ground	0.15
High crops, hedges and shrubs	0.20
Wooded countryside, many trees	0.25
Small town with trees and shrubs	0.30
Large city with tall buildings	0.40

Table 1-I : US Commonly Used Roughness Parameters [32]

In Europe a different method is commonly used as seen below in

$$v = v_o \frac{\ln(H/z)}{\ln(H_o/z)}$$

Eq 1-21 : European height correction method

The value of α varies with the roughness factor of the terrain surrounding the site. Common values of this parameter are seen in Table 1-I.

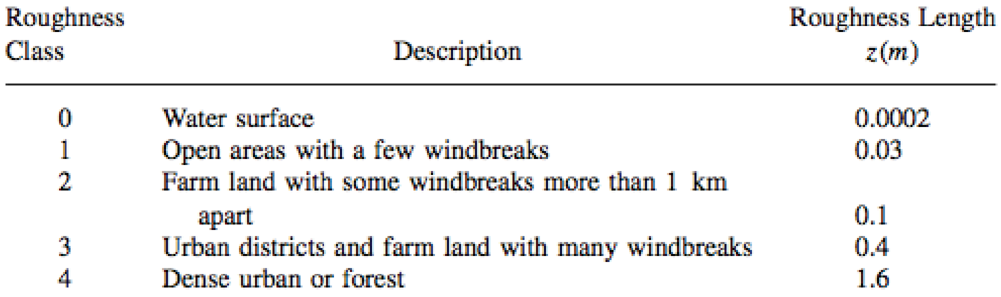

Roughness Class	Description	Roughness Length $z(m)$
0	Water surface	0.0002
1	Open areas with a few windbreaks	0.03
2	Farm land with some windbreaks more than 1 km apart	0.1
3	Urban districts and farm land with many windbreaks	0.4
4	Dense urban or forest	1.6

Table 1-II : Commonly Used Roughness Parameters [32]

Chapter five investigates the reliability of differing wind measurement and scaling methods.

1.11. WT Types and Grid Interconnection Methods

There have been eight main types of WT topologies developed since the 1970's. The power electronic interfaces required for grid interconnection are dependant upon the type of the WT generators. WTs can be classified into synchronous or asynchronous machines dependant upon the relationship between the stator frequency and generators rotational frequency. This is fixed for an asynchronous machine and variable for a synchronous generator. The synchronous relationship of the generator also defines the ability for it to operate as a fixed or variable speed machines allowing optimal tracking of the wind power co-efficient over all wind speeds. Fixed speed machines rotate at a fairly synchronous speed irrespective to the wind speed, they are designed to produce the maximum power at a certain wind speed and are thus operating at a lower power co-efficient at all other times [11]. These WTs use asynchronous machines such as a squirrel cage induction machine or a wound rotor concept as seen in Figure 1-26, Figure 1-27, Figure 1-28 and Figure 1-29.

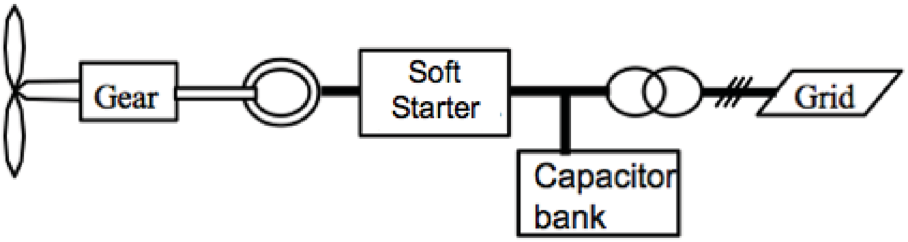

Figure 1-26 : (A) Asynchronous cage rotor induction machine with soft starter and capacitor bank, fixed at one or two speed with switched poles [46]

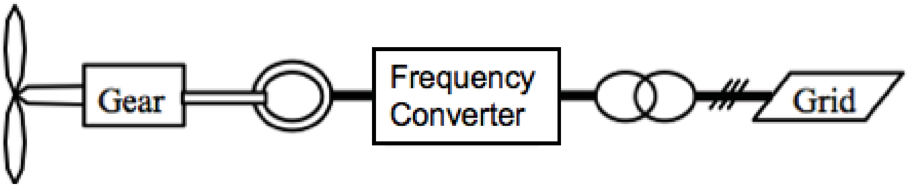

Figure 1-27 : (B) Asynchronous cage rotor induction machine with front end frequency converter allowing variable speed operation [46]

Asynchronous cage rotor induction machines rotate at a frequency based upon the frequency of alternating current at the stator, which creates the rotating magnetic field for the rotor. Active power will be produced when the rotor creates a positive torque in the direction of the rotating magnetic field. The magnitude of the torque produces a positive slip causing active power to be produced, however the stator still has large reactive power requirement drawn from the grid or capacitor bank, Figure 1-26. Figure 1-27 shows the same concept with the addition of a fully rated frequency converter that allows the stator frequency to be varied allowing variable speed operation. This concept is not readily adopted due to the cost of the required back to back inverter however Wind World [63] uses this approach for low wind speed operation allowing a smaller inverter component, it switches to standard operation as per Figure 1-26 for higher wind speeds.

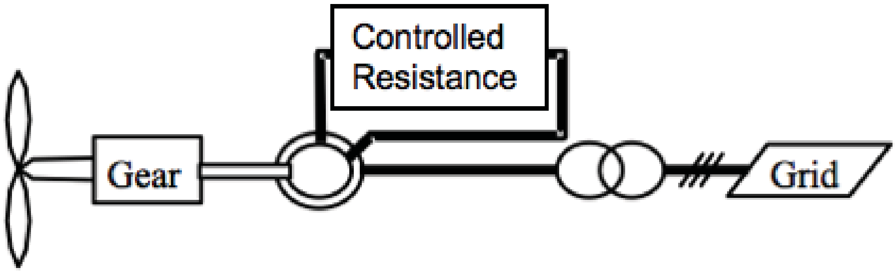

Figure 1-28 : (C) Wound rotor induction machine with variable rotor resistance concept allows slip control of up to 10% [46]

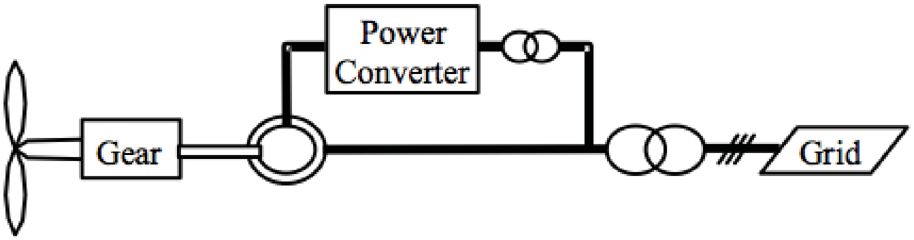

Figure 1-29 : (D) Wound rotor doubly fed induction machine concept allows wind speed range control with only 30% power rated converter [46]

Wound rotor induction machines allow the phases of the rotor to be passed out via slip rings to allow injection of alternating current. A differing magnetic field on the rotor interacts with the field on the stator allowing the rotor to spin at a ratio not determined by the stator frequency. Figure 1-28 uses a back to back converter to mimic a controlled rotor resistance, this allows the slip of the machine to be varied, by approximately 10%, allowing some speed variation. This is the concept used by Vestas known as OptiSlip [63]. The wound rotor doubly fed induction machine method, Figure 1-29, is currently the most popular due to its ability to operate over a large wind speed range with variable speed operation while only requiring a 30% sized power converter.

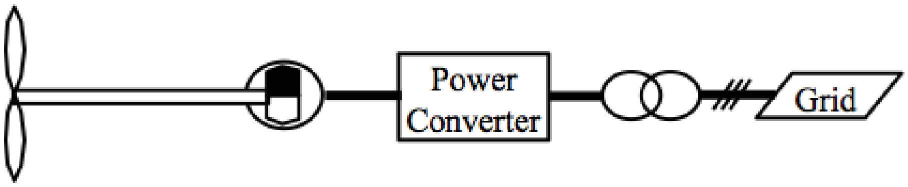

Figure 1-30 : (E) Permanent magnet synchronous machine [46]

PMSGs are self-excited removing the need for any direct connection to an AC source or control of the rotor magnetic field. PMSG induce a current in the stator for any rotation of the rotor, with the voltage produced being proportional the angular frequency of the rotation. The current is proportional to the torque developed on the generator. In cases of high wind speed causing high rotational speed a dump load controller is required to ensure the excess energy does not lead to an over voltage on the dc bus potentially destroying the inverter. The Denmark project discussed in chapters four and five is of this type.

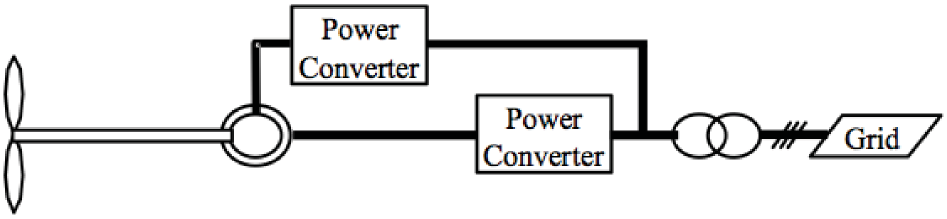

Figure 1-31 : (F) Multipole doubly fed wound rotor synchronous machine with both rotor and stator back to back power converters [46]

The preceding WT interfacing topology uses the wound rotor induction machine. Figure 1-31 is expensive extension to the standard doubly fed strategy seen in Figure 1-29. It utilises a second full power level four quadrant back to back converter to allow complete frequency control of the stator allowing the optimal power to be extracted at all times. The need for a gear box is also removed by using a multipole wound rotor induction machine.

Manufacturer	Wind Turbine	Topology	Control	Q Control	Variable Speed
NEG Micon	NM 2000/72	A	Active Stall	No	2 speed
Vestas	V80 – 2MW	D	Pitch	Yes	Yes

Gamesa	G52 – 850kW	D	Pitch	Yes	Yes
Enercon	E66 – 1.8MW	F	Pitch	Yes	Yes
Enron Wind	1.5s – 1.5MW	D	Pitch	Yes	Yes
Bonus	2MW	A	Active Stall	No	2-speed
Nordex	N80/2.5MW	D	Pitch	Yes	Yes
Dewind	D6 – 1.25MW	D	Pitch	Yes	Yes

Table 1-III : Summary of industry utilised topologies

Table 1-III shows that the most commonly implements power electronic and generator strategies used for large scale wind systems are the double fed induction machine topologies with the stator directly coupled to the grid, D and H. The older Danish type, A, is also still utilised by some companies.

In renewable hybrid systems applications the WT is often interconnected to a weak grid which is effected by the large reactive power component of the directly coupled types. This issue prevents the interconnection of the configurations C and D. Small scale applications of configuration A are possible where the local grid can be relied upon to provide the required reactive support. Options B and F all require full power frequency converters which are expensive to implement for most hybrid energy systems. Topology E utilising the PMSG is the most suitable for interconnection into remote hybrid systems due to its simple construction and requirement of only a single inverter and controller to allow interconnection to the local or utility grid [64, 65].

1.12. Power Electronic Elements

Power electronics is the technology that enables the controlled extraction of renewable energy. One focus of this research is the power electronics and control for the extraction of energy from solar and wind power systems. The other central aim of this research is to efficiently combine renewable sources to form a stable, reliable, low harmonic power system, which is able to operate efficiently for both on and off grid. This incorporates the use of traditional power generation techniques in the form of diesel generators with energy storage in batteries. This section provides background on the key power electronic components which are used throughout this dissertation.

1.12.1. Rectifiers

A rectifier is simplest power electronic building block and coverts AC to unregulated DC electricity. Rectifiers are inexpensive, require no active control and are very robust and reliable. A signal phase bridge rectifier contains four diodes, which conduct when the incoming voltage forces them to be forward biased in opposite pairs. A capacitor is then added to the output to allow some storage of energy, minimise the decrease in output voltage and reduce the output voltage ripple. However, the capacitor causes the voltage to be held higher at the load so the diodes only become forward biased for a much shorter period of time. The effect of this is the capacitor must quickly receive the loads power requirement, twice, in only a fraction of the switching period. This creates a triangular current pulse of short duration causing harmonic currents be drawn from the source. A filter is then usually applied to the input minimising the generation of these harmonic currents on the utility supply[12-14, 66, 67].

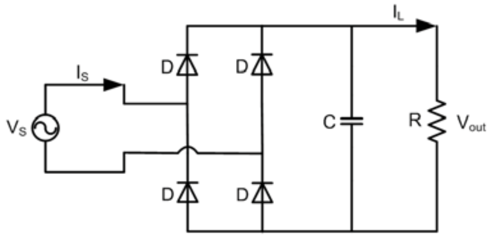

Figure 1-32 : Single phase rectifier

The output voltage waveform of a single phase rectifier without any filtering is the same as the absolute value of the input signal.

$$
\begin{aligned}
\left|V_m \sin(\omega t)\right| &= \frac{2V_m}{\pi} + \frac{4V_m}{\pi}\sum_{n=1}^{\infty}\frac{\sin(2n\omega t - n\pi)}{1-4n^2}\\
V_{dc} &= \frac{2V_m}{\pi}\\
V_{rms} &= \frac{V_m}{\sqrt{2}}
\end{aligned}
$$

Eq 1-22 : Fourier series expansion expression

The addition of an output capacitor increases the average output DC voltage while minimising the AC component.

$$
\begin{aligned}
\Delta V_{rip(p-p)} &\approx \frac{V_m \Delta t}{RC} = \frac{I_O \Delta t}{C} = \frac{V_m}{2\,fRC}\\
V_{dc} &= V_m - \frac{\Delta V_{dc}}{2} = V_m\left(1 - \frac{1}{4\,fRC}\right)\\
V_{ac} &= \frac{\Delta V_{rip(p-p)}}{2\sqrt{2}} = \frac{V_m}{4\sqrt{2}\,fRC}\\
RF &= \frac{V_{ac}}{V_{dc}} = \frac{1}{\sqrt{2}(1-fRC)}
\end{aligned}
$$

Eq 1-23 : Rectifier design equations

Figure 1-33 shows the simulation of a basic single phase rectifier with an AC line inductor. The four diodes have the effect of forcing an absolute value output voltage waveform with the capacitive storage element storing and releasing energy to reduce the output voltage ripple. The triangular input current can also been seen below, however it is smoothed by the inductor causing fewer harmonics on the source side.

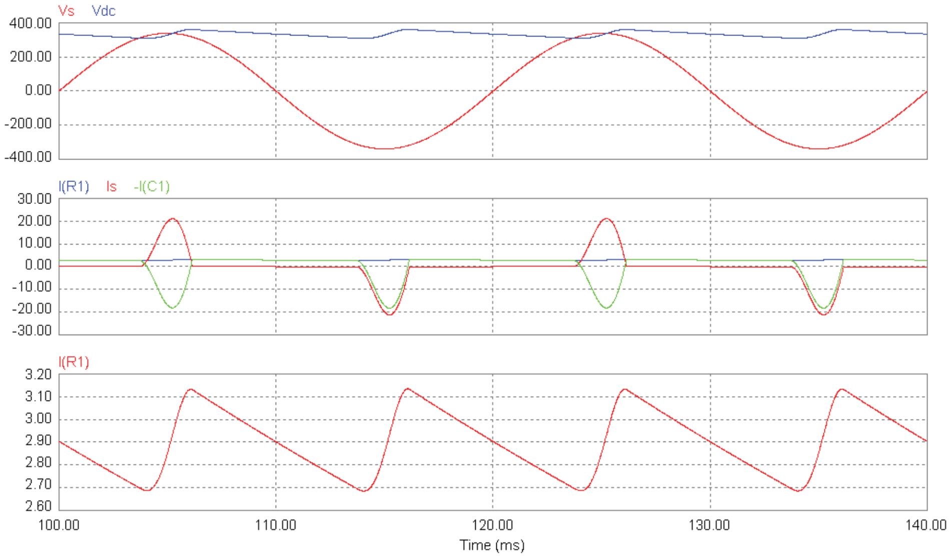

Figure 1-33 : Single phase rectifier V=240V, R=115.2Ω, C=440µF, L=1mH

For this research rectifiers are used to convert the variable voltage and frequency power from permanent magnet WTs to a more controllable DC voltage and current. They have also been used to charge batteries and create non linear loads in laboratory testing scenarios. Controlled rectifiers where the diodes are replaced with MOSFET’s or IGBT’s are used to charge batteries. The control of the switching of the gates allows accurate control of the current fed to the batteries. This concept is simulated in chapter two.

1.12.2. Inverters

An inverter is used to convert DC voltage to fixed frequency alternating voltage. Inverters can draw their power from either a voltage or current source, these are termed voltage source inverters (VSI) and current source inverters (CSI). This research only explores VSIs. Three sub classes of inverters exist which refer to the representation of the output voltage waveforms, these are square-wave, phase shifted square-wave and sinusoidal. The non sinusoidal classes exhibit significantly higher lower order harmonics which create extra losses in the system. This research only uses sinusoidal inverters using pulse width modulation to create the desired voltage or current waveform [68]. The basic schematic of a full bridge inverter is shown in Figure 1-34.

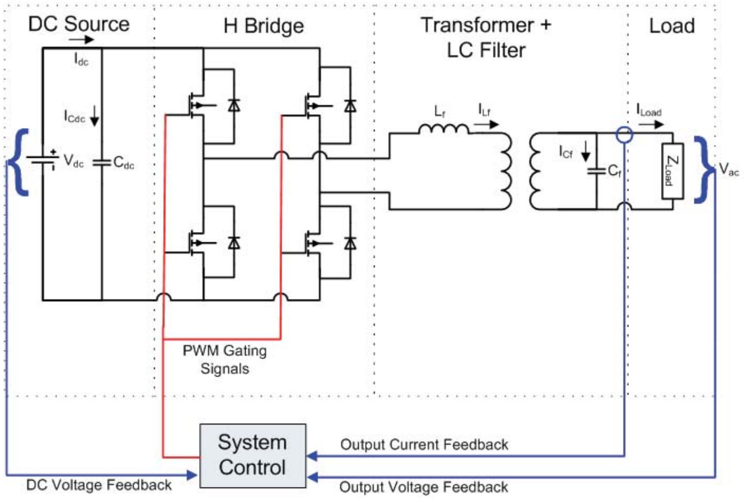

Figure 1-34 : Basic inverter topology

Bipolar PWM sinusoidal inverters force the gates to switch at required intervals to cause the output filtered waveform to represent a sinusoid. To implement this a carrier waveform such as a reference sinusoid is compared to a higher frequency triangular waveform. The reference waveform should be of the same frequency as the desired fundamental output voltage. In a full bridge inverter opposite MOSFET's or IGBT's are switched simultaneously so that no two switches are on in a single leg at the same instant. This would short the DC bus, potentially destroying the inverter, also known as "shoot through." A dead time is implemented in the controller to prevent this from occurring, The input capacitor reduces the current ripple from the DC source increasing the longevity of the battery. In many situations the input voltage is greatly less then the peak of the sinusoid created on the AC side, so a transformer is required to be added to the system as seen in Figure 1-34. Different methods of PWM are investigated and simulated in chapter two.

The spectrum of harmonics generated by a PWM method is distinctly dependant upon the switching instants used. Voltage and current harmonics are produced around the switching frequency which are removed from the output by a low pass LC or LCL filter. The fundamental frequency is usual 50 or 60Hz and the switching frequency is usually above 10kHz. A higher switching frequency allows for a smaller filter design but a more complicated switching strategy. A trade off between the two is required for any inverter design.

Two main methods of controlling VSIs exist, voltage controlled VSI (VC-VSI) and current controlled VSI (CC-VSI) [18, 68-73]. VC-VSIs are used for stand-alone systems in remote areas, which have no interconnection with the utility grid. Alternatively they can be used to perform an uninterrupted power supply function, and power local loads in the case of a grid failure. Typically VC-VSIs use output voltage feedback to set and regulate the load voltage, the input DC voltage is also required to ascertain the exact required modulation index limits for the desired output voltage. The output current is sensed to ensure over current and short circuit protection for the inverter.

CC-VSIs are used in grid connected applications where the available renewable energy is fed to the utility grid or generator controlled grid [39, 74-77]. The system looks for a grid voltage, which is within the required specifications of voltage and frequency, from the grid voltage sensor. A psuedo current waveform reference is then generated through a PLL and the gates are driven in such a way to create the desired current waveform. Various techniques have been proposed to perform such current control such as periodic sampling, hysteresis band control, triangular carrier and ramptime current control [18, 78-80]. The final requirement of a CC-VSI is to provide anti-islanding protection to ensure that the grid is energised from the utility when feeding current. This is to ensure that the CC-VSI disconnects when any maintenance is performed on the line [81].

1.12.3. DC-DC Converters

DC-DC converters can be used to transform one DC voltage level to another at high efficiencies. A conversion from a higher voltage to a lower one requires the output current to increase proportionally to the difference in voltage to ensure energy conservation. The inductor is the power electronic element central to this class of converters. An inductor allows the energy to be stored in the form of a magnetic field, which it can then convert to a voltage proportional to the control of the current, Faraday's Law Eq 1-24. The switching open and close of a power electronic switch controls the current through the inductor, which in turn controls the output voltage[13, 67].

$$\begin{aligned} v_L(t) &= L\frac{di_L(t)}{dt} \\ i_L(t) &\approx \frac{\Delta v_L}{L\Delta t} \end{aligned}$$

Eq 1-24 : Faraday's law

The two most common forms of DC-DC converter are the buck converter and boost converter, both which are regularly utilised within this dissertation. These converters contain a single switching element in the form of a MOSFET or IGBT, a diode, inductor and capacitor. The control of the converters can be defined into two modes, continuous current mode and discontinuous current mode. The distinction between the modes is shown by the current flowing in the inductor, if all energy is released from the inductors magnetic field before being reenergized by the switching the current in the inductor will fall to zero. This defines the boundary between continuous and discontinuous modes of operation [14].

The buck converter allows a higher voltage to be transferred to a lower one, Figure 1-35. Buck converters are used for battery charging application where both the output voltage or the output current can be carefully regulated. Solar MPPT systems where the PV array voltage is high utilise buck converters to maximise power extraction from the array.

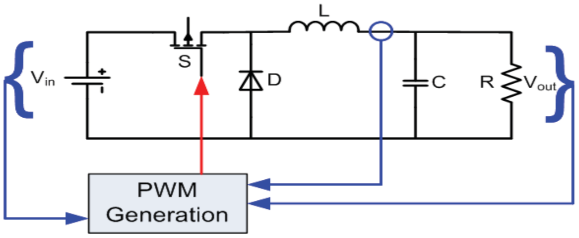

Figure 1-35 : Buck converter topology

Buck converters are the most efficient DC-DC converter with efficiencies in excess of 97%. The design equations for the buck converter in CCM, which is the usual mode of operation for battery charging and solar applications, are defined below.

$$D = \frac{t_{on}}{T_{sw}}$$
$$V_{out} = DV_{in}$$

Eq 1-25 : Buck converter overall design

$$\Delta I_L = i_{L,rip(pk-pk)} = \frac{V_{out}(1-D)}{f_{sw}L}$$
$$i_{L,rip(rms)} = \frac{\Delta I_L}{2\sqrt{3}} = \frac{V_{out}(1-D)}{2\sqrt{3}f_{sw}L}$$
$$\Delta V_{out} = v_{out,rip(pk-pk)} = \frac{V_{out}(1-D)}{8LCf_{sw}^2}$$
$$v_{out,rip(rms)} = \frac{\Delta V_{out}}{2\sqrt{2}} = \frac{V_{out}(1-D)}{16\sqrt{2}LCf_{sw}^2}$$

Eq 1-26 : Buck converter induction and capacitor design equations

$$RF_I = \frac{i_{L,rip(rms)}}{i_{L(ave)}}$$
$$RF_V = \frac{v_{out,rip(rms)}}{v_{out(ave)}}$$

Eq 1-27 : Buck converter performance criteria

The performance of a buck converter is defined by the purity of its output waveform that is measured by the voltage and current ripple factors, as calculated by Eq 1-27.

To design a buck converter for solar application the range of input voltage will determine the operating duty cycle range[14, 67, 82]. The maximum input current and the permissible output current ripple are then used to define the size of the inductor. The maximum current will determine the winding insulation and gauge, the ripple will determine the inductance. Finally, the capacitor can be chosen based upon the permissible voltage ripple of the load.

The boost converter topology converts a lower voltage to a higher one. The boost converter, seen in Figure 1-36, is more common in wind systems due to the WT producing a lower voltage at low wind speeds, which requires increasing to allow grid connection.

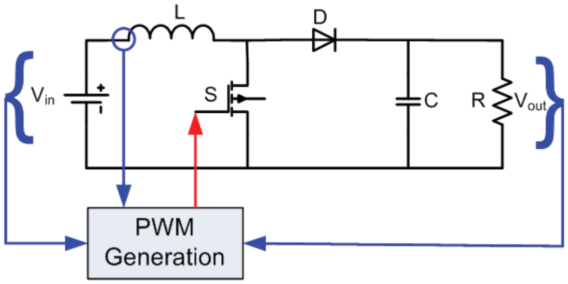

Figure 1-36 : Boost Converter Topology

The design equations for the boost converter in CCM, which is the usual mode of operation for battery charging and solar and wind applications, are defined below.

$$D = \frac{t_{on}}{T_{sw}}$$
$$V_{out} = \frac{V_{in}}{1-D}$$

Eq 1-28 : Boost converter overall design

$$\Delta I_L = i_{L,rip(pk-pk)} = \frac{V_{out}(1-D)D}{f_{sw}L}$$
$$i_{L,rip(rms)} = \frac{\Delta I_L}{2\sqrt{3}} = \frac{V_{out}(1-D)D}{2\sqrt{3}f_{sw}L}$$
$$\Delta V_{out} = v_{out,rip(pk-pk)} = \frac{I_{out}D}{f_{sw}C}$$
$$v_{out,rip(rms)} = \frac{\Delta V_{out}}{2\sqrt{3}} = \frac{I_{out}D}{2\sqrt{3}f_{sw}C}$$

Eq 1-29 : Boost converter induction and capacitor design

$$RF_I = \frac{i_{L,rip(rms)}}{i_{L(ave)}}$$

$$RF_V = \frac{v_{out,rip(rms)}}{v_{out(ave)}}$$

Eq 1-30 : Boost converter performance criteria

Boost converters are used and controlled in chapter two and three to increase and control the output voltage of a WT. The careful control of the voltage and current through a boost converter allows MPPT of solar and wind applications be possible.

1.13. Overview of Types of Renewable Systems

The interconnection of renewable power sources into the most energy efficient topology is central to the research conducted for this thesis. Any renewable energy generated can be either used immediately or stored. The simplest interconnection topology is the DC coupled system as seen in Figure 1-37 [24, 34, 83]. This system is centrally linked through a DC bus, which is usually directly coupled to a battery. The battery voltage sets the bus voltage and all interfaced generation sources or loads must feed or draw current from this bus. To charge the battery DC power sources require a DC-DC converter and all ac sources require a rectifier and also a DC-DC converter[84]. Control issues can result as the controllers interacting confusingly as each attempts to charge the battery with its own method. In large DC coupled systems some overall controller must inform the other chargers of the battery SOC and amount of current each charger can supply[85, 86]. An inverter is then required to convert the DC bus voltage to AC to power a traditional load.

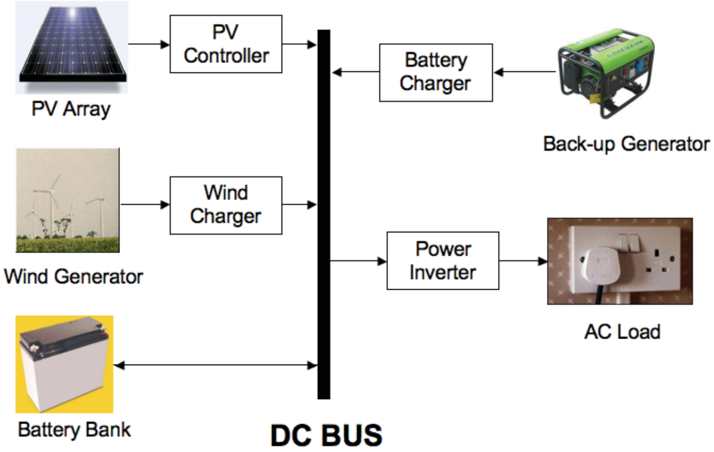

Figure 1-37 : DC coupled system [12]

DC coupled systems provide the most efficient way to power a remote area system while including storage, this is due to this configuration having the minimal number of conversion steps. A drawback of this system is that a certain percentage, known as the LOLP, exists when a power source is not available for certain amount of time which occurs when no renewable energy is available and the storage is empty. A backup generator is often included in this scenario to increase the overall reliability of the system and keep the battery at a minimum state of charge and extend its lifetime. Simple remote area systems with a single generation source, battery and load can be successfully and reliably DC coupled. The Eucla border village in Western Australia operates using this topology.

Another form of a DC coupled system, Figure 1-38, allows the backup generator to directly power the load [24, 87, 88]. This option increases the overall LOLP and is desired in situations where a loss of load for any time may be critical.

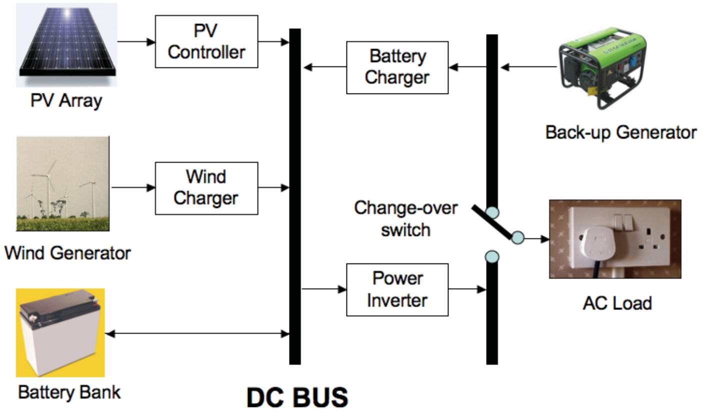

Figure 1-38 : DC Coupled System with Change-over option [12]

AC coupled systems are interconnected through a single central AC bus, Figure 1-39. An AC bus requires the voltage, frequency and phase of the system to be synchronised. An inverter or generator is required to set these parameters and the subsequent inverters will synchronise to this master as slaves. In the case where the generator ceases to set the voltage and frequency, the inverter must change to be the master[8]. The intricacies of this change over are explored in chapter six and seven of this thesis.

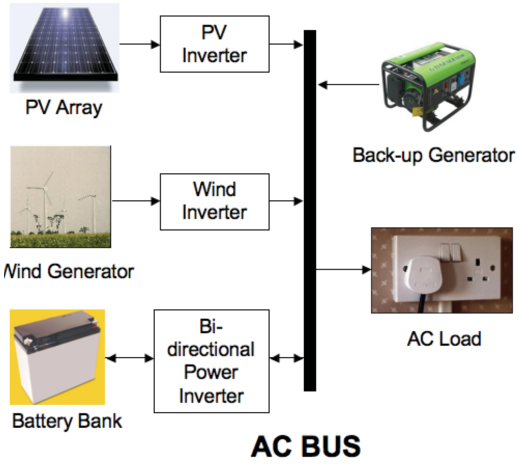

Figure 1-39 : AC Coupled System

Larger hybrid energy systems interconnection design is primarily based upon the locations of the renewable resources with respect to the loads. A system, which includes PV generation near the battery bank, can easily be DC coupled, however PV solar generation away from the DC source is usually ac coupled, due to the cost and power loss associated with using extra DC cables. These situational requirements ensure that many real world systems are mixed coupled system as per Figure 1-40 [89-92].

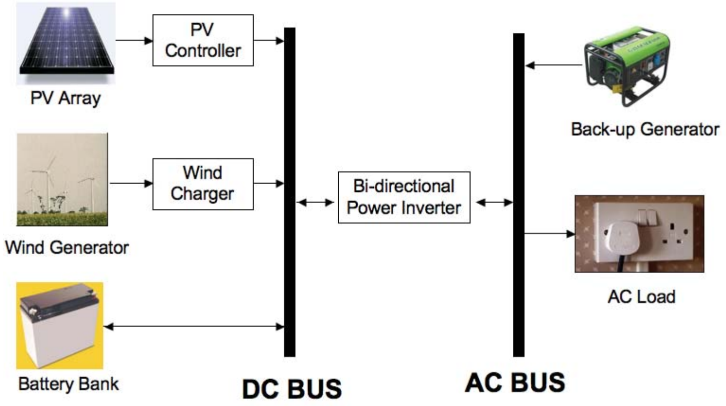

Figure 1-40 : Mixed Coupled System [12]

In chapter six and seven the author will present some work through the industry partner Regen Power. Through this link he will present systems he has design and are now operational, namely the Eco Beach Wilderness Resort and the Maldives one hundred island preliminary project and the Denmark wind/PV home system.

1.14. References

1. IEA, *Key World Energy Statistics*. 2008, International Energy Agency: Paris.
2. Witoelar, R. *The Bali Roadmap*. in *UN Climate Change Conference*. 2007. Bali.
3. Sayigh, A. *World renewable energy*. in *3rd World Conference on Photovoltaic Energy Conversion*. 2003: IEEE.
4. Zobaa, A.F. and J.S. McConnach. *International Response to Climate Change: An Overview*. in *IEEE Power Engineering Society General Meeting*. 2006.
5. Zorpette, G., *Fish and hydroelectricity: engineering a better coexistence*, in *IEEE Spectrum*. 1990. p. 68 - 70.
6. El-Ashry, M., *Renewables 2007 Global Statue Report*, in *REN21*. 2007, Renewable Energy Policy Network for the 21st Century.
7. Aberle, D. *Delivering Renewable Power to our Cities*. in *The Renewable City*. 2008. Carnegie Wave Energy Research Facility, Western Australia.
8. Nayar, C.V., M. Tang, and W. Suponthana. *An AC Coupled PV/Wind/Diesel Microgrid System Implemented in a Remote Island in the Republic of Maldives*. in *AUPEC 2007*. 2007. Curtin University of Technology.
9. Plunkett, K. *Eco Beach Broome Resort*. 2009 [cited 2009 22 Dec]; Available from: www.ecobeach.com.au.
10. Blaabjerg, F., C. Zhe, and S.B. Kjaer, *Power electronics as efficient interface in dispersed power generation systems.* IEEE Transactions on Power Electronics, 2004. **19**(5): p. 1184-1194.
11. Blaabjerg, F. *Power Electronics in Renewable Energy Systems*. in *Workshop Energy Technology*. April 2006. Aalborg University Institute of Energy Technology
12. Khanniche, S., *Power Electronics for Renewable Energy Systems*. 2006, Welsh Energy Training Sector: Swansee. p. 33.
13. Krein, P.T., *Elements of Power Electronics*. 1998, New York: Oxford University Press.
14. Mohan, N., T.M. Undeland, and W.P. Robbins, *Power Electronics - Converters, Applications, and Design*. 3nd ed. 2003: John Wiley & Sons, Inc.
15. Rashid, M.H., *Power Electronics Circuits, Devices, and Applications*. 3rd ed. 2004: Pearson Education, Inc.
16. Carrasco, J.M., et al., *Power-Electronic Systems for the Grid Integration of Renewable Energy Sources: A Survey.* IEEE Transactions on Industrial Electronics, 2006. **53**(4): p. 1002 - 1016.
17. Bose, B.K., *Energy, environment, and advances in power electronics.* IEEE Transactions on Power Electronics, 2000. **15**(4): p. 688-701.
18. Brod, D.M. and D.W. Novotny, *Current Control of VSI-PWM Inverters.* IEEE Transactions on Industry Applications, 1985. **21**: p. 562-570.
19. Bollen, M.H.J. and A. Sannino, *Voltage Control With Inverter-Based Distributed Generation.* IEEE Transactions on Power Delivery, 2005. **20**(1): p. 519-520.
20. Ashari, M., *Multi-Function Voltage Source Inverters for Weak-Grid and Off Grid Applications*, in *Electrical and Computer Engineering*. 2001, Perth: Curtin University of Technology. p. 286.
21. Chen, Y., et al., *Multi-Input Inverter for Grid-Connected Hybrid PV/Wind Power System.* IEEE Transactions on Power Electronics, 2007. **22**(3): p. 1070-1077.

22. Merwe, G.J.v.d. and L.v.d. Merwe, *Inverters - the investigation to the optimal topology to the designing of a sinewave inverter range for the use in static as well as mobile applications.* IEEE International Symposium on Industrial Electronics, 1998. **1**: p. 51-56.
23. Milanovic, M. and A. Roskaric. *Battery Charger Based On Double-Buck And Boost Converter*. in *IEEE International Symposium on Industrial Electronics*. 1999.
24. Nayar, C.V., S.J. Phillips, and W.L. James, *Novel Wind/Diesel Battery Hybrid Energy Systems.* Solar Energy, 1993. **51**: p. 65-78.
25. Borowy, B.S.S., Z.M, *Optimum photovoltaic array size for a hybrid wind/PV system.* Energy Conversion, IEEE Transaction on, June 1995. **10**(2): p. 326-332.
26. Hongxing Yang, Z.W., Lou Chengzhi, *Optimal design and techno-economic analysis of a hybrid solar–wind power generation system.* Applied Energy, February 2009. **86**(2): p. 163-169.
27. W. Kellogg, M.H.N., G. Venkataramanan, V. Gerez, *Optimal unit sizing for a hybrid wind/photovoltaic generating system.* Electric Power Systems Research, October 1996. **39**(1): p. 35-38.
28. Wichert, B., *Control of Photovoltaic-Diesel Hybrid Energy Systems*, in *School of Electrical and Computer Engineering*. 2000: Perth: Curtin University of Technology.
29. Batteries, T., *Trojan Deep-Cycle Gel Usage and Benefits*, in *Technical Brief*. 2007.
30. Powercorp. *Powercorp Project Examples*. 2009 [cited 2009; Available from: http://www.pcorp.com.au/.
31. EcoNomics and WorleyParsons, *Advanced Solar-Thermal, Utility-scale renewable power for Australia*. 2008, WorleyParsons resources & energy.
32. Masters, G., *Renewable and Efficient Electric Power Systems*. 2004: Wiley Interscience.
33. Lasnier, F. and T.G. Ang, *Photovoltaic Engineering Handbook*. 1990, New York: IOP Publishing.
34. Markvart, T., *Solar electricity*. 2nd ed. 2000: Wiley & Sons, 2000.
35. Asiminoaei, L., et al., *A digital controlled PV-inverter with grid impedance estimation for ENS detection.* IEEE Transactions on Power Electronics, 2005. **20**(6): p. 1480 - 1490.
36. NREL, *Best Laboratory PV cell efficiencies for various technologies*. 2003, National Renewable Energy Laboratories.
37. V. Salas, E., Olias, A. Barrado and A. Lazaro, *Review of the maximum power point tracking algorithms for stand-alone photovoltaic systems.* Solar Energy & Solar Cells, 2005. **10**.
38. Walker, G.R., *Evaluating MPPT converter topologies using a MATLAB PV model.* Journal of Electrical & Electronics Engineering, Australia, 2001. **21**(1): p. 49-56.
39. J. Darbyshire, C.V.N. *Modelling, Simulation and testing of grid connected PV system*. in *Symposium on Power Electronics for Distributed Generation Systems*. 2007. Hefei: IEEE.
40. Altas, L. and A.M. Sharaf, *Novel on-line MPP search algorithm for PV arrays.* IEEE Transactions on Energy Conversion, 1996. **11**: p. 748 -754.

41. Mingliang Li, C.W., *Research on optimization of wind and PV hybrid power systems*, in *Intelligent Control and Automation, 2008. WCICA 2008. 7th World Congress on*. August 2008.
42. Enslin, J.H.R. and D.B. Snyman, *Combined low-cost, high-efficient inverter, peak power tracker and regulator for PV applications.* IEEE Transactions on Power Electronics, 1991. **6**: p. 73 -82.
43. T. Kim, H.A., S. Park and Y. Lee. *A Novel Maximum Power Point Tracking Control for Photovoltaic Power System Under Rapidly Changing Solar Radiation*. in *IEEE International Symposium on Industrial Electronics*. 2001.
44. Lorentz, B., *High-efficiency PV Module LA130-24S*, in *PV Datasheet*. 2007, Lorentz Data Sheet.
45. Burton, T., *Wind Energy Handbook*. 2001: John Wiley & Sons, Ltd.
46. Ackermann, T., *Wind Power in Power Systems*, ed. T. Ackermann. Vol. 1. 2005, Stockholm: John Wiley & Sons, Ltd.
47. GWEC, *Global Wind Energy Report 2007*, in *Global Wind Report*. 2007, Global Wind Energy Council.
48. J. Darbyshire, C.V.N. *Modelling, simulation and testing of grid connected small scale wind systems*. in *Australasian Universities Power Engineering Conference*. 2007. Perth.
49. Raju, A.B., *Application of power electronic interfaces for grid connected variable speed wind energy conversion systems*, in *Department of Electrical Engineering*. 2005, Indian Institute of Technology: Bombay.
50. Carlin, P.W., *The History and State of the Art of Variable-Speed Wind Turbine Technology*, in *NREL Technical Report*. 2001, National Rewnwable Energy Laboratory: Golden.
51. Kelvin Tan, S.I., *Optimum Control Strategies in Energy Conversion of PMSG Wind Turbine System Without Mechanical Sensors* IEEE Transactions on Energy Conversion, 2004. **19**(No 2).
52. Nevis, A.S., N.A. Vovos, and G.B. Giannakopoulos, *Variable Speed Wind Energy Conversion Scheme For Connection To Weak AC Systems. IEEE, Transactions on Energy Conversion*, 1999. **14**.
53. Venkataramanan, G., et al., *Variable Speed Operation Of Permanent Magnet Alternator Wind Turbine Using A Single Switch Power Converter. Journal of Solar Energy Engineering, Transaction of ASME*, 1996.
54. Sharma, H.e.a. *Dynamic Response of a Remote Area Power System to Fluctuating Wind Speed*. in *Proceedings of the IEE/PES Winter Meeting*. Jan 2000. Singapore: IEEE.
55. Huang, H. and L. Chang. *Energy-Flow Direction Control of Grid-Connected IGBT Inverters for Wind Energy Extraction*. in *IEEE 2000 Canadian Conference on Electrical and Computer Engineering*. 2000. Halifax, Canada.
56. Boutot, T. and L. Chang, *Development of a Single-Phase Inverter for Small Wind Turbines.* IEEE Canadian Conference on Electrical and Computer Engineering, 1998. **1**: p. 305-308.
57. McVanInstruments, *Series 706 Heavy Duty Wind Speed and Direction Transmitter* 2001: Victoria, Australia.
58. Nchrir, M.H., et al., *An Approach to Evaluate The General Performance of Stand-Alone Wind/Photovoltaic Generating Systems.* IEEE Transactions on Energy conversion, 2000.

59. Jangamshetti, S.R., Guruprasada, *Site Matching of Wind Turbine Generators : A Case Study.* IEEE Transactions on Energy Conversion, 1999. **14**(4, December): p. 1538.
60. Kanellos, F.D. and N.D. Hatziargyriou, *Control of Variable Speed Wind Turbines in Islanded Mode of Operation* IEEE Transactions on Energy Conversion, 2008. **23**(2).
61. *Matlab 6, Release 12.1*. 2006, The MathWorks (www.mathworks.com): Natick, Massachusetts.
62. Yeh, T.-H. and L. Wang, *A Study on Generator Capacity for Wind Turbines Under Various Tower Heights and Rated Wind Speeds Using Weibull Distribution* IEEE Transactions on Energy Conversion, 2008. **23**(2, June): p. 592.
63. Panahi, I., Z. Yu, and M. Arefeen, *Generate Advanced PWM Signals Using DSP*. 2003: Electronic Design
64. Khan, M.S., *Hybrid Control of a Grid-Interactive Wind Energy Conversion System* IEEE Transactions on Energy Conversion, 2008. **23**(3).
65. Valenciaga, F. and P.F. Puleston, *High-Order Sliding Control for a Wind Energy Conversion System Based on a Permanent Magnet Synchronous Generator* IEEE Transactions on Energy Conversion, 2008. **23**(3).
66. Skvarenina, T.L., ed. *The Power Electronics Handbook*. Industrial Electronics Series, ed. J.D. Irwin. 2002, CRC Press.
67. Erickson, R.W. and D. Marksimovic, *Fundamentals of Power Electronics*. Second ed. 2001: Kluwer Academic Publishers.
68. Borle, L.J., *Power Electronics 304 Lecture Notes in PE304* in *School of Electrical and Computer Eng.* 2001, Curtin University of Tech. Perth.
69. Ko, S.-H., et al., *Application of voltage- and current-controlled voltage source inverters for distributed generation systems.* Energy Conversion, IEEE Transaction on, 2006. **21**(Sept): p. 782-792.
70. Borle, L.J., *Zero Average Current Error Control Methods for Bidirectional AC-DC Converters*, S.o.E.a.C. Engineering, Editor. 1999: Perth: Curtin University of Technology.
71. Dehbonei, H., C.V. Nayar, and L. Borle, *A Combined Voltage Controlled and Current Controlled 'Dual Converter' for a Weak Grid Connected Photovoltaic System with Battery Energy Storage*, in *IEEE Power Electronics Specialists Conference*. 2002: Cairns.
72. Kukrer, O., *Discrete-Time Current Control of Voltage-Fed Three-Phase PWM Inverters.* IEEE Transaction on Power Electronics, 1996. **11**: p. 260-269.
73. Trigg, M.C., H. Dehbonei, and C.V. Nayar. *DC Bus Compensation for a Sinusoidal Voltage Source Inverter with Wave-Shaping Control*. in *IEEE Industrial Electronics Conference*. 2006. Paris, France.
74. Rodríguez, J., et al., *Predictive Current Control of a Voltage Source Inverter.* IEEE Transactions on Industrial Electronics, 2007. **54**(1): p. 495-503.
75. Ye, Z., M. Dame, and B. Kroposki, *Grid Connected Inverter Anti – Islanding Test Results for General Electric Inverter – Based Interconnection Technology*. 2005, National Renewable Energy Laboratory (NREL).
76. Marion, B., Hayden, H., Shugar, D., Rich, G. *Performance Parameters for Grid Connected PV Systems*. in *31st IEEE Photovoltaics Specialists Conference and Exhibition*. 2005. National Renewable Energy Laboratory, Colorado, United States of America.

77. Calais, M. and V.G. Agelidis, *Multilevel converters for single-phase grid connected photovoltaic systems - an overview*, in *IEEE International Symposium on Industrial Electronics*. 1998. p. pp. 224-229.
78. Borle, L.J. and C.V. Nayar, *Zero Average Current Error Controlled Power Flow for AC-DC Power Converters.* IEEE Transactions on Power Electronics, 1995. **10**: p. l-8.
79. Rahman, K.M., et al., *Variable-Band Hysteresis Current Controllers for PWM Voltage-Source Inverters.* IEEE Transactions on Power Electronics, 1997. **12**.
80. Sepe Jr, R.B. *A Unified Approach to Hysteric And Ramp Comparison Current Controllers*. in *IEEE Industry Applications Society Annual Meeting*. 1993.
81. Z. Ye, R.W., L. Garces, R. Zhou, L. Li, and T. Wang *Study and Development of Anti-Islanding Control for Grid-Connected Inverters* N.R.E. Laboratory, Editor. May 2004, General Electric Global Research Center Niskayuna, New York New York.
82. Wang, C., *A Novel Single-Stage Full-Bridge Buck-Boost Inverter.* IEEE Transactions on Power Electronics, 2004. **19**(1): p. 150-159.
83. Bossanyi, *Wind Energy Handbook*. 2000: John Wiley and Sons.
84. Jain, S. and V. Agarwal, *An Integrated Hybrid Power Supply for Distributed Generation Applications Fed by Nonconventional Energy Sources* IEEE Transactions on Energy Conversion, 2008. **23**(2).
85. Schönberger, J., R. Duke, and S.D. Round, *DC-Bus Signaling: A Distributed Control Strategy for a Hybrid Renewable Nanogrid.* IEEE Transactions on Industrial Electronics, 2006. **53**(5): p. 1453-1460.
86. Dehbonei, H., C.V. Nayar, and L. Chang. *A New Modular Hybrid Power System*. in *IEEE International Symposium on Electronics*. 2003. Rio de Janeiro, Brazil.
87. Ashari, M., W.W.L. Keerthipala, and C.V. Nayar, *A Single Phase Parallel Connected Uninterruptible Power Supply / Demand Side Management System.* IEEE Transactions on Energy Conversion, 2000. **15**.
88. Nayar, C.V., *A Solar/Mains/Diesel Hybrid Uninterrupted Power System*, in *ANZSES, Solar'97 Conference*. 1997: Canberra, Australia.
89. Nayar, C.V., M. Ashari, and W.W.L. Keerthipala, *A Single Phase Uninterruptible Power Supply System Using A Bi-Directional Sinusoidal PWM Inverter*, in *PESDES*. 1998.
90. Durisch, W. and D. Tille, *Testing Of Small Sinusoidal-Inverters For Photovoltaic Stand-Alone Systems.* Applied Energy, 1998. **64**.
91. Masheleni, H. and X.F.Carelse, *Microcontroller-Based Charge Controller For Stand-Alonc Photovoltaic Systems.* Solar Energy, 1997. **61**.
92. Bower, W., S. Phillips, and F. Schallcs. *Performance and Characteristics of Inverters in Remote and Stand-Alone Applications*. in *IEEE Photovoltaic Specialists Conference*. 1988.

"Every reasonable effort has been made to acknowledge the owners of copyright material. I would be pleased to hear from any copyright owner who has been omitted or incorrectly acknowledged."

2. Power Electronic Interfaces and Control for Renewable Energy Applications

This chapter investigates the power electronic topologies and control aspects which are applied to renewable energy systems. The mathematical models that are used to design the components are developed and the power electronic and control simulation program PSIM is extensively used [1]. The main building blocks that show the multi-function aspect of power electronics and control are explained in this chapter to be further applied in following sections.

The first section of this chapter goes through the design and control process for inverters. Two types of overall control techniques are used to control VSIs, voltage control and current control. The bi-polar and unipolar switching methods and design expressions are defined as they are used extensively for modelling in later chapters. The methods which an inverter can either control the voltage and frequency on the bus or simply supplement the load is extensively used as hybrid system grow in size. Design and modelling of various voltage and current control techniques are presented. In later chapters stand-alone inverter systems utilise the VC-VSI control application and CC-VSI apply the PI or hysteresis control technique.

Finally the power electronic topologies are applied to solar and wind systems. The various circuit designs are presented and explained with special mention of those topologies used throughout this research.

2.1. Voltage Control Methods for Inverters

VC-VSIs are required wherever a utility grid or generator is not available. VSIs operated in a voltage control mode, allow the output voltage to be carefully regulated to the desired magnitude and frequency. Comparing a reference sinusoid of the required output frequency to a triangular waveform creates the desired voltage sinusoid. The comparison of these two waveforms creates a succession of high and low signals of varying width, known as PWM. Varying the peak height of the reference sinusoidal waveform controls the magnitude of the output voltage, known as the modulation index. Three main forms of sinusoidal PWM exist, namely bi-polar, uni-polar and space vector modulation. Bi-polar and uni-polar are used for both single and three phase inverters. Space vector modulation is generally confined to three phase applications as it allows direct control of the flux vector within an electric machine, so is readily used to control the machines rotational speed such as in variable speed drives. Recently, work has been carried out to implement a single phase space vector modulation strategy. However its improvements over the standard uni-polar technique are still being investigated[2-10].

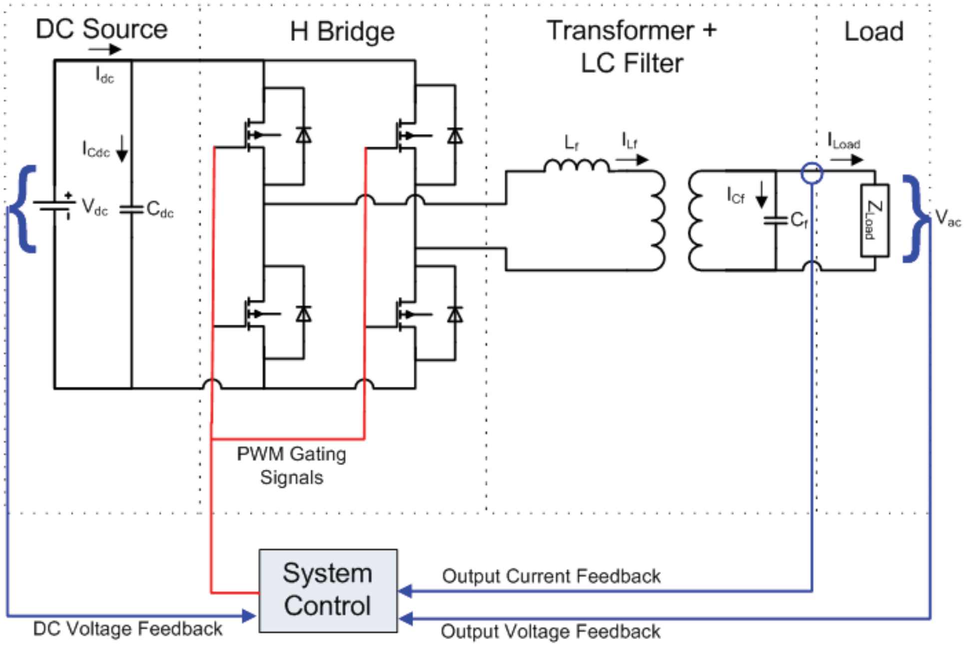

Figure 2-1 : VC-VSI Topology

The key expressions required to design a signal phase inverter depend upon the peak value of the desired AC waveform and the battery voltage. In order to prevent distortion in the output waveform, a modulation index above 0.9 is not recommended, as it creates excess harmonics from which the output filter is not designed to remove. In many cases the dc battery voltage is insufficient to create the peak value of the output AC sinusoid, to solve this issue a transformer is added at the output of the H-bridge. The output filter inductor can also be made into the transformer to increase the inverter's efficiency. In order to minimise the size of the low pass filter components the inductor should be placed on the higher current side of the transformer and the capacitor on the higher voltage side.

The switching at the H-bridge causes a pulsed current waveform to be required from the dc source. An input capacitor is added to reduce the inrush current from the battery to extend its life. The size of this capacitor is based upon the maximum tolerated current ripple from the battery. Various methods have been adopted to ensure that the voltage droop on the dc bus does not cause the magnitude of the output voltage to be affected [11, 12]. This issue is more prevalent for higher power inverters operating from a lower voltage dc source. In most cases a more efficient design is possible by using a higher dc voltage source, which reduces both the i^2R losses and reduces the transformer losses.

2.1.1. Bipolar PWM

An inverter can be designed using the bi-polar PWM method from the following expressions, Eq 2-1; which show the relationship between the input voltage, output voltage and modulation index for the VC-VSI [13-15]. The fundamental harmonic of the PWM occurs at the desired frequency of the grid, 50Hz in Australia. All other harmonics which are generated by the PWM pattern should be attenuated by the low pass filter at the output of the inverter.

$$\mathrm{V}_{\mathrm{O1,rms}} = \frac{V_{DC} m_a}{\sqrt{2}}$$

$$\mathrm{V}_{\mathrm{O,rms}} = V_{DC}$$

$$V_{O,rip} = \sqrt{1 - \frac{m_a^2}{2}}$$

$$THD = \sqrt{\frac{2 - m_a^2}{m_a^2}}$$

Eq 2-1 : Bipolar PWM Inverter Design Expressions

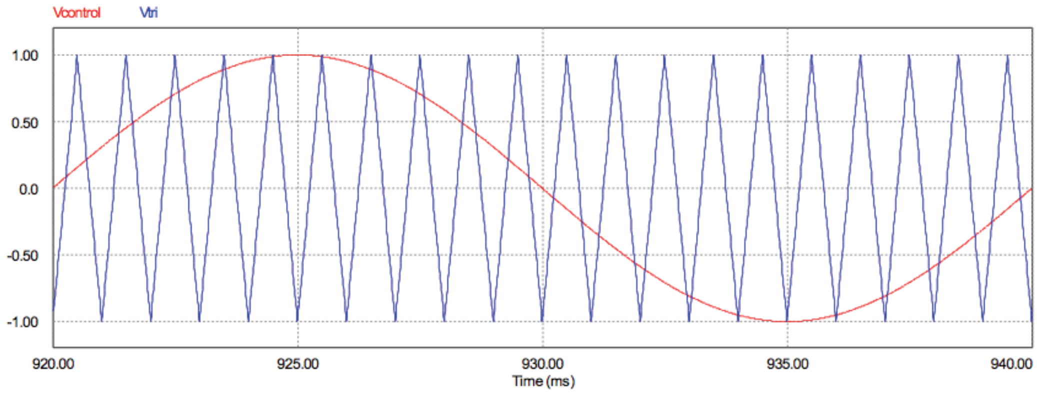

Figure 2-2 : Bi-polar switching control waveforms

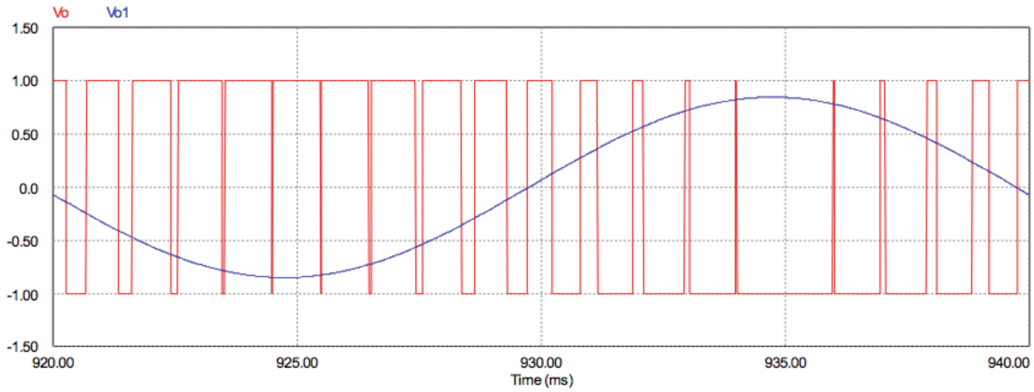

Figure 2-3 : Bi-polar switching output waveform, $m_a = 0.9$

Figure 2-2 shows the triangular carrier waveform and usual micro controller generated reference sinusoid. A comparator is used to produce the PWM signal as seen in Figure 2-3. This PWM signal is then passed through a gate drive circuit, which controls the MOSFET or IGBT switching instants. Generally a delay is introduced in the gate drive control that prevents the upper and lower switches ever being closed at the same instant, a condition known as shoot through, which can cause the switches immediate and permanent damage.

The voltage waveform seen at the midpoint of the H-bridge is the same as the bipolar PWM signal with the magnitude set to the level of the input dc voltage. Effectively a succession of pulses that are filtered to provide the smooth AC output waveform. A Fourier transform of the PWM pulses create harmonics at two distinct frequencies, the fundamental and the switching frequency. Figure 2-4 shows the frequency analysis of the PWM signal simulated above, with a fundamental of 50Hz and a switching frequency of 1kHz. The sidebands of the switching frequency can also be seen. The low pass filter is then applied to attenuate these components from the output voltage waveform.

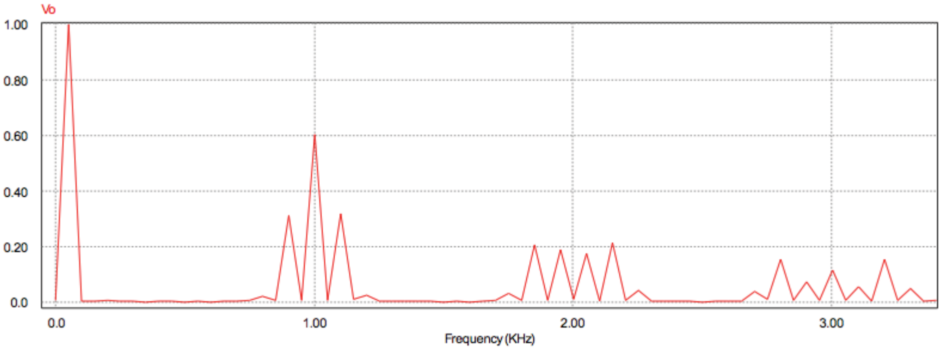

Figure 2-4 : Bi-polar switching harmonics

2.1.2. Unipolar PWM

Unipolar PWM techniques allow the switching frequency at the mid points of the H bridge to appear to be double that of the base switching frequency. This is an advantage over the bipolar method as the distance in frequency between the fundamental and the switching frequency seen at the filter is larger. This allows the output filters cut off point to be at a higher frequency allowing smaller sized inductors and capacitors and an overall cheaper and lighter solution. The trade off is the digital processing requirement for the unipolar method is greater. However, with the increase in DSP technology this hurdle is becoming less of a challenge [16, 17].

$$\mathrm{V}_{\mathrm{O1,rms}} = \frac{V_{DC} m_a}{\sqrt{2}}$$

$$\mathrm{V}_{\mathrm{O,rms}} = V_{DC}\sqrt{\frac{2m_a}{\pi}}$$

$$V_{O,rip} = V_{DC}\sqrt{m_a\left(\frac{2}{\pi} - \frac{m_a}{2}\right)}$$

$$THD = \sqrt{\frac{4}{\pi m_a} - 1}$$

Eq 2-2 : Unipolar PWM Inverter Design Expressions

Eq 2-2 shows the design equations for the unipolar PWM method. The unipolar method requires two carrier waveforms which are exactly 180 degrees out of phase with each other, Figure 2-5. Each leg of the H-bridge is controlled with reference to one of these two reference sinusoids. This ensures that the switching voltage seen at the mid point of the H-bridge does not oscillate between $+V_{dc}$ and $-V_{dc}$ like it would for bipolar, but it will switch between 0 and $+V_{dc}$ or 0 and $-V_{dc}$ dependent upon the portion of the output sinusoid, as seen in Figure 2-6. This has the effect of allowing the switching frequency at the mid point to appear to be double that of the actual switching frequency. This also has the advantageous effect of reducing the output THD and slightly increasing efficiency as the full dc voltage is not always seen at the midpoint.

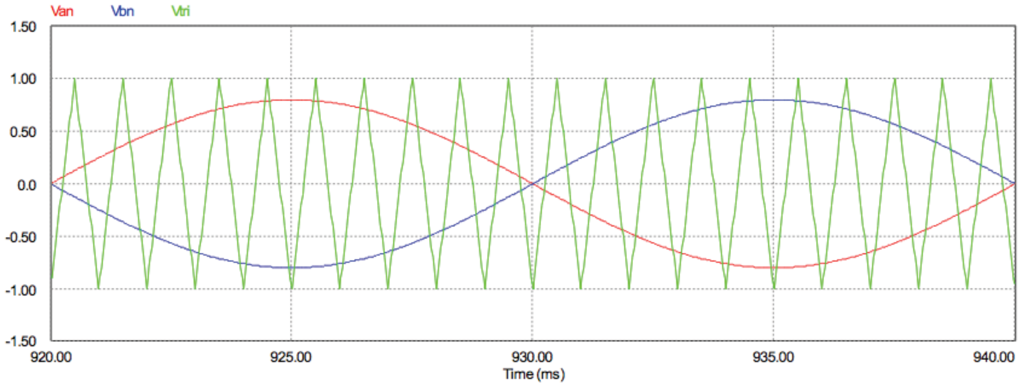

Figure 2-5 : Uni-polar switching control waveforms

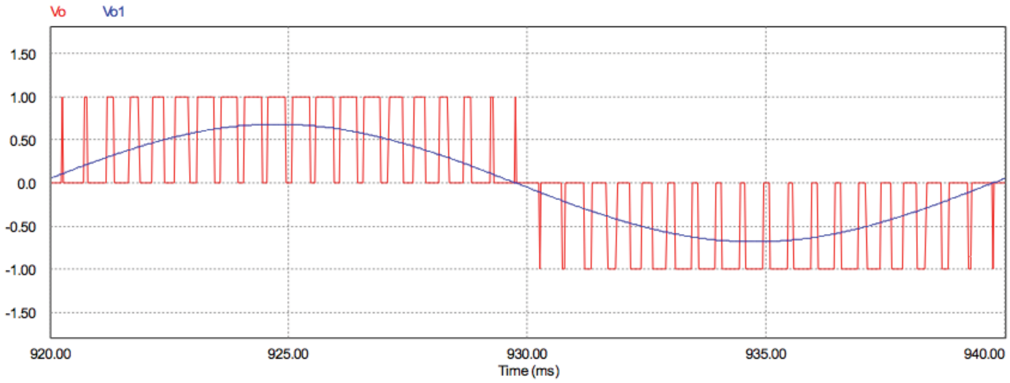

Figure 2-6 : Uni-polar switching output waveform

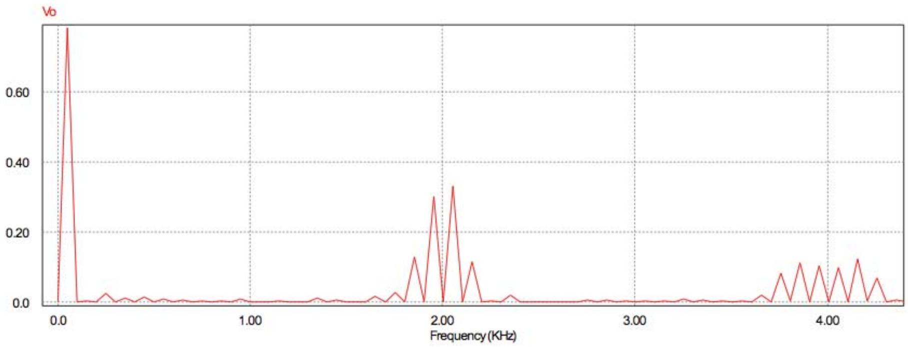

Figure 2-7 : Uni-polar switching harmonics

The Fourier transform of the output voltage waveform of the unipolar method is shown in Figure 2-7. The fundamental harmonic as for the bipolar method is seen at 50Hz. However, the main switching frequency is at 2kHz while the actual switching frequency is at 1kHz, showing the correct implementation of the unipolar method.

2.1.3. Control of VC-VSIs

A simulation was carried out in the power electronic modelling software PSIM [1]. The model was based upon the 2kVA Leonics S216C inverter charger. This VC-VSI uses a 48V dc battery bank and a 25.9:220 ratio step up low frequency transformer. This simulation illustrates the uni-polar method at a switching frequency of 10kHz. The model used is seen as Figure 2-8, it is operating as an open loop control whereby the modulation index has been set to allow the desired output voltage.

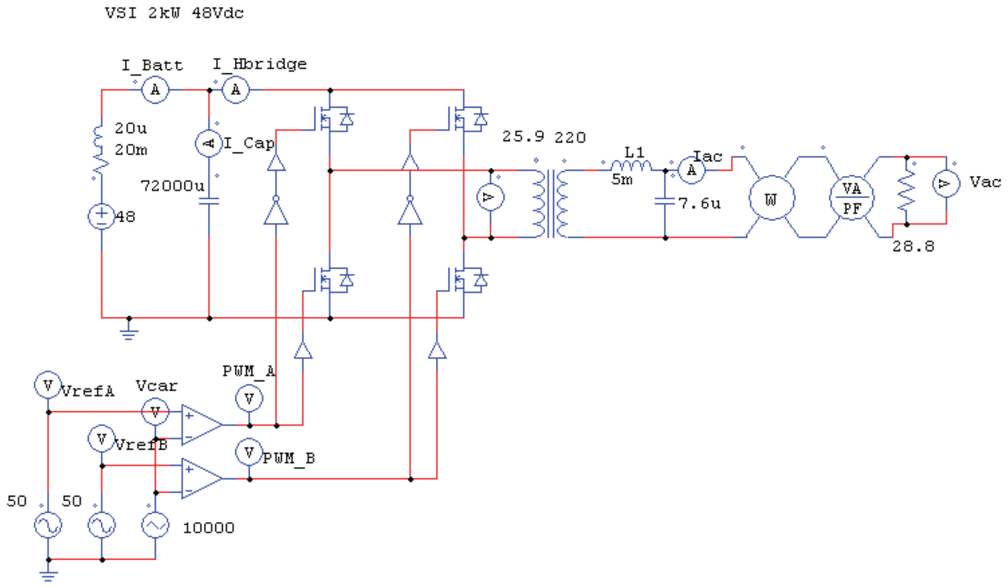

Figure 2-8 : Open Loop VSI 10kHz Unipolar PWM; 2kW@48Vdc

The load is set by a 28.8Ω resistor, which corresponds to a 2kW load. Figure 2-9 shows that the voltage and current are in phase as expected for a purely resistive load. The battery current is seen to be double the output frequency however it is slightly out of phase due to the inductance of the battery leads. The pulsed current waveform is seen at the H-bridge and this ripple is absorbed by the input capacitor as it is not seen in the battery current waveform.

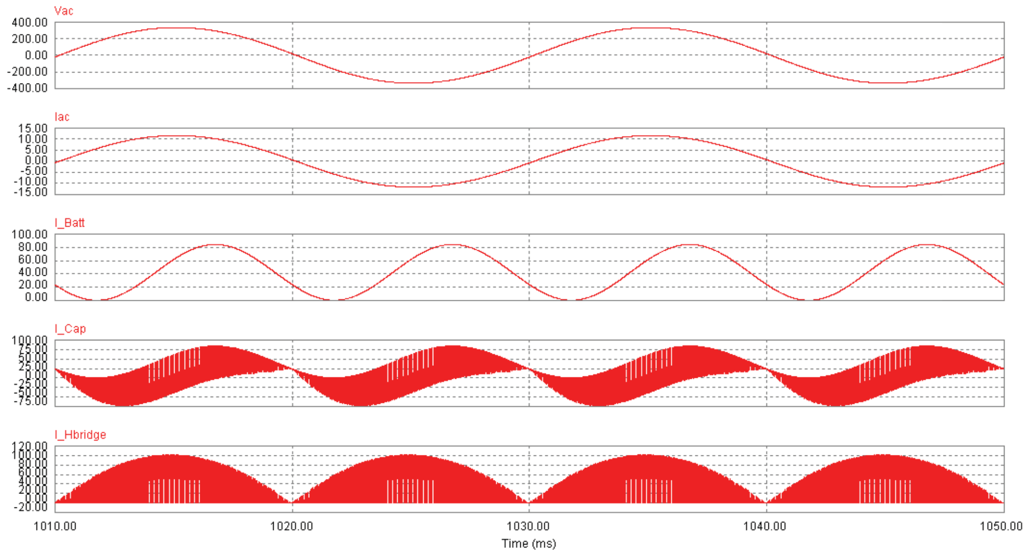

Figure 2-9 : Simulated Waveforms: Output Voltage; Output Current; Battery Current; Capacitor Current; H-Bridge Current

The controllability of an inverter, is usually carried out by sensing the output voltage and either output current or inductor current. Figure 2-8 shows an open loop control whereby the output voltage is only regulated by the preset modulation index. Figure 2-10 shows a closed loop controller where the output voltage is compared with a desired reference voltage, this creates an error signal which is passed through a PI controller to directly regulate the modulation index. The PI controller generates a multiplier which increases or decreases the modulation index to keep the desired output voltage. In VC-VSI inverters, the output current is sensed to provide short circuit protection and calculate the current output power of the inverter. This is usually a trigger for the thermal management system of the inverter.

Figure 2-10 shows a PI implemented closed loop control for a 240VAC nominal inverter. A perturbation was introduced into the dc bus through a larger lead resistance. As a higher current is drawn, the voltage from the source as seen by the inverter also decreases. This requires the inverter to increase its modulation index to ensure that the output voltage remains constant [11, 18-20].

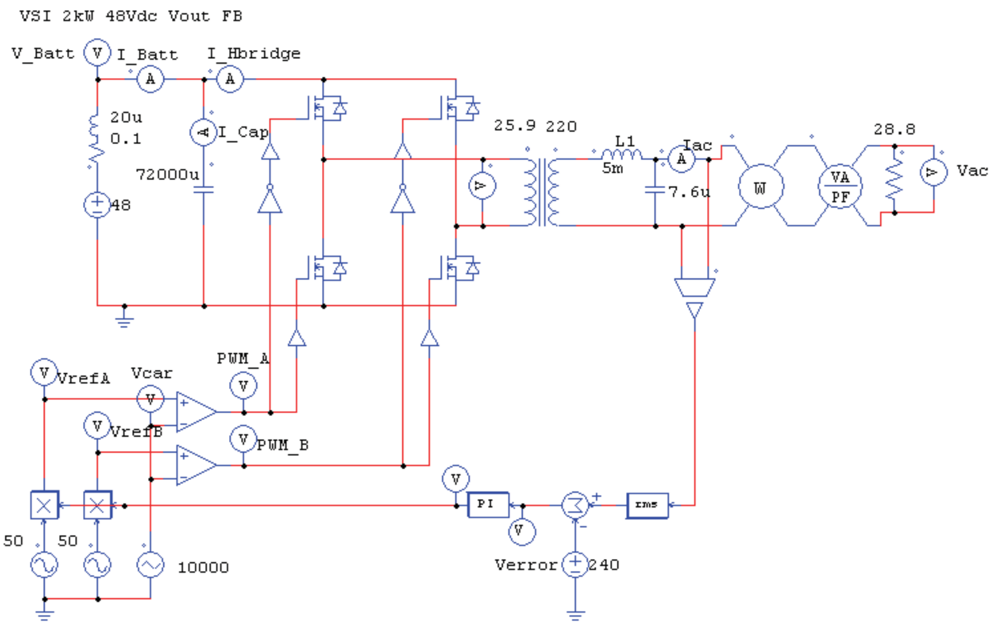

Figure 2-10 : Output Voltage Feedback VSI 10kHz Unipolar PWM; 2kW@48Vdc

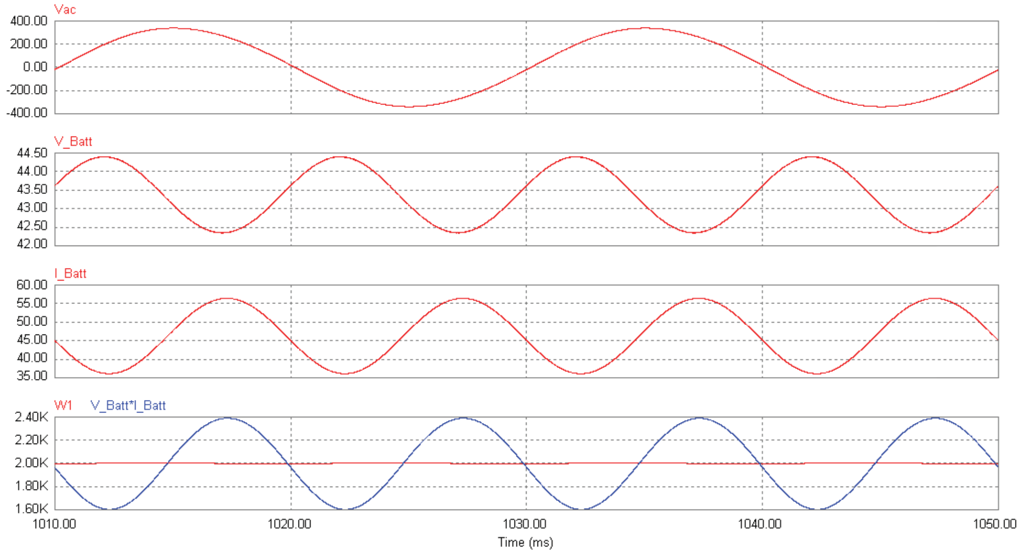

Figure 2-11 : Simulated Waveforms: Output Voltage; Battery Voltage; Battery Current; Output and Battery Power

2.2. Grid Connecting VC-VSI

Grid connecting a VC-VSI requires careful control of the voltage and phase of the inverter waveform with respect to the grid. A filter inductance is required to soften the effects of any instantaneous differences in phase during connection. A small mismatch in phase can create a large current flow in either direction. The grid connection inductor limits the rate of increase of change in current flow to or from the grid.

This technique of grid interfacing was used for some of the first PV installations in Western Australia such as the Kalbarri Wind Farm. With the increased safety requirements of islanding detection this method has become less popular. The grid inductor can also be quite large and be removed completely if modern current control techniques are used.

The VC-VSI grid connection method uses two parameters; the inverter voltage magnitude and the phase angle difference to control the active and reactive power flow to the grid. The expressions used to control the power flow are seen in Eq 2-3 [21-23].

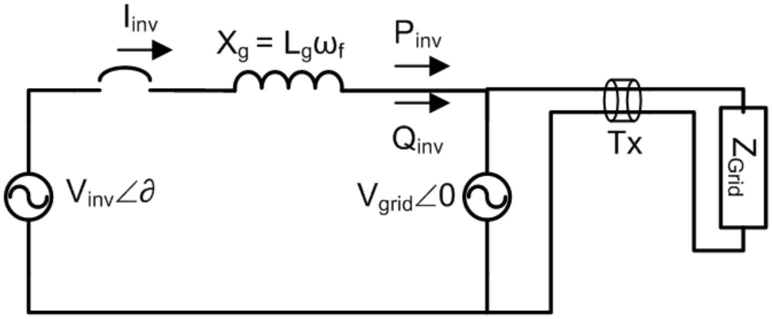

Figure 2-12 : VC-VSI grid connection diagram

$$P_{inv} = \frac{V_{grid}V_{inv}}{X_g}\sin\partial$$

$$Q_{inv} = \frac{V_{grid}V_{inv}}{X_g}\cos\partial - \frac{V_{grid}^2}{X_g}$$

Eq 2-3 : Expressions controlling the active and reactive power flow

Technically this control method can be implemented with only a voltage sensing control loop which will measure the utility voltage and phase and compare with the inverter's output voltage, Figure 2-13. However this approach does not allow the output current to be instantaneously known, which makes MPPT on the dc side or short circuit protection difficult to implement. To resolve this issue, a faster output current loop is added, this allows the instantaneous current and power be compared to an available dc reference value.

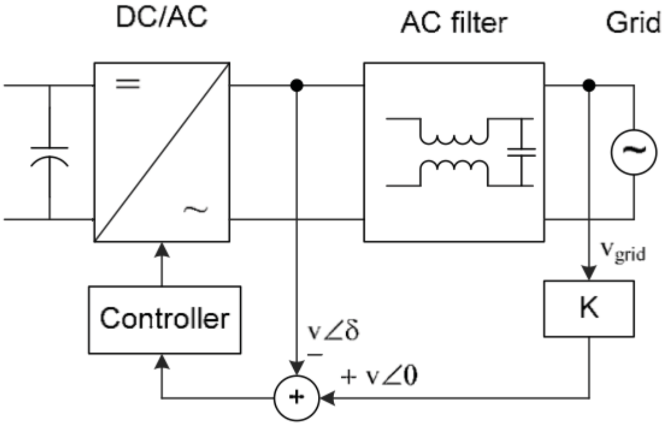

Figure 2-13 : Voltage control loop for resultant magnitude and phase difference

The difference in the grid and inverter voltage is seen across the grid inductor, which indirectly controls the inductor and grid current, Figure 2-14. The main drawback to this technique is that the voltage active and reactive power supplied to the grid are proportional to both the voltage magnitude and phase. No single parameter can be changed to allow active or reactive power to be independently modified. The voltage magnitude and grid phase angle are in both the active and reactive power components in Eq 2-3.

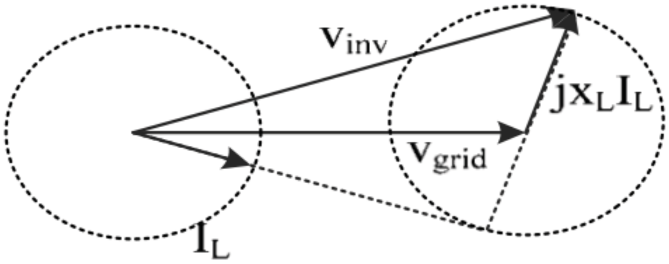

Figure 2-14 : VC-VSI control phasor diagram

2.3. Current Control Methods for Inverters

The main method used to implement a grid connection for a VSI is to use a current control technique. All current control techniques require the sensing of the output voltage and current, Figure 2-15. The input voltage is measured to ensure that the crest of the AC waveform can be created. The output voltage is sensed and its phase is passed through a PLL, which is used to create a unity phasor template for the control system.

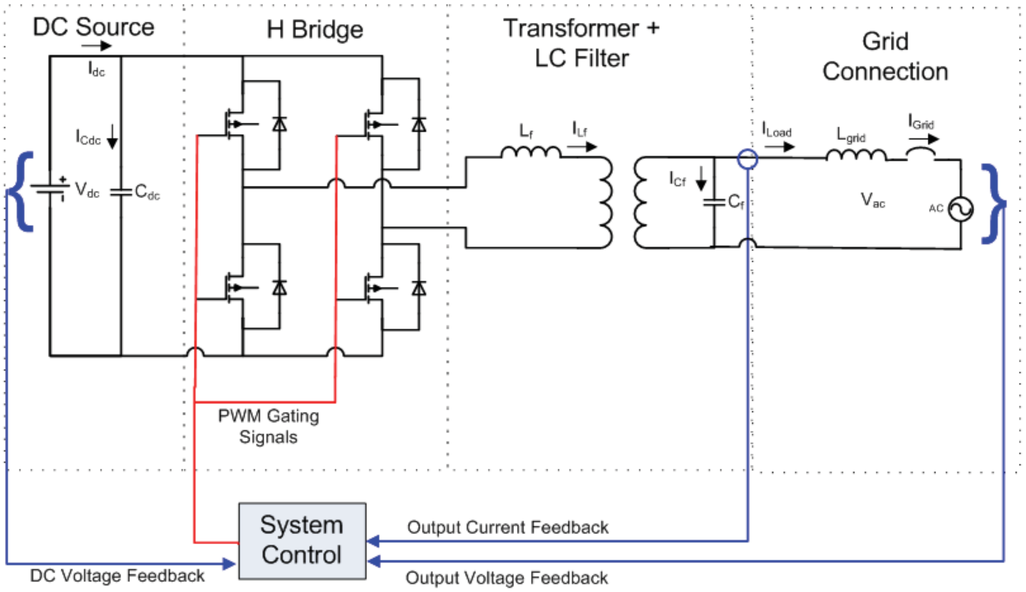

Figure 2-15 : Normal CC-VSI topology

Multiplying the PLL unity reference signal with the magnitude of the desired current or power, controls the desired active power transfer to the grid. Reactive power can be supplied to the grid by varying the phase angle of the current reference signal. The sum of the active and reactive waveform defines the template of the desired current waveform to be fed to the grid. Figure 2-16 outlines this control strategy. The method to create the current waveform template is similar for all CC-VSI, however various different methods are used to drive the switches to force the current to follow the reference. The main advantage of this technique is the active and reactive power can be controlled independently or decoupled. This ensures the inverter can provide reactive power support easily.

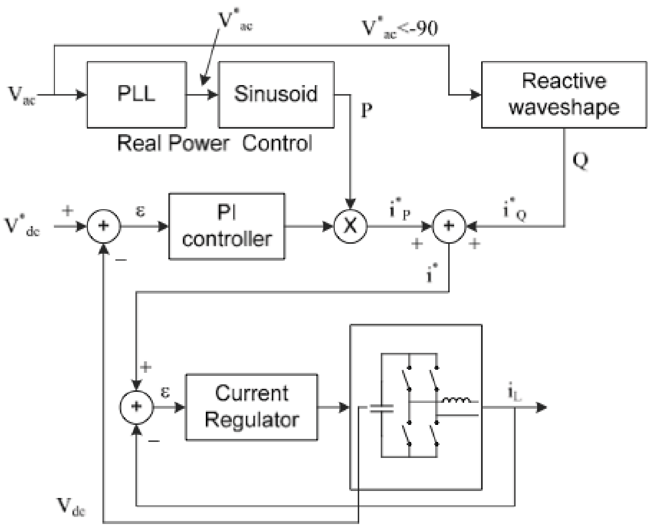

Figure 2-16 : Current control topology

Figure 2-16 shows the standard control topology of a CC-VSI where both active and reactive components can be controlled. All CC-VSI controllers must implement a PLL which is a control system employed to synchronize the inverter output current with the grid voltage [24]. This ensures the active power output current template is locked in phase with the grid voltage. The output of the phase lock loop control block is actually a unity sinusoidal waveform template which creates the phase reference for the output current.

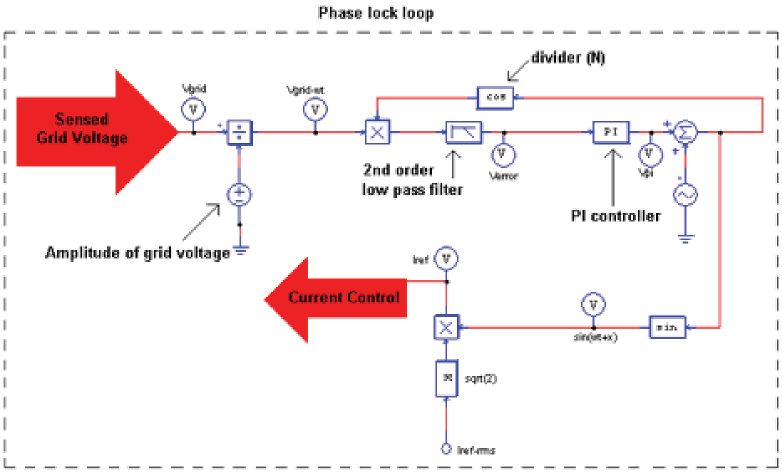

Figure 2-17 : PSIM PLL implementation

The unity signal from the voltage sensor is passed through a low pass filter to prevent any higher frequencies affecting the PLL. A PI controller is used to drive any error in the reference and grid phasers to zero. Some islanding detection methods use this as a limit. If the discrepancy is greater than a preset value the system will island. The output of the PI is added to a continuous cycling ramp from 0 to 360. The ramp represents the “ωt” while the PI output is the “x.” The sum of these signals is fed to a SINE function which creates the desired unity reference signal of “sin (ωt+x).” This waveform is multiplied by the available current to form the grid current reference waveform.

Many different methods have been used to drive to H-bridge switches in such a way to create a current sinusoid that will follow the grid current reference. These methods can be broadly split into PI triangular carrier current control, hysteresis current control, ramptime current control and predictive current control. The two most commonly implemented techniques are the standard PI current control and hysteresis current control.

2.3.1. PI Current Control Techniques

A PI current controller is a closed loop feedback system, which attempts to correct the error between a measured variable and a desired set point [25]. The proportional value determines the reaction to the current error, whereas the integral determines the reaction based on the sum of recent errors. In practice the PI controller operates by comparing the actual output current waveform with the desired reference. The output of the PI controller is then fed into a triangular based PWM switching scheme, which will drive the gates of the inverter. The advantages of the PI controller method are constant switching frequency and small output current ripple [26].

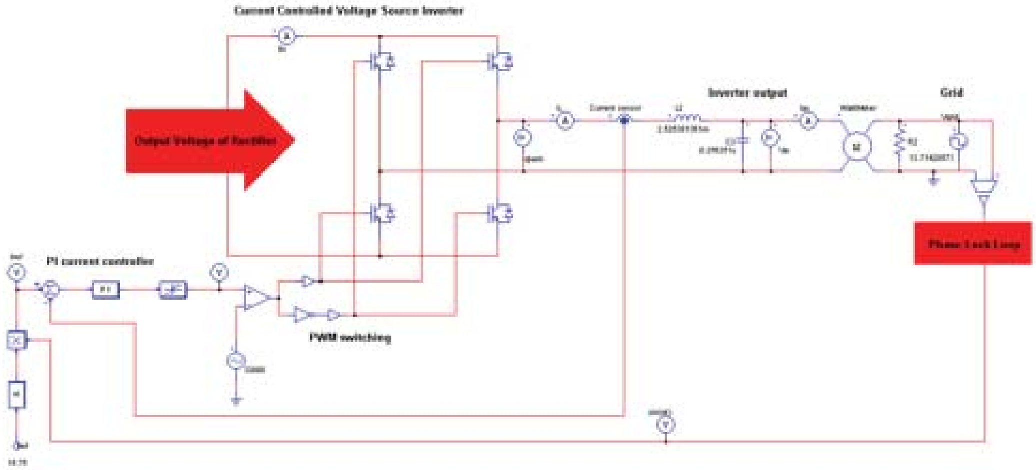

Figure 2-18 : PSIM simulation of PI current control method

Figure 2-18 shows the PI controller method with unipolar PWM switching scheme. The reference current is compared to the actual output current and the error is being fed into the PI controller. The output of the PI controller is then compared to a saw tooth (triangular) waveform with a switching frequency of 32 kHz. Figure 2-19 shows the current waveform following the reference; Figure 2-20 shows the magnified current switching. The PI is continuously correcting to as the reference is cycling. Figure 2-21 shows the FFT of the output current waveform, the main additional harmonic is the switching frequency at 32kHz, all other harmonics have been minimised by the unipolar switching method or attenuated by the low pass filter.

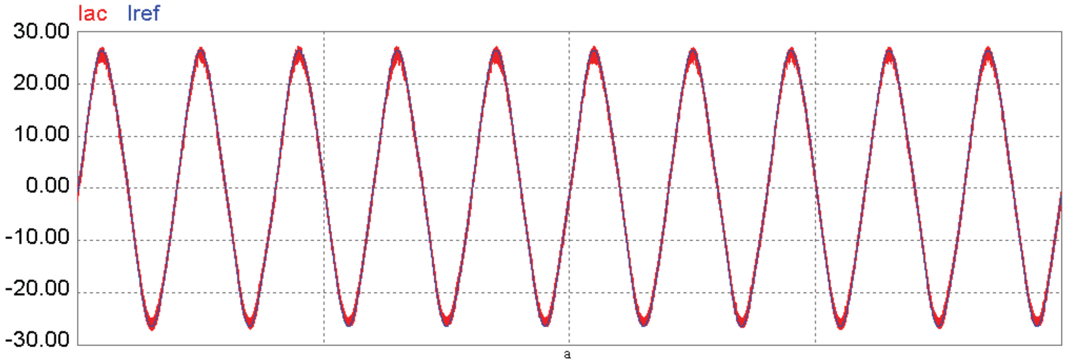

Figure 2-19 : PI controller output current and reference waveform

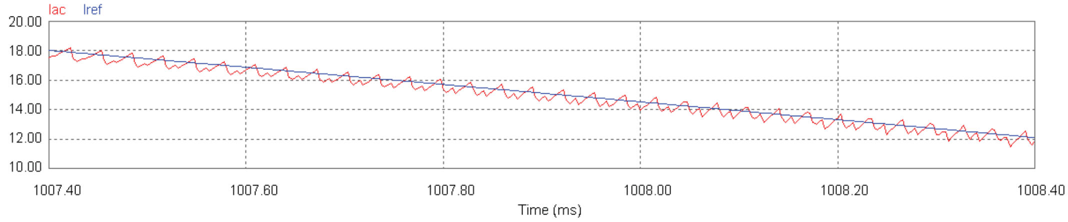

Figure 2-20 : Errors between actual and reference current waveforms

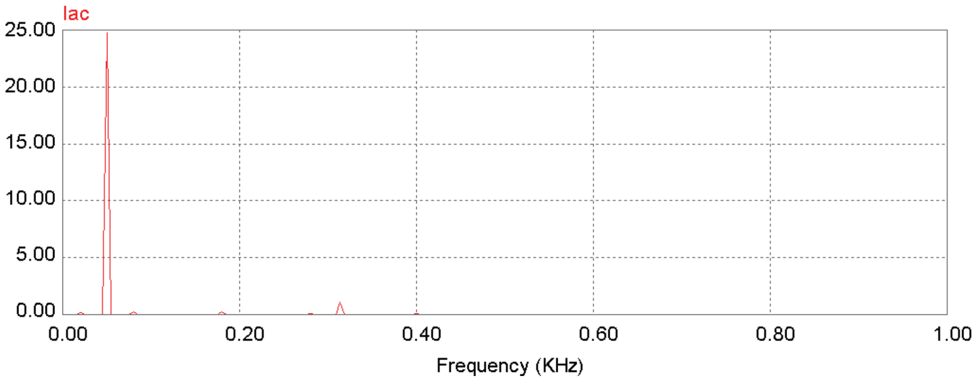

Figure 2-21 : FFT plot showing current harmonics in frequency domain

2.3.2. Hysteresis Current Control Techniques

A hysteresis current control technique implements fixed upper and lower bands, which the output current waveform is not permitted to cross [27], seen in Figure 2-22. The error between the actual output current and the reference waveform is determined by the difference between the upper and lower bands. The tighter the band will create smaller the error but an increased spectrum of switching frequencies. Figure 2-22 shows that when the sensed output current (red) is touching the upper band (pink), the hysteresis comparator will determine the switching scheme so that the current is decreased. On the other hand, when the output current is sensed to be touching the lower band (green), the switching scheme will be configured to increase the output current. The fixed reference is represented as a sinusoidal waveform (blue).

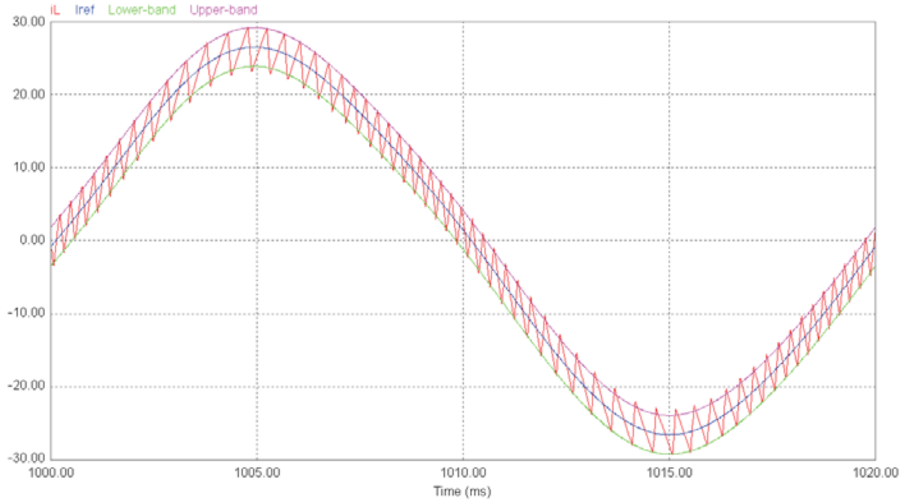

Figure 2-22 : Hysteresis current controller bands

Hysteresis comparator switching scheme can be implemented with a RS Flip-Flop and has an average error of zero as the bands are equally spaced above and below the reference. The rate of increase or decrease in current is proportional to the size of the inductor, this current gradient when superimposed into the reference bands produces varying times of switching as the current touches the band. The hysteresis current control method has no fixed switching frequency. This can be an advantage as no prominent switching frequency peak exists in the FFT broad spectrum, however the filter design must enable attenuation over a much greater range [28]. A compromise is require when selecting the inductor value as it cannot be set too high otherwise the current may not touch the band, but a too low value will increase the ripple component of the output waveform.

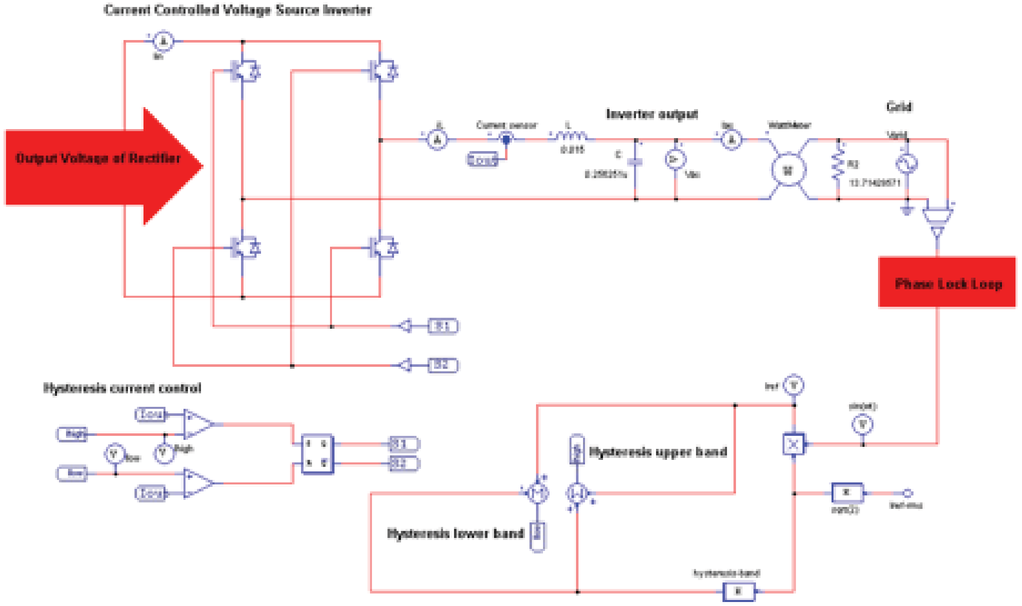

Figure 2-23 : PSIM hysteresis current control implementation

In the simulation set the error band was set to be 0.1% of the reference (i.e upper band is 1.001 x reference and lower band is 0.999 x reference). The values of sensed actual output current and the error band are compared; the outcome of this is fed to a set-reset (S-R) flip flop. The logic output of the flip-flop determines the switching configuration of the inverter. The truth table of a S-R flip-flop is shown below:

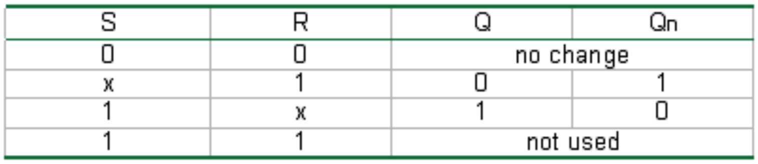

S	R	Q	Qn
0	0	no change	
x	1	0	1
1	x	1	0
1	1	not used	

Figure 2-24 : Truth Table of Set-Reset Flip Flop

S =1 when the output current is larger than the upper band, and R =1 when the output current is smaller than the lower band. The outputs Q and Q_n are used to control the switches. Figure 2-25 shows the output current waveform superimposed on the reference. In Figure 2-26 the switching can be seen between the hysteresis bands, a slight error is caused due to the time it takes to execute and calculate the next switching point The FFT, Figure 2-27 shows no prominent switching peaks and exhibits many more frequency components but at lower magnitudes.

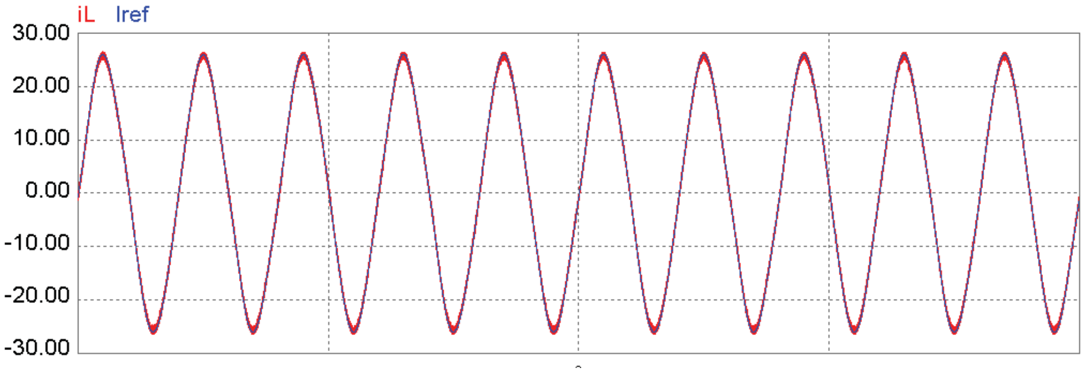

Figure 2-25 : Inverter output and reference current waveforms

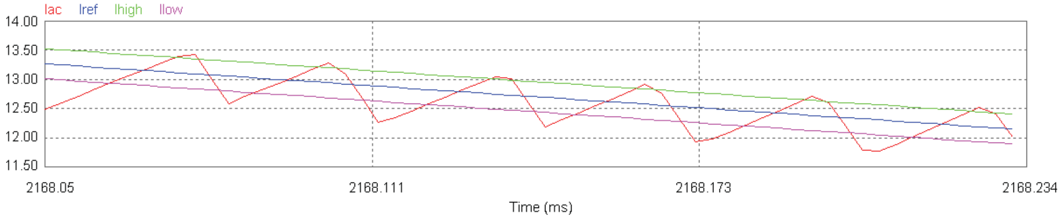

Figure 2-26 : Magnified output and reference current with hysteresis bands

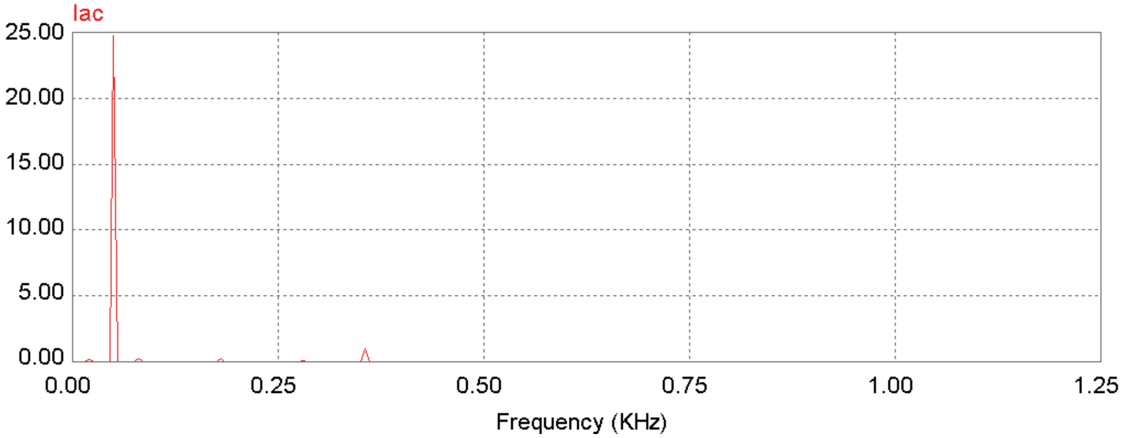

Figure 2-27 : FFT plot showing current harmonics in frequency domain

2.4. Commercial Grid Connected Inverters

All grid connected inverters connected to the SWIS are required to comply to the AS4777[29] standard which defines the requirements for disconnection during a grid fault. The inverter must detect a disturbance in the utility supply and island itself so that work may be carried out on the transmission line safely. The islanding detection techniques are generally classified into two categories, active and passive methods. Passive detection methodology is concerned with monitoring selected system parameters and will detect islanding when a certain disturbance is perceived. Active methods create some disturbance on the line which is then monitored to determine if the grid is still connected.[30]

A generic commercial PV grid connected inverter uses a DC-DC converter front end to perform the MPPT function. These inverters will operate over a range of input voltages while MPPT based upon the input voltage and current. Most commercial inverters also exhibit an initial start up voltage, which is higher than the minimum MPPT voltage. Table 2-I shows these typical commercial grid connected inverter parameters.

Parameter	Variable	Typical
Start Voltage	$V_{INV\text{-}Start}$	200 V
Minimum MPPT Range	$V_{INV\text{-}MPPT,min}$	165 V
Maximum MPPT Range	$V_{INV\text{-}MPPT,max}$	300 V
Maximum Input Voltage	$V_{INV\text{-}max}$	350 V

Table 2-I: Key Inverter Set points

The important parameters of the PV array are the open circuit string voltage ($V_{OC,string}$) and the expected maximum power point voltage of the string ($V_{MP,string}$). The $V_{OC,string}$ is required to be greater than the start voltage so that the hybrid system will start in PV only conditions. Once operating the MPPT function of the inverter will track down the input voltage to the $V_{MP,string}$, so this voltage is required to be greater then the minimum inverter tracking voltage.

$$V_{OC,string} > V_{INV-Start}$$
$$V_{MP,string} > V_{INV-MPPT,\min}$$

Eq 2-4 : PV system design constraints

2.5. *Bi-directional Operation of the H bridge*

The H-bridge as used for single phase inverters can also be implemented to create either a buck or boost converter to allow the flow of current from the AC side to the dc side. Careful control over the switches A, B, C and D will allow this current to be controlled and flow to the dc bus or battery bank. The AC grid sinusoid can be broken into a positive segment (A), and a negative segment (B), Figure 2-28. In order to obtain boost converter characteristics each segment requires the current to be absorbed by the magnetic field and then released, this creates two modes per segment. These are denoted in Figure 2-29 as mode 1-4.

Figure 2-28 : Grid waveform segments

To create the desired boost converter switches A and B can be open while a PWM signal with the desired duty cycle is applied to C during the positive segment and D during the negative segment. The magnitude of the current allowed to flow to the battery depends upon the state of charge of the battery. Extra control is required to maintain and charge the battery in either constant voltage or constant current charging regimes. Both charging techniques can be implemented using the bi-directional H-bridge.

During: A	Mode 1:	DC closed	AB open
	Mode 2:	BC closed	AD open
During: B	Mode 3	CD closed	AB open
	Mode 4	AD closed	CB open

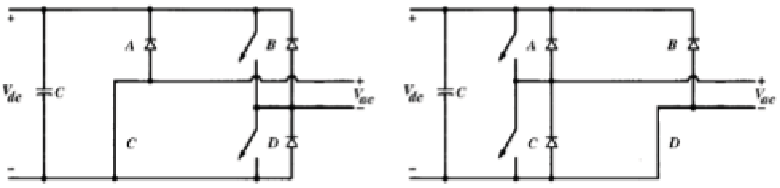

(a) During: A

(b) During: B

Figure 2-29 : H-bridge to boost converter

2.6. Power Electronic Topologies for Solar Applications

The requirements for a PV inverter are based upon the interconnection approach of the PV modules. These can be connected in series strings, then paralleled with blocking diodes to a single central inverter Figure 2-30(a); or each series string has a grid connected inverter Figure 2-30(b), or each PV module having its own inverter Figure 2-30(c). A central approach is generally adopted for larger scale three phase PV systems up to 250kW, this method exhibits high efficiency and reduced power electronic cost, however not optimal MPPT and no redundancy. Large MW level plants usually adopt a few of these systems in parallel. The series approach is usually utilised in systems up to 5kW single phase for roof top type installations. Each string has its own MPPT allowing optimal extraction of power and the loss of one inverter only deducts a single strings power from the system. The individual module approach is generally not adopted due to the increased power electronics components cost and low efficiency due to parasitic inverter losses.

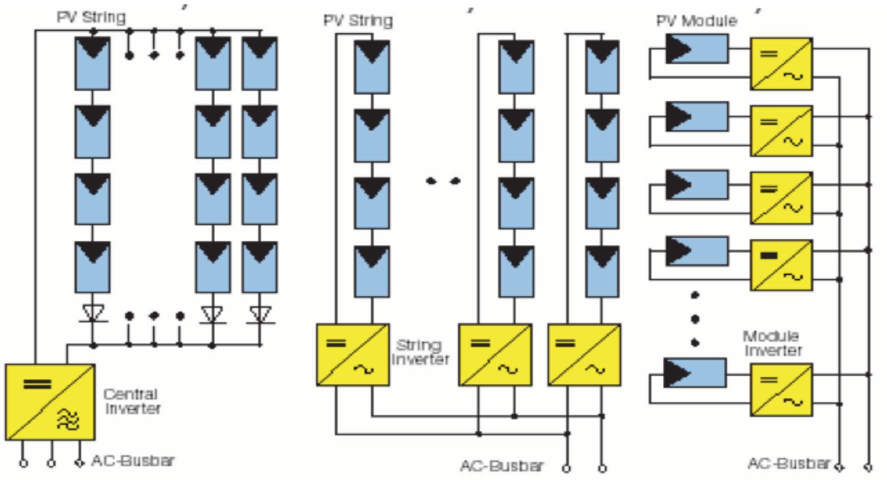

Figure 2-30 PV interconnection topologies (a) Central inverter (b) String inverter (c) Module inverter [31]

The PV power electronic topologies mainly rely upon the requirement of MPPT and galvanic isolation. These criteria depend on the grid connection requirements of the utility, in Australia this is covered by the AS4777. Figure 2-31 shows the different possible design constraints.

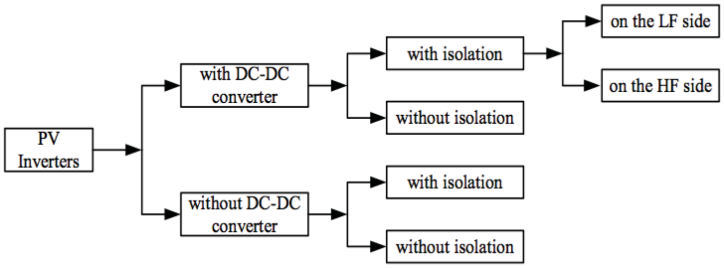

Figure 2-31 : PV power electronic design options [31]

The standard inverter topology, Figure 2-32, adopted by almost all manufacturers is the full bridge inverter, previously described as the CC-VSI. However this standard approach cannot perform MPPT or provide isolation between the source and grid. It also depends on the PV string voltage generating a voltage high enough to recreate the crest of the AC grid voltage.

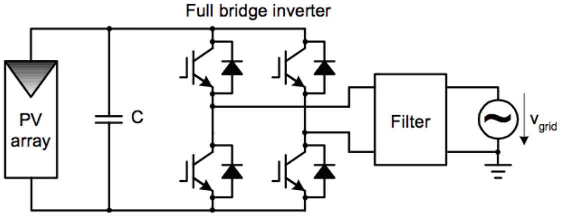

Figure 2-32 : Transformerless full bridge inverter [31]

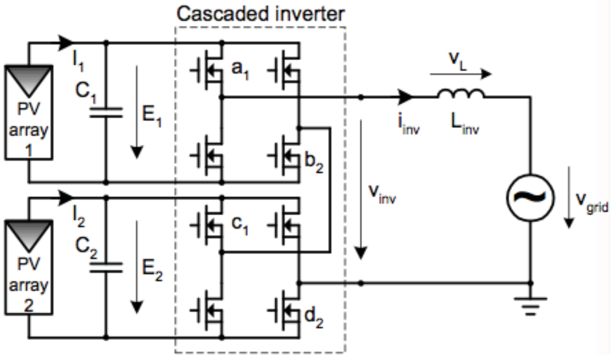

Figure 2-33 : Transformerless multilevel cascaded inverter topology [31]

Figure 2-33 presents a method which cascades the PV arrays on the dc side allowing the voltage to be increased and the PV operating point to be closer to the maximum voltage point of the PV array. Figure 2-34 shows the typical inverter topology with a grid side low frequency transformer providing galvanic isolation. However the low frequency transformer introduces additional losses through winding resistance and magnetic hysteresis losses. Power Solutions Australia currently adopt this topology.

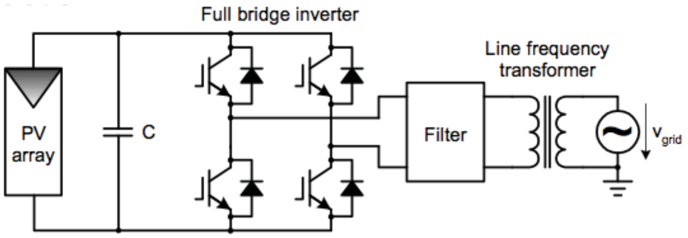

Figure 2-34 : Standard full bridge inverter with low frequency transformer [31]

To carry out MPPT operation the PV module or string voltage must be controlled, this is achieved through a dc-dc converter at the input to the full bridge. Figure 2-35 uses a boost converter which also increases the voltage seen at the output of the full bridge which controlling the PV voltage using some MPPT technique.

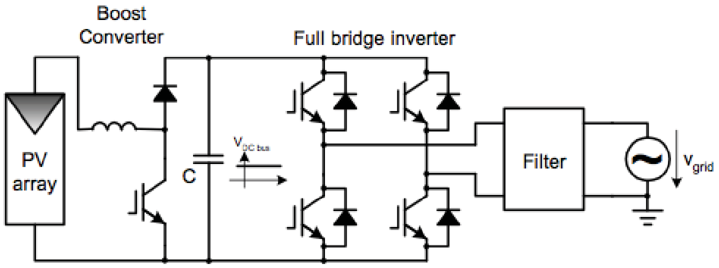

Figure 2-35 : Front end boost converter on transformerless full bridge inverter

The front end converter can also be utilised as a switching converter to allow the inclusion of a high frequency transformer. The push pull front end converter has become very popular commercially as it keeps the transformer losses low while providing galvanic isolation. The switching of the front end converter can also be controlled to allow MPPT operation. Figure 2-36 shows this approach. SMA, Fronius, KACO and Leonics all use this topology in their standard grid connected, galvanically isolated inverter.

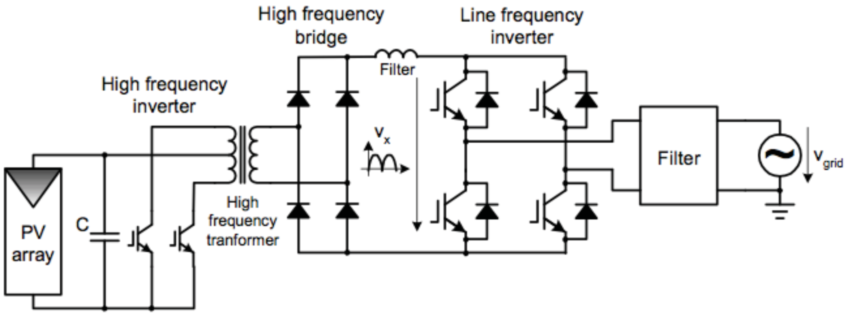

Figure 2-36 : Front end converter with high frequency transformer [31]

2.7. Power Electronic Topologies for Small Wind Applications

2.7.1. Interfaces for permanent magnet synchronous generators

For small and medium scale wind turbines permanent magnet type generators are growing in popularity. Some wind turbines, generally less than 20kW, use multiple pole permanent magnet machines as the generator. This creates a variable voltage, variable frequency output which is rectified into a variable voltage dc bus. A DC-DC converter then performs MPPT to feed the available energy from the WT to a controlled central dc bus. The rotational speed of the WT determines the voltage. In very high wind conditions the WT can over speed, which can lead to the destruction of the machine. A WTC is usually implemented to control the upper voltage limit to the other sensitive components. Excess energy is diverted to the dump load forcing the slowing of the rotational speed and also the voltage. The WTC is also required in situations where the energy for the WT cannot be utilised effectively, such as a grid failure [32-41].

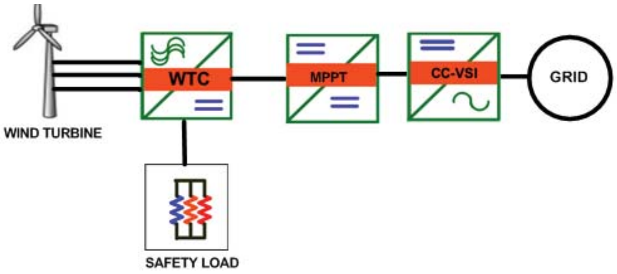

Figure 2-37 : Standard grid connected topology

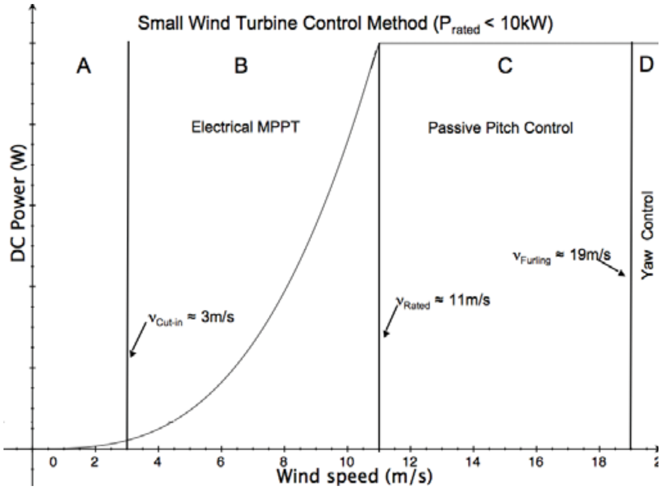

Figure 2-38 : Small wind turbine control methods

Region	Wind Speed	Power Relationship
A	$0 > \nu > \nu_{CUT\text{-}IN}$	$P_{WT} = 0$
B	$\nu_{CUT\text{-}IN} > \nu > \nu_{RATED}$	$P_{WT} = Cp(\lambda)0.5\rho A\nu^3$
C	$\nu_{RATED} > \nu > \nu_{FURLING}$	$P_{WT} = P_{RATED}$
D	$\nu_{FURLING} < \nu$	$P_{WT} = 0$

Table 2-II : Wind turbine operation regions

A small WT's operation can be defined into four main regions, based upon the wind speed as given in Table 2-II. The DC-DC converter is only required to perform the MPPT operation during region B, where the tip-speed ratio (λ) is optimised and kept constant to allow the WT to operate at its maximum Cp value. This is known as variable speed operation.

No power is generated until the wind speed is greater then the cut in wind speed for the wind turbine, this is due to the frictional force required to rotate being greater then the incident wind force. For increasing wind speed up to the rated wind speed the power generated obeys the wind power cubic relationship, in this region the tip-speed ratio (TSR) needs to be optimised to allow the maximum power to be generated. For wind speeds greater than the WT rated wind speed the blades begin to flex and reduce the Cp, decreasing the generated power. This is termed passive pitch control. At very high wind speeds yaw control is adopted to rotate the WT out of the direction of the wind. For smaller WTs, doubly fed induction type machines are not used due to the excess power electronic cost with respect to the wind turbine itself.

2.8. Summary

This chapter presented, explained and modelled various multi-function power electronic interfaces, which are applied to renewable energy sources. The main investigated component is the inverter that converts the DC power for either PV or WT (through a rectifier) to the same voltage and frequency of the utility. The chapter focuses on the control methods of the H-bridge single phase inverter; however, all the techniques shown may be applied to three phase systems. A summary of the contents of the chapter is seen below.

- Inverters
    - Switching methods
    - VC-VSI stand alone with output voltage feedback
    - VC-VSI grid connected
    - CC-VSI
    - CC-VSI PI controller implementation
    - CC-VSI hysteresis implementation
- Commercial grid connected inverters
- Bi-directional H-Bridge
- Power electronic topologies for solar systems
- Power electronic topologies for wind systems
    - Power electronic topologies for PMSG

2.9. References

1. *PSIM Version 7.0*. 2006, Powersim Inc. (www.powersimtech.com): Woburn, MA.
2. Dehbonei, H., et al., *A Solar Photovoltaic In-line UPS System Using Space Vector Modulation Technique.* IEEE Power Engineering Society Summer Meeting, 2001. **1**: p. 632-637.
3. Pinheiro, H., et al., *Space Vector Modulation for Voltage-Source Inverters: A Unified Approach.* 28th Annual Conference of the Industrial Electronics Society, 2002. **1**: p. 23-29.
4. Yu, Z., *Space-Vector PWM with TMS320C24x/F24x Using Hardware and Software Determined Switching Patterns*. Application SPRA524. 1999: Texas Instruments.
5. Dehbonei, H., L. Borle, and C.V. Nayar, *A Review and a Proposal for Optimal Harmonic Mitigation in Single-Phase Pulse Width Modulation.* 4th IEEE International Conference on Power Electronics and Drive Systems, 2001. **1**: p. 408-414.
6. Trigg, M.C., H. Dehbonei, and C.V. Nayar, *Digital Sinusoidal PWMs for a Micro-controller based Single-Phase Inverter. Part 1: Principles of digital sinusoidal PWM generation.* International Journal of Electronics, (Submitted 2005).
7. Trigg, M.C., H. Dehbonei, and C.V. Nayar, *Digital Sinusoidal PWMs for a Micro-controller based Single-Phase Inverter. Part 2: Performance assessment - experimental.* International Journal of Electronics, (Submitted 2005).
8. Holmes, D.G. and B.P. McGrath, *Opportunities for Harmonic Cancellation with Carrier-Based PWM for Two-Level and Multilevel Cascaded Inverters.* IEEE Transactions on Industry Applications, 2001. **37**: p. 574-582.
9. Holmes, D.G., *Pulse Width Modulation for Power Converters: Principles and Practice*. IEEE Press Series on Power Engineering, ed. T.A. Lipo. 2003, New York: IEEE.
10. Holmes, D.G., *The Significance of Zero Space Vector Placement for Carrier Based PWM Schemes.* IEEE Transactions on Industry Applications, 1996. **32**: p. 1122-1129.
11. Trigg, M.C., H. Dehbonei, and C.V. Nayar. *DC Bus Compensation for a Sinusoidal Voltage Source Inverter with Wave-Shaping Control*. in *IEEE Industrial Electronics Conference*. 2006. Paris, France.
12. Trigg, M.C., H. Dehbonei, and C.V. Nayar, *A Low-cost and Reliable Sinusoidal Wave-shaping Controller for a Voltage Controlled Voltage Source Inverter supplying Non-linear Loads*. Recent Advances in Control Systems, Robotics and Automation, ed. S. Pennacchio. 2006, Palermo, Italy: Associazione Internationalsar.
13. Mohan, N., T.M. Undeland, and W.P. Robbins, *Power Electronics - Converters, Applications, and Design*. 3nd ed. 2003: John Wiley & Sons, Inc.
14. Skvarenina, T.L., ed. *The Power Electronics Handbook*. Industrial Electronics Series, ed. J.D. Irwin. 2002, CRC Press.
15. Krein, P.T., *Elements of Power Electronics*. 1998, New York: Oxford University Press.

16. Kwon, S.H., et al., *A New Direct Digital PWM Technique for Microprocessor-Based PWM Inverters.* 27th Annual IEEE Power Electronics Specialists Conference, 1996. **2**: p. 1300-1304.
17. Lin, C., et al., *A New Method of Optimized PWM Based on 8XC196MC.* Proceedings of The Third International Power Electronics and Motion Control Conference, 2000. **3**: p. 1266-1270.
18. Ryan, M.J., W.E. Brumsickle, and R.D. Lorenz, *Control Topology Options for Single-Phase UPS Inverters.* IEEE Transactions on Industry Applications, 1997. **33**(2): p. 493-501.
19. Trigg, M.C. *Digital Sinusoidal PWM Generation using a Low-cost Micro-controller Based Single-Phase Inverter*. in *10th IEEE International Conference on Emerging Technologies and Factory Automation*. 2005. Catania, Italy: IEEE.
20. Bowes, S.R., D. Holliday, and S. Grewal, *Regular-Sampled Harmonic Elimination PWM Control of Single-Phase Two-Level Inverters.* IEF. Proc-Electric Power Applications, 2001. **148**: p. 309-314.
21. Ashari, M., *Multi-Function Voltage Source Inverters for Weak-Grid and Off Grid Applications*, in *Electrical and Computer Engineering*. 2001, Perth: Curtin University of Technology. p. 286.
22. Ashari, M., W.W.L. Keerthipala, and C.V. Nayar, *A Single Phase Parallel Connected Uninterruptible Power Supply / Demand Side Management System.* IEEE Transactions on Energy Conversion, 2000. **15**.
23. Prasad, B.S.J., S.; Agarwal, V., *Universal Single-Stage Grid-Connected Inverter.* IEEE Transactions on Energy Conversion, 2008. **23**(1): p. 128 - 137.
24. Marion, B., Hayden, H., Shugar, D., Rich, G. *Performance Parameters for Grid Connected PV Systems*. in *31st IEEE Photovoltaics Specialists Conference and Exhibition*. 2005. National Renewable Energy Laboratory, Colorado, United States of America.
25. Brod, D.M. and D.W. Novotny, *Current Control of VSI-PWM Inverters.* IEEE Transactions on Industry Applications, 1985. **21**: p. 562-570.
26. Bower, W., Whitaker, C., Fitzgerald, M., Erdman, W., Behnke, M, *Performance Test Protocol for Evaluating Inverters Used in Grid – Connected Photovoltaic Systems*. 2004, Sandia National Laboratories: Albuquerque, United States of America. .
27. Ingram, D., Round, S, *A Novel Digital Hysteresis Current Controller for an Active Power Filter*. 2005, Dept of Electrical and Electronic Engineering, University of Canterbury: Christchurch, New Zealand.
28. Gatlan, C., Gatlan, L, *AC to DC PWM Voltage Source Converter Under Hysteresis Current Control.* IEEE ???, ???
29. Australia, S., *AS 4777.1-2005 : Grid connection of energy systems via inverters - Installation requirements*, in *Australian Standards*, S. Global, Editor. 2005: Melbourne, Australia.
30. Stevens, J., et al., *Development and Testing of an Approach to Anti Islanding in Utility-Interconnected Photovoltaic Systems*. 2000, Sandia National Laboratories, Albuquerque, United States of America.
31. Blaabjerg, F., et al., *Overview of Control and Grid Synchronization for Distributed Power Generation Systems.* IEEE Transactions on Industrial Electronics, 2006. **53**(5): p. 1398-1409.

32. Kelvin Tan, S.I., *Optimum Control Strategies in Energy Conversion of PMSG Wind Turbine System Without Mechanical Sensors* IEEE Transactions on Energy Conversion, 2004. **19**(No 2).
33. Venkataramanan, G., et al., *Variable Speed Operation Of Permanent Magnet Alternator Wind Turbine Using A Single Switch Power Converter. Journal of Solar Energy Engineering, Transaction of ASME*, 1996.
34. Carlin, P.W., *The History and State of the Art of Variable-Speed Wind Turbine Technology*, in *NREL Technical Report*. 2001, National Rewnwable Energy Laboratory: Golden.
35. Chen, J., C.V. Nayar, and L. Xu, *Design and finite-element analysis of an outer-rotor permanent-magnet generator for directly coupled wind turbines.* IEEE Transactions on Magnetics, 2000. **36**: p. 3802 -3809.
36. Chen, J., *Performance enhancement of AC machine and permanent magnet generator for sustainable energy applications*. 1999, School of Electrical and Computer Engineering.: Perth: Curtin University of Technology.
37. J. Darbyshire, C.V.N. *Modelling, simulation and testing of grid connected small scale wind systems*. in *Australasian Universities Power Engineering Conference*. 2007. Perth.
38. Whaley, D.M., et al. *Investigation of a Low-Cost Grid-Connected Inverter for Small-Scale Wind Turbines Based on a Constant-Current Source PM Generator*. in *IEEE Industrial Electronics, IECON 2006 - 32nd Annual Conference on* 2006. Paris, France: IEEE.
39. Raju, A.B., *Application of power electronic interfaces for grid connected variable speed wind energy conversion systems*, in *Department of Electrical Engineering*. 2005, Indian Institute of Technology: Bombay.
40. Valenciaga, F. and P.F. Puleston, *High-Order Sliding Control for a Wind Energy Conversion System Based on a Permanent Magnet Synchronous Generator* IEEE Transactions on Energy Conversion, 2008. **23**(3).
41. Huang, H. and L. Chang. *Energy-Flow Direction Control of Grid-Connected IGBT Inverters for Wind Energy Extraction*. in *IEEE 2000 Canadian Conference on Electrical and Computer Engineering*. 2000. Halifax, Canada.

"Every reasonable effort has been made to acknowledge the owners of copyright material. I would be pleased to hear from any copyright owner who has been omitted or incorrectly acknowledged."

3. Maximising Energy Extraction for Solar and Wind Systems

This chapter investigates MPPT for wind and solar hybrid power systems. The mathematical models for the control algorithms are developed, modelled and simulated. Test cases are presented which cause the algorithms to fail and modifications are made to improve the systems.

A solar PV model is created in PSIM from a mathematical model of a solar cell. The cell model is extrapolated to an array model, which uses the Newton-Raphson algorithm to solve for the I-V cell curve. The final PSIM sub-circuit represents a PV array in which commonly available data sheet specifications may be used to create a complete array model. The irradiance and temperature can be varied throughout the simulation and the curve is updated as required by the simulation. This accurate model is required to allow modelling of the MPPT algorithms to be carried out.

Three methods of MPPT are presented, constant voltage, perturb and observe and incremental conductance. The constant voltage type is not a continual algorithm and is inaccurate so is not investigated in detail. The P&O and CI algorithms are developed in Microsoft Visual Studio C++ and implemented into PSIM. The irradiatnce and temperature are changed to show the failure in the MPPT algorithm. The CI algorithm is shown to be better under rapidly changing conditions.

A wind MPPT system needs to respond to rapid and continually changing wind conditions. An implementation of the solar CI algorithm is shown to be able to track changing wind conditions and can be used for small wind turbines. To simulate this concept a complete wind turbine model is developed from the energy in the wind to the transfer of torque to the PMSG. The electrical output is then rectified and the dc current controlled allowing MPP optimisation and testing of the CI algorithm. Finally a CC-VSI is simulated to show the generated power and islanding capability.

3.1. Solar Cell Mathematical Modelling

The basic mathematical model of the solar cell is created by subtracting the diode forward current expression from the generated light current [2]. In dark conditions the light current is zero and hence the expression is an inverted diode expression. The light current will vary linearly throughout the day with changes in solar radiation and slightly with temperature [3-7].

$$I_O = I_L - I_F$$

$$I_O = I_L - I_S\left[\exp\left(\frac{qV_{cell}}{AkT}\right) - 1\right]$$

$$V_{cell} = V_{OC} = \frac{AkT}{q}\ln\left[1 + \frac{I_L}{I_S}\right]$$

Eq 3-1 : PV cell model equations

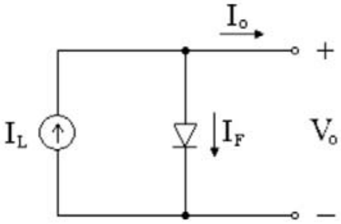

Figure 3-1 : Basic model equivalent circuit

The basic equivalent circuit for a solar cell can be seen in Figure 3-1, it contains a current source representative of current generated by the photons incident on the cell and a diode. The I-V characteristics of a solar cell can be shown to be the same as the basic diode model with a constant current increase as shown in Figure 3-2. As the irradiance changes throughout the day the light current changes proportionally.

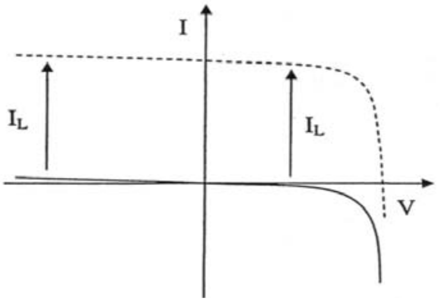

Figure 3-2 : Basic photovoltaic cell I-V curve

The photovoltaic cell will only produce power for the forward biased and positive current region. The intersect of the I-V curve with the y axis is denoted the cells short circuit current and the x-axis is the open circuit voltage. The point on the curve where current derivative is greatest with respect to the voltage is the MPP for the cell and is commonly termed the knee. Another analogy is the MPP occurs when the largest rectangle can be fit under the curve. This is shown in Figure 3-3, which is derived from the basic PV cell model. The direct relationship between changing conditions of solar irradiation and current can be seen in Figure 1-14, note the changes in irradiance also cause the maximum operating power point to change.

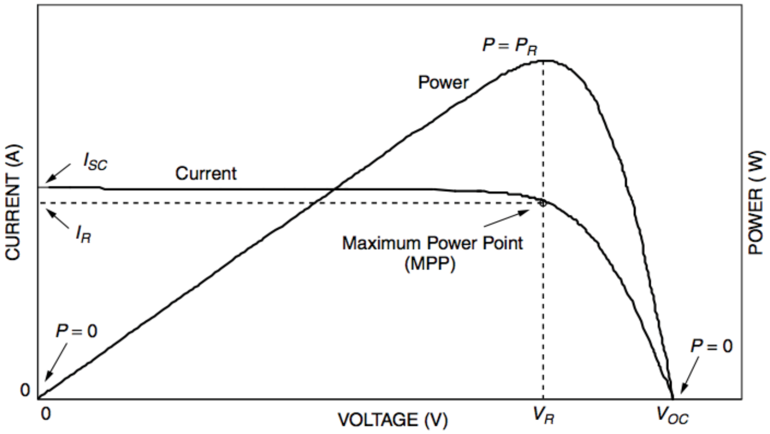

Figure 3-3 : P-V and I-V curves predicted by basic model [8]

A comparison of the theoretical I-V curve derived from the basic model in Figure 3-3 and the actual curve generated empirically from testing the Lorentz model in Figure 1-14 shows some inaccuracies in the model. These are summarised below.

Difference	**Result**	**Solution**
$\left[\frac{dI}{dV}\right]_{MODELLED} < \left[\frac{dI}{dV}\right]_{ACTUAL} : V < V_{MPP}$	$I_{MPP,MODELLED} > I_{MPP,ACTUAL}$	Add Rp
$\left[\frac{dV}{dI}\right]_{MODELLED} > \left[\frac{dV}{dI}\right]_{ACTUAL} : V > V_{MPP}$	$V_{MPP,MODELLED} > V_{MPP,ACTUAL}$	Add Rs

Table 3-I : Inaccuracies in the basic PV model

In summary, the basic model gives an adequate approximation of short circuit current and open circuit voltage parameters but fails to accurately predict the maximum voltage and current points for ideal operation. Accurate prediction of these points is required to create a complete mathematical description of the PV cell or module. The addition of a series resistor and a parallel resistor increases the gradient of the two linear-like components of the IV curve and allows for a more accurate model of the maximum operating power points.

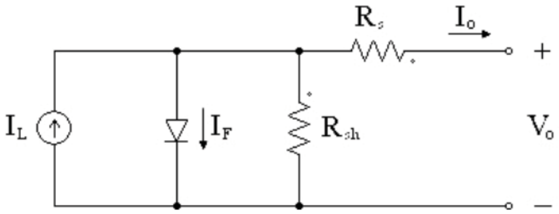

Figure 3-4 : PV cell equivalent circuit

The addition of a series resistor will decrease the output cell voltage linearly with current. This series resistor is representative of the resistance of the materials, which form the pn junction, and from the ohmic cell contacts. This substituted into the basic PV cell expression yields;

$$V_{cell} = V_O + I_O R_S$$

$$I_O = I_L - I_S\left[\exp\left(\frac{q(V_O + I_O R_S)}{AkT}\right) - 1\right]$$

Eq 3-2 : PV cell model with series resistance

This has the effect of decreasing the gradient after the maximum power point, decreasing the maximum power point while not affecting the short circuit current. This can be seen in Figure 3-5. For a new cell the series resistance should not create a loss greater then 1%. This allows an upper limit for the series resistance to be calculated. Typical values of the series resistance are less then 1mΩ. [3, 5]

$$R_S < \frac{0.01V_{OC}}{I_{SC}}$$

Eq 3-3 : Series resistance approximation

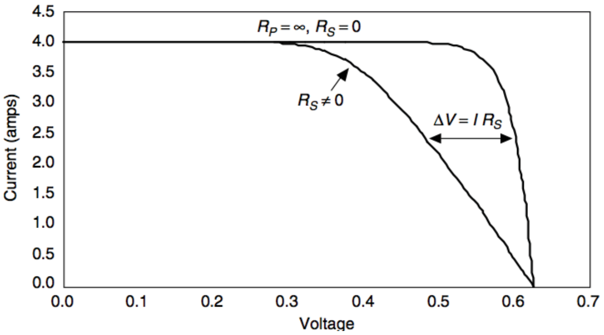

Figure 3-5 : Effect of a series resistance on the PV model [8]

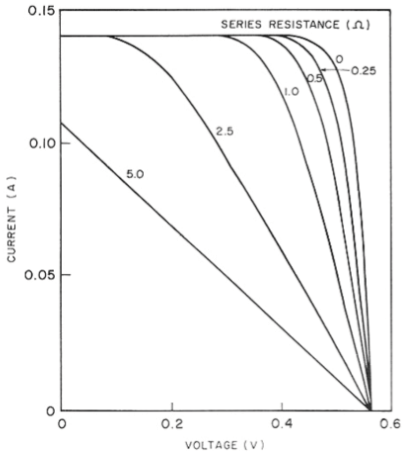

Figure 3-6 : Effect of different values of series resistance [9]

The basic diode model predicts that during a cell shading condition the current in the string will be limited to the reverse saturation current passed through the diode. For an actual PV cell the gradient of the IV curve is not close to zero implying that the cell will conduct some current. The addition of a parallel resistor solves this by allowing an alternative path for the current to flow, as seen in Figure 3-4. In reality the parallel resistance represents the junction leakage current which is larger then that for a usual diode. Substituting this into the PV cell equation yields the full model equation.

$$I_O = I_L - I_D - \frac{V_O}{R_P}$$
$$I_O = I_L - I_S\left[\exp\left(\frac{q\left(V_O + I_O R_S\right)}{AkT}\right) - 1\right] - \frac{V_O + I_O R_S}{R_P}$$

Eq 3-4 : Mathematical description of a PV cell

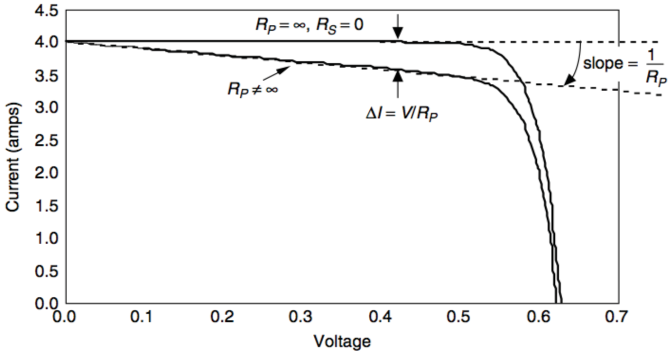

Figure 3-7 : Effect of a parallel resistance on the PV model [8]

The addition of the parallel resistor increases the gradient of the IV curve up to the MPP, decreases the MPP while not affecting the short circuit current. The differences between the basic model the complex model are seen in Figure 3-7.

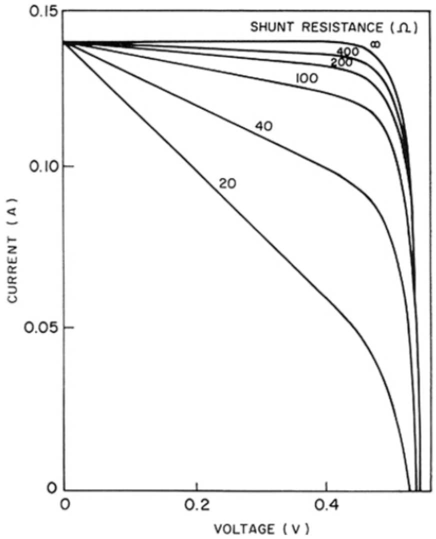

Figure 3-8 : Effect of different values of parallel resistance [9]

The new mathematical model presents an equation which is implicitly complex to solve as neither current or voltage expressions can be isolated. The series and shunt resistance parameters are difficult to calculate and are not readily available from the data sheet of a solar module. In order to accurately characterise the cell, module or array to predict the energy output they are required. A technique to extract the model parameters from common data sheet values of open circuit voltage, short circuit current and maximum power voltage and current will be presented in the next section.

3.2. Solar Photovoltaic Modelling

The characteristics of a PV module and array cannot easily be determined by PV module data sheet information alone. Typically only the maximum power voltage and current, short circuit current and open circuit voltages are given. A model was required to assess the accuracy and reliability of MPPT algorithms. In order to fully characterise a PV module the series and shunt resistances of the module need to be determined. These are the internal losses that characterise the knee region or maximum power point of the PV module.

A PSIM model was created that could easily model any PV module based upon the usually available data. This model was extended to allow a complete array be simulated for any temperature and irradiance level. The inputs for the simulation are broken into three sections, data sheet data, array connections and environmental parameters, Figure 3-9. A voltage controlled voltage source is used to control the arrays output voltage based upon the current drawn from the PV array, this allows an external MPPT to be attached which may use any algorithm while both the PV temperature and irradiance may be perturbed.

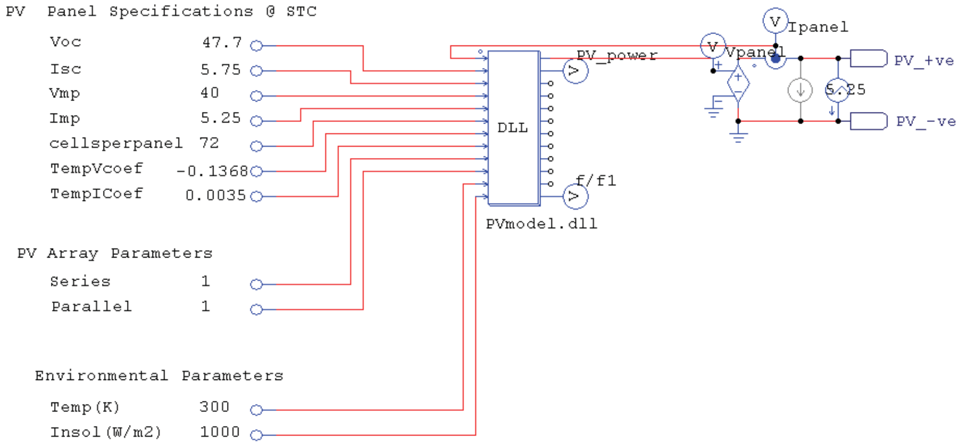

Figure 3-9 : PSIM PV characterisation simulation

A dynamic link library (DLL) is a compiled section of C code, which can perform the required mathematical calculations used for the simulation. The DLL reduces the PV array into a PV module and then to a single cell model. The Newton-Raphson algorithm is used to solve for the single cell voltage and current using a large number of iterations. This solution is then extrapolated to the PV module and then PV array solution.

The mathematical modelling of the system can be broken down into the following steps:

- Calculation of environmental parameters:

$$V_{OC} = V_{OC,STP} + V_{temp}(T - 298)$$
$$I_{SC} = I_{SC,STP} + I_{temp}(T - 298)$$

Eq 3-5 : PV temperature variations

- Calculation of per cell equivalents:

$$I_{cell} = \frac{I_{array}}{N_{branches}}$$
$$V_{OC,cell} = \frac{V_{OC}}{N_{series}}$$
$$V_{MP,cell} = \frac{V_{MP}}{N_{series}}$$

Eq 3-6 : PV array parameters

- Calculation of individual cell parameters:

$$I_S = \frac{I_{SC}}{\exp\left[\frac{qV_{OC,cell}}{nkT}\right]}$$

Eq 3-7 : PV cell diode saturation current

$$R_s = \frac{N_{panel} V_{OC,cell} I_{SC,cell}}{V_{MP,cell} I^3_{MP,cell}}$$
$$R_{sh} = \frac{N_{panel} V^2_{MP,cell}}{V_{OC,cell} I_{SC,cell} - V_{MP,cell} I_{MP,cell}}$$

Eq 3-8 : Series and shunt resistance parameters

- Calculation of light generated current

$$I_{light} = \frac{S}{1000} I_{SC,cell}\left(1 + \frac{R_s}{R_{sh}}\right)$$

Eq 3-9 : Light generated current expression

- Newton Raphson algorithm where the basic premise is to iterate towards a solution of Eq 3-10 until Eq 3-11.

$$V_{k+1} = V_k - \frac{f(V_k)}{f'(V_k)}$$

Eq 3-10 : Newton-Raphson algorithm

$$\frac{f(V_k)}{f'(V_k)} \approx 0$$

Eq 3-11 : Iteration tolerance parameter

An initial approximation is required which is based upon the data sheet maximum power point current or the previous iterations final current. This determines the area in which the cell is operating and so the required iteration equations. These regions and expressions in terms of current are defined by Eq 3-12 and Eq 3-13.

$$\begin{aligned}
&\text{Region A}: 0 > I_{cell} > I_{MP,cell}\\
&\text{Initial approximation}:\\
&V = -I\frac{V_{OC,cell} - V_{MP,cell}}{I_{MP,cell}} + V_{OC,cell}\\
&V_k = R_{sh}I_{light} - R_{sh}I_S\left(\exp\left[\frac{q}{nkT}\left(V + R_sI_{cell}\right)\right] - 1\right) - I(R_{sh} + R_s) - V\\
&V_k' = -\frac{qR_{sh}I_S}{nkT}\left(\exp\left[\frac{q}{nkT}\left(V + R_sI_{cell}\right)\right] - 1\right) - 1\\
&V_{k+1} = V_k - \frac{V_k}{V_k'}
\end{aligned}$$

Eq 3-12 : Iterative procedure for region A

$$
\begin{aligned}
&\text{Region B}: I_{MP,cell} > I_{cell} > I_{SC,cell} \\
&\text{Initial approximation}: \\
&V = -\frac{V_{MP,cell}(I - I_{SC,cell})}{I_{SC,cell} - I_{MP,cell}} \\
&V_k = R_{sh} I_{light} - R_{sh} I_S \left(\exp\left[\frac{q}{nkT} \left(V + R_s I_{cell} \right) \right] - 1 \right) - I(R_{sh} + R_s) - V \\
&V_k' = -\frac{q R_{sh} I_S}{nkT} \left(\exp\left[\frac{q}{nkT} \left(V + R_s I_{cell} \right) \right] - 1 \right) - 1 \\
&V_{k+1} = V_k - \frac{V_k}{V_k'}
\end{aligned}
$$

Eq 3-13 : Iterative procedure for region B

The algorithm responds to any current which is seen to be outside the range of regions A and B with zero voltage. An exit to the calculation loop is also provided to prevent time intensive calculation if the operating current has not changed appreciably. This is defined by Eq 3-14.

$$
\begin{aligned}
&\text{Region A}:\ 0 > I_{cell} > I_{MP,cell} \\
&\frac{I_{previous} - I}{I} > 0.0001 \\
&\text{Region B}:\ I_{MP,cell} > I_{cell} > I_{SC,cell} \\
&\frac{I_{previous} - I}{I} < 0.0001
\end{aligned}
$$

Eq 3-14 : Current Region Definitions

Once the desired tolerance has been achieved the iterated voltage is passed as an output of the DLL for use within PSIM. The power and error are also passed into the simulator to provide further information to the end user. The complete code as written in Microsoft Visual C++ is seen in the following few pages.

```
//PVmodel.dll

 // You may change the variable names (say from "t" to "Time").
 // But DO NOT change the function name, number of variables, variable type, and sequence
 // Variables:
 //      t: Time, passed from PSIM by value
 //   delt: Time step, passed from PSIM by value
 //     in: input array, passed from PSIM by reference
 //    out: output array, sent back to PSIM (Note: the values of out[*] can be modified in PSIM)
 // The maximum length of the input and output array "in" and "out" is 20.
 // Warning: Global variables above the function simuser (t,delt,in,out) are not allowed!!!

 #include <math.h>
 __declspec(dllexport) void simuser (t, delt, in, out)
 double t, delt;
 double *in, *out;
 {
            double I_FB, Voc, Isc, Vmp, Imp, cellperpanel, series, parallel, TempVcoef, TempIcoef, T, Insol, k, q, n;
            double Is, Voccell, Vmpcell, Rs, Rsh, Ilight, f, f1, Varray, I_FB_Array, P;
            static double V, I_previous; //Make sure u use a static double for counters!!!

 //INPUTS
 I_FB_Array         =in[0];
 Voc                            =in[1];
 Isc                            =in[2];
 Vmp                            =in[3];
 Imp                            =in[4];
 cellperpanel=in[5];
 TempVcoef          =in[6];
 TempIcoef          =in[7];
 series             =in[8];
 parallel  =in[9];
 T                              =in[10];
 Insol              =in[11];

 //Constants
 q = 1.6*pow(10,-19);
 k = 1.38*pow(10,-23);
 n=1.6;

 //CODE

 I_FB = I_FB_Array/parallel;

 //Temperature effects
 Voc = Voc + TempVcoef*(T - 298);
 Isc = Isc + TempIcoef*(T - 298);

 //Per cell equivalents - currents are the same due to series connection of panel
 Voccell = Voc/cellperpanel;
 Vmpcell = Vmp/cellperpanel;

 //Calc of Is
 Is = Isc/(exp((Voccell*q)/(n*k*T)));

 //Calculation of series resistance
 Rs = ((Voccell*Isc)/(Vmpcell*Imp*Imp*Imp))/(cellperpanel);

 //Calculation of shunt resistance
 Rsh = cellperpanel*(Vmpcell*Vmpcell)/(Voccell*Isc-Vmpcell*Imp);
 //Rsh = 20;
```

```
//Calc of light current
Ilight = (Insol/1000)*Isc*(1+Rs/Rsh);//Iteration to calculate Vcell based upon I
//Estimate of Vcell

if(I_previous > I_FB){
        if(((I_previous - I_FB)/I_FB) > 0.0001){

//Calculation code

if (I_FB < 0){
        V = 0;
}

if(I_FB < Imp){
        V = -I_FB*(Voccell-Vmpcell)/Imp + Voccell;

        //Newton-Raphson Algorithm Code
        f = Rsh*Ilight - Rsh*Is*(exp(q*(V + Rs*I_FB)/(n*k*T))-1) - Rsh*I_FB - Rs*I_FB - V;
        f1 = -(q*Rsh*Is)/(n*k*T)*(exp(q*(V + Rs*I_FB)/(n*k*T))-1)-1;
        V = V - f/f1;
//Repeat 100 times for more for greater accuracy
}

if (I_FB > Imp && I_FB < Isc){
        V = -(Vmpcell*(I_FB - Isc))/(Isc - Imp);

        //Newton-Raphson Algorithm Code
        f = Rsh*Ilight - Rsh*Is*(exp(q*(V + Rs*I_FB)/(n*k*T))-1) - Rsh*I_FB - Rs*I_FB - V;
        f1 = -(q*Rsh*Is)/(n*k*T)*(exp(q*(V + Rs*I_FB)/(n*k*T))-1)-1;
        V = V - f/f1;
//Repeat 100 times or more for greater accuracy
}

if(I_FB > Isc){
        V = 0;
}
}
}

if(I_previous < I_FB){
        if(((I_previous - I_FB)/I_FB) < 0.0001){

//Calculation code

if (I_FB < 0){
        V = 0;
}

if(I_FB < Imp){
        V = -I_FB*(Voccell-Vmpcell)/Imp + Voccell;

        //Newton-Raphson Algorithm Code
        f = Rsh*Ilight - Rsh*Is*(exp(q*(V + Rs*I_FB)/(n*k*T))-1) - Rsh*I_FB - Rs*I_FB - V;
        f1 = -(q*Rsh*Is)/(n*k*T)*(exp(q*(V + Rs*I_FB)/(n*k*T))-1)-1;
        V = V - f/f1;

//Repeat 100 times for more for greater accuracy

}

if (I_FB > Imp && I_FB < Isc){
        V = -(Vmpcell*(I_FB - Isc))/(Isc - Imp);
```

```
        //Newton-Raphson Algorithm Code
        f = Rsh*Ilight - Rsh*Is*(exp(q*(V + Rs*I_FB)/(n*k*T))-1) - Rsh*I_FB - Rs*I_FB - V;
        f1 = -(q*Rsh*Is)/(n*k*T)*(exp(q*(V + Rs*I_FB)/(n*k*T))-1)-1;
        V = V - f/f1;

//Repeat 100 times for more for greater accuracy

}

if(I_FB > Isc){
        V = 0;
}
}
}

Varray = V*cellperpanel*series;
P = Varray * I_FB_Array;

//OUTPUT
out[0]    = Varray;
out[1]    = P;
out[2]    = f/f1;
out[3]    = t;
out[9]    = Ilight;
out[10] = Rs;
out[11] = f/f1;
}
```

Using a parametric sweep of the current from 0 to the short circuit current the following I-V curve for the specified PV array, which consists of a single module at a solar insolation of 1-sun at 25C. The current at voltages less then 25VDC are seen to be the same as the short circuit current in the model. This does not create a large error in the simulated model as a PV module will invariably not operate in this region.

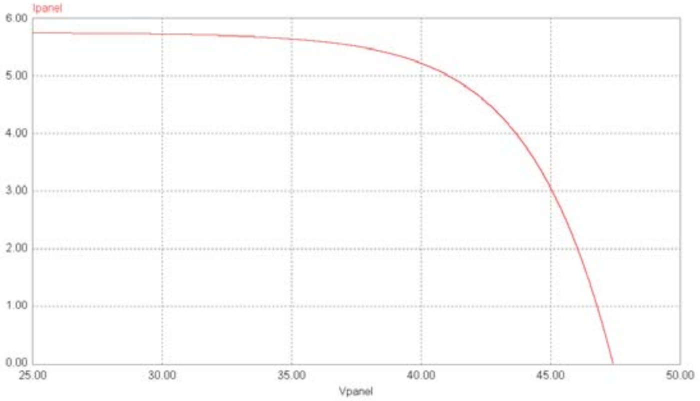

Figure 3-10 : Simulated I-V curve for single PV module – Sunpower SPR-210 [10]

The PV array model allows any solar panel to be simulated from only data sheet parameters and knowledge of the arrays interconnection.

3.3. *MPPT Techniques for Solar Systems*

MPPT is the ability to hold the PV module or string voltage at the level, which optimises the extracted power. This point changes with solar irradiation and temperature so a closed loop control that tracks the voltage with a certain range while measuring the power is required. The benefits of MPPT have been readily published and now most standard PV inverters perform this function through a front end DC-DC converter [11-14]. Recently, single stage GC-VSI have been seen in the literature, the methods employed within this paper are applicable to any grid connected inverter [15]. The main algorithms used to implement this closed loop controller can be aligned to one of three defined methods: Constant Voltage; Perturb and Observe; Incremental Conductance.

3.3.1. Constant Voltage Method

The constant voltage method makes the presumption that the MPP voltage occurs at 76% of the open circuit voltage under a set irradiance of 1kW/m^2. The controller will allow the panel to be open circuit for a short time to allow calculation of the open circuit voltage [11]. The front end DC-DC converters duty cycle is then varied to hold the input voltage at 0.76V$_{OC}$. The major drawback of this technique is its inability to change the operating point as the solar irradiation varies naturally throughout the day.

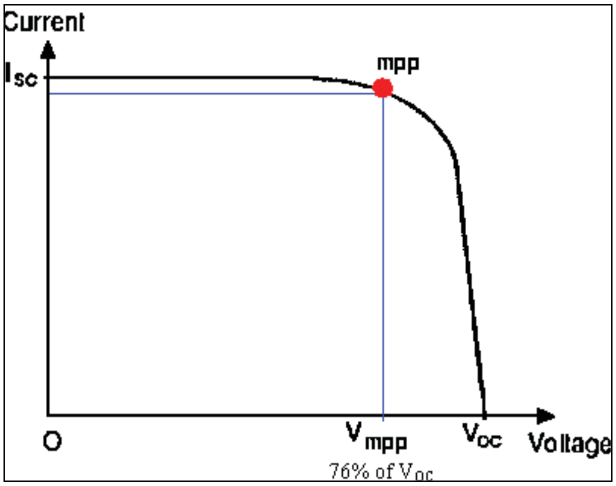

Figure 3-11 : Constant Voltage Method

3.3.2. Perturb and Observe Method

The P&O or hill climbing algorithm is the most commonly implemented maximum power point tracking algorithm. This algorithm forces one variable to change and observes the change to the other measured variable. If the outcome is favourable to the system continues to perturb in that direction, if unfavourable it changes direction. For a PV implementation the voltage is perturbed and the current is observed. If the total power since the perturbation has increased the voltage is again incremented in the same direction until it decreases. Limitations to this algorithm are that the controller oscillates at the maximum power point and the desired direction of perturbation is unknown under rapidly changing irradiation conditions [12]. The incremental step size can also be an issue as the system may take longer then desired to reach the new operating point. Various methods have been used to alleviate these issues such as larger step sizes at low power levels [11, 16, 17]

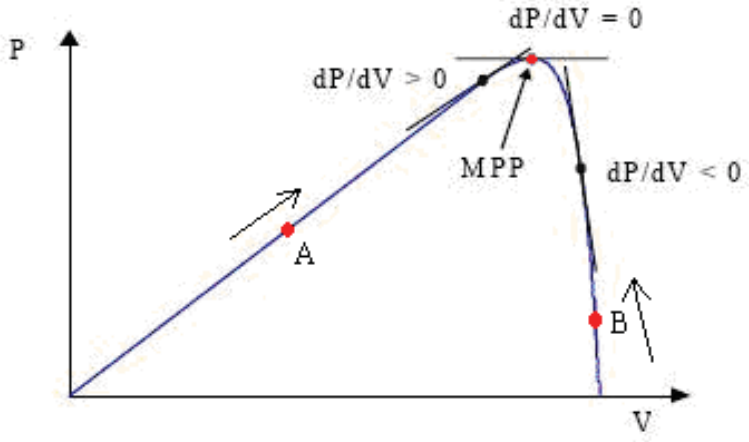

Figure 3-12 : P&O control technique

Figure 3-12 shows the three possible states in which the system may operate. The MPP will occur at the peak of the P-V curve, when the rate of change of power with respect to voltage (dP/dV) is zero. At this point the system is optimised and no perturbation is required, however in order to calculate whether the system is at this point it must be perturbed. This creates a problem such that the system requires incremental changes at the optimal point to ensure it is at the optimal point. If the system is operating at point A the dP/dV is observed to be positive so the controller must increase the voltage towards the MPP. If the system is operating at point B the dP/dV is observed to be negative so the controller must decrease the voltage towards the MPP. The speed at which the controller can get to the MPP from point A and B depends upon the size of the incremental change. Some controllers include a secondary scaling factor which can accelerate the speed towards the MPP based upon the predicted difference from the actual operating point and the likely operating point. Figure 3-13 shows the implementation of this controller in the form of a flow chart.

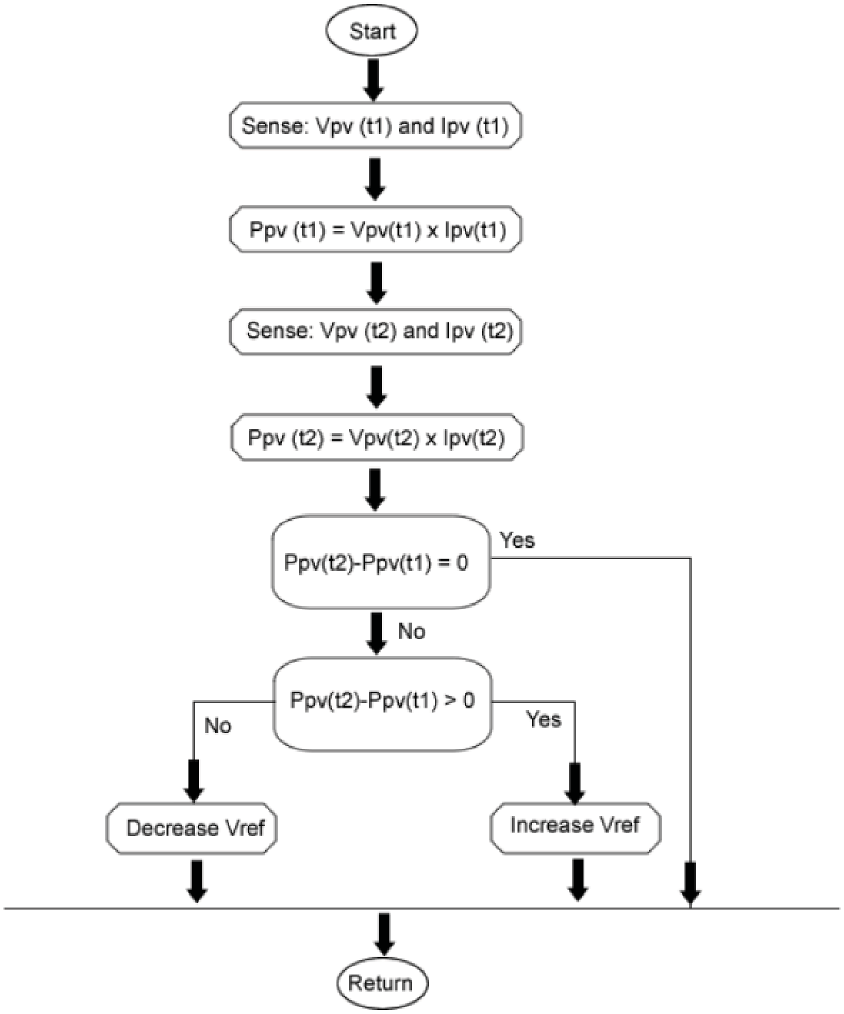

Figure 3-13 : P&O operational flow chart

A main advantage of the P&O algorithm is that it can be implemented easily in a micro controller. However the undesirable oscillations around the MPP reduce the conversion efficiency and maximum energy extraction. The controller has also been seen to be slow and unstable tracking under fluctuating climatic conditions when the irradiation is suddenly increased or decreased, for example due to the presence of thick clouds[18].

3.3.3. Incremental Conductance Method

The incremental conductance algorithm was developed to improve the P&O in rapidly changing irradiation conditions[19-23]. The advantages of this algorithm over the P&O are that it does not need to perturb the voltage if the gradient of dP/dV is zero and it can ensure the direction of the perturbation is correct. Like the P&O algorithm it senses the voltage however the incremental conductance also measures the current gradient. From the product of these parameters the incremental conductance can be calculated so the dI/dV can be determined. Figure 3-14 shows the states in which the controller can operate.

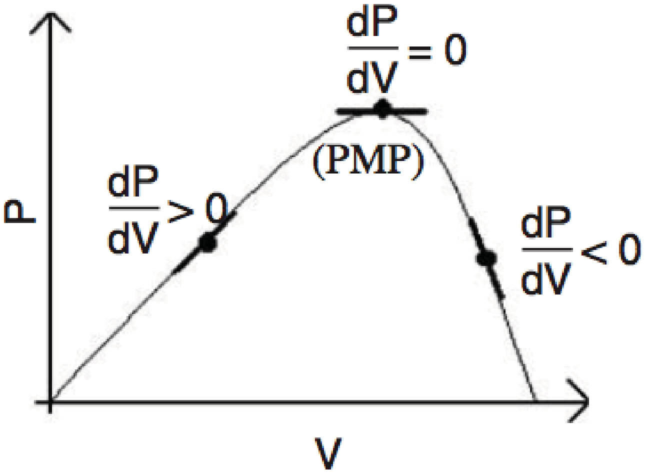

Figure 3-14 : Incremental conductance technique [12]

The sign of the incremental conductance dI/dV determines the direction of tracking over the measured time period. This can be shown through application of the the chain rule. When the system reaches the MPP the dP/dV is zero and the incremental conductance is –I/V, Eq 3-15. This condition shows the system is operating at MPP so further perturbation is not required.

$$\frac{dP}{dV} = \frac{d(VI)}{dV} = I\frac{dV}{dV} + V\frac{dI}{dV}$$

$$\frac{dP}{dV} = 0 \Rightarrow \frac{dI}{dV} = -\frac{I}{V}$$

Eq 3-15 : Incremental Conductance at MPP

The implementation of this controller requires a faster microprocessor and a higher resolution current sensing device. A flow diagram of the implementation of this controller is seen in Figure 3-15. The main advantage of this type of controller is that it does not exhibit the same issues as the P&O under rapidly changing irradiance levels as the direction of the MPP is always known.

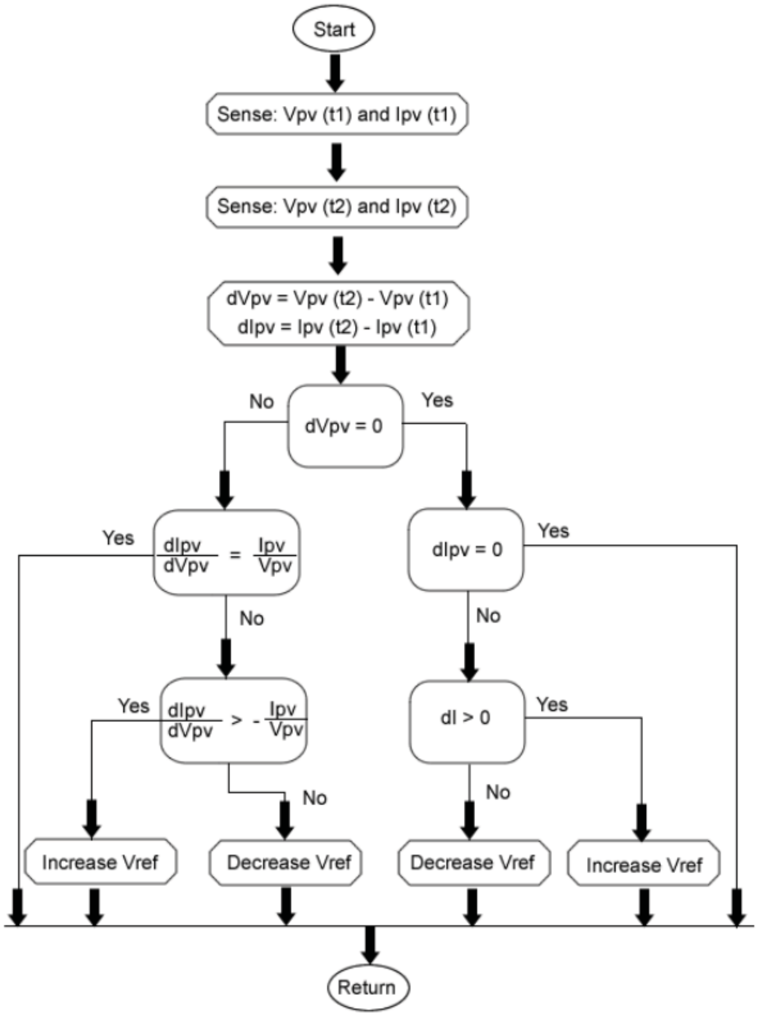

Figure 3-15 : Incremental Conductance method flowchart

3.4. Comparison of PO and Incremental Conductance Algorithms

3.4.1. Development of P&O and IC models

In order to assess the reliability of the Perturb & Observe and Incremental Conductance algorithms both were modelled in PSIM under rapidly changing irradiation conditions. These algorithms were written and compiled in C++, after which they were implemented in PSIM using the DLL block as shown in Figure Figure 3-16.

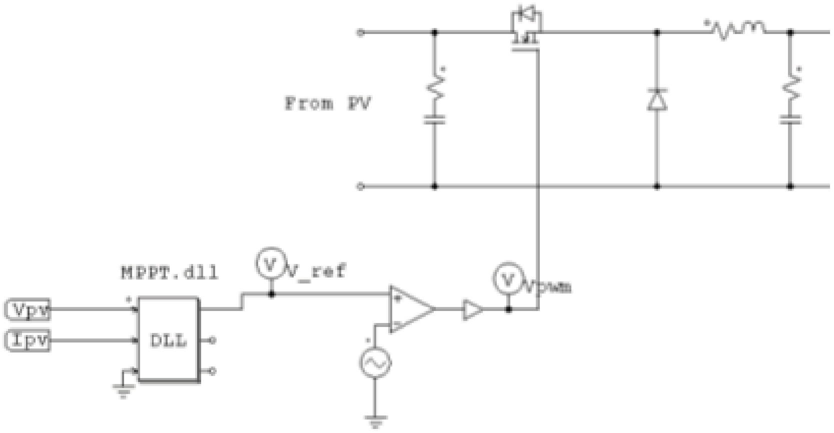

Figure 3-16 : PSIM Implementation with Buck converter

The P&O method uses the change in power to determine whether the MPP has been reached, Figure 3-13 while the CI uses the inequalities, Figure 3-14 to determine the MPP. The MPPT DLL block as shown in Figure 3-16 receives current and voltage information from the PV module block, Figure 3-9. It then executes the MPPT algorithm and outputs a reference voltage into the comparator for the buck converter to operate. In both the algorithms, a counter was used to prevent the algorithms from executing every cycle.

To stabilise the DC link voltage, a capacitor was inserted between the PV model and the step-down converter as shown in Figure 3-16. Similarly on the output of the buck converter, a capacitor was added to reduce the voltage ripple across the load; whereas an inductor was inserted to smooth the current waveform. The combined action of the inductor-capacitor (LC) filter reduced the ripple in the output.

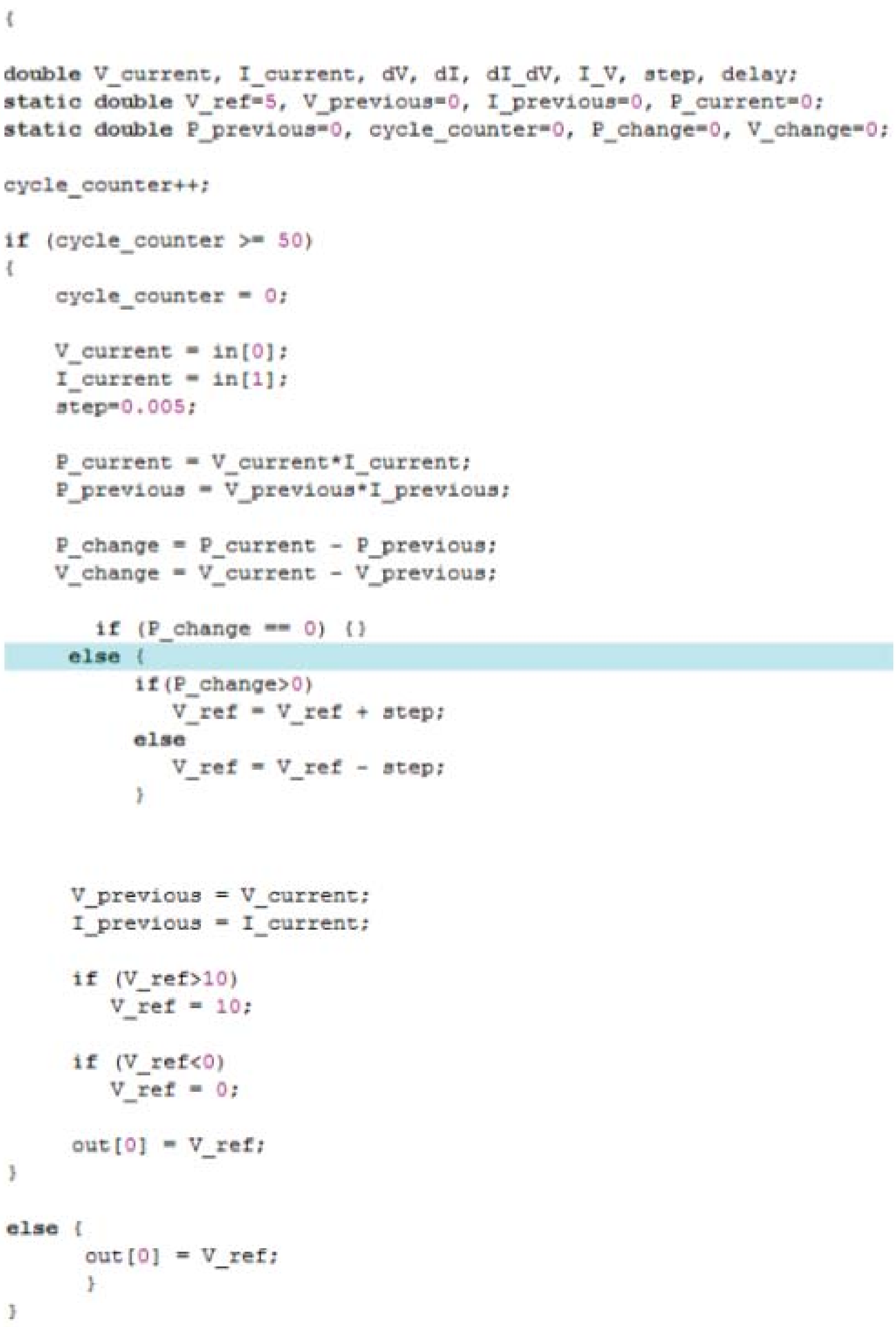

```
{

double V_current, I_current, dV, dI, dI_dV, I_V, step, delay;
static double V_ref=5, V_previous=0, I_previous=0, P_current=0;
static double P_previous=0, cycle_counter=0, P_change=0, V_change=0;

cycle_counter++;

if (cycle_counter >= 50)
{
    cycle_counter = 0;

    V_current = in[0];
    I_current = in[1];
    step=0.005;

    P_current = V_current*I_current;
    P_previous = V_previous*I_previous;

    P_change = P_current - P_previous;
    V_change = V_current - V_previous;

       if (P_change == 0) {}
     else {
          if(P_change>0)
             V_ref = V_ref + step;
          else
             V_ref = V_ref - step;
          }


     V_previous = V_current;
     I_previous = I_current;

     if (V_ref>10)
        V_ref = 10;

     if (V_ref<0)
        V_ref = 0;

     out[0] = V_ref;
}

else {
      out[0] = V_ref;
      }
}
```

Figure 3-17 : P&O algorithm implementation C++ PSIM code [24]

```
{
double V_current, I_current, dI_dV, I_V, step;
static double V_ref=5, V_previous=0, I_previous=0;
static double cycle_counter=0, dV=0, dI=0;

cycle_counter++;

if (cycle_counter >= 50)
{
    cycle_counter = 0;
    V_current = in[0];
    I_current = in[1];
    step=0.05;

    dV = V_current - V_previous;
    dI = I_current - I_previous;

    if(dV==0) {
              if (dI==0)
              {}
              else {
                   if (dI>0)
                        V_ref = V_ref + step;
                   else
                        V_ref = V_ref - step;
                   }
              }


    else {
         if( (V_current*dI + I_current*dV == 0) ) {}
         else {
              if (dI*V_current > -1*dV*I_current)
                 V_ref = V_ref + step;
              else
                 V_ref = V_ref - step;
              }
         }

  V_previous = V_current;
  I_previous = I_current;

  if (V_ref>10)
     V_ref = 10;
  if (V_ref<0)
     V_ref = 0;

  out[0] = V_ref;
}
 else {
      out[0] = V_ref;
      }
}
```

Figure 3-18 : CI algorithm implementation C++ PSIM code [24]

3.4.2. Simulations of the P&O and IC models

Simulations were carried out at STC for both the P&O and CI algorithms to determine the better of the two to be used in a PV pumping system. Results were plotted as shown in Figure 3-19 and Figure 3-20. Both plots show that the PV output power and produce algorithms produce very similar results up to a steady state at 60W[25]. It can also be observed that a steady state response was achieved within 0.2 milliseconds without any noticeable oscillations for both power curves.

Figure 3-19 : P&O MPPT output power characteristics

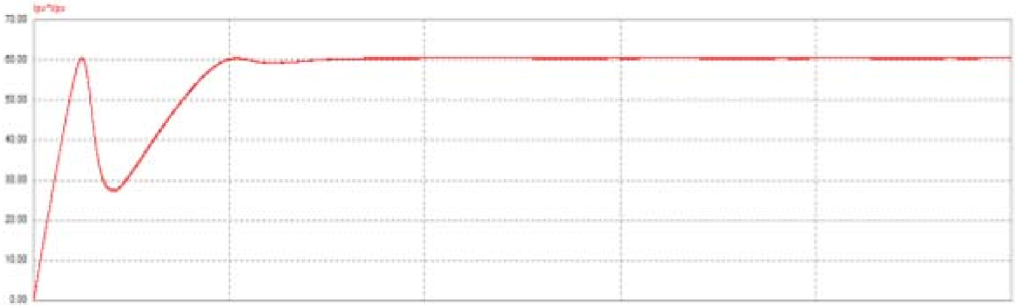

Figure 3-20 : CI MPPT output power characteristics

The next simulation was to assess the P&O and CI algorithms under rapidly changing irradiation and temperature. The changing irradiance levels were carried out using a step source as shown in Figure 3-21. A rapid change in irradiance of 400W/m2 was executed within a time frame of one tenth second and the results are shown in Figure 3-22 and Figure 3-23. Temperature in this simulation was kept constant at 25^{o}C.

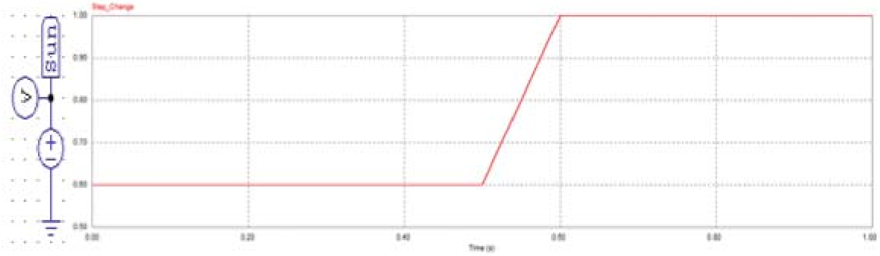

Figure 3-21 : Step change, increase in irradiance from 600W/m^2 to 1kW/m$_2$

Figure 3-22 : P&O MPPT output power characteristics under changing irradiation

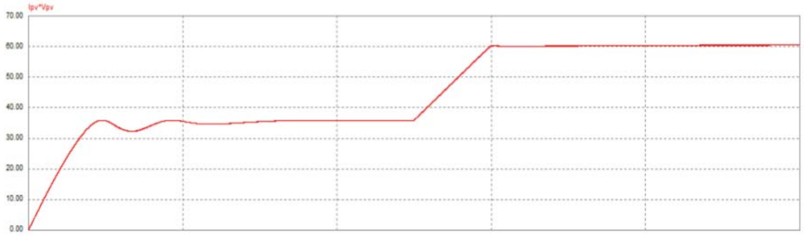

Figure 3-23 : CI MPPT output power characteristics under changing irradiation

Both methods are quick to respond to the sudden change in irradiation as they essentially produce the same power output at 0.6 seconds. However, a closer look at the P&O curve shows that it was unable to maintain the 60W output as was predicted by the theory. The CI curve was able to produce a constant 60W output power even after the sudden irradiation change, Figure 3-21 and Figure 3-22.

The final simulation was to observe the effect of a suddenly changing temperature. A quick drop in temperature from 37^{o}C to 25^{o}C was simulated within the same time frame, Figure 3-24, and the results for both algorithms are plotted as Figure 3-25 and Figure 3-26. The irradiance was kept constant at 1000W/m^2. Initially at a temperature of 37^{o}C, the output power using the P&O algorithm is 57.11W. However, even with a sudden temperature change the output power remains constant at 57.11W. This implies that the P&O algorithm was not able to detect the quick change in temperature levels. In contrast, the CI curve illustrated in Figure 3-26 responded quickly to the sudden change in temperature and produces the accurate output of 60W at 25°C.

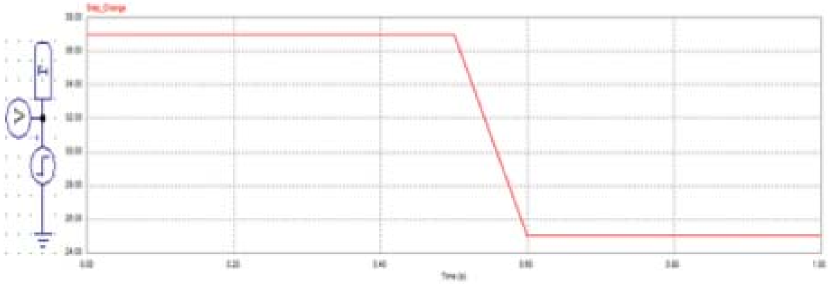

Figure 3-24 : Simulated step change in temperature

Figure 3-25 : P&O MPPT output power characteristics under changing temperature

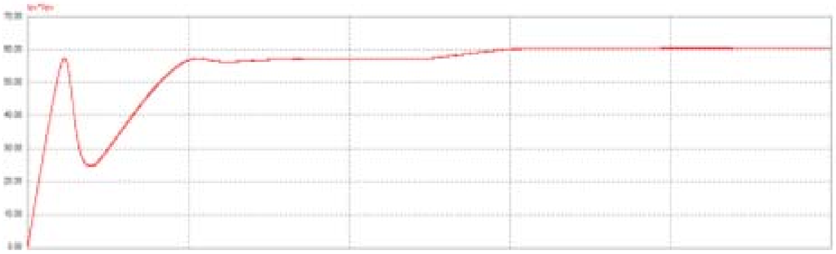

Figure 3-26 : CI MPPT output power characteristics under changing temperature

This series of simulation testing performed on both the MPPT algorithms is crucial in determining whether the system is able to adapt to different changes in environmental conditions. The simulations show that in rapidly changing environmental conditions the IC algorithm performs better then the P&O. In a wind system an analogy can be drawn between rapidly changing solar irradiation levels and varying wind speeds.

3.5. Wind Turbine System Modelling

3.5.1. PSIM Wind Turbine, Controller & Inverter Model

The modelling of a wind system is far more complex then the equivalent solar system. The basic changing input variables are the wind speed and air density, however these variables must be applied to the complex mechanism of the PMSG. The force from the air on the blade will impart a torque on the PMSG, which is proportional to both the rotational speed and power rating of the machine.

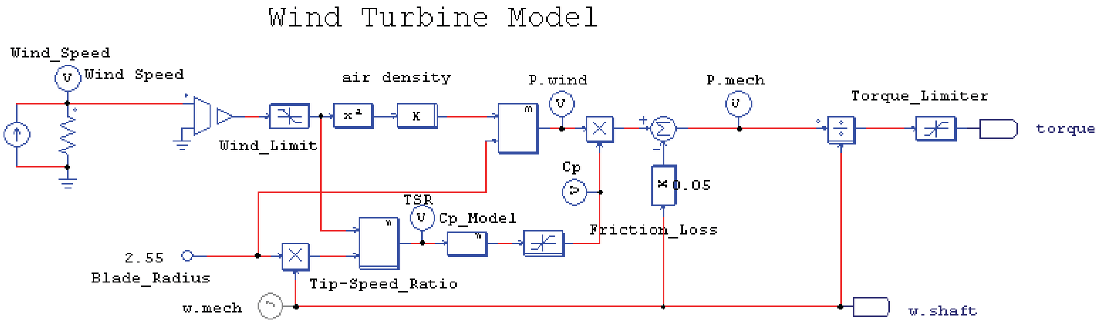

Figure 3-27 : Wind turbine model

The wind turbine model, Figure 3-27, takes the input value as a wind speed and converts this to a torque given the instantaneous rotational speed. The model initially calculates the power in the wind from the wind speed; air density and wind swept area, and multiplies this value by the instantaneous operational performance co-efficient of the WT. The result is the instantaneous operational power of the WT. The torque is then calculated by the divisor of shaft speed. The shaft speed is sensed and fed back from the PMSG model, Figure 3-29, which takes into account the inertia of the PMSG. A balance between these two variables allows a dynamic model of the operation of the WT to be developed. A simulation was carried to verify the performance co-efficient calculation. For a set wind speed the rotational speed of the wind turbine was varied to confirm the performance co-efficient calculation. The results are shown in Figure 3-28.

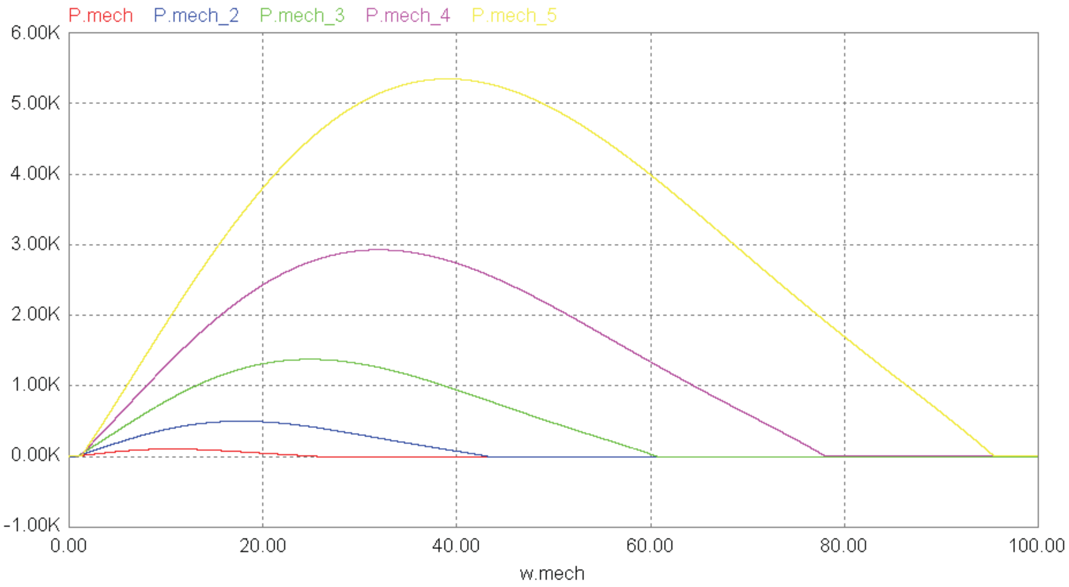

Figure 3-28 : Cp verification for WT rotational speed for 3, 5, 7, 9 and 11m/s.

In Figure 3-28 for the differing wind speeds the characteristic Cp curve can be seen superimposed on the power output as the rotational speed variable is changed. This verifies the power output is being tracked against the tip speed to Cp relationship.

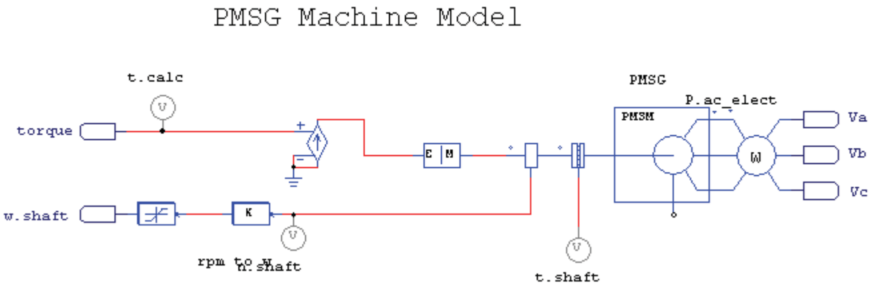

Figure 3-29 : PMSG machine model

PSIM has a model of a PMSM, which was set up with the parameters required for a 5kW PMSG WT, Figure 3-30. In terms of the PSIM model the torque is a voltage, which is converted to a current through unity voltage controlled current source. This current is pushed through the electrical to mechanical interface block into the PMSG. The output of the PMSG is a variable voltage variable frequency thee phase output, which is fed to the rectifier block, Figure 3-31.

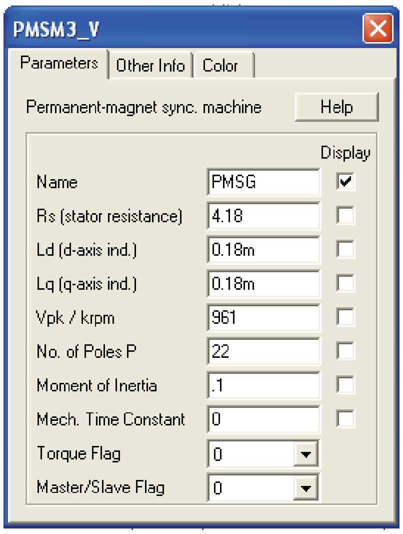

Permanent-magnet sync. machine

		Display
Name	PMSG	☑
Rs (stator resistance)	4.18	☐
Ld (d-axis ind.)	0.18m	☐
Lq (q-axis ind.)	0.18m	☐
Vpk / krpm	961	☐
No. of Poles P	22	☐
Moment of Inertia	.1	☐
Mech. Time Constant	0	☐
Torque Flag	0	
Master/Slave Flag	0	

Figure 3-30 : PMSG parameters

The rectifier block consists of an input delta – delta three phase 1:2 step up transformer. This was included in the model to allow accurate representation of the Denmark project, which is referred to in chapter four. A power meter was added to the DC bus to allow measurement of the DC power before the inverter. This allows for more accurate analysis of the MPPT methodology as it removes any delays due to the grid side inverter.

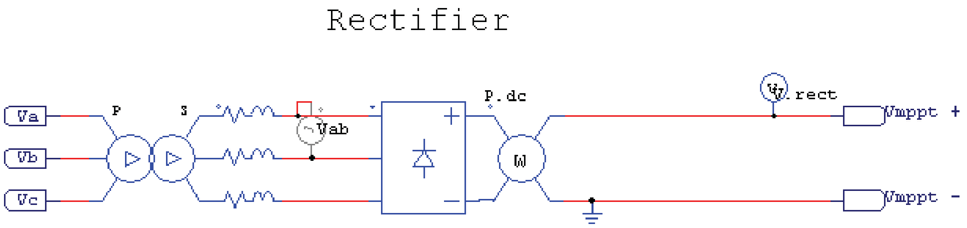

Figure 3-31 : Three phase rectifier model with dc bus power measurement

At the output from the three phase rectifier is a boost type DC-DC converter. This block allows the voltage or current to be controlled from the rectifier, controlling the WT. This control for a PMSG allows it to operate at the MPP over the range of wind speeds. The MPPT block is a complied piece of C++ code where the different algorithms can be tested in differing wind regimes. In some cases it is easier to test these methods by feeding current into a constant voltage source removing the need of the complicated CC-VSI.

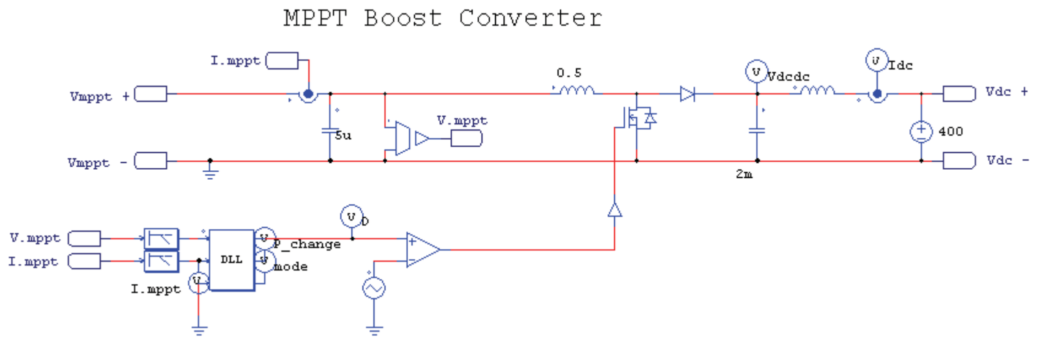

Figure 3-32 : Boost converter with MPPT algorithm input model

The CC-VSI was initially completely modelled and operated correctly under differing wind conditions. However, due to the switching frequency and control complexity it wasn't used to carry out the MPPT optimisation as it increased simulation times to unrealistic levels. Six hours per wind speed increment. Figure 3-33 presents the single phase H-bridge topology for the CC-VSI, which was used to demonstrate the grid connection.

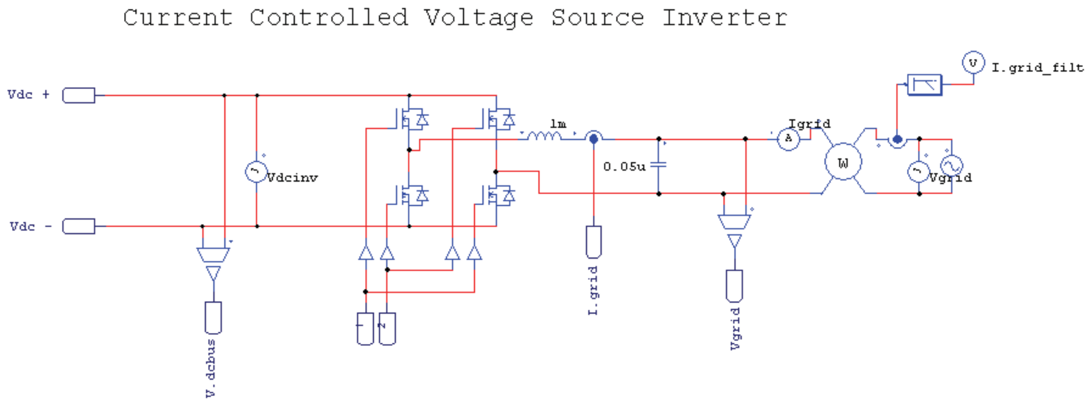

Figure 3-33 : CC-VSI grid connected inverter model

The control method used for the CC-VSI implementation was a hysteresis PI current controller, Figure 3-34. This method determined the switching pattern using an RS flip flop. The controller was designed to keep the voltage on the input DC bus at 400V. An increase in voltage on the DC bus would drive the current reference higher, a decrease in voltage would drive the current reference lower. This control method allowed the DC bus to be held fairly constant while varying the current fed to the grid based upon the wind variations. A fast closed loop controller on the DC bus is required to keep this voltage stable enough for the upstream DC-DC converter to regulate the constant bus voltage. A fluctuating DC bus voltage will cause errors with any MPPT algorithm implementation on the DC-DC converter sidr. Finally, a PLL, Figure 3-35, was used to keep the inverter at the fixed frequency of the grid.

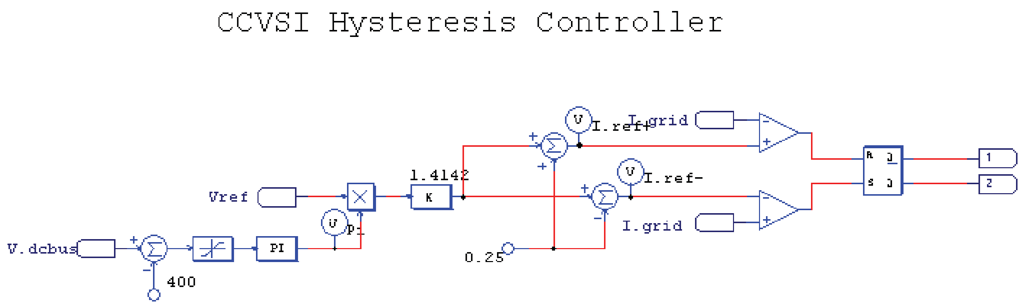

Figure 3-34 : CC-VSI controller implementation

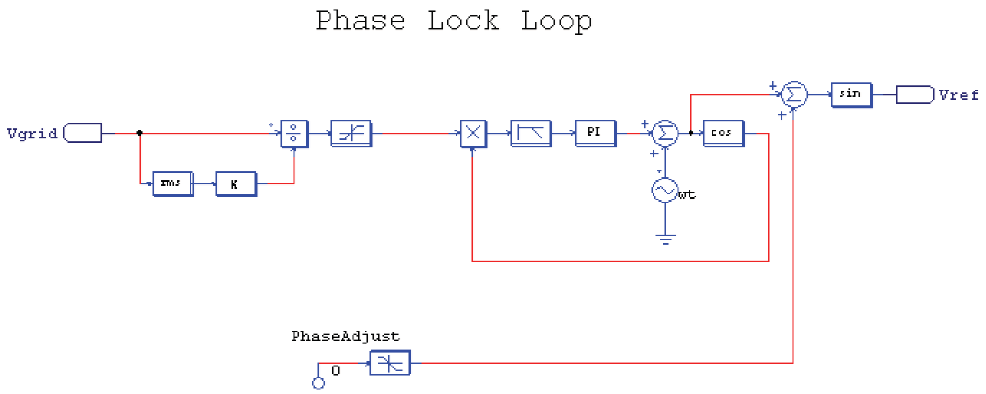

Figure 3-35 : PLL for CC-VSI implementation

3.5.2. Verification of the PSIM Wind System Model

Steady state tests at various wind speeds were carried out to assess the wind power generation and PMSG model. The wind speeds of 3, 6, 9, 12, 15 and 18 m/s are shown in Figure 3-36 and Figure 3-37.

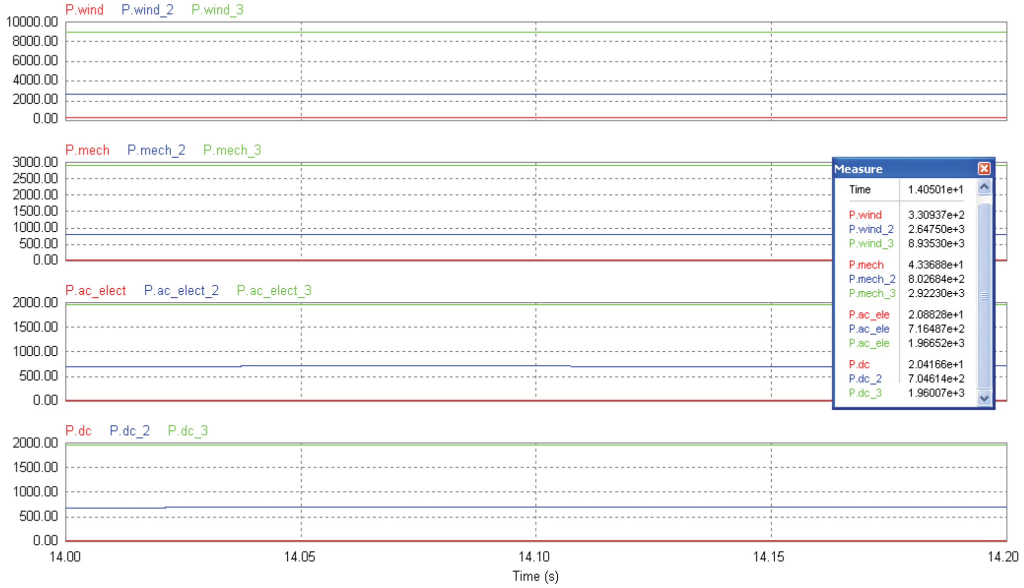

```
Time        1.40501e+1

P.wind      3.30937e+2
P.wind_2    2.64750e+3
P.wind_3    8.93530e+3

P.mech      4.33688e+1
P.mech_2    8.02684e+2
P.mech_3    2.92230e+3

P.ac_ele    2.08828e+1
P.ac_ele    7.16487e+2
P.ac_ele    1.96652e+3

P.dc        2.04166e+1
P.dc_2      7.04614e+2
P.dc_3      1.96007e+3
```

Figure 3-36 : Power in the wind, generated mechanical power, ac power generated, power at the dc bus (W) for 3, 6 and 9 m/s.

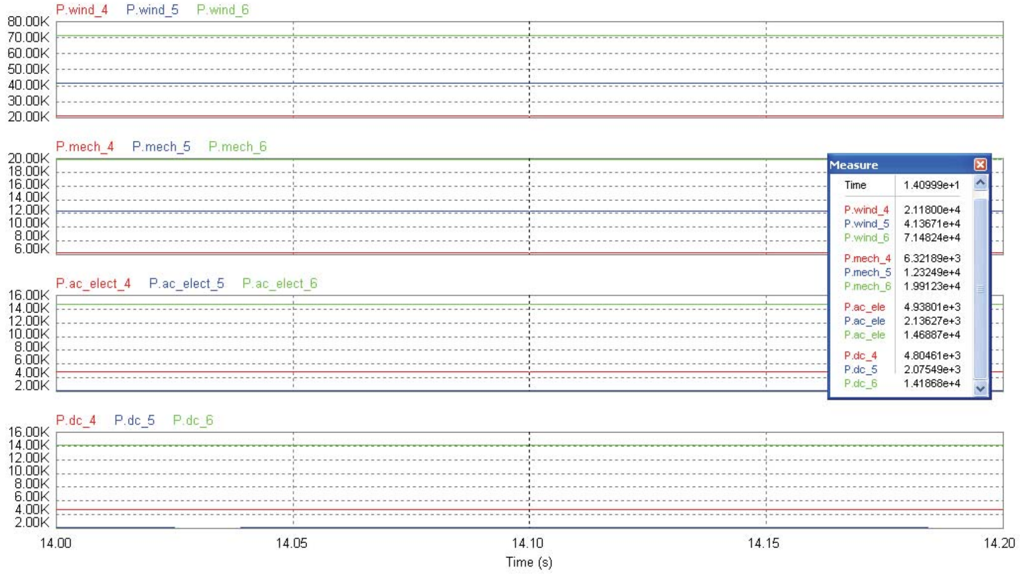

```
Time        1.40999e+1

P.wind_4    2.11800e+4
P.wind_5    4.13671e+4
P.wind_6    7.14824e+4

P.mech_4    6.32189e+3
P.mech_5    1.23249e+4
P.mech_6    1.99123e+4

P.ac_ele    4.93801e+3
P.ac_ele    2.13627e+3
P.ac_ele    1.46887e+4

P.dc_4      4.80461e+3
P.dc_5      2.07549e+3
P.dc_6      1.41868e+4
```

Figure 3-37 : Power in the wind, generated mechanical power, ac power generated, power at the dc bus (W) for 12, 15 and 18 m/s.

The ac output current of the CC-VSI was limited to 17.5 A which corresponds to 4.2kW which was the rating of the inverter as used in the demonstration system at

Denmark. A simulation of the full model at 15 m/s was carried out to assess the CC-VSI and controller.

A parametric sweep of the wind speed was carried out to show the power at the dc bus across all wind speeds. The CC-VSI was taken out of this simulation due to the inability of the software to complete the sweep without creating an error. This is not expected to cause any difference in the results above a wind speed of 7m/s. The voltage generated at the dc bus below 7m/s is lower then the required 400Vdc by the inverter, in reality the PMSG would produce a greater voltage but the Denmark wind turbine is originally a 110Vdc machine. In this case the match of wind turbine and inverter do not allow power to be produced until the wind speed is at least 5m/s. The placement of a 400V dc source prevents the DC-DC converter from correctly operating below this wind speed, as seen in Figure 3-38.

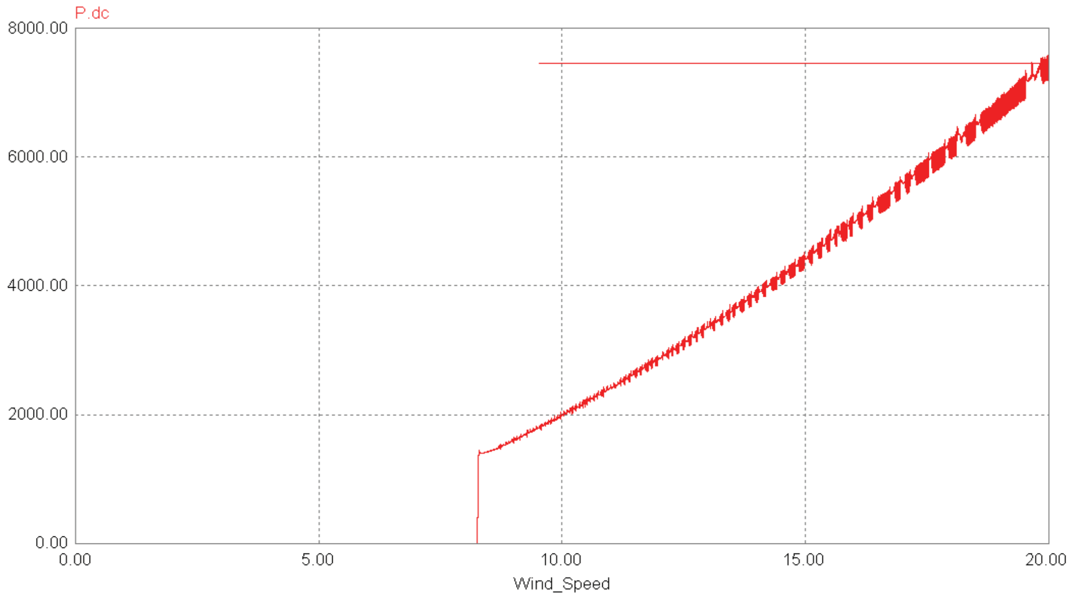

Figure 3-38 : Power v wind speed parametric sweep for the Denmark WT

Some error is seen in Figure 3-38 as the wind speed increases, this is caused by a simulation error within the accuracy of the feedback system between the PMSG and wind turbine model. The set points within the TSR block with the model are quantised, this creates a small error as the operational point of the PMSG is calculated. The error grows proportionally cubically with the wind speed. The controller can resolve the magnitude of the error when the time scale of the sweep is decreased or the rate in change of wind speed is slower. This simulation ramps the wind speed from 0m/s to 25 m/s in 120 s, unrealistically fast to create the parametric sweep. A limiting error is also seen as the simulation reaches its maximum WT power set point.

The model created in PSIM allows the power of the WT be controlled by varying the current drawn. This allows dynamic MPPT modelling to be carried out as the mechanical link between the wind resource , blade aerodynamics and PMSG is made. The errors in the model are resolved by the implementation of the closed loop PI controller. This model was used in the following section.

3.6. MPPT Techniques for Wind Systems

3.6.1. Methodology of MPPT for variable speed wind turbines

The power a wind turbine can extract from the wind is related to the speed that it rotates and the wind speed, the TSR. All wind MPPT regimes for attempt to keep this ratio constant to maximise the Cp [26], Eq 3-17. The TSR is given by Eq 3-16.

$$\lambda = \frac{n_s \pi R}{30v} = \frac{\omega R}{v}$$

Eq 3-16 : Tip speed ratio expression

$$C_P = \frac{2V_{WT}I_{WT}}{\eta_{GEN}\rho A v^3}$$

Eq 3-17 : Performance co-efficient applied to operation

As the ratio of rotational speed and wind speed changes the power co-efficient changes. A typical three blade 5kW permanent magnet machine is used to create the experimental data, this machine was the one installed for the Denmark project. A model of its Cp-λ curve based upon experimental data was produced and is shown in Fig. 3-39. The mathematical model of this curve is included in the PSIM model.

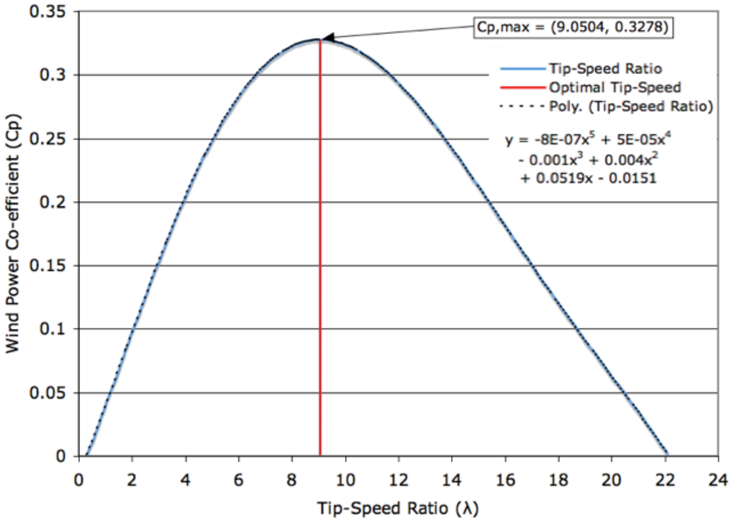

Fig. 3-39 : 3 blade, 5kW WT Cp-λ curve

3.7. Wind MPPT algorithms

An analogy can be drawn between rapidly changing solar conditions and gusty wind conditions. The input control variable to the DC-DC converter is the same in both cases as the power from the source is required to be optimised. The difference between wind and solar sources is the variable that is controlled. P&O solar algorithms hold the PV voltage constant while observing a change in the current to optimise the power output. This is analogous to holding the rotational speed constant and watching the torque and current from the wind turbine change. The problem with this method is the controller cannot determine whether the voltage should be increased or decreased toward the ideal operational point. A novel approach for a wind control algorithm is to use the current drawn as the control variable while monitoring a change in voltage or power. The controller then moves the system in the direction that increases the power output. This method is similar to the PV MPPT incremental conductance algorithm. The similarity in the control approach allows an IC algorithm type inverter be used for both PV and wind MPPT with only minor control modifications which relate to the tracking speed of the algorithm.

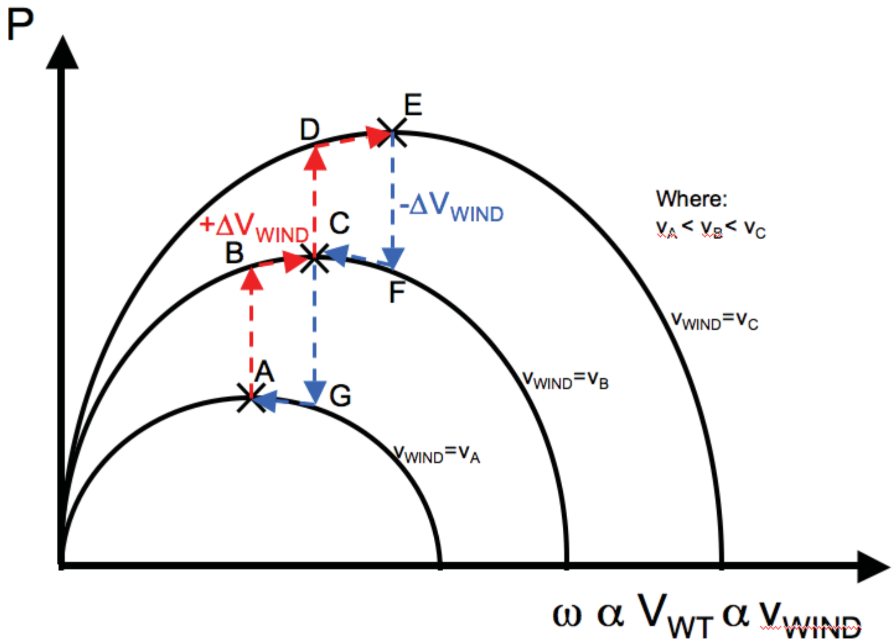

Figure 3-40 : Wind MPPT control methodology

If both the voltage and current are sensed such as with an IC algorithm the direction of required perturbation can be found. To extract the maximum power over a range of wind speeds the current drawn from the WT must be known. With reference to Figure

3-40, if the system is operating at points A, C or E it is at the MPP for the wind speeds v_A, v_B and v_C respectively. Points B and D are transient operation points after an increase in wind speed and F and G represent transient points for a decrease in wind speed.

For the increase in wind speed through points A to B to C; the initial gust will be seen as a current increase which will correspond to a power increase as the rotational speed is fairly constant due to the DC-DC converter. The system is now operating at point B and the combination of simultaneous increasing power and current are indicative of the WT rotating slower then ideal for the MPP. The DC-DC converter should then allow the voltage from the WT to increase by limiting the current flow from the WT, which will result in more net power as the controller moves to operating at point C.

The expressions that relate the variables can be shown through the following relationships.

$$\begin{aligned}&\uparrow \Delta v_{WIND} \Rightarrow \uparrow \Delta i_{WT} \Rightarrow \uparrow \Delta P_{WT} \text{ (low TSR - slow rotation)}\\ &\therefore \uparrow V_{WT} \Rightarrow \downarrow D \text{ (boost type DC - DC converter)}\end{aligned}$$

Eq 3-18 : Expression for increasing wind speed

$$\begin{aligned}&\downarrow \Delta v_{WIND} \Rightarrow \downarrow \Delta i_{WT} \Rightarrow \downarrow \Delta P_{WT} \text{ (high TSR - fast rotation)}\\ &\therefore \downarrow V_{WT} \Rightarrow \uparrow D \text{ (boost type DC - DC converter)}\end{aligned}$$

Eq 3-19 : Expression for decreasing wind speed

In terms of a controller flow chart the following diagram shows how the controller was implemented in C++ code to a dynamic link library for use in PSIM.

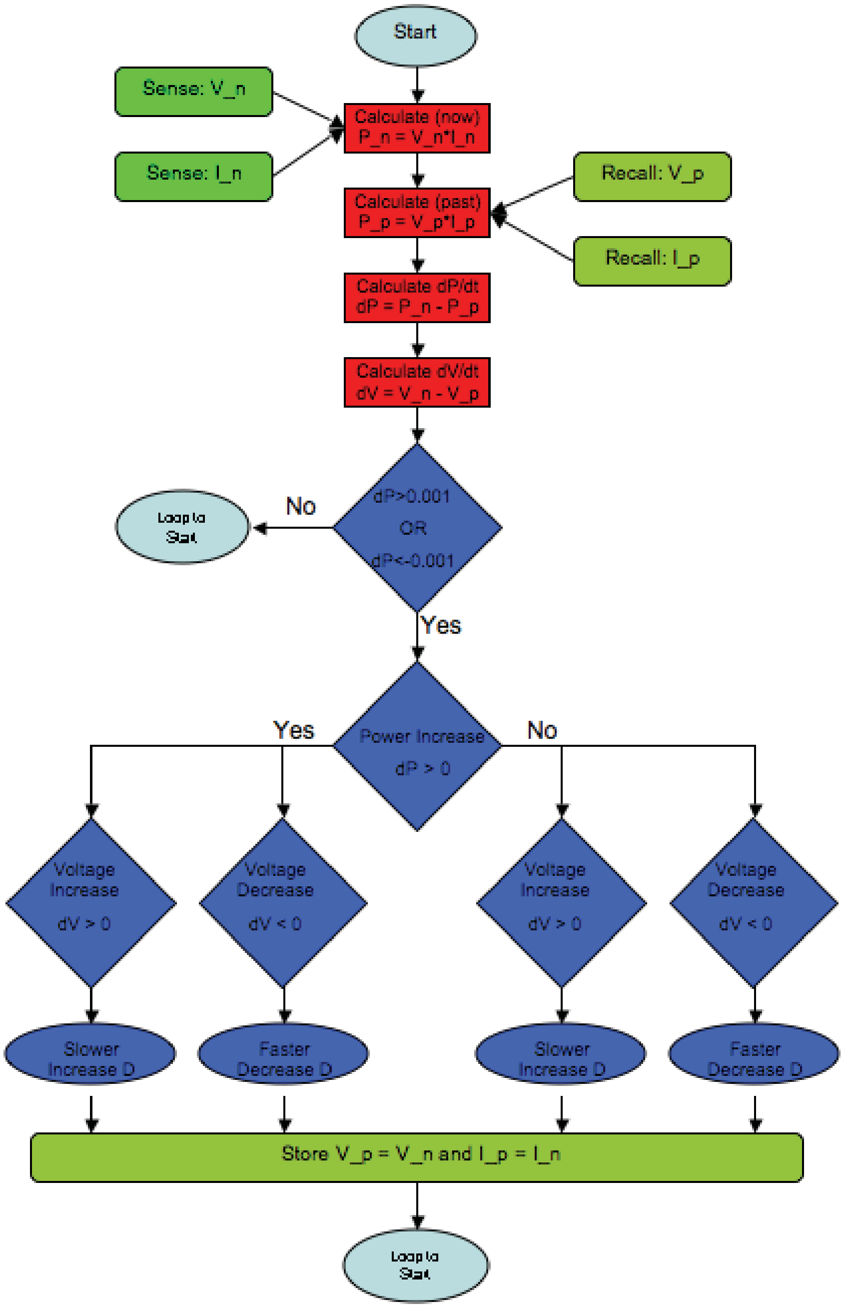

Figure 3-41 : Wind MPPT flowchart

A controller was developed upon this flow chart, Figure 3-41, in C++ code. The code for this is seen below.

```
//MPPT_PO_WIND.dll

//James Darbyshire
//Copyright 2008

#include <math.h>
__declspec(dllexport) void simuser (t, delt, in, out)
double t, delt;
double *in, *out;
{
    double V_now, I_now, increment, mode, timer;
    static double E, V_prev, I_prev, P_now, P_prev, counter, P_ave, I_ave, P_change=0, V_change=0, D,
Dlook, D_prev, I_change=0, cycle, P_change0, P_change1, P_change2 ,P_change3, I_change0, I_change1,
I_change2 ,I_change3; //Make sure u use a static double for counters!!!

//INPUTS
    V_now = in[0];
    I_now = in[1];
    timer = in[2];

//CODE
counter++;

P_now = V_now*I_now;
P_prev = V_prev*I_prev;
P_ave = P_now - P_prev;
I_ave = I_now - I_prev;

increment = 0.0005;

if(counter <= 1)
{
    D = 0.5;
    mode = 5;
}

else
{
    if(cycle == 100)
    {

        if(P_ave > 0.00001) //up hill
        {
            if(I_ave > 0) //speed up rotation, increase Vin
            {
                D = D - increment; //decrease D
                mode = 1;
            }
            else  //slow down rotation
            {
                D = D + increment;
                mode = 2;
            }
        cycle = 0;
        }
        else{}
```

```
                if(P_ave < -0.00001) //down hill - wrong way
                {
                        if(I_ave < 0) //
                        {
                                D = D + increment/4; //slow
                                mode = 3;
                        }
                        else
                        {
                                D = D - increment;
                                mode = 4;
                        }
                cycle = 0;
                }
                else{}
        }
        else
        {
                cycle++;
        }
}

//Limit Check
if(D>0.95)
{
        D=0.95; //bound to max 0.95
}
else
{
        if(D<0.05)
        {
                D=0.05;  //bound min to 0.05
        }
        else{}
}

E = E + P_now*timer;

I_prev = I_now;
V_prev = V_now;


//OUTPUT
//Increase D to decrease current drawn.
out[0]  = D;
out[1]  = E/3600;
out[2]  = mode;
}
```

Figure 3-42 : IC wind MPPT controller algorithm

The key control variables for the system are:

Controller adjustment rate (CAR)

This variable determines how often the control algorithm checks the system to see if a change in operational set point is required. This is implemented in PSIM though the internal simulation timer and a cycle count within the code. For the simulations presented the PSIM model creates operational points every 0.1ms. A cycle count was used in the C++ code and set at 100. These counters combine to check the systems operational point every 10ms.

Duty cycle increment magnitude (IM)

This parameter sets the increment on the duty cycle whenever the algorithm requires a movement of the duty cycle. This was set at 0.0005 as a discrete value.

Determination of useful change in power (ΔP)

The change in power is used within the algorithm to prevent minimal changes in power and noise in the system from constantly changing the operational point. This static state check allows the IC type algorithm to determine if it is operating at a point, which is acceptably ideal for the system.

The combination of the controller adjustment rate and duty cycle increment magnitude allow maximum controller rate of change (CRoC) to be determined.

$$CRoC = \frac{CAR}{IM} = \frac{0.0001}{0.0005} = 0.2$$

Eq 3-20 : CRoC determination

This value is representative of the maximum step change or wind gust of which the controller can capture the energy. The DC bus voltage for the inverter determines the operational input voltage range for the wind turbine.

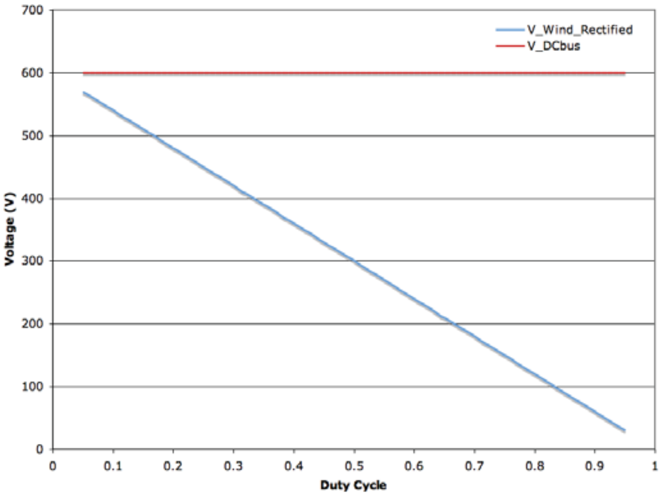

Figure 3-43 : DC-DC converter operational zone

Wind turbines voltage is proportional to its rotational speed, if the assumption is made that operation is at MPP then a voltage wind speed load line can be derived. From Experimental data on the 5kW Denmark wind turbine, presented in chapter four this was derived to be:

$$V_{dc} = Av_{WIND} + B \approx 26.65v_{WIND} + 6.67$$

Eq 3-21 : 5kW WT voltage – wind speed relationship

Applying this relationship the maximum wind speed that MPPT will occur is 21.1m/s and the lowest is 0.87m/s, however the static friction or cogging of most wind turbines requires 2-3m/s to start. Extrapolation from the CRoC and wind speed relationship allows the derivation of the maximum change in wind speed, which the controller is able to accurately track.

$$\Delta v_{WIND} \approx \frac{\Delta DV_{dc-bus} - B}{A} = 4.25m/s^2$$

Eq 3-22 : Algorithm and WT tracking speed

This controller and WT combination should allow a 4.25m/s change in wind speed over one second to be accurately tracked. Any larger gust of wind will result in energy not captured by the system.

3.7.1. Simulation of MPPT IC algorithm for wind systems

The concept of this controller relies upon the premise of controlling the rotation speed of the WT with the boost type DC-DC converter. A PSIM simulation was created to simulate the controllers operation over a changing wind regime and the Cp, D, power, current, WT voltage, shaft speed were plotted to review the results. The mode of operation as defined in is also shown in Figure 3-43.

Figure 3-44 shows the simulated wind profile, the wind speed gusts from 8 – 10m/s in 5s, a rate of 0.4m/s^2 then follows through rates of -0.3 m/s^2, 1.2 m/s^2, -0.1 m/s^2. This initial wind regime was defined to allow the design of a suitable ΔP to be determined.

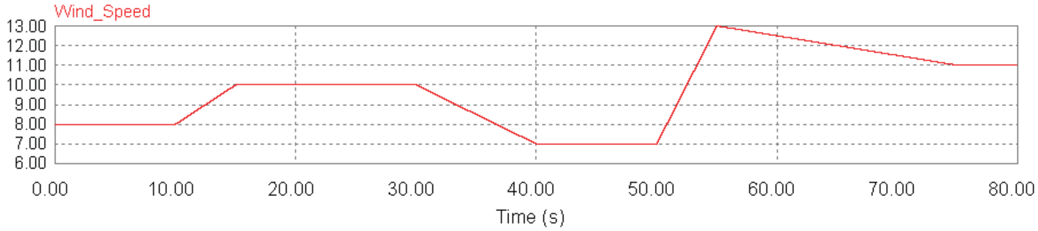

Figure 3-44 : Simulated wind profile

The first simulation Figure 3-45 is carried out with a ΔP = 0.01. This is the power change required over the internal simulation timer (0.0001) to trigger a controller set point change, so 100W/s is the rate required for a controller increment action.

Figure 3-45 : MPPT simulation with CRoC = 0.2; ΔP = 100W/s, E = 9.116Wh

Figure 3-45 shows the duty cycle (D) smoothly decrease for increasing wind speed and increase for decreasing wind speed. The Cp co-efficient stays steady at approximately 0.33 throughout the entire simulation exhibiting good control of the WT over the given range of wind speeds. The mechanical power is extracted electrically in a continuous method with no pulsations occurring within the power electronic controller. The rectified WT voltage and mechanical speed follow each other closely. The mode of operation define the state of the controller. With a ΔP of 100W/s the controller only operates during clearly defined changes in power. The following simulations show how decreasing the ΔP effects the controllers operation and energy generation.

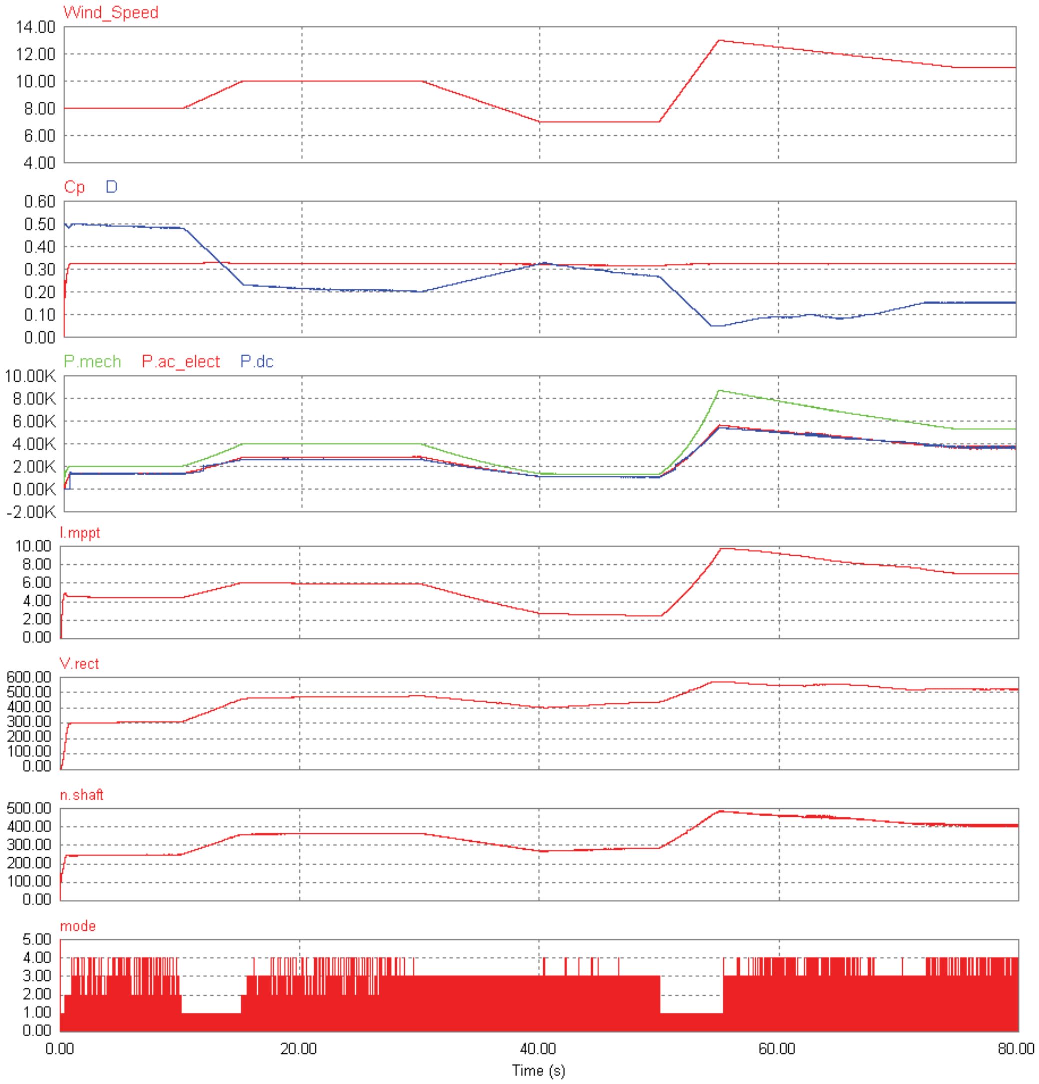

Figure 3-46 : MPPT simulation with CRoC = 0.2; ΔP = 10W/s; P = 9.254Wh

At a ΔP of 10W/s the controller is operating more often as it constantly refines the systems operational set point to extract the maximum energy available.

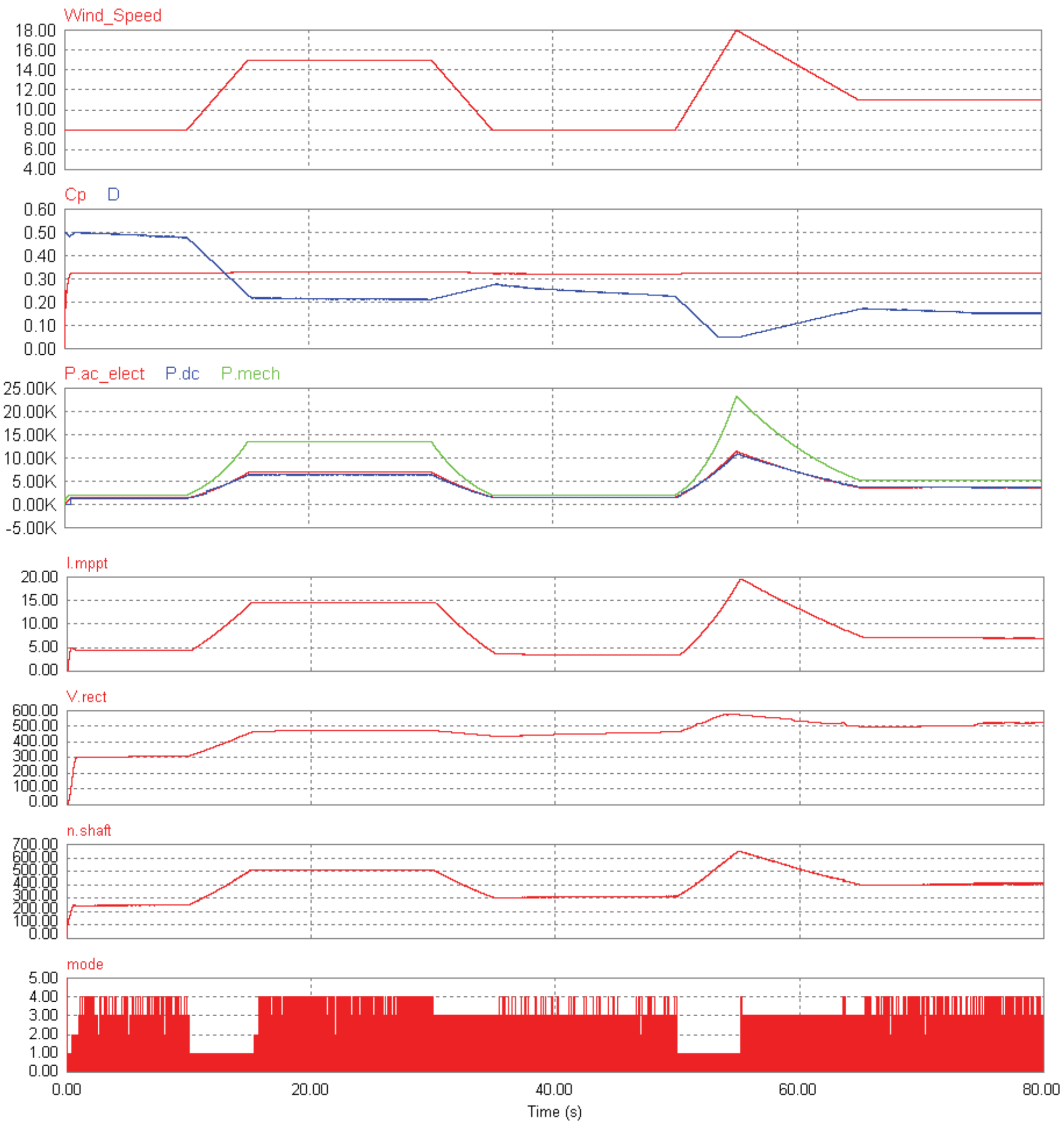

Figure 3-47 : MPPT simulation with CRoC = 0.2; ΔP = 1W/s, E = 9.263Wh

For a ΔP of 1W/s the controller is constantly adjusting the set point as the noise within the system is beginning to affect the controller. Table 3-II supports this as simulations for a smaller ΔP caused a reduction in net energy output. From the simulated results for the modelled 5kW wind turbine and controller the rate at which the controller should adjust the set point for approximately optimised between 1-5W/s.

ΔP (W/s)	Energy Produced (Wh)	% power inc from 500W/s
500	9.046	0.00
100	9.116	0.77
50	9.121	0.80
10	9.254	2.30
5	9.262	2.39
1	9.263	2.40
0.5	9.249	2.24

Table 3-II : Summary of ΔP and energy collection gain

To test the gust response characteristics of the controller a quickly increasing wind gradient was modelled. Initially a $2m/s^2$ ramp from 8 to 10m/s was modelled over a second, then 4.25 and $5.5m/s^2$.

Figure 3-48 shows the controller quickly decrementing the duty cycle to increase the voltage at the wind turbine in an attempt to increase the Cp. Delays due to the capacitors on the DC bus force the controller to lag by approximately 0.1s. However the controller recovers from the gust quickly and maintains the Cp within 0.01.

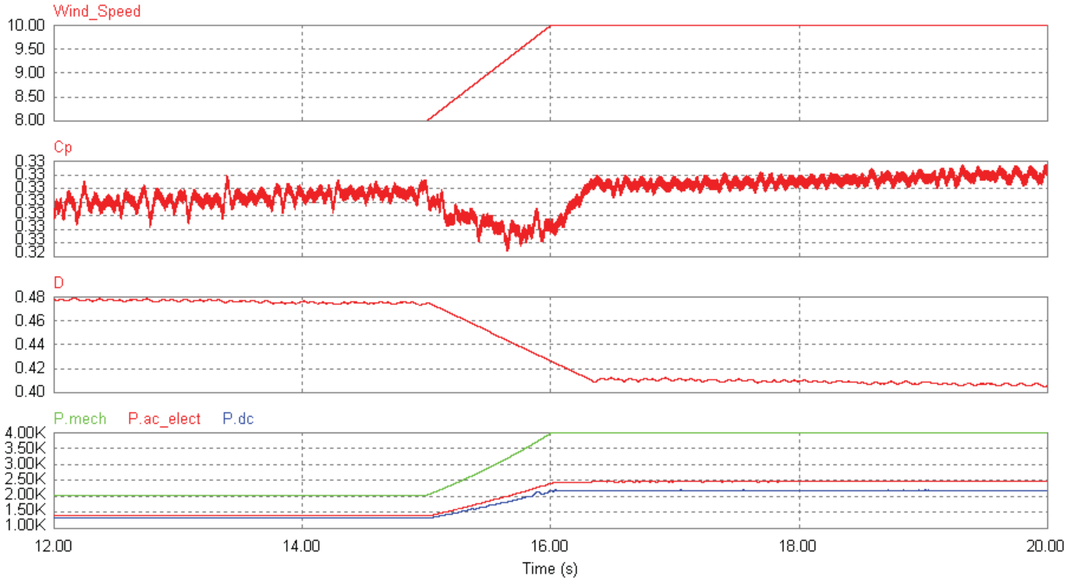

Figure 3-48 : Controller response to gust at $2m/s^2$

As the gust magnitude increases the controller struggles to maintain the Cp, other effects such as losses in the wind turbine also cause slight variations in the maximum attainable Cp for higher wind conditions. This is evident in Figure 3-49 and Figure 3-50 as the gust creates a greater droop in the Cp. The controller is still responding satisfactorily to the rapid increasing wind and generating additional energy from the gust. However the simulated accurate tracking speed, approximately 2.5m/s^2 is less then the predicted 4.25m/s^2.

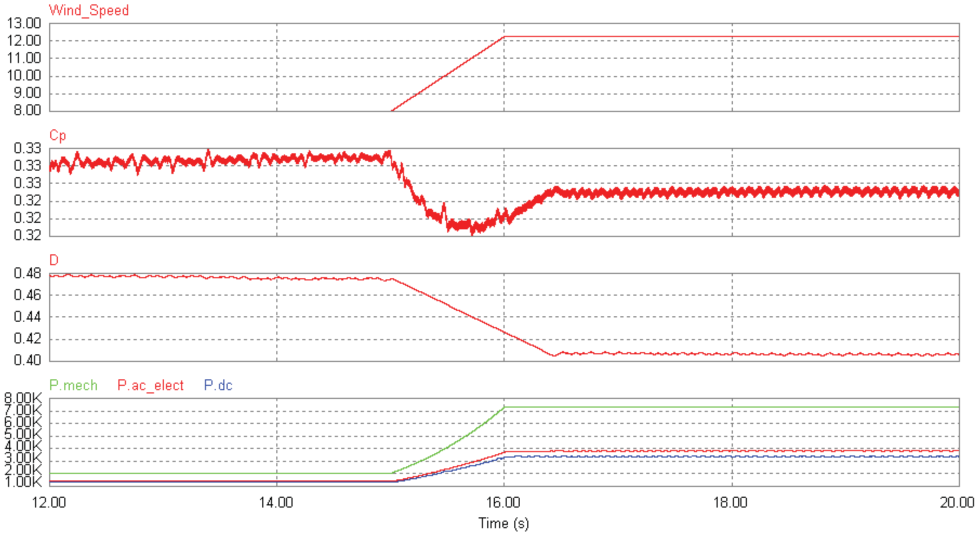

Figure 3-49 : Controller response to gust at 4.25m/s^2

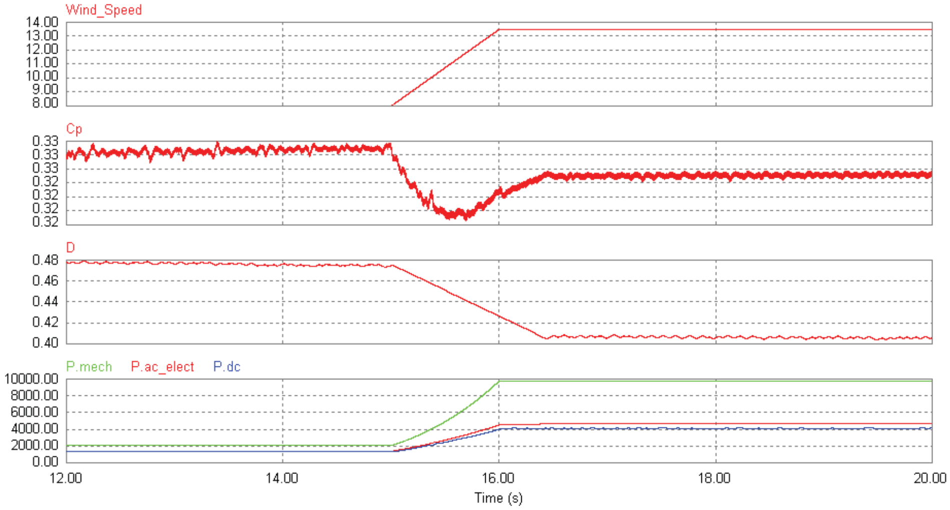

Figure 3-50 : Controller response to gust at 5.5m/s^2

3.8. Summary

This chapter initially presents a summary of currently existing MPPT techniques used to control power electronic dc-dc converters, usually buck or boost converters, which allow an increased yield of renewable energy. To test the differing MPPT regimes an accurate model was developed to mimic the properties of a solar module. This model was based upon a PV cell model incorporating both series and shunt resistances. A mathematical expression for this PV cell was determined with its parameters being evaluated from commonly available PV module data sheet values. The complete mathematical description of the PV array was implicit, requiring an iterative solution to be developed. A C++ algorithm was developed based upon the Newton-Raphson algorithm to allow the simulation to be solved within the software PSIM.

Once a precise PV model was developed it could be used to verify the accuracy of any MPPT algorithm. The author was aware that the P&O algorithm had previously failed under rapidly changing irradiation whereas the IC had been shown to be better at tracking inclement conditions. To prove this concept both MPPT techniques were used to simulate a water pumping system. Irradiance and temperature variations were simulated with the results showing an IC algorithm to be better suited to variable weather conditions. The author drew an analogy between rapidly changing solar conditions and nominal wind conditions to explore the concept of applying a type of IC algorithm to a small wind system.

To simulate a wind MPPT algorithm a model of the wind resource and wind turbine were developed. The physics of the force from the wind impacting the blades and rotating the turbine were all modelled in PSIM. Comprehensive tests on the wind turbine model were carried out independently to ensure the correct power and torque was generated at differing wind speeds. This wind turbine model was coupled to the PMSG, rectified and fed to through a boost converter to a GCI. The PMSG characteristics were determined through testing of a real Westwind 5kW machine.

The wind MPPT algorithm uses the previous voltage and current values and the instantaneous voltage to determine required direction of the controller. The speed of the tracking and the resilience noise are determined by the CAR, IM and ΔP parameters. Testing of these parameters allows for the optimal wind energy extraction before the sensitivity of the controller decreases the energy yield. A CRoC rate of 0.2 with a ΔP 0f between 1 – 5W were found to give the optimal solution.

The key research points of this chapter are:

- Creation of PSIM model and C++ code for PV model array based upon commonly available data sheet values utilising the Newton-Raphson algorithm;
- Development of a MPPT P&O PV model;
- Development of a MPPT IC PV model;
- Application of MPPT IC PV algorithm to create a wind MPPT algorithm;
- Development of PSIM wind turbine and inverter model;
- Creation and testing method for wind IC MPPT algorithm;

3.9. References

1. Durisch, W. and D. Ti1le, *Testing Of Small Sinusoidal-Inverters For Photovoltaic Stand-Alone Systems.* Applied Energy, 1998. **64**.
2. Neamen, D., *Semiconductor Physics & Devices : Basic Principles*. 2nd ed, ed. S. Isenberg. Vol. 2nd. 1997: McGraw-Hill.
3. Kunz, G. *Internal Series Resistance Determined of Only One IV-curve Under Illumination*. in *19th European Photovoltaic Solar Energy Conference*. 2004. Paris, France.
4. J. Darbyshire, C.V.N. *Modelling, Simulation and testing of grid connected PV system*. in *Symposium on Power Electronics for Distributed Generation Systems*. 2007. Hefei: IEEE.
5. Walker, G.R., *Evaluating MPPT converter topologies using a MATLAB PV model.* Journal of Electrical & Electronics Engineering, Australia, 2001. **21**(1): p. 49-56.
6. Chen, Y., et al., *Multi-Input Inverter for Grid-Connected Hybrid PV/Wind Power System.* IEEE Transactions on Power Electronics, 2007. **22**(3): p. 1070-1077.
7. NREL, *Best Laboratory PV cell efficiencies for various technologies*. 2003, National Renewable Energy Laboratories.
8. Masters, G., *Renewable and Efficient Electric Power Systems*. 2004: Wiley Interscience.
9. Lasnier, F. and T.G. Ang, *Photovoltaic Engineering Handbook*. 1990, New York: IOP Publishing.
10. SunPower, *SPR-210-WHT: High Efficiency PV Module*, in *Document: 001-03296*. May 2007, SunPower Corporation: California.
11. Ropp, D.P.H.a.M.E., *Comparative Study of Maximum Power Point Tracking Algorithms Using an Experimental, Programmable, Maximum Power Point Tracking Test Bed*, in *IEEE Photovoltaic Specialists Conference*. 2000.
12. V. Salas, E., Olias, A. Barrado and A. Lazaro, *Review of the maximum power point tracking algorithms for stand-alone photovoltaic systems.* Solar Energy & Solar Cells, 2005. **10**.
13. Masoum, M.A.S. and H. Dehbonei. *Design, Construction and Testing of a Voltage-based Maximum Power point tracker (VMPPT) for Small Satellite Power Supply*. in *13th Annual Conference on Small Satellite AIAA/IJSU*. 1999. Utah, USA.
14. Altas, L. and A.M. Sharaf, *Novel on-line MPP search algorithm for PV arrays.* IEEE Transactions on Energy Conversion, 1996. **11**: p. 748 -754.
15. Prasad, B.S.J., S.; Agarwal, V., *Universal Single-Stage Grid-Connected Inverter.* IEEE Transactions on Energy Conversion, 2008. **23**(1): p. 128 - 137.
16. C. Hua, J.L., and C. Shen, *Implementations of a DSP-controlled Photovoltaic System With Peak Power Tracking.* IEEE Transactions on Industrial Electronics, February 1998. **45**(1): p. 99-107.
17. Dunford, W.X.a.W.G., *A Modified Adaptive Hill Climbing MPPT Method for Photovoltaic Power Systems*, in *35th Annual IEEE Power Electronics Specialists Conference*. 2004.
18. T. Kim, H.A., S. Park and Y. Lee. *A Novel Maximum Power Point Tracking Control for Photovoltaic Power System Under Rapidly Changing Solar Radiation*. in *IEEE International Symposium on Industrial Electronics*. 2001.

19. Hussein, K.H., et al. *Maximum photovoltaic power tracking: and algorithm for rapidly changing atmospheric conditions*. in *IEEE Proc. Generation Transmission Distribution*. 1995.
20. Enslin, J.H.R., et al., *Integrated photovoltaic maximum power point tracking converter.* IEEE Transactions on Industrial Electronics, 1997. **44**: p. 769 -773.
21. Enslin, J.H.R. and D.B. Snyman, *Combined low-cost, high-efficient inverter, peak power tracker and regulator for PV applications.* IEEE Transactions on Power Electronics, 1991. **6**: p. 73 -82.
22. Masoum, M.A.S., H. Dehbonei, and E.F. Fuchs, *Theoretical and Experimental Analyses of Photovoltaic Systems with Voltage and Current-Bascd Maximum Power Point Tracking.* IEEE Transactions on Energy Conversion, 2002. **17**: p. 514-522.
23. Masoum, M. and H. Dehbonei. *Optimal Power Point Tracking of Photovoltaic System under all Operating Conditions*. in *17th World Energy Congress*. 1998. Houston, TX, USA.
24. Tan, L.T.L., *Development and Testing of a Solar Pumping System*, in *Department of Electrical and Computer Engineering*. 2008, Curtin University of Technology: Perth.
25. Vetter, G. and W. Wirth, *Suitability of eccentric helical pumps for turbid water deep well pumping in photo-voltaic systems.* Journal of Solar Energy, September 1993. **51**(3).
26. Kelvin Tan, S.I., *Optimum Control Strategies in Energy Conversion of PMSG Wind Turbine System Without Mechanical Sensors* IEEE Transactions on Energy Conversion, 2004. **19**(No 2).

"Every reasonable effort has been made to acknowledge the owners of copyright material. I would be pleased to hear from any copyright owner who has been omitted or incorrectly acknowledged."

4. Small Scale Wind/PV Hybrid System Design and Optimisation

The combination of solar and wind into a hybrid system will often result in a more reliable power system. The energy producing methods of solar and wind are not exclusively complimentary, however quite often low solar irradiation levels occur in times of high winds, such as storms. Solar energy is naturally limited to producing power in day light conditions, but wind energy is possible any time of day or night. So a combination of the two resources can yield a more dependable power system.

Depending upon the solar and wind conditions of the location, the exact combination of sizes of renewable sources and the method of interconnection, the system can be optimised for maximum energy production. For any location the main variables required to design a renewable system are average daily solar exposure, average daily sun hours, average wind speed, geographic latitude and the height of an installed wind turbine. These variables define the approximate energy yield for any installed system, which allows the utilities' financial rebate, and so, system feasibility to be realised.

The complementary hybrid Wind/PV system [1, 2] is presented in this chapter as an alternative to the traditional type of hybrid system. The theory, modelling, probability analysis, experimental testing and comparison for a complementary hybrid Wind/PV system is presented. An approach is developed to appropriately size the components to maximise the systems energy yield. Using probability analysis the energy generation is quantified and the possible loss of energy due to solar and wind resource crossover is calculated. The chapter utilises the common sense aspect that the intersection between full sun conditions and windy conditions is rare. Exploiting this characteristic allows for a greatly increased yield of energy generation. Four systems are examined for various locations across Australia.

4.1. Hybrid Systems Interconnection Topologies

Grid connected solar and wind systems are now readily being implemented on the outskirts of utility networks in order to decrease the power demand on the line and its associated transmission losses. In rural Australia a significant portion of energy generated is lost through the transmission of the electric energy. Any locally generated renewable electricity significantly decreases the overall carbon emissions. Thus, economic conditions that allow rural customers to become more electrically sustainable will develop in the next few years.

This section presents methods used to allow end of line users to invest in renewable energy hybrid systems, that can both stabilise a customers' power supply while exporting any surplus energy to the utility grid. This produces a dual effect of increasing the reliability of the power supply while providing a financial incentive through a feed in tariff for the customer. From the utilities point of view the decrease in line losses can directly offset the required feed in tariff.

The combination of a solar photovoltaic system with a wind turbine allows an increased reliability and yield in the generation of electricity. There is a convenient synergy in the combination of these energy sources as generally during sunny conditions it is not windy, and when it is windy it is normally cloudy. The coalescing of these technologies is compounded through the realisation that there is generally very little wind energy available below a wind speed of 4 m/s and PV energy rapidly decreases under cloud cover. A single grid connected inverter is modified to allow energy production from both wind and PV sources. The drawback is that it cannot feed power simultaneously from both sources. The design of such a system to find the most effective strategy to convert this energy to electricity is developed.

4.1.1. Grid Connected Interfaces

Standard solar grid connected systems, Figure 4-1, have rapidly been installed across Australia and the world. A significant drawback of these systems is the requirement of a stable utility grid, in order to generate electricity. In remote areas the utility grids reliability is greatly decreased and many customers are not impressed when they are unable to use the free solar energy when the grid goes down. The solution to this predicament is to include a second inverter that can act like the grid when the real utility grid is down, commonly called a mini-grid. This second inverter will supply a stable voltage and frequency, which will allow the other conventional grid connected inverters to connect and power the local loads or recharge the battery. For any fringe grid connected system a mini-grid topology is required to increase the systems reliability.

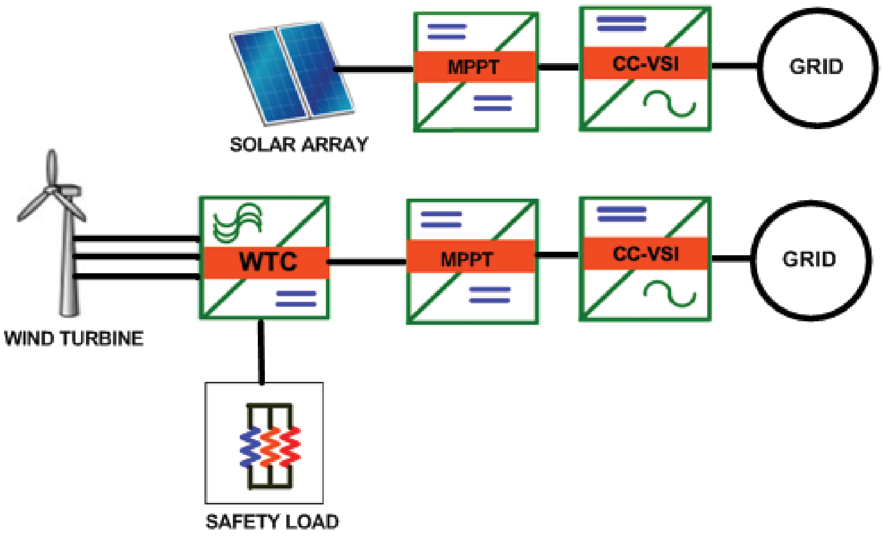

Figure 4-1 : Conventional grid connected system

An AC coupled system such as Figure 4-2, uses a CC-VSI to interface each renewable energy generator to the grid. All solar or wind energy is fed through a DC-DC converter, then its own independent CC-VSI. This system is electrically equivalent to Figure 4-1 and has no increased efficiency of conversion from two isolated wind and PV systems.

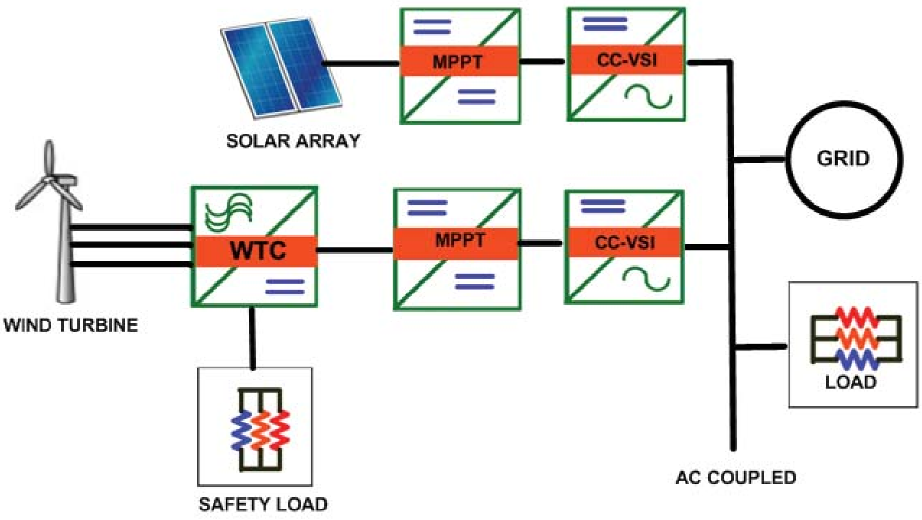

Figure 4-2 : Typical AC coupled hybrid system

DC coupled systems are interconnected around a central DC bus. The sensing of a voltage rise on this DC bus triggers the CC-VSI to feed current to the grid, as per Figure 4-3. A single suitably sized CC-VSI is used which creates a more efficient hybrid system and increases the inverters utilisation. This system is ideal where a utility wishes to implement a renewable hybrid system to feed energy into directly to the grid and the crossover of energy production between the solar and wind generation is quite high.

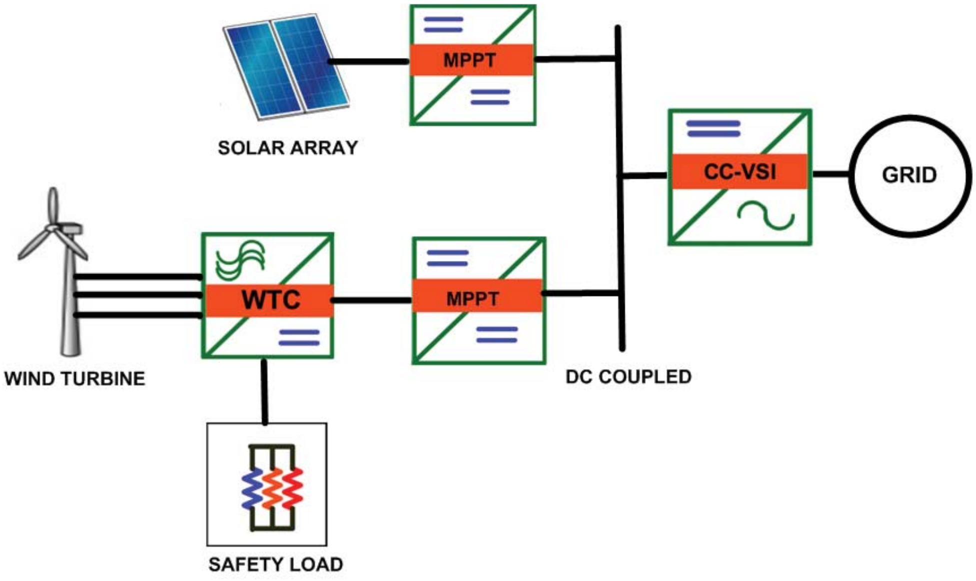

Figure 4-3 : Typical DC coupled configuration

The final novel hybrid system configuration, Figure 4-4, the complementary hybrid system exploits the premise that the wind and solar resources rarely generate electricity simultaneously. A single diode is used between the sources, which allows the generator with the greater voltage have its power passed to the grid. Figure 4-5 shows the voltage regions of operation of such a system. The PV string length can be varied to attain the desired transition wind speed. A system can be designed to produce maximum power production from the renewable sources, while minimising the crossover loss. This system also only requires a single DC-DC converter and CC-VSI, minimising the power electronics components cost.

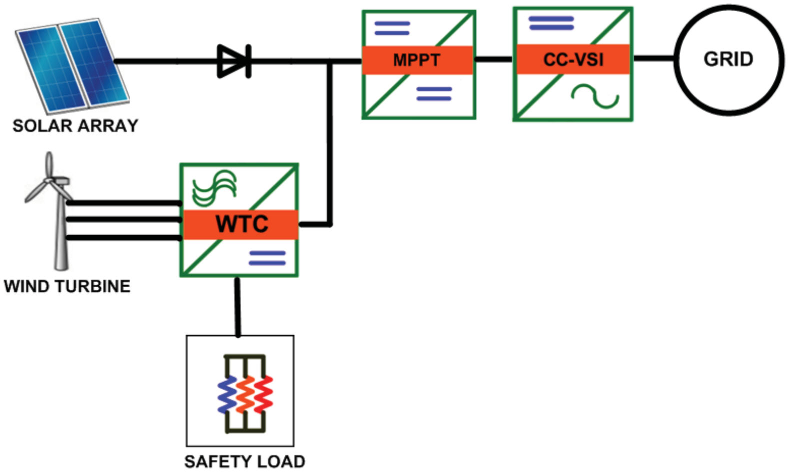

Figure 4-4 : Novel complimentary type configuration

The complementary type system operates by allowing the generation source with the greater input voltage to pass its power to the MPPT and the inverter. The variation in PV output voltage only changes slightly with respect to a change in irradiation conditions. The WT's voltage is based upon the blades rotational speed, which is proportional to the wind speed through the tip-speed ratio relationship. A transition wind speed can be selected where its related voltage will be greater then the expected V_{MP} of the PV array. Wind speed above this point will allow wind energy to be generated. During night conditions the transition wind speed will decrease to the inverters minimum start up voltage requirements. Figure 4-5 outlines these regions of operation based upon the DC bus voltage at the input to the MPPT and the wind speed. An open circuit test of the WT is required to create the desired DC voltage to rotational speed relationship, assuming optimal tip-speed ratio this can be extrapolated to the wind speed.

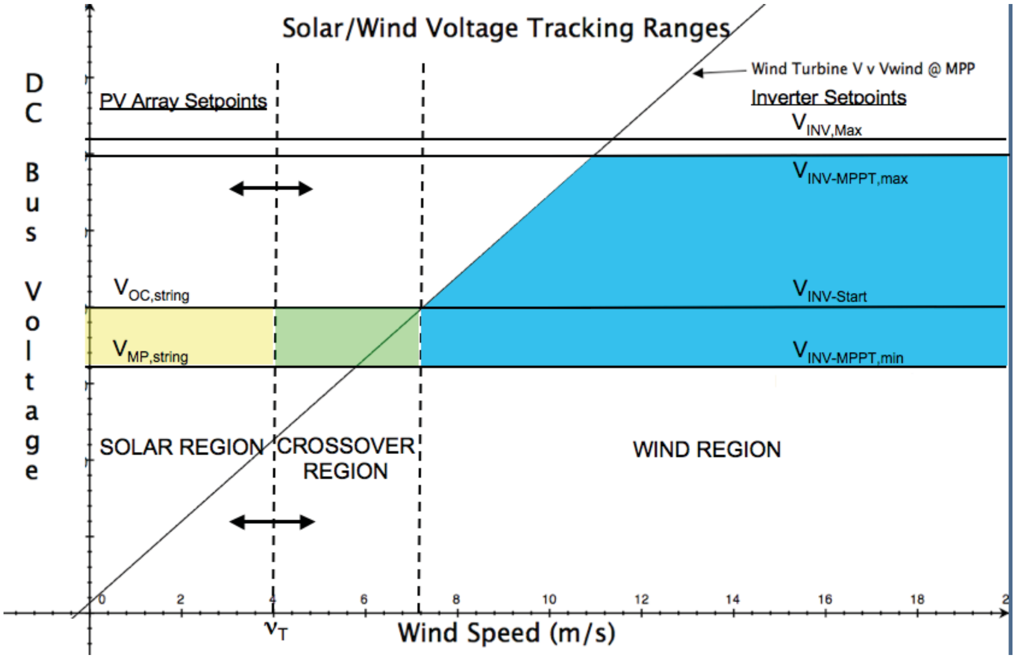

Figure 4-5 : Complimentary system tracking ranges

The power extracted from a WT is proportional to the cube of the wind speed. At low wind speeds very little power is available to be captured by the WT. This premise is coupled with the observation that generally sunny conditions do not exhibit wind, and during storm conditions very little solar energy is available. Also winds during favourable sun conditions are usually light, so little overall power is available. Most previously developed hybrid system rely on either two grid connected inverters or a common DC bus fed by two DC-DC converters from the energy sources. The hybridising of a single inverter to feed power from solar and wind complementarily vastly increases the inverter utilisation, while only decreasing the net energy yield by a few percent [3-5]

The interconnection of the PV and WT occurs at the output of the PV array and the output of the rectified WT. The WTC is used as a voltage clamp to prevent the input voltage of the inverter exceeding its maximum specifications. The selection of the power producing source is done through an appropriately rated diode as seen in Figure 4-4. Whichever source is producing the higher voltage will feed its available power to the grid. A small portion of time, conditions will exist where the solar array and WT could produce power. This loss of energy is termed the crossover loss and is mathematically modelled in the next section.

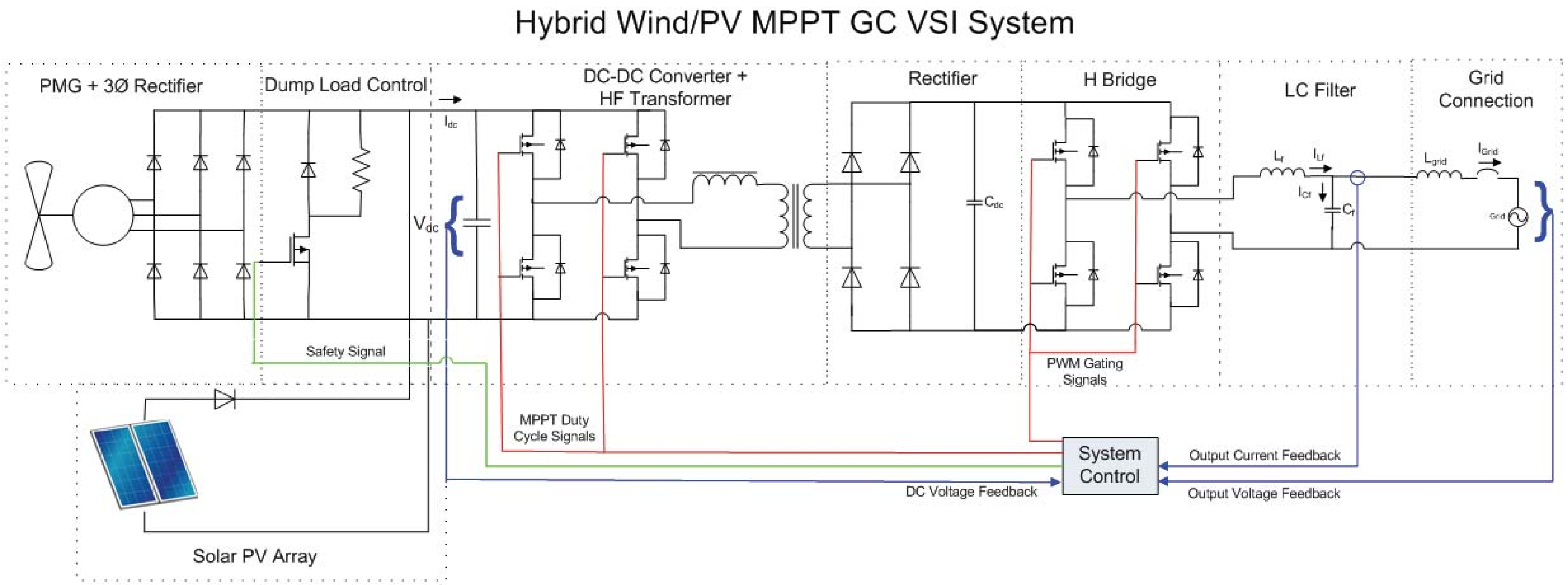

Figure 4-6 : Complementary wind/PV CCVSI Diagram

4.1.2. Edge of grid hybrid system topologies

A hybrid system owner's priority is to maximise any offered government rebates while creating a reliable independent power supply for their residence. Some form of energy storage device such as a battery is required to ensure that power can be provided during blackout conditions. A further complexity is that the inverter control required for a grid connected and stand-alone application invariably requires the use of two inverters to perform the require functions. The VC-VSI control system must also monitor the grid connection and battery SOC. The VC-VSI must quickly react to any grid disturbance and re-energise the load from the battery. The final condition must be to protect the battery and not allow it to be over charged, for this the hybrid system controller must disconnect the renewable sources when the battery is full in stand alone mode [6, 7].

For a DC coupled edge of grids system two different interconnection topologies are possible, Figure 4-7 and Figure 4-8. Figure 4-7 directly connects the DC bus to the battery. The charging regime of the battery is controlled by the DC-DC converters from the solar and wind generators, requiring some control communication between these controllers. The VC-VSI must also control the generation source contactors to prevent the battery from being over charged. Overall this DC coupled configuration while ideal for a simple grid connected system requires excessive control to be safely operated as a grid connected back up system.

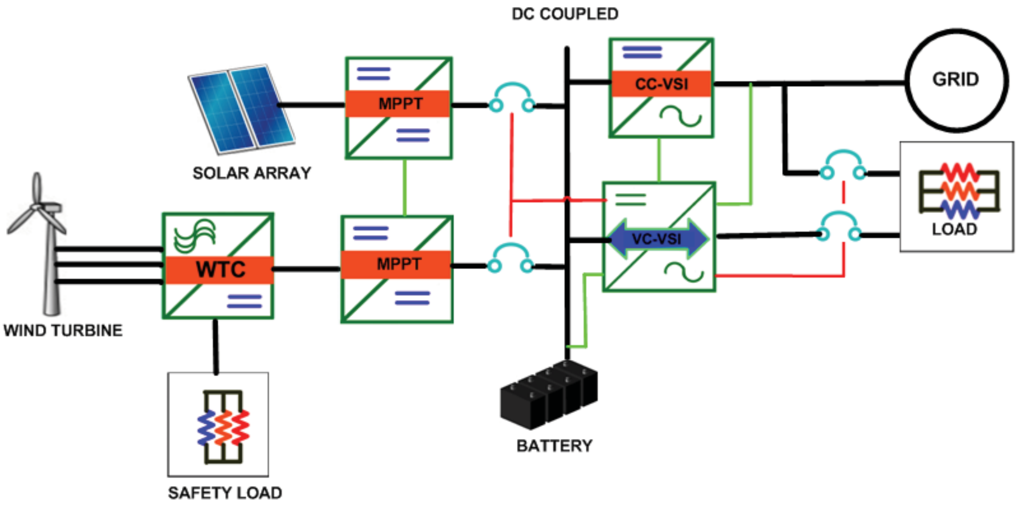

Figure 4-7 : Hybrid DC coupled battery bus edge of grid system

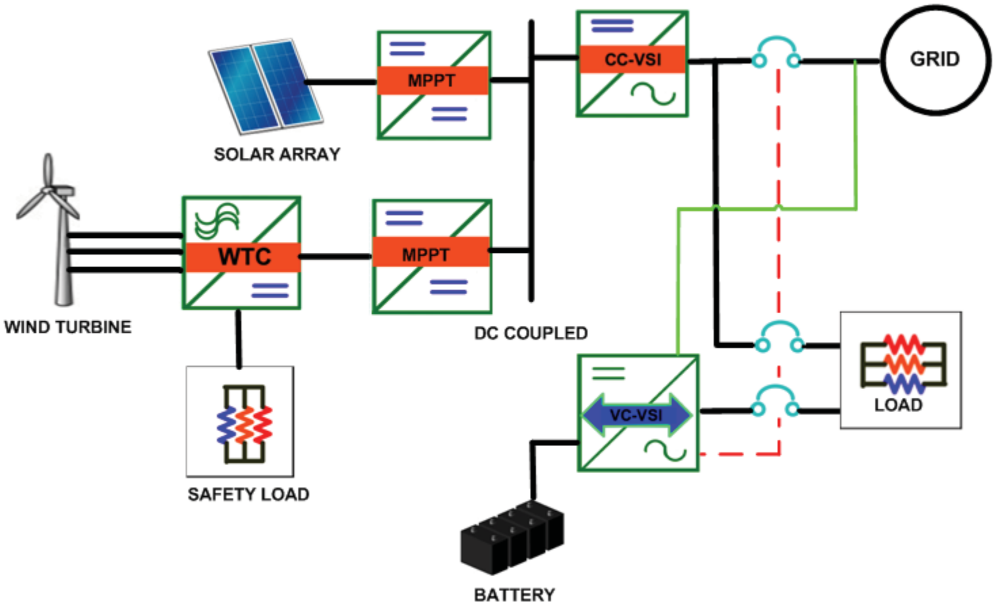

Figure 4-8 : Hybrid DC coupled independent edge of grid system

Figure 4-8 presents a simpler DC coupled edge of grid system. The battery is controlled and monitored by the VC-VSI only, resolving the requirement for communication of the current from the sources feeding to the DC bus. The CC-VSI feeds whatever power is available on the DC bus to the AC grid or local load. The VC-VSI monitors the grid connection and switches from charging to providing the grid through the VC-VSI during a utility blackout. Also in the case of low load, grid failure, high SOC and excess renewable generation the VC-VSI can easily isolate the CC-VSI to prevent over charging. This DC coupled system is the most efficient back up grid feeding topology. The complimentary coupled edge of grid system, Figure 4-9, is similar to the conventional type system, Figure 4-8, with the removal of the generation sources independent MPPT's. This complimentary edge of grid system has been developed through this research and represents one of the novel aspects of this dissertation.

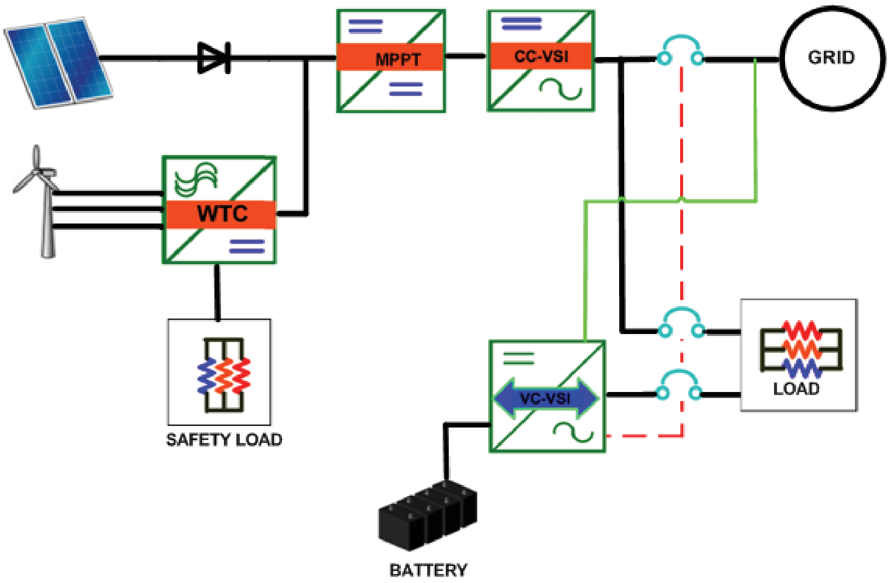

Figure 4-9 : Hybrid DC coupled complimentary edge of grid system

Figure 4-10 presents the most commonly installed AC coupled system, each renewable generation source is coupled to a common local AC bus. The grid connection is controlled by the VC-VSI which both reacts to a grid failure and isolates the renewable generation when the battery reaches a high SOC during an off-grid situation. This topology is very similar to Figure 4-8, with the difference being in the use of extra source defined CC-VSI's. The extra CC-VSI's increase the reliability of the overall system however also increases the cost.

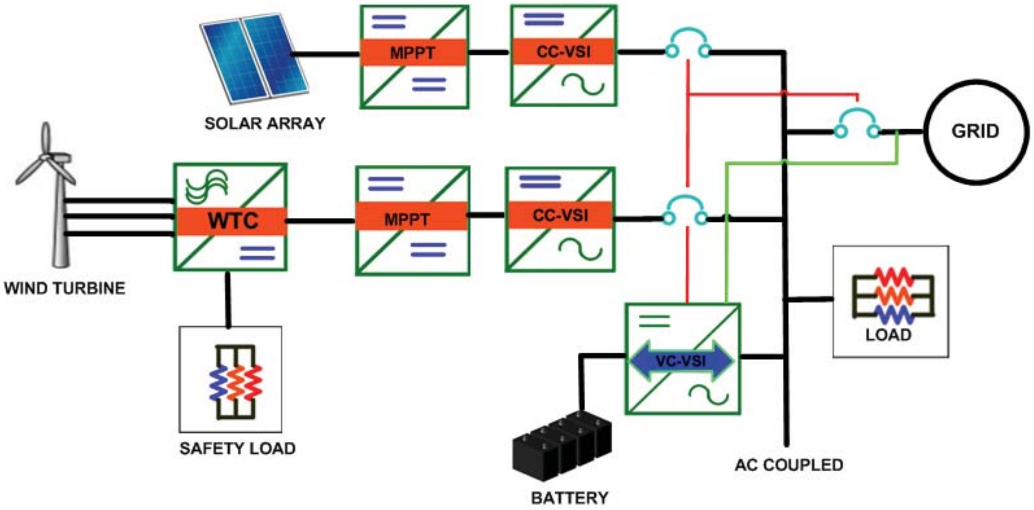

Figure 4-10 : Hybrid AC coupled edge of grid system

4.2. Development, Design and Analysis of the Complementary Hybrid System

4.2.1. Principles of The Complementary Hybrid System

The complimentary hybrid system is required to operate as a PV inverter at the low end of the voltage window and a wind inverter for the higher end. The voltage of the PV strings is crucial for the system to operate effectively. The sizing of the PV string voltage also sets the nominal voltage which determines the new WT cut-in voltage which directly corresponds to a cut-in wind speed.

The hybrid systems operational modes can be defined into three distinct regions. When either one of the energy sources are available without interaction they will feed the available energy providing input voltage conditions are met. When both sources are producing the one with the greater voltage will be selected and feed power to the inverter. This is summarised in Table 4-I.

Mode	**Sun**	**Wind**	**Operational Condition**	
A	Yes	No	$V_{MP,array} > V_{INV\text{-}MPPT,min}$	
B	No	Yes	$V_{WT,dc} > V_{INV\text{-}MPPT,min}$	
C	Yes	Yes	$V_{MP,array} > V_{WT,dc}$	$V_{MP,array} > V_{INV\text{-}MPPT,min}$
			$V_{MP,array} < V_{WT,dc}$	$V_{WT,dc} > V_{INV\text{-}MPPT,min}$

Table 4-I : Operational Conditions

The tracking ranges can be defined into three regions, solar generation, wind generation and the crossover region. Diagrammatically the inverters' input DC bus voltage can be segmented into regions of operation with respect to the wind speed, Figure 4-11. This outlines the regions of operation defined by the PV array voltages and the open circuit rectified voltage from the WT. The intercept between the minimum input voltage of the DC-DC converter and the WT's rectified output voltage determines the minimum operational wind energy capture voltage. Many WT's start voltage is approximately equivalent to 3.5m/s, however, very little annual energy is collected between 4m/s and 5m/s. This allows the transition voltage to bet set at some optimum point within the crossover region allowing the total energy yield to be maximised. The transition voltage is directly proportional to the transition wind speed.

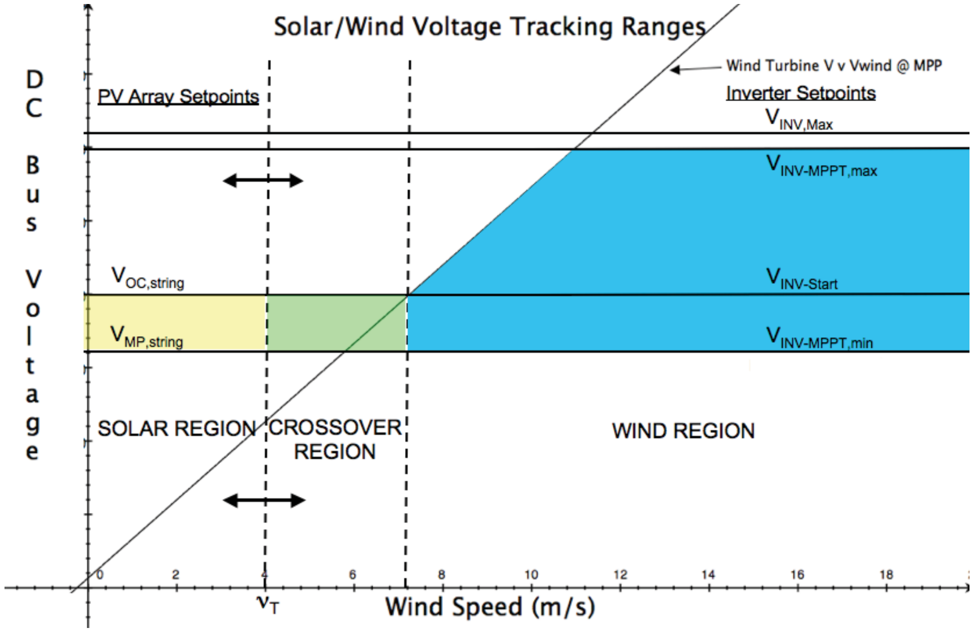

Figure 4-11: Regions of operation

In designing the PV array two conditions must be met. Firstly to ensure PV only operation the open circuit voltage of the PV array must be greater then the inverter start voltage. Secondly the PV array MPP voltage must be above the minimum inverter tracking range. A lower PV array MPP allows a lower selection of the ν_T so allows a lower wind energy cut-in voltage during sun conditions. It is a requirement that the commercial inverter used to implement the MPPT uses the IC algorithm as explained the chapter three.

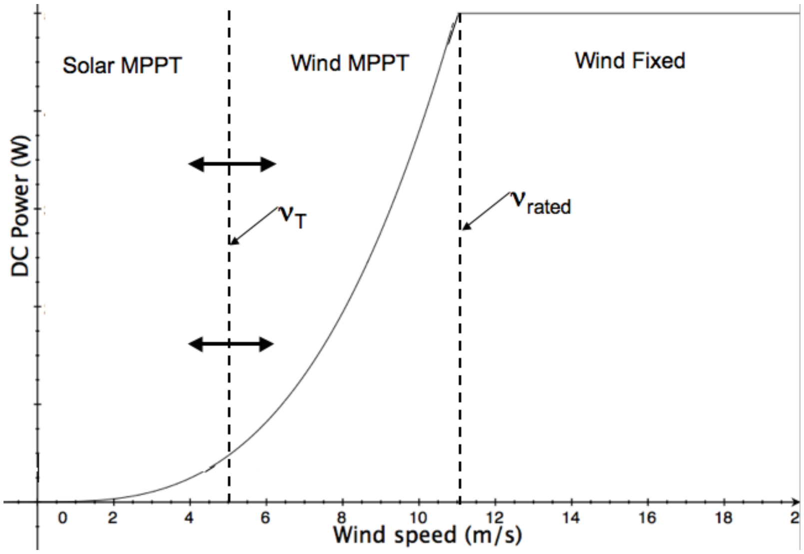

Figure 4-12: Inverter operational tracking ranges

The hybrid systems operational regions can be superimposed onto the wind power curve, as seen in Figure 4-12. With respect to the wind speed the MPPT will solar track for no or low wind speeds and wind track for wind speeds greater then the transitional speed. The sizing of the PV array to the rated power of the wind turbine requires an analysis of the energy generation. The wind is a variable entity, which can be modelled using probability theory. The sun is predictable however its uncertainty due to weather or cloudy conditions is also unpredictable. Knowledge of a generic sites wind characteristics, solar resource and average sun hours allows this technique to be applied to any location. Figure 4-14 outlines this process and quickly concludes whether this type of system is ideally suited to a location. Generally areas where the average daily sunshine hours is between 5 and 9 hours, from Figure 4-13, and exhibit moderate wind conditions are ideal for a hybrid PV/Wind system.

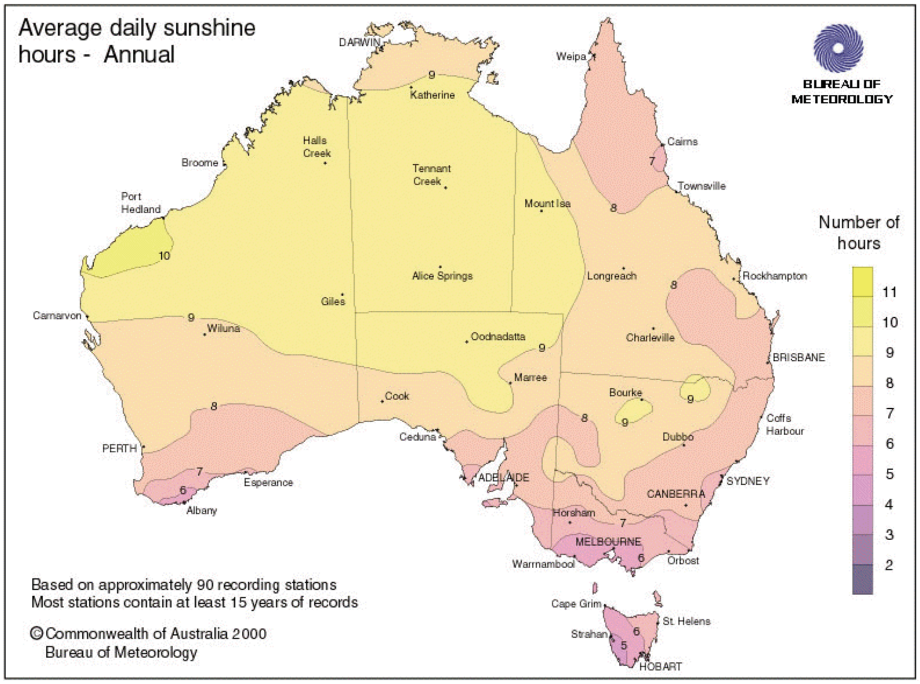

Figure 4-13 : Australian average daily sunshine map [8]

The process to determine the crossover loss and maximise the energy generated at the location is shown in Figure 4-14.

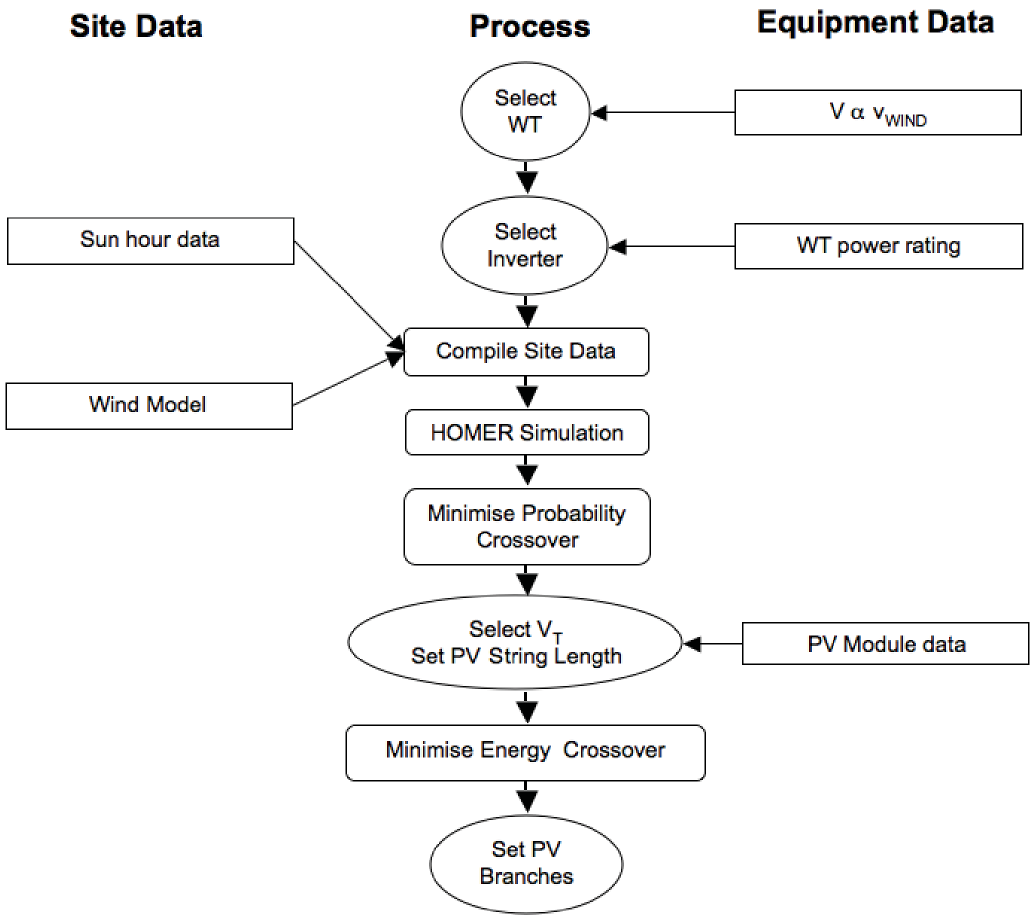

Figure 4-14 : Design process flow diagram

4.2.2. Mathematical Modelling for the Complimentary System

To calculate the gain in energy capture, and the possible loss due to any crossover by the wind/PV hybrid system, the probability that the wind speed at a site will be above a certain speed must be known. The losses attributed to any crossover in the system are two fold. Firstly, the V_T set by the V_{MP} during sun conditions prevents wind energy being generated at low wind speeds. Secondly during higher wind speeds any solar energy is not available. These losses are defined and modelled separately. The variation in V_T is based upon the possible PV string V_{MP} and the open circuit rectified voltage characteristics of the WT.

Once a Rayleigh or Weibull probability distribution, as defined in chapter one, is fitted to the site's wind statistics, the amount of time for various wind speed intervals can be calculated. Using bin widths of 1m/s the probability can be numerically evaluated about the integer as per Eq 4-1, where f(v) represents the wind distribution and x the bin wind speed.

$$P(x-0.5 \le x \le x+0.5) = \int_{x-0.5}^{x+0.5} f(v).dv$$

Eq 4-1 : Bin width expression of wind speed

To evaluate the annual theoretical energy production the power must be attained for the various wind speeds. This can be seen from the wind turbines power curve, superimposed on Figure 4-12. The summation of the various wind intervals allows a prediction of the monthly and annual energy to be made, from Eq 4-2.

$$E = 8760\sum_{n=\infty}^{n=1} P(n) \int_{n-0.5}^{n+0.5} f(v).dv$$

Eq 4-2 : Annual wind only energy generation

In order to calculate the overall inverter utilisation and the probabilities of solar or wind energy being generated some definitions are required. The average length of day for a month is defined as the time interval between sunrise and sunset. The average sun hours is a useful measurement from which the proportion of sun during a day can be obtained. The final parameter is the wind only hours, or night time.

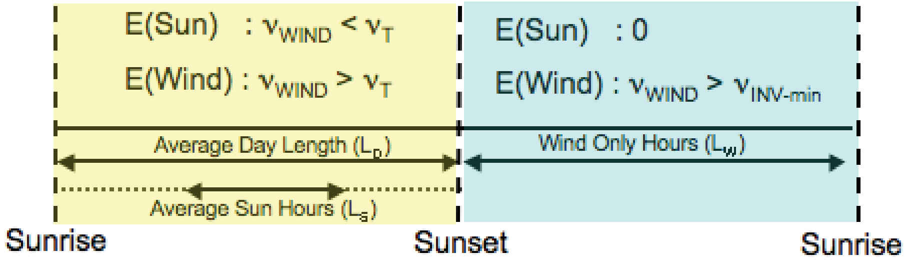

Figure 4-15 : Operation time zones

The overall probabilities can be broken into two sections as seen in Figure 4-15. The average day length is can be calculated based upon the latitude of the location and the day of the year.

$$L_D = \frac{24\cos^{-1}(1-m)}{\pi}$$
$$m = 1 - \tan(k \cdot Lat)\tan\left(k \cdot \varphi \cos\left(\frac{2\pi D}{365}\right)\right)$$
$$k = \pi/180$$

Eq 4-3 : Calculation for length of day [9]

Each section can then be allocated a probability that solar or wind energy is generated given it is day or night.

$$P(Day) = \frac{L_D}{24}$$
$$P(Night) = 1 - P(Day) = 1 - \frac{L_D}{24}$$
$$P(Sun \mid Day) = \frac{P(Sun \cap Day)}{P(Day)} = \frac{L_S}{L_D}$$
$$P(Wind \mid Day) = 1 - P(Sun \mid Day) = 1 - \frac{L_S}{L_D}$$
$$P(Sun \mid Night) = 0$$
$$P(Wind \mid Night) = 1 - P(Sun \mid Night) = 1$$

Eq 4-4 : Conditional zone probabilities

The crossover loss is the amount of energy lost using this wind/PV complimentary hybrid system with respect to two individual independent systems. The annual energy generated by an independent wind system at the given site is denoted by E_{WIND}. The annual energy generated by an independent solar system at the given site is denoted by E_{PV}. The total combined hybrid system energy is denoted by E_{SYSTEM}. The system losses contain two components from the PV and wind.

$$
\begin{aligned}
E_{SYSTEM,loss} &= E_{WIND,loss} + E_{SUN,loss} \\
\%_{CROSSOVER} &= \frac{E_{SYSTEM,loss}}{E_{WIND} + E_{PV}}
\end{aligned}
$$

Eq 4-5 : Definition of crossover loss

The wind energy loss is due to the wind turbines cut–in voltage being less than the inverters start voltage. During no sun conditions this will be the lowest operating input voltage of the inverter, during the day this will be the V_{MP} of the PV array. The solar energy loss is due to the wind speed being greater then the V_T during sun conditions. The combination of these probabilities allows the calculation of the likelihood that energy will be generated from either the wind E_{WIND} or sun E_{SUN}. The inverter utilisation is the probability that the hybrid system will generate energy and is denoted by E_{SYSTEM}.

$$
\begin{aligned}
&P(E_{WIND}) = P(Day)P_{Wind}(v > v_T) + P(Night)P_{Wind}(v > v_{cut-in}) \\
&P(E_{SUN}) = P(Day)\left[P(Sun) - P_{Wind}(v > v_T)\right] \\
&P(E_{SYSTEM}) = P(E_{WIND}) + P(E_{SUN})
\end{aligned}
$$

Eq 4-6 : Hybrid system zones probabilities

The application of these probabilities allows the system to be design to maximise the energy yield and minimise the crossover loss.

4.2.3. Simulation of Complimentary Hybrid Concept

The software package PSIM [10] was used to simulate the energy yield from the various different system topologies. Individual models were developed for the WT, PV array and controller, all written in C++ and converted into a dynamic link library blocks. PSIM allows the inputs and outputs of each block to be specified and the code be executed for each simulation step, the simulation time was set to 86,400 seconds for one day.

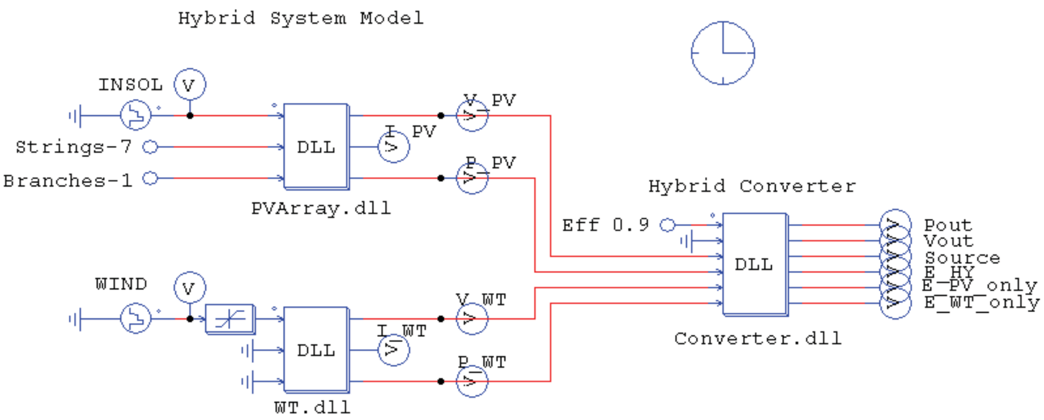

Figure 4-16 : PSIM simulation model

The PV array block is modelled on the Sunpower SPR-200 PV module and the model developed in chapter three [11]. The string module length and number of branches set the PV array size parameters. The irradiance can then be varied as expected throughout the day. The block internally calculates the V_{MP} and I_{MP} based upon the current irradiation level. The PV model makes two assumptions on the operation of the array. It assumes the temperature variation from 25°C causes minimal effects, and a MPPT is used at the output of the array.

The wind turbine model assumes it is operating at its optimal tip speed ratio at all times. The rotational speed of the WT is directly calculated from the wind speed. The rectified voltage can then be calculated from the relationship between the rotational speed and the permanent magnet machine phase voltage. The DC voltage can then be approximated for any wind speed. The wind turbine modelled was a 5kW Westwind permanent magnet machine, as used for the Denmark project. A polynomial fit of the data sheet power curve allows the power at any wind speed to be known, the current is then derived.

Finally, the converter block tracks the energy production from the WT and PV array independently over the simulation time, ensuring each time step is equal to one second. To test the complimentary hybrid system the voltage from the WT and PV is passed to the converter block. The generation source with the greater voltage, within the inverters' operational window is denoted as the active source and generates energy. If the WT voltage falls below the V_{MP} of the array during a time with high irradiace solar energy will then be generated.

A generic day of wind speed (m/s) and solar irradiance conditions (W/m^2) was created and simulated, Figure 4-17.

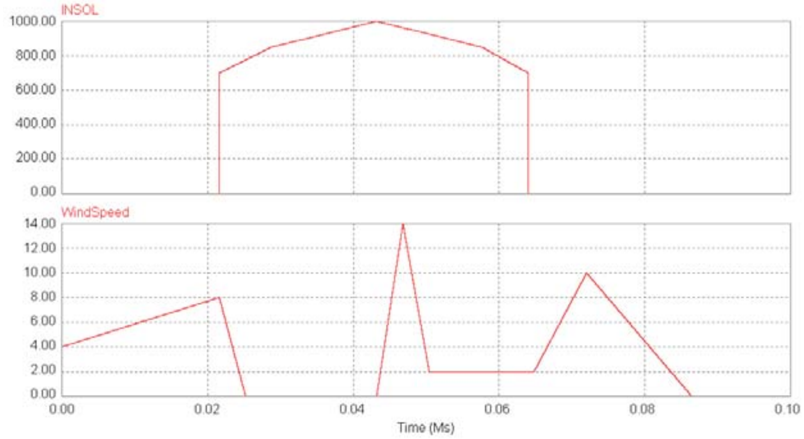

Figure 4-17 : Simulated Irradiance and Wind Conditions

The solar array simulated was constructed from seven panels in series, yielding a total of 1.4kW. The power and voltage generated by the solar array and wind turbine is shown in Figure 4-18. The hybrid system ratio of peak powers P_{WT}/P_{PV} is then 3.57.

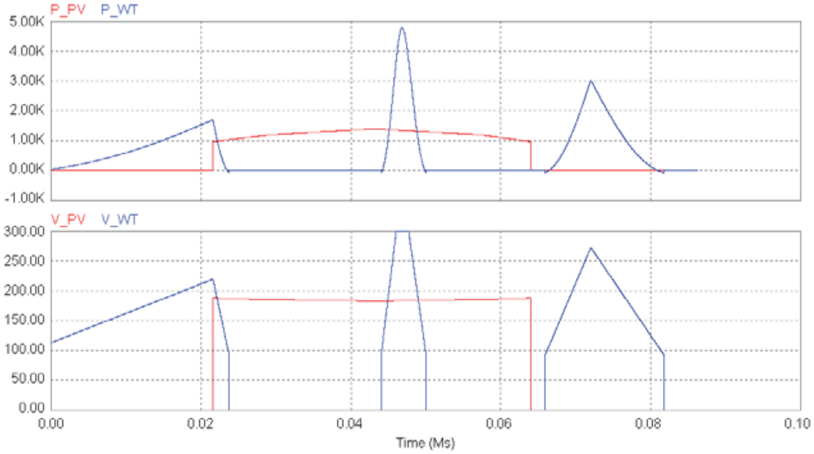

Figure 4-18 : Power and voltage generated by the hybrid system

Figure 4-18 shows the power generated from the PV or wind sources throughout the day. The greater voltage generated by the source determines the one which will supply the DC power to the inverter.

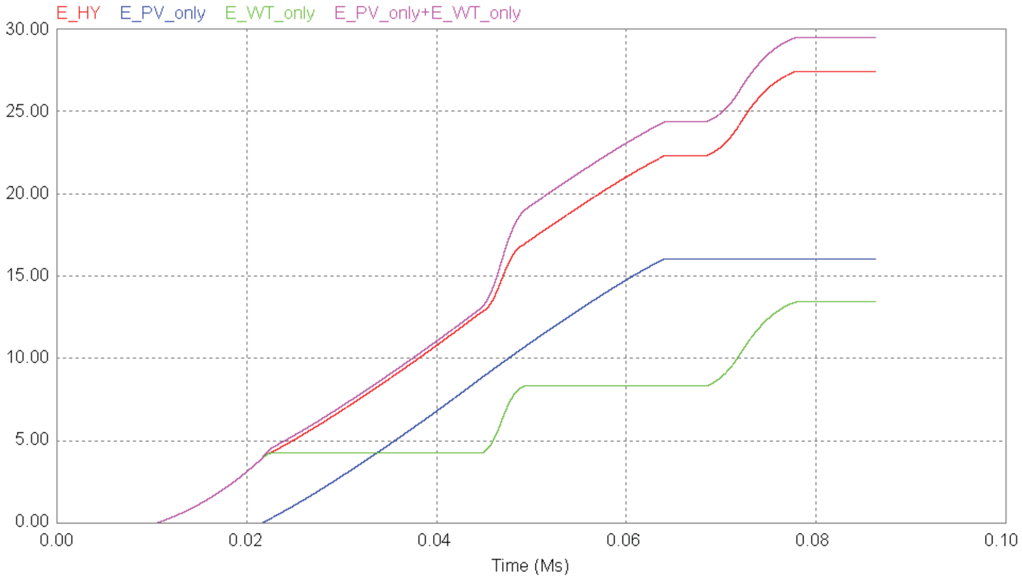

Figure 4-19 : Hybrid system comparison

The complimentary hybrid system, Figure 4-19 (red), will generate power from whichever generation source has the higher input voltage. During the night this must be wind energy, in daytime solar energy will be generated unless strong wind conditions are present. Figure 4-19 shows the net energy generated throughout the day from the different sources using the solar and wind conditions as shown in Figure 4-17. The complimentary system produces significantly more energy then either a PV only or wind only system, however slightly less then the combination of the two systems, Figure 4-19 (pink). The crossover loss for this system on this typical day is 6.9%.

4.2.4. Simulation Results for Denmark

A second software package, HOMER[12] was utilised to create a more generalised yearly based model to assist in the selection of the type and size of hybrid system. Using monthly data of the solar irradiation, latitude and longitude the annual energy generated from a PV only system can be calculated. Similarly from monthly average wind speeds, height and knowledge of the wind turbines power curve the annual wind only energy generation can be calculated for any location. A conventional hybrid wind/PV systems energy generation is the sum of the PV only and wind only components.

Wind and sun data for the Denmark experimental site were collected from the Bureau of Meteorology in Western Australia, this is shown in Figure 4-20 and Figure 4-21.

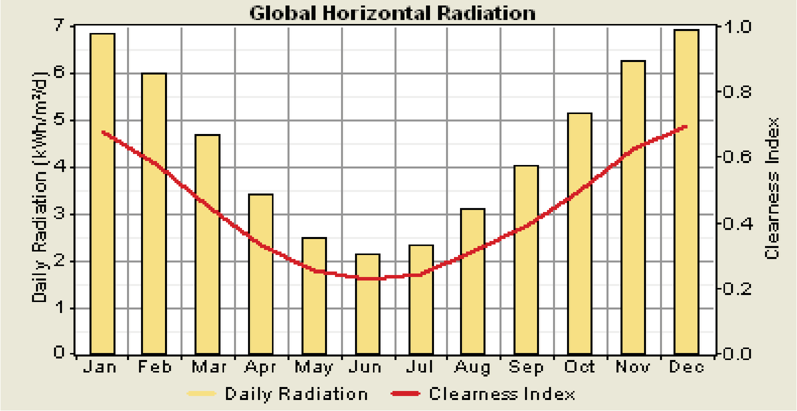

Figure 4-20: Solar irradiation data

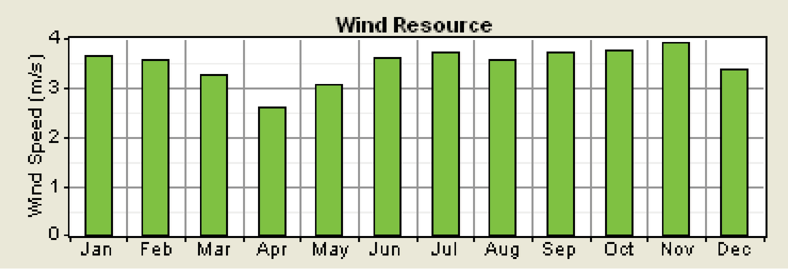

Figure 4-21 : Height scaled wind data

Comparative data was generated using a standard DC coupled system. The simulation results of the monthly energy production for a 5kW wind turbine and a 1kW PV array are shown in Figure 4-22.

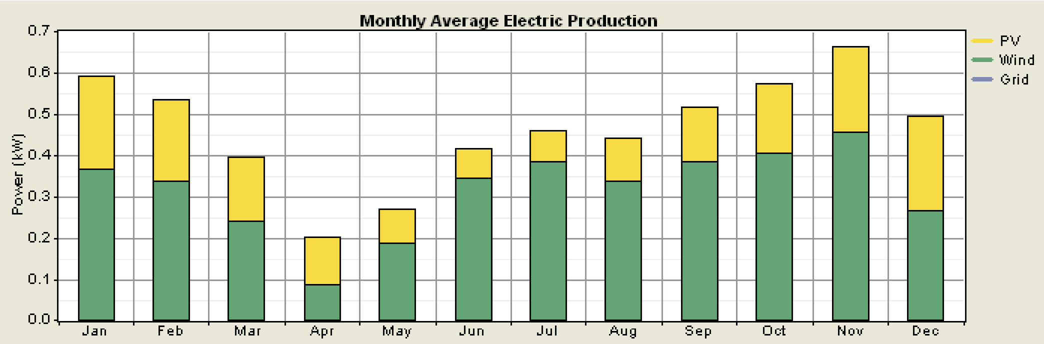

Figure 4-22: Simulated monthly energy yield

The aim of the simulations was to ascertain the ideal V_T that would be used to set an ideal V_{MP} for the array to minimise the crossover loss. The second aim was to investigate the total energy loss from the differing wind to PV peak power ratio.

The loss of wind turbine utilisation is given by the difference between the standard cut-in wind speed of the WT and new v_T given the energy is generated during sun conditions. The sun conditions are site dependent and so the annual average sun hours are used to predict the average energy lost. Simulations were conducted to calculate the energy generation from a WT if its cut-in speed was varied. Table 4-II shows the energy lost as a percentage of the total generated by the WT independently, and the average lost when this crossover occurs during the day. This represents the likely wind energy loss annually due to the selection of the V_T. As the power generated is different for changing wind speeds it is convenient to express the wind energy lost as a percentage of that generated. These percentages are WT dependent as they are related the wind power curve and the wind characteristics of the site.

Wind speed (m/s)	**Energy Gen** (kWhr)	**Energy Lost** (kWhr)	**Max Lost** %	**Ave Lost** (kWhr)	**Ave Lost** %
4.0	2765	0	0.00%	0.00	0.00%
4.5	2742	23	0.83%	0.05	0.21%
5.0	2708	57	2.06%	0.29	0.52%
5.5	2528	237	8.57%	5.08	2.14%
6.0	2277	488	17.65%	21.53	4.41%
6.5	1987	778	28.14%	54.73	7.03%
7.0	1672	1093	39.53%	108.02	9.88%

Table 4-II : Wind energy loss for L_S = 6 hrs

The solar energy loss is the probability the wind speed is greater then V_T during sun conditions. The annual sunshine hours affects the probability that a crossover event will occur. Within Australia the average annual sunshine data varies from 11 to 5 hrs average per day, with the experimental site averaging 5.9 hours, Table 4-III.

Wind speed (m/s)	**P(v>x)**	**Max Lost** %	**Ave L_S=6** %	**Ave L_S=11** %
4.0	0.23593	23.59%	5.90%	10.81%
4.5	0.17473	17.47%	4.37%	8.01%
5.0	0.12703	12.70%	3.18%	5.82%
5.5	0.09073	9.07%	2.27%	4.16%
6.0	0.06373	6.37%	1.59%	2.92%
6.5	0.04403	4.40%	1.10%	2.02%
7.0	0.02993	2.99%	0.75%	1.37%

Table 4-III : Solar Energy Loss

Eq 4-5 and the average sunshine hours the probable loss of solar energy collection can be realised and seen in Table 4-III and Figure 4-23. For this to be extrapolated to a loss of energy the size of the PV array must be known.

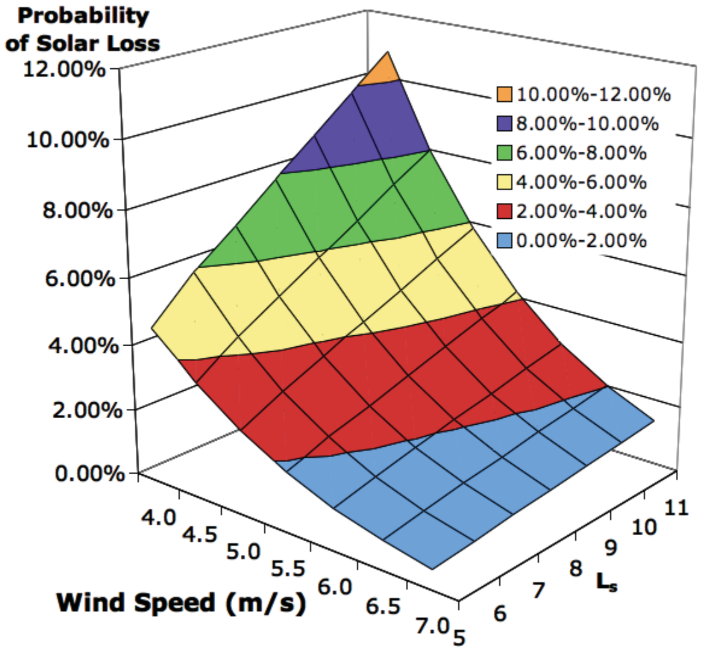

Figure 4-23 : Probability of solar loss

For a given WT and site details the wind and solar losses can be combined to represent an overall crossover probability loss. Figure 4-24 shows a region of wind speeds, which allow the wind and solar losses to be minimised. The system is also most effective in regions where the annual sunshine hours are below 10 hours.

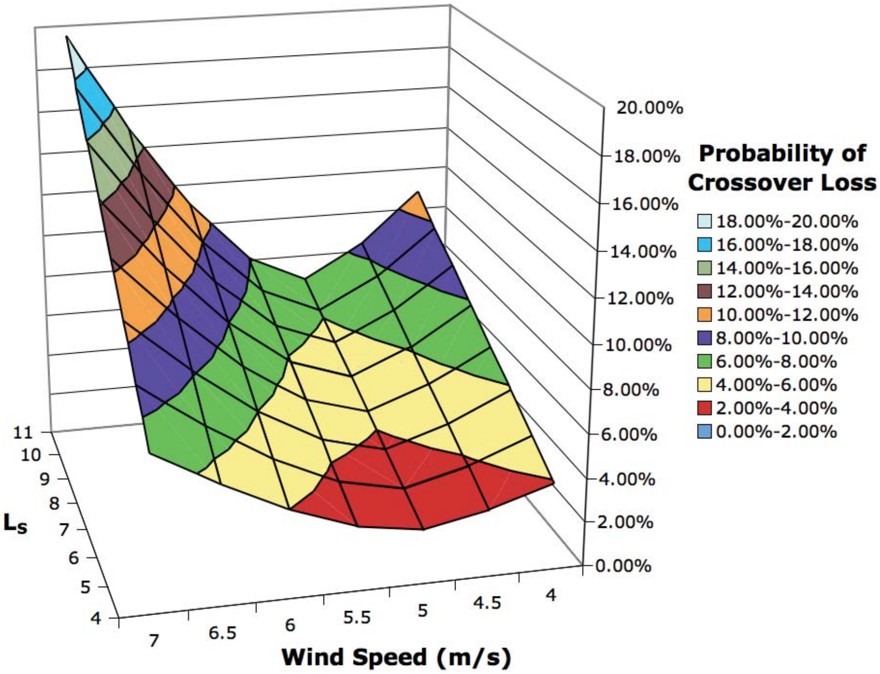

Figure 4-24: Crossover Probability Loss

Three parameters of the system define the predicted total crossover energy loss. These are the annual sunshine hours for the location, the ratio of wind rated power to solar peak power and the transition wind speed ν_T that maps to the V_{MP}. An assumption was made that the rating of the wind turbine should be greater then the peak PV power of the array. This correlates with the economic cost per watt principles and average energy yield. Hybrid system sizes where the PV array ranged from 0.33kW up to 5kW, with the 5kW WT were simulated. The percentage crossover energy loss as per Eq 4-6 from simulation results is presented in Figure 4-25 and Figure 4-26 for different annual average sun hour location data.

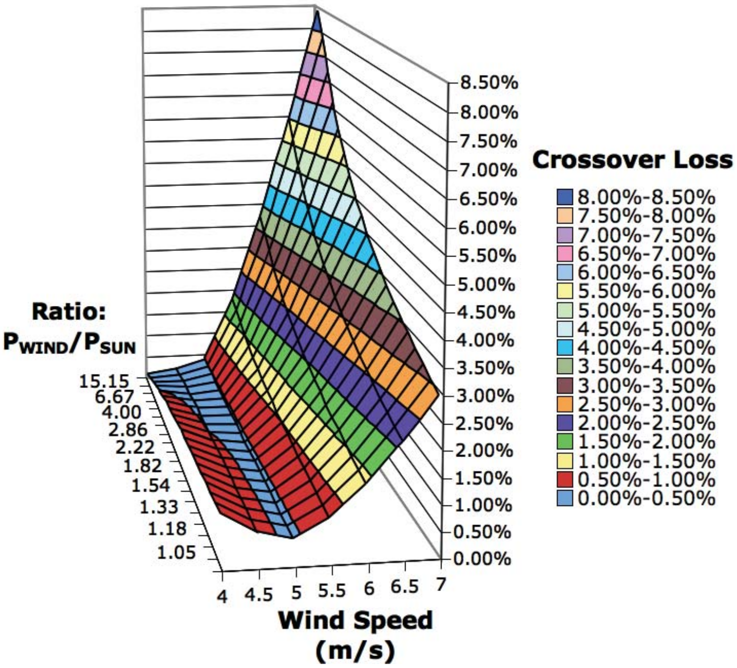

Figure 4-25 : Average crossover energy loss, L_S = 5.9hrs

The experimental results show that by carefully setting the V_{MP} of the solar array low average crossover energy losses can be found for any location. The system also tends to minimise the total losses for systems where the average sun hours is less than 9 hours. This implies that worldwide sites which exhibit average annual sunshine hours between 5 and 9 hours, would be ideally suited for this kind of complimentary hybrid system.

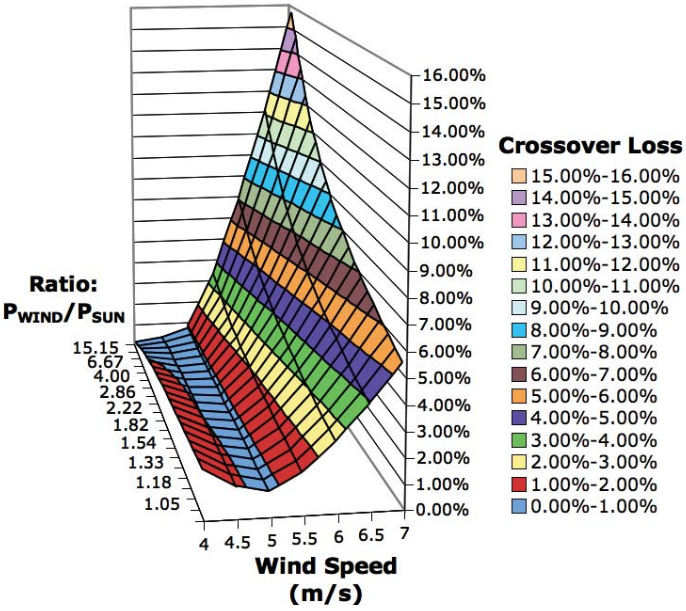

Figure 4-26 : Average crossover energy loss, L_S = 11hrs

A complimentary systems energy generation will vary based upon the selection of the transition wind speed as seen in Figure 4-11. This allows the ideal ratio of solar to wind energy generation to be optimised minimising the crossover loss. This analysis of the crossover loss was created using a combination of HOMER and data analysis software. For the specific sites Rayleigh wind probability distribution and the wind turbines power curve the annual energy generated for a specific wind speed range can be calculated. This is shown in Figure 4-27 as the average monthly energy generation.

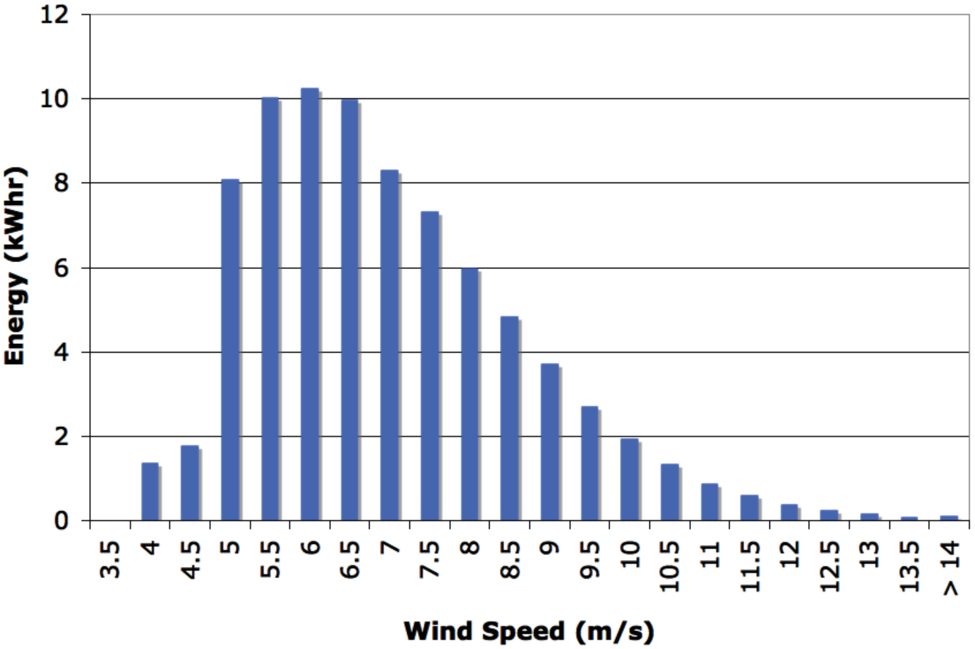

Figure 4-27 : Energy generated from various wind speed bin widths

Using the probability expressions Eq 4-6, Figure 4-27 and HOMER, solar energy generation for various sized PV arrays, the crossover loss can be plotted against the ratio of wind/PV rated power and the transition wind speed. This crossover loss surface defines the type of system that is ideally suited to the location.

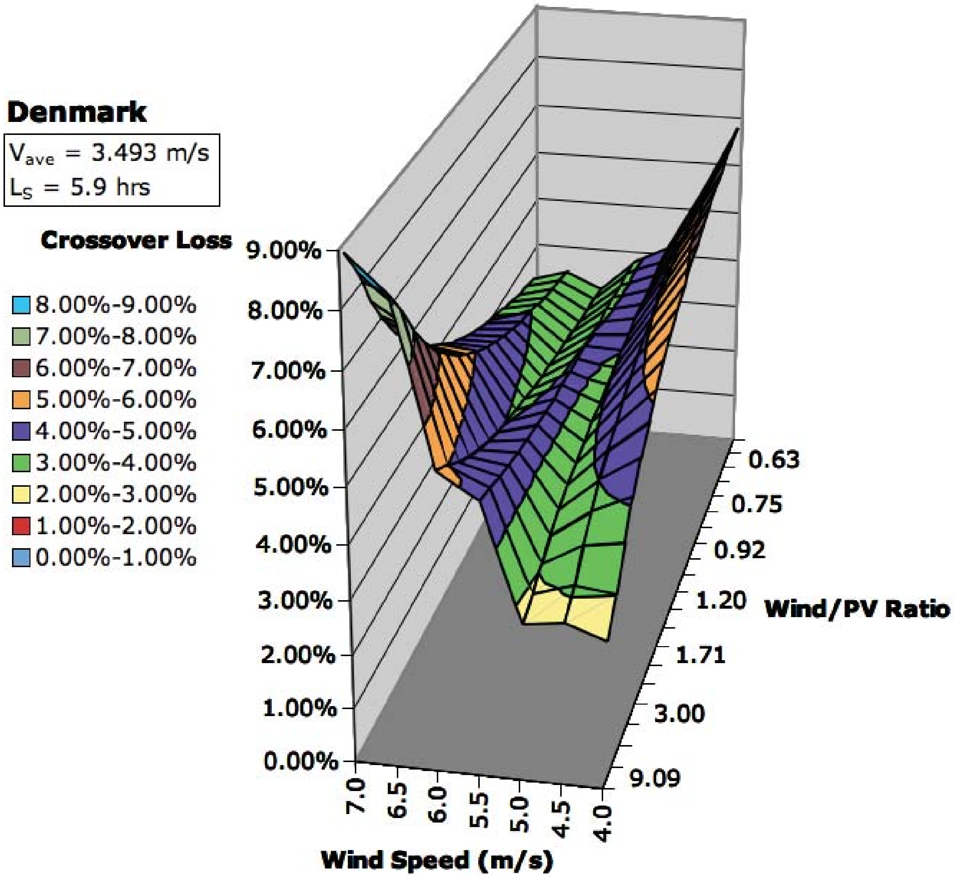

Figure 4-28 : Denmark system crossover loss

The crossover loss surface presented for Denmark in Figure 4-28 exhibits quite low losses for most practical hybrid systems. However, two minimisation lines at 6m/s and 5m/s can be seen from the plot. These optimisation lines infer that for a complimentary type hybrid system the transition wind speed should be set to 6m/s for a PV dominated system and 5m/s for a wind dominated type. The Denmark system is a clear example where the complimentary type hybrid system has a significant increase in energy production while minimising the crossover loss. A hybrid system which has a greater wind to solar rated power ratio, and the transition wind speed designed to be at approximately 5m/s would be ideal.

4.3. Denmark Project – Application of the complementary system

4.3.1. Denmark Experimental Set up

A demonstration system was assembled to prove the complimentary concept at a remote property in the south west of Western Australia. A 5kW permanent magnet wind turbine was hybridised with 330W of monocrystalline PV modules. A 5kVA 2:1 step up transformer was used to increase the output voltage from the wind turbine as the WT was designed to charge a 120V battery bank.

Figure 4-29 : Fully furled Denmark demonstration WT

The wind turbine used was an old 5kW Westwind light wind model. This WT had originally been installed at CRESTA at Curtin University approximately 10 years previous. The basic component design of the WT is shown in Figure 4-30 with it installed at the property on a 12m tower seen in Figure 4-29. The verified power curve is shown as Figure 4-31

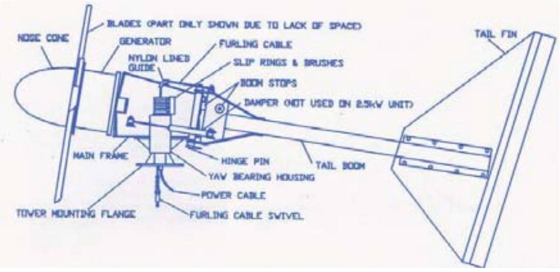

Figure 4-30 : Denmark WT, nacelle and tail assembly

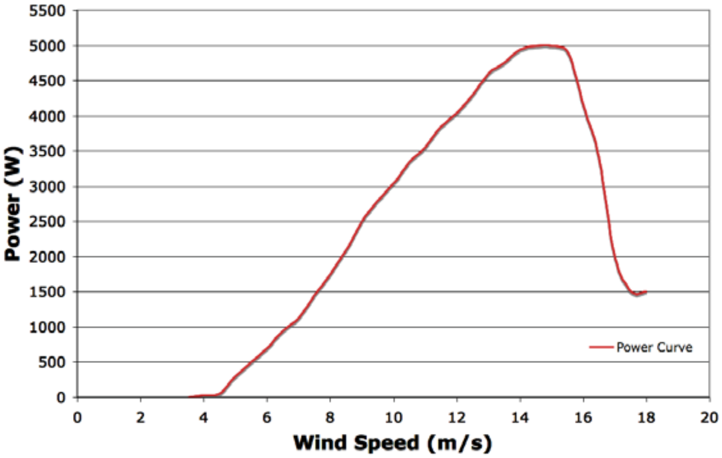

Figure 4-31 : Denmark WT measured power curve

In order to verify the complimentary concept, some old solar panels were found and used with the system. 330Wp of monocrystalline panels from a previous communications application were installed north facing at an angle on the side of the shipping container. The power electronics and monitoring equipment was installed inside the shipping container.

Figure 4-32 : PV monocrystalline 330Wp array

The output from the WT was a delta configuration and a transformer was found that could be configured to allow an approximate doubling of the WT output voltage. An old three phase, 5kVA, 50Hz iron core transformer was configured into a star-star winding and connected between the WT and the WTC, Figure 4-33. The implementation of this is seen in Figure 4-34, this transformer was installed inside the box in Figure 4-35.

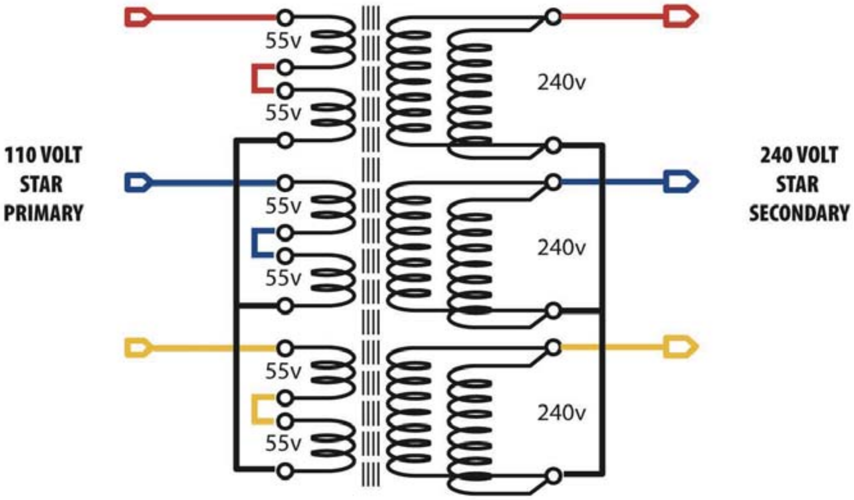

Figure 4-33 : Step up transformer connection drawing

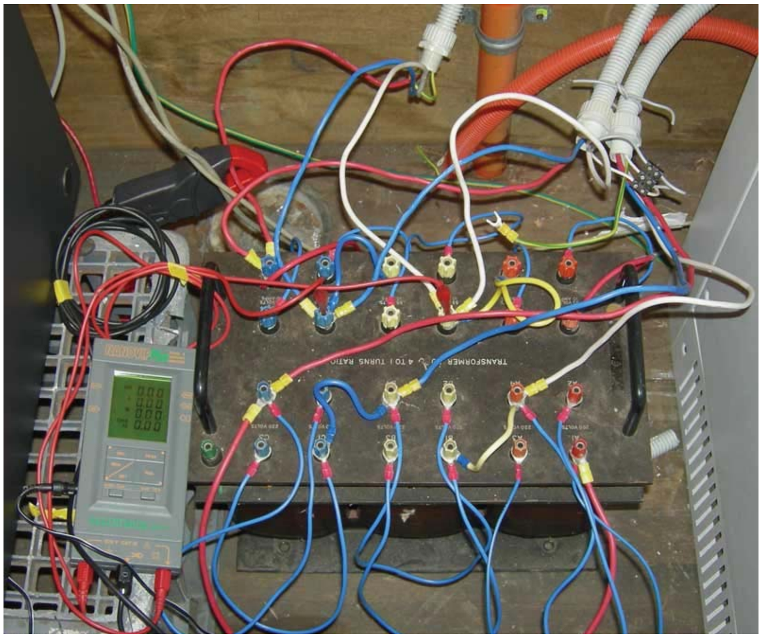

Figure 4-34 : Transformer implementation

INSIDE:

OUTSIDE:

Figure 4-35 : Transformer box and inverter (left), dump load and emergency brake (right)

The dump load was installed outside the shipping contained, Figure 4-35, and under a removable cover. The white purely resistive elements are seen at the top of the figure. The lower resistive bars form the emergency brake in the case of a WTC failure. A NC contactor connects these across the primary of the transformer, any problem with the WTC power source will cause this contactor to close automatically shorting the WT.

4.3.2. Demark System Data Monitoring and Recording

The many system parameters were logged to a central computer through serial RS-232 communications interfaces. Figure 4-36 shows the basic layout of these interconnections. The WTC and CC-VSI were directly poled for data every five seconds and this was received to the GUI as seen in Figure 4-37, which then saved to a CSV file. Parameters recorded were DC voltage/current/power/energy, dump load current/power, inverter voltage/frequency/current/power/energy and grid voltage/frequency. The nanovip power monitoring device was used at the output of the transformer to directly monitor the WT phase voltage/current/frequency. This additional device allowed the rotational speed of the WT to be calculated as well as the transformer losses. The final measuring device was the Lacrosse weather station which wirelessly received the wind data and stored this data via its Heavy Weather software package, Figure 4-38.

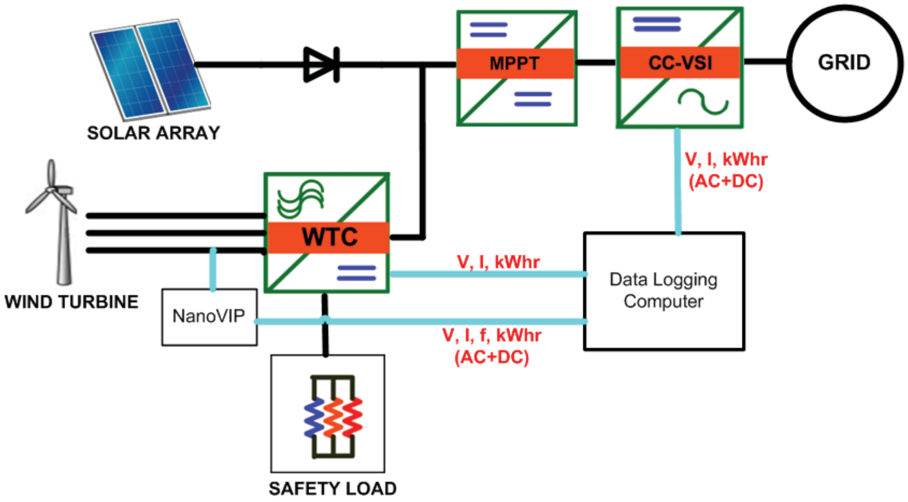

Figure 4-36 : Demark complimentary system and monitoring

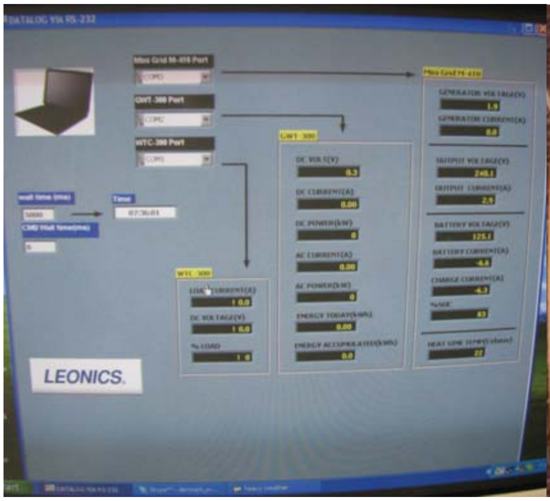

Figure 4-37 : Computer data logging interface (left)

Figure 4-38 : LaCrosse Professional weather monitoring device, WS-2308 (right)

4.3.3. Denmark Complimentary System Design

To ascertain a relationship between the rotational speed of the WT and the generated voltage a no load test was carried out. This was assumed to be linear for the region of operation and from multiple testing methods Figure 4-39 was produced. Two tests one with the transformer and one without were carried out to assess the relationship. The correlation of the measured points showed a strong linear trend in both cases. Measurements of frequency below 30Hz were not possible due to the accuracy of the Nanovip frequency measurement device. Frequency points above 40Hz triggered the safety operation of the WTC which skewed the results, so analysis was carried out only for the AC frequency range 30-40Hz.

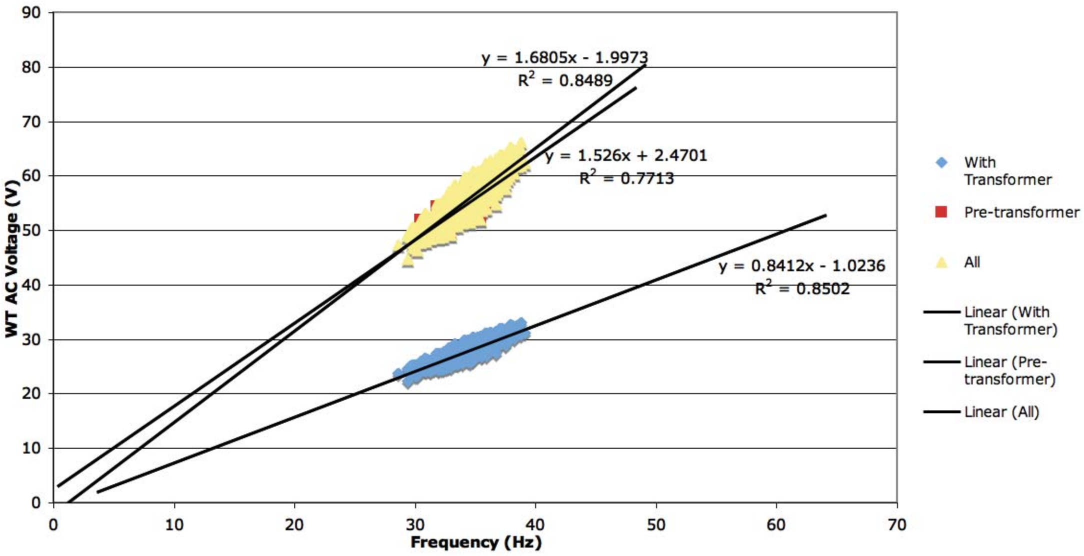

Figure 4-39 : Denmark WT AC Voltage vs Frequency

The results were averaged and a linear extrapolation carried out, the final model showed an extrapolation seen in Eq 4-7.

$$V_{ac} = Af_e + B$$
$$\text{For the Tested Wind Turbine:}$$
$$V_{ac} = 1.526 f_e + 2.4701$$

Eq 4-7 : Linear fitting for voltage/frequency for tested WT

The voltage which will determine the energy source will be the highest on the DC bus at the input to the CC-VSI. The expressions for a three phase rectifier were applied to develop the relationship between dc bus voltage and frequency, Eq 4-8.

$$V_{rect} = \frac{3\sqrt{2}}{\pi} V_{ac}$$

$$V_{dc,bus} = \frac{3n\sqrt{2}}{\pi}(Af_e + B)$$

For Tested Wind Turbine

$$V_{dc,bus} = \frac{3 \times 2\sqrt{2}}{\pi}(1.526 f_e + 2.4701) = 4.12165 f_e + 6.6716$$

Eq 4-8 : DC bus voltage/frequency relationship

Assuming that the IC MPPT method for the WT is operating correctly the rotational speed should be directly proportional to the wind speed. This assumption is valid for a fairly constant wind speed however will vary with turbulent conditions. However it is assumed that for the majority of the operational time this rotation frequency will be in a band quite close to that predicted from this assumption. The tip speed curve for this wind turbine was measured and modelled as Figure 4-40.

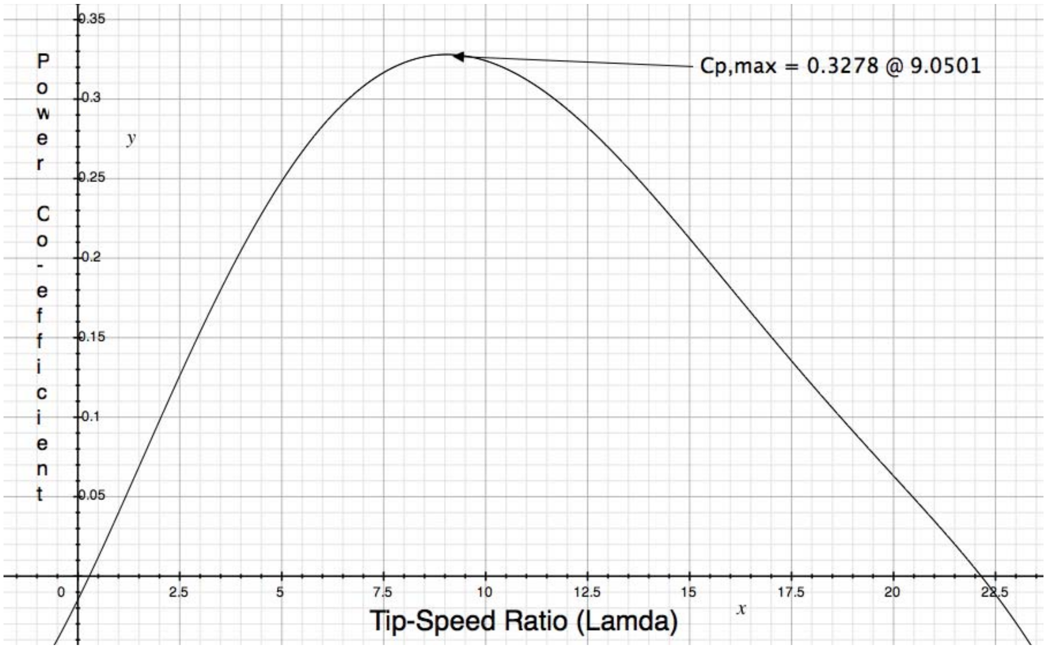

Figure 4-40 : Denmark WTs approximate Cp curve

So, if the system MPPT is working the relationship between the tip-speed and wind speed is constant and described by Eq 4-9.

$$\lambda_{MPP} = \frac{\omega R}{v_{WIND}} \approx 9.0501$$

Eq 4-9 : Optimal TSR

The relationship between the PMSG electrical frequency and the wind turbines rotational speed is given by the shaft speed and number of poles, Eq 4-10.

$$n_s = \frac{120 f_e}{P}$$
$$\omega_{mech} = \frac{2\pi n_s}{60} = \frac{4\pi f_e}{P} \equiv \frac{\lambda v_{WIND}}{R}$$
$$\therefore \lambda = \frac{4\pi R f_e}{P v_{WIND}}$$

Eq 4-10 : Optimal TSR for frequency and wind speed

So, at the maximum power point for a given wind turbine the relationship between the electrical frequency and wind velocity can be expressed as Eq 4-11

$$f_e = \frac{P \lambda_{MPP} v_{WIND}}{4\pi R}$$

For the Tested Wind Turbine

$$f_e = \frac{22 \times 9.0501 \times v_{WIND}}{4\pi \times 2.45} = 6.46696 v_{WIND}$$

Eq 4-11 : Electrical frequency for a given wind speed at the MPP

Combining Eq 4-8 and Eq 4-11 allows the DC bus voltage to be calculated at any wind speed at the maximum power point.

$$V_{dc,bus} = \frac{3n\sqrt{2}}{\pi}\left(A \frac{P \lambda_{MPP} v_{WIND}}{4\pi R} + B\right)$$

For the Tested Wind Turbine

$$V_{dc,bus} = 26.6545 v_{WIND} + 6.6716$$

Eq 4-12 : DC bus voltage for given wind speed at the MPP

The inverters cut in voltage is 160VDC, which is attained at a wind speed of 5.75m/s. So, the solar array was arranged so that the string VOC occurred slightly above the inverter start voltage of 200V. A string of 12 modules yielded a V_{OC} of 234V and V_{MP} of 168V. Three parallel strings were utilised which created a peak-measured power of 330W. The V_T for the system is set to be 168V at a ν_T of 5.75m/s.

4.3.4. Denmark System Experimental Results

The relative proportions of energy generated from the sources each day from the system are seen in Figure 4-41 and Figure 4-42 for the month of August. On average 60% of the hybrid systems energy is generated from the wind. In the month of August, a total of 76.31kWh was generated, PV generated 25.13kWh and wind produced 64.16kWh, transformer losses from the WT attributed to 12.98kWh, an ideally sized system would not require a step up transformer. The ratio of wind energy generated to solar is 2.55:1 where the rated wind turbine power to peak PV is 15.1:1. An ideal system should aspire to sizing wind to PV power ratings such that the ratio is approximately 5:1 however an analysis should be performed given a generic sites data and the chosen WT. For this location and WT, the PV should be increased to approximately 1kW to achieve this.

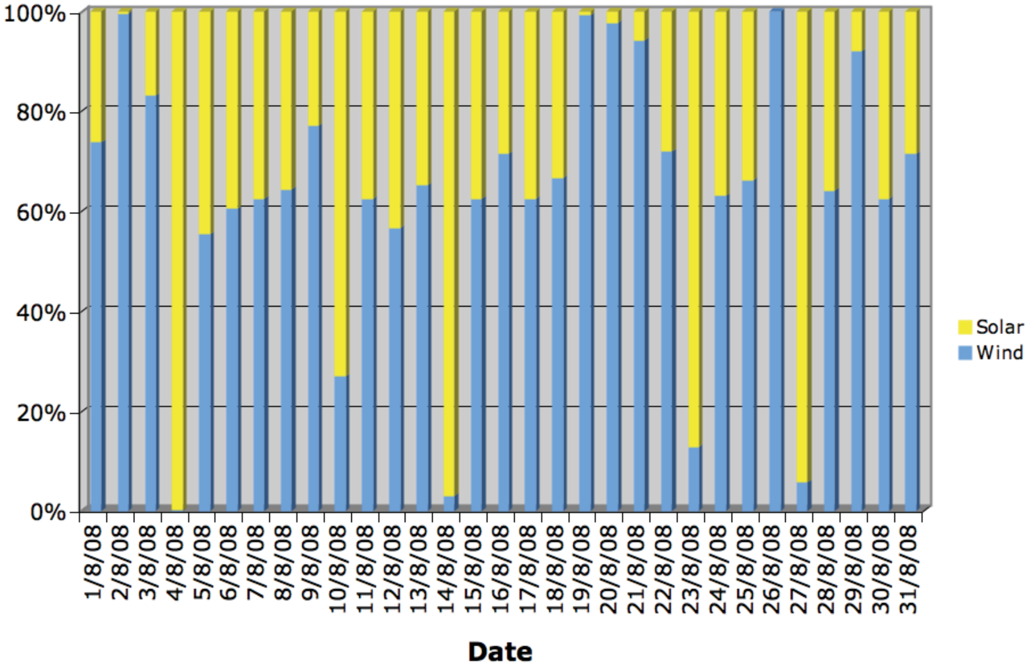

Figure 4-41: August daily energy proportions

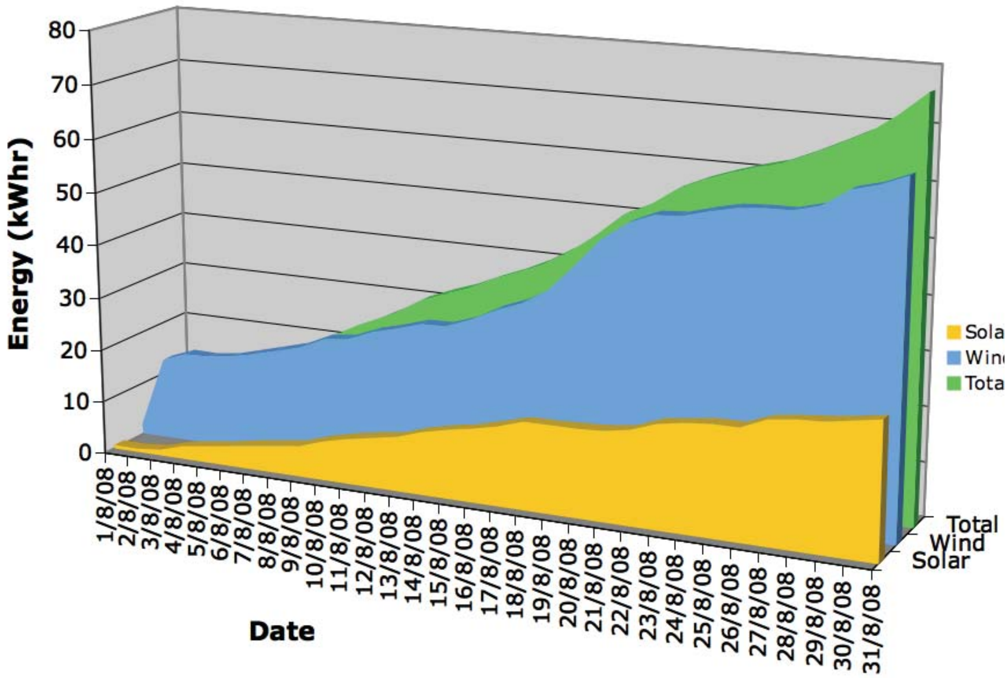

Figure 4-42: August culminative energy yield

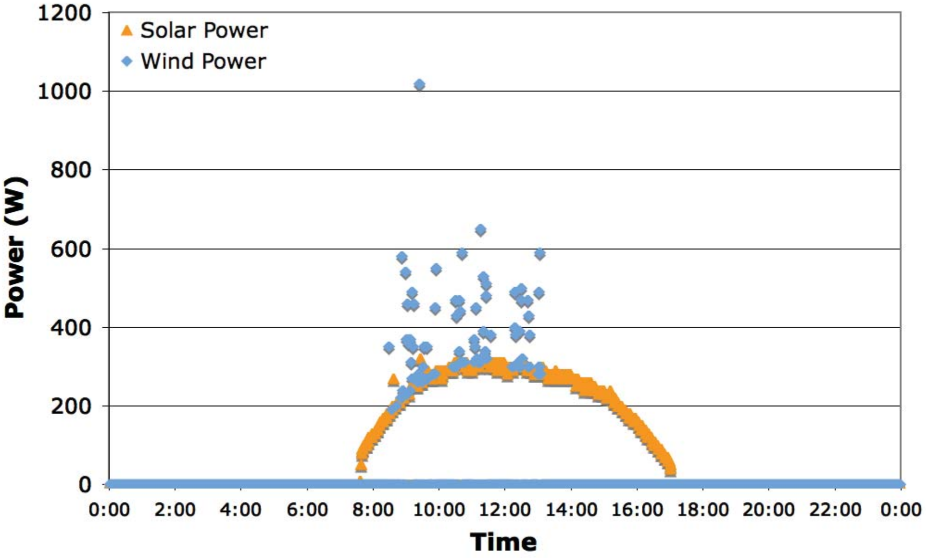

Figure 4-43 : Typically sunny day, 23/08/08

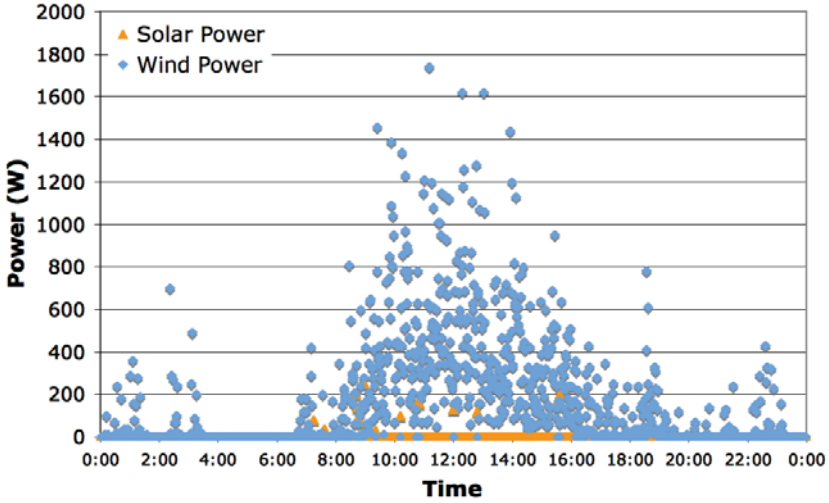

Figure 4-44 : Typically windy day, 19/08/08

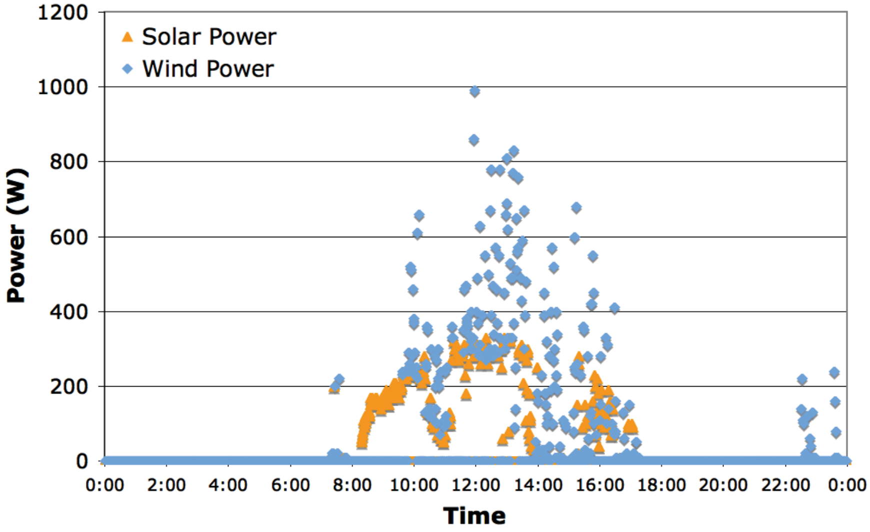

Figure 4-45 : Usual mixed conditions day, 06/08/08

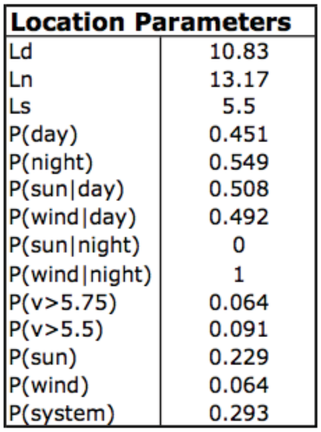

Location Parameters	
Ld	10.83
Ln	13.17
Ls	5.5
P(day)	0.451
P(night)	0.549
P(sun|day)	0.508
P(wind|day)	0.492
P(sun|night)	0
P(wind|night)	1
P(v>5.75)	0.064
P(v>5.5)	0.091
P(sun)	0.229
P(wind)	0.064
P(system)	0.293

Table 4-IV : Denmark Parameters

To ascertain the increase in overall energy generation and the system crossover energy loss for the hybrid system, the following location parameters and probabilities are calculated in Table 4-IV. These values are calculated from the expressions in Eq 4-4. The maximum and average crossover probability losses for the given site, based upon Table 4-IV is given in Figure 4-46 and Figure 4-47. The V_{MP} of the system corresponds to an average probability crossover loss of approximately 8%.

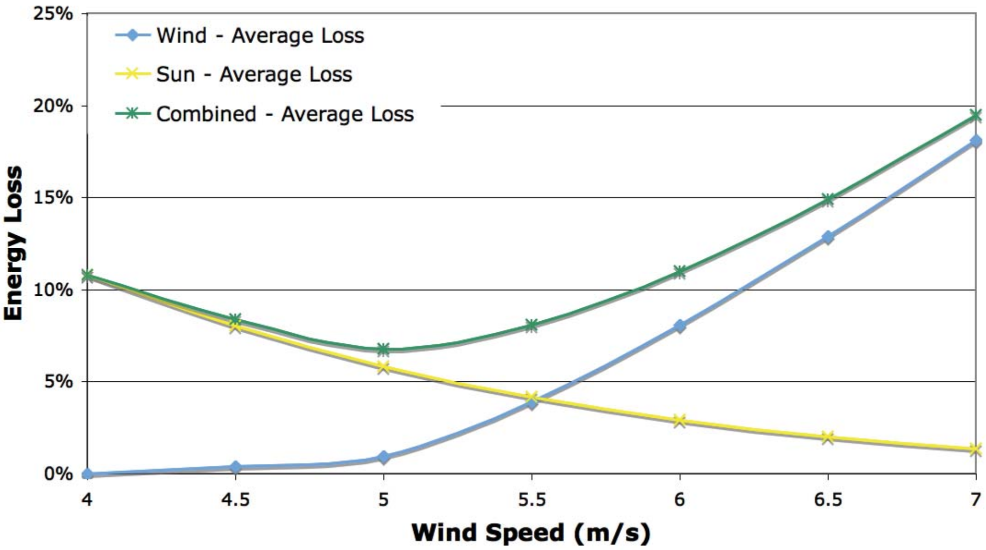

Figure 4-46 : Average crossover loss, L_S = 5.9 hrs

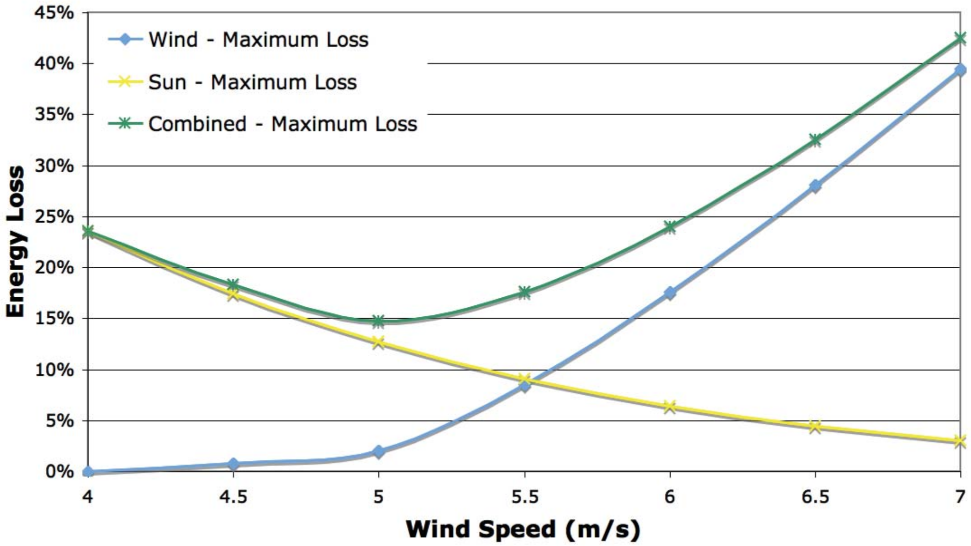

Figure 4-47 : Maximum crossover loss, L_S = 5.9 hrs

The hybrid PV/Wind hybrid system at the test site increases the inverter utilisation to 29.3% from 22.9% or 6.4% respectively for a PV only or wind only system. A comparison of the energy generated by the experimental system with that of the simulation using HOMER was conducted. Table 4-V, quantifies the energy generated with that predicted and defines the crossover energy loss. The energy from the sources was measured on the DC side, this does not take into account any inverter losses.

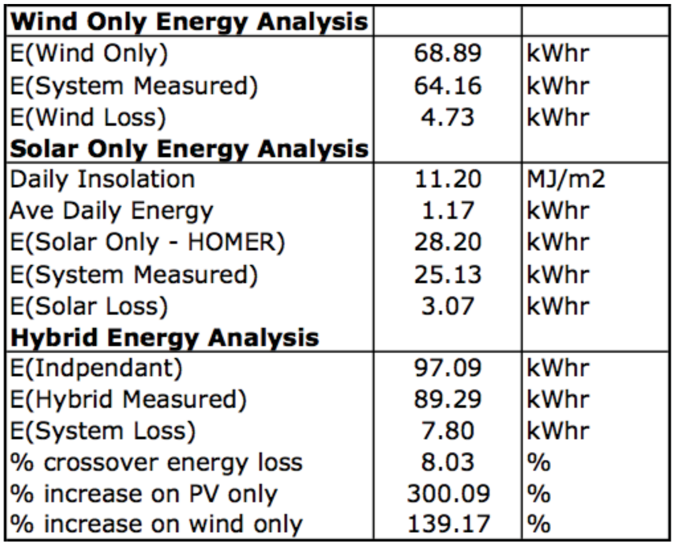

Wind Only Energy Analysis		
E(Wind Only)	68.89	kWhr
E(System Measured)	64.16	kWhr
E(Wind Loss)	4.73	kWhr
Solar Only Energy Analysis		
Daily Insolation	11.20	MJ/m2
Ave Daily Energy	1.17	kWhr
E(Solar Only - HOMER)	28.20	kWhr
E(System Measured)	25.13	kWhr
E(Solar Loss)	3.07	kWhr
Hybrid Energy Analysis		
E(Indpendant)	97.09	kWhr
E(Hybrid Measured)	89.29	kWhr
E(System Loss)	7.80	kWhr
% crossover energy loss	8.03	%
% increase on PV only	300.09	%
% increase on wind only	139.17	%

Table 4-V : Denmark Energy Analysis [2]

The theoretical and experimental results match quite accurately. The installed wind/PV hybrid system increases the energy generation by 300% with respect to a PV only system and 139% with respect to a wind only system. The possible crossover energy loss is only 8.03%, slightly higher than that predicted from Figure 4-46, which can be attributed to degradation of the 20 year old solar array. The test system was not ideal as the PV resources to optimise the system were not available. The theory predicts that the PV array should be increased to approximately 1kW to idealise the system.

4.4. Selecting the ideal type of hybrid system for a given location

The method applied to the Denmark system was used to select the ideal type of hybrid system for various other locations across Australia, as denoted on Figure 4-48. The natural parameters of average daily sun exposure, average daily sun hours and average wind speed vary significantly across the locations. The simulations were carried out on a monthly basis and the results averaged annually.

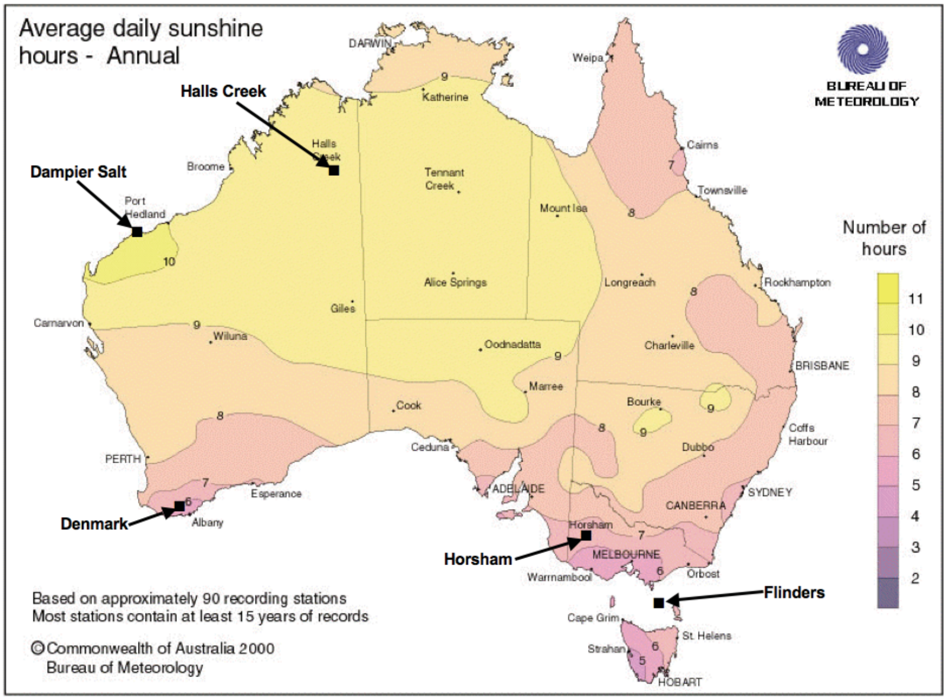

Figure 4-48 : Random design example locations[13]

Location	Average Daily Sun Exposure (MJ/m^2)	Average Daily Sun Hours	Average Wind Speed at 10m (m/s)
Dampier Salt	23.0	10.2	5.67
Denmark	16.0	5.9	3.49
Flinders Island	15.2	6.4	6.34
Halls Creek	22.6	9.4	3.78
Horsham	17.3	6.5	3.48

Table 4-VI : Location parameters

4.4.1. Location: Dampier Salt

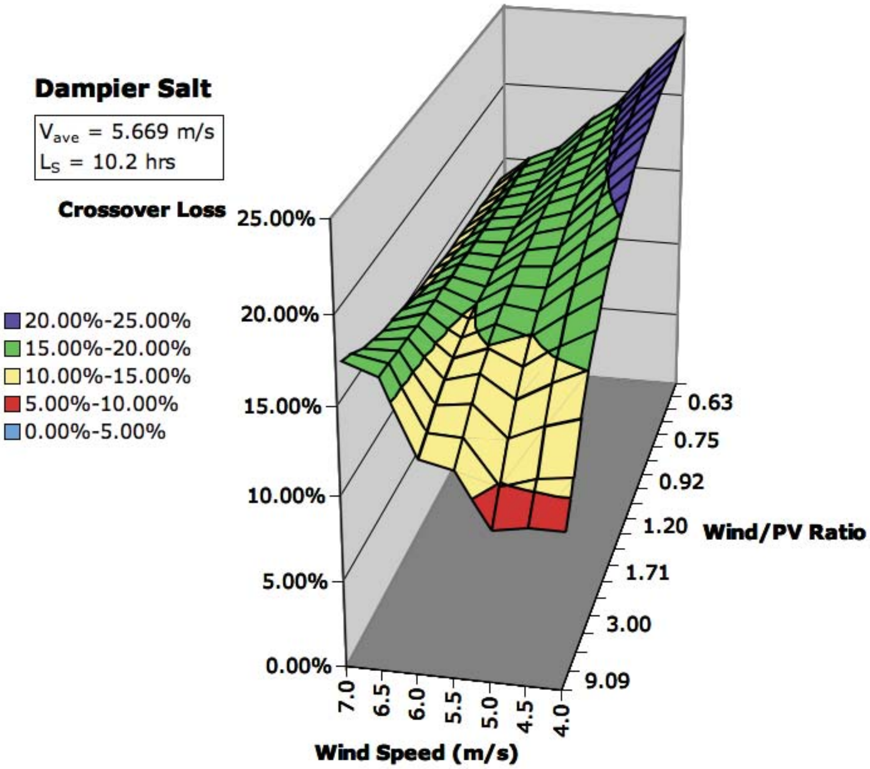

Figure 4-49 : Dampier Salt crossover loss surface

The crossover loss at Dampier Salt is seen to be high across all ratios of generation sources, also no wind speed lines are seen to optimise the design. This disregards the possibility of complimentary type system for this site. The average wind speed is high indicating a potentially strong wind site. The solar exposure and high average sun hours indicating often clear solar conditions, a good solar resource. This evidence leads to Dampier Salt being an ideal location for a hybrid wind/PV system with the conventional topology, as seen in Figure 4-3.

4.4.2. Location: Flinders Island

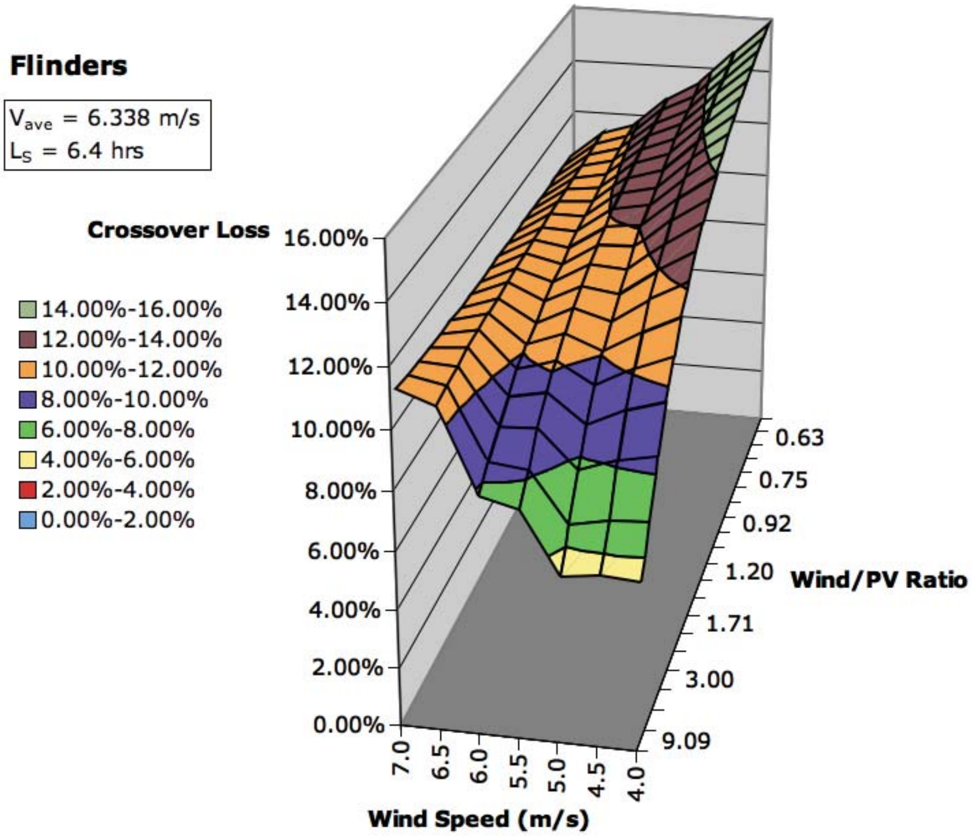

Figure 4-50 : Flinders Island crossover loss surface

The crossover losses for Flinders Island are quite high across all ratios of wind/PV hybrid systems. This ensures that a complimentary type system would not suit this location. The average wind speed is high, the site is also an island so the air turbulence is likely to be quite low, very good for a wind generation site. The average sun hours is quite low, indicating often cloudy conditions. Being the furthest southern location the annual daily solar exposure is also quite low. Consequentially, Flinders Island would be ideal for a wind only based type system as per Figure 4-1.

4.4.3. Location: Halls Creek

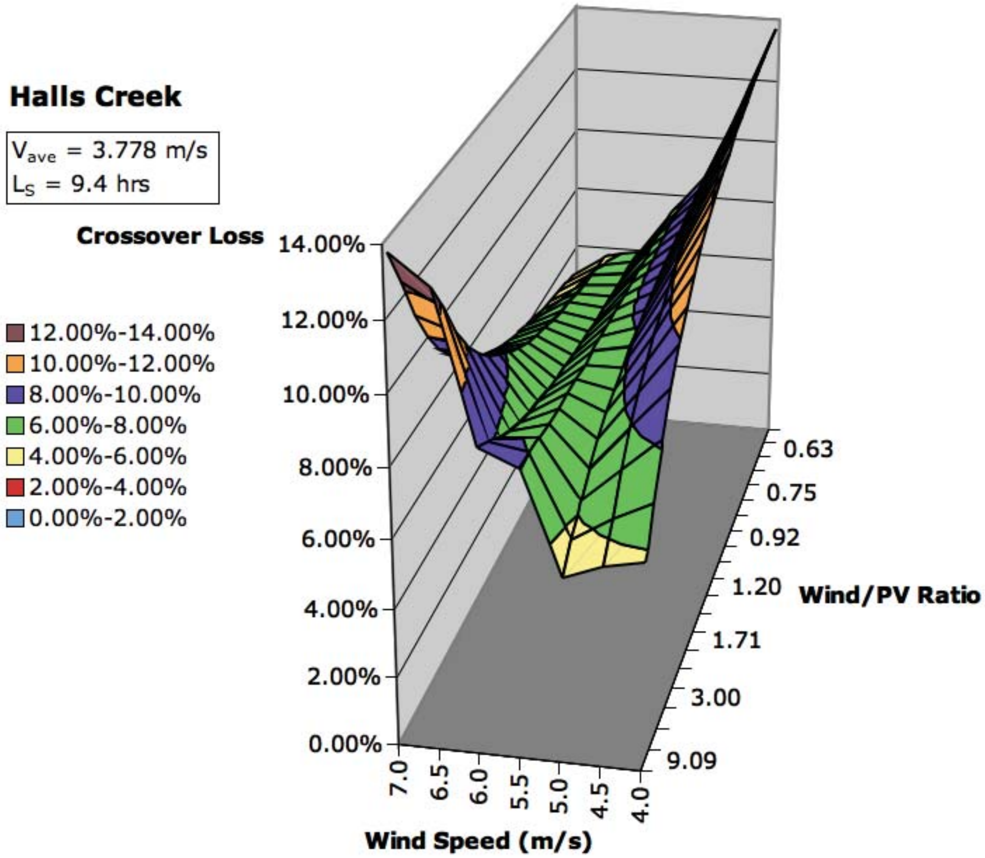

Figure 4-51 : Halls Creek crossover loss surface

The crossover surface at Halls Creek shows medium levels of overall crossover losses for differing ratios of wind to solar generation capacity. Crossover loss minimisation lines can be seen at 5m/s and 6m/s. This indicates an average location for the complimentary type of hybrid system. The solar resource at this location is very strong with a high average daily sun hours. The average wind speed is quite mediocre and the financial expense of the WT would determine its implementation at this location. Overall Halls Creek lends to a PV only system, however a complimentary system with a high PV ratio could also be considered, especially if some natural features enhanced the possible energy production. Features such as hills with low levels of local wind instabilities or the presence of valleys that can funnel air through the site. These types of features are not unusual in this area.

4.4.4. Location: Horsham

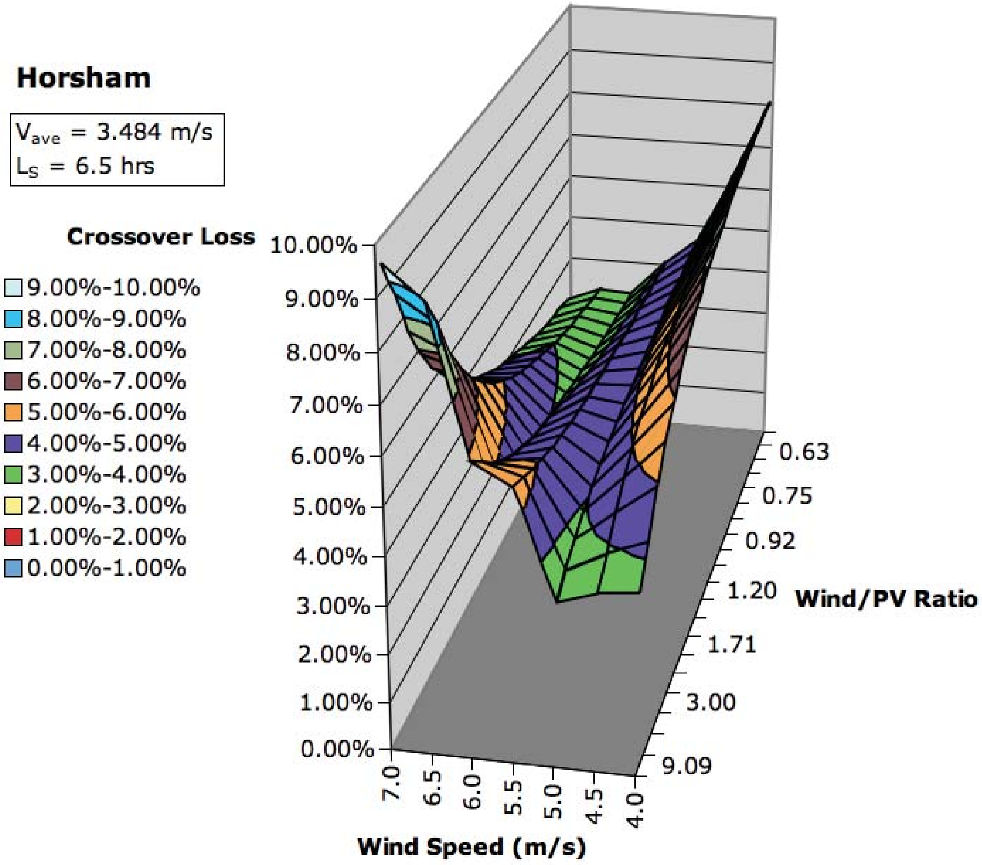

Figure 4-52: Horsham crossover loss surface

From Figure 4-52 a complimentary system can be designed at Horsham to minimise the crossover loss when the transition wind speed is set at approximately 6m/s. The wind/PV ratio of approximately 0.9 would ensure good overall energy production while minimising the losses. The wind and solar resources are quite average at the location which does not favour a wind only or PV only type of system. A complimentary system at Horsham would provide the best overall energy generation and reliability if included into the topology as outlined in Figure 4-4.

4.5. Summary

This chapter presents a method to design the interconnection topology of a renewable hybrid system for any location based upon only the daily solar exposure, average daily sun hours and the sites average wind speed. The software package HOMER was used to calculate the available energy on a monthly basis. This data was analysed to evaluate the systems crossover loss if a complimentary type system was applicable. The development of the crossover surface allows a quick way to determine the ideal type of system from the four possibilities. These four possible systems are PV or wind only systems, conventional and the novel complimentary hybrid system. The application of these systems to the peripheral of the grid allows the utility to simultaneously reduce transmission line losses and reduce the required grid reliability from approximately 99.99% to something around 98%. Remote grid customers can take responsibility of their own energy production while ensuring a more reliable system for their household and yielding some income from a feed in tariff. This approach can assist in reducing the net carbon emissions from electricity generation. The only drawback to this incentive is the upfront financial cost, which would be carried by both the client and the utility.

A summary of this chapters key section is below

- Hybrid system interconnection topologies
    - Grid connected systems
    - Stand alone systems
    - Edge of grid systems
- Hybrid complementary design and analysis
    - Principles of the complementary system
    - Mathematical modelling of the complementary system
    - Power electronic simulation of the complementary system
    - HOMER analysis of the complementary system
- Denmark project overview
    - Denmark experimental system design results
    - Denmark experimental results and analysis
- Application of the complementary system to other locations

4.6. References

1. James W. Darbyshire , C.V.N., *A Wind and Solar Hybrid System Utilising a Single Grid Connected Inverter* IEEE TRANSACTIONS ON ENERGY CONVERSIONS, 2009. **(under revision)**.
2. James W. Darbyshire, C.V.N., *Hybrid wind/solar energy systems for peripheral grid connected areas* Renewable Energy Journal, 2009. **(under revision)**.
3. Hongxing Yang, Z.W., Lou Chengzhi, *Optimal design and techno-economic analysis of a hybrid solar–wind power generation system.* Applied Energy, February 2009. **86**(2): p. 163-169.
4. Markvart, T., *Sizing of hybrid photovoltaic-wind energy systems.* Solar Energy, October 1996. **57**(4): p. 277-281.
5. S. Diaf, G.N., M. Belhamel, M. Haddadi, A. Louche, *Design and techno-economical optimization for hybrid PV/wind system under various meteorological conditions.* Applied Energy, October 2008. **85**(10): p. 968-987.
6. Bower, W., S. Phillips, and F. Schallcs. *Performance and Characteristics of Inverters in Remote and Stand-Alone Applications*. in *IEEE Photovoltaic Specialists Conference*. 1988.
7. Nchrir, M.H., et al., *An Approach to Evaluate The General Performance of Stand-Alone Wind/Photovoltaic Generating Systems.* IEEE Transactions on Energy conversion, 2000.
8. Webclim, *Average daily solar exposure - Annual*, in *Bureau of Meteorology*. 2000, Climate Information Services, National Climate Centre: Melbourne.
9. Glarner, H., *Length of Day and Twilight (Formulas)*, in *Herbert Glarner Articles*. 2008: Switzerland.
10. *PSIM Version 7.0*. 2006, Powersim Inc. (www.powersimtech.com): Woburn, MA.
11. SunPower, *SPR-210-WHT: High Efficiency PV Module*, in *Document: 001-03296*. May 2007, SunPower Corporation: California.
12. Lambert, T., *HOMER: the micro-power optimisation model*. 2008, NREL.
13. Webclim, *Average daily sunshine hours - Annual*, in *Bureau of Meteorology*. 2000, Climate Information Services, National Climate Centre: Melbourne.

“Every reasonable effort has been made to acknowledge the owners of copyright material. I would be pleased to hear from any copyright owner who has been omitted or incorrectly acknowledged.”

5. Wind Turbine Selection Methods

In order to select the most appropriate wind turbine for a given location a balance between, energy generation, capital cost, wind turbine technology and environmental concerns must be considered. This chapter analyses the first three of these four conditions that are relevant for this research. A central issue when designing a wind farm is which is the most suitable WT for the given location. The author develops two new methods, economic feasibility and conversion efficiency to complement capacity factor as methods to assist in this selection.

Locating a wind farm requires a wind speed profile to be developed for the proposed area. Free wind data is available from BoM and NASA satellites through the Internet [1, 2]. A correlation analysis of this data is presented with the goal of determining which is the most reliable data to use for site location. An economic tool, a box a whiskers plot is utilised and presents a novel method to interpret this data.

Once an ideal wind farm location has been ascertained the size and type of wind turbines must be selected. This requires an accurate power curve of the possible WTs to be implemented. A simple but accurate method to digitalise a WTs power curve is presented through the use of some free third party software.

Three methods to allow direct cross correlation of differing WTs at the same site are proposed. The first method capacity factor analysis is presented in its traditional form. A problem with this method is low wind speed WTs always achieve a greater CF when compared to traditional machines. To alleviate this issue two new methods of WT analysis are presented. Conversion efficiency analysis takes the cross sectional area of the WT, this mitigates the effect of over sizing the blades for the generator. Finally economic efficiency is presented as a method to calculate the annual payoff cost of energy generated by the WT.

5.1. Accessibility to wind data

Over the past three years the author has routinely searched for reliable sources of wind speed data. Two types of data are readily available to the public, these are ground level surface data from local government departments and satellite data from the NASA weather satellite. The Bureau of Meteorology in Australia provides wind data and a direction at a height of 10 metres for most locations across Australia and its territories [1]. Some other agricultural government departments also record data at varying heights across Australia. The reliability of this ground based data is generally +/- 3% at the specified height and is usually recorded using cup type anemometers.

Figure 5-1 : Synchrotac 706 Series cup type anemometer [3]

NASA weather based satellite data is readily accessible through the internet [2]. This data is available for any integer value of latitude and longitude co-ordinate across the Earth. The method used to measure the wind speed via a satellite is through the use of a radar based scatterometer. This device sends a microwave based pulse and receives the reflected energy. By combining the sigma-0 measurements from Bragg scattering over a few azimuth angles the wind speed and direction can be estimated [4]. This data is usually calculated and averaged for a height of 50 metres, however its accuracy is given as +/- 15%., a summary of this across the Earth is shown in Figure 5-3.

Google Earth is also readily used to ascertain the distance between a WT site and the location of data recording. Figure 5-2 shows the distance between the BoM monitoring site and the Denmark project location at Roy's Farm.

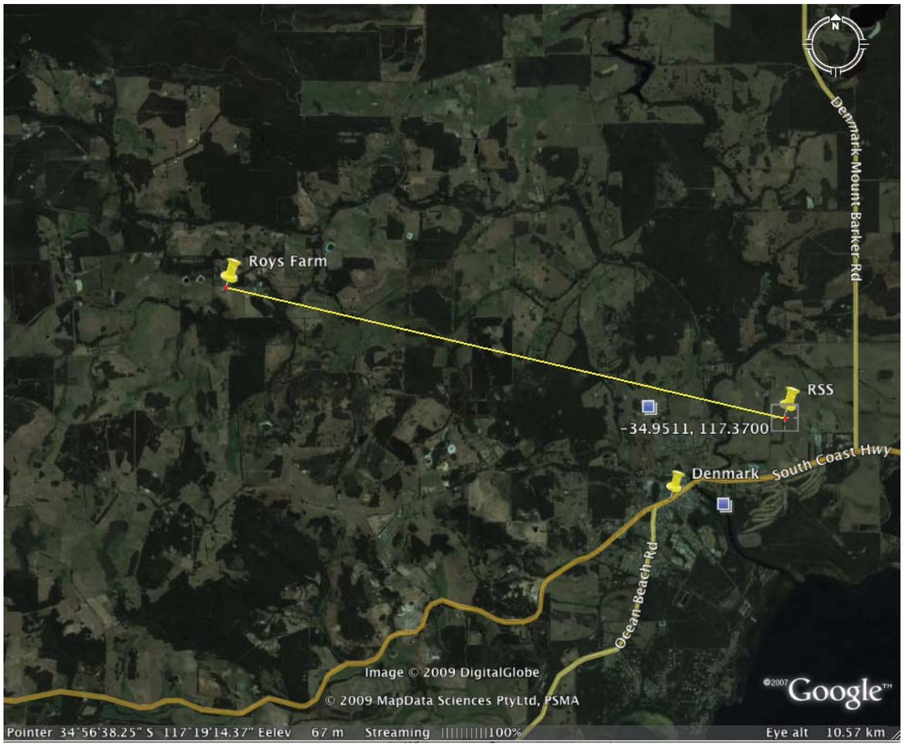

Figure 5-2 : Google Earth screenshot

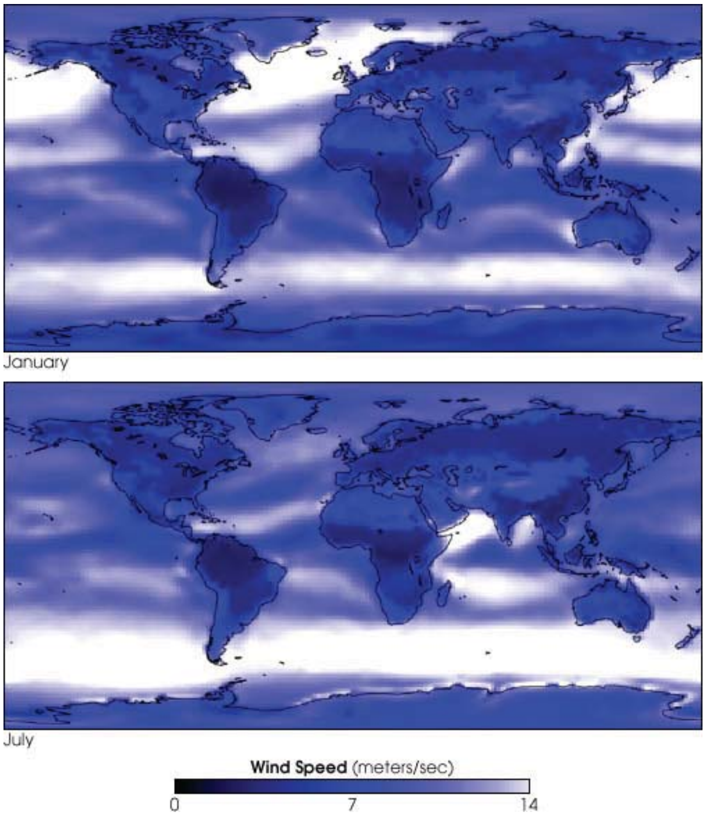

Figure 5-3 : Earth average wind speed at 50m from satellite data [2]

5.2. Reliability of Wind Data Sources

In order to obtain a measure of the usefulness and accuracy of the wind data two sets of wind data are collected and compared for a single site. The raw data is collected from the Bureau of Meteorology and the NASA satellite data. BoM data is recorded twice a day at 10 metres, NASA data is recorded intermittently at an average height of 50 metres.

Albany	**Raw Data @10m**			**Satellite Data @50m**
	9am	3pm	**Mean**	**Mean**
Month	m/s	m/s	m/s	m/s
Jan	3.694	5.750	4.722	7.390
Feb	3.500	5.722	4.611	7.730
Mar	3.389	5.250	4.319	7.280
Apr	3.111	4.361	3.736	6.670
May	3.667	4.194	3.931	6.890
Jun	3.722	4.056	3.889	7.130
Jul	4.139	4.750	4.444	7.300
Aug	4.250	5.056	4.653	7.840
Sep	4.333	5.500	4.917	7.070
Oct	4.250	5.750	5.000	7.110
Nov	4.028	5.972	5.000	7.400
Dec	3.861	5.806	4.833	7.580
		Mean	**4.505**	**7.283**

Table 5-I : Albany Raw Wind Speed Data

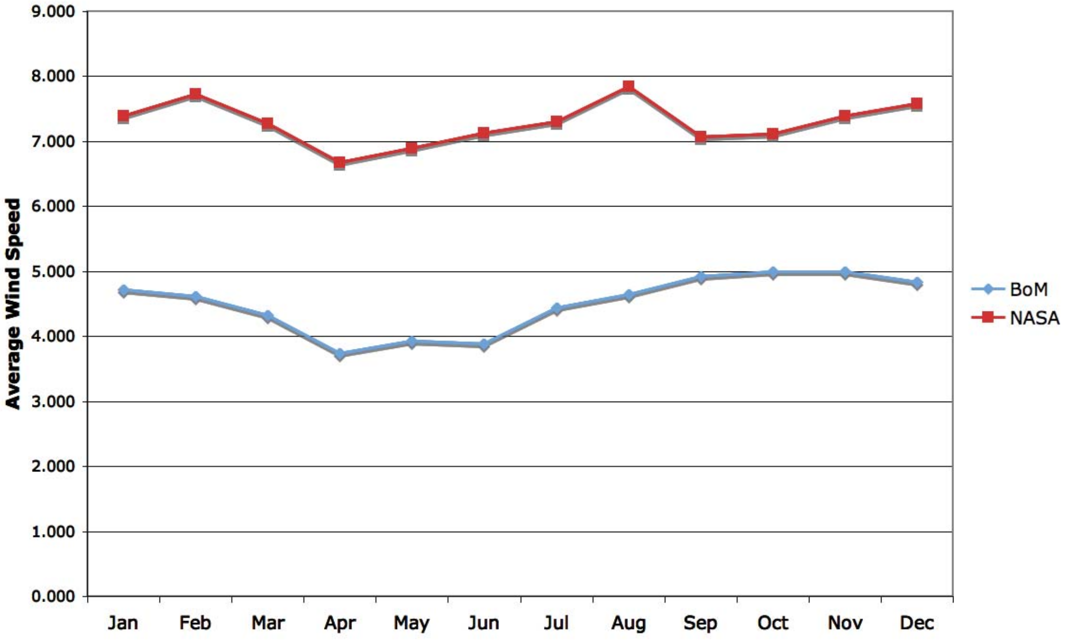

Figure 5-4 : Raw Albany Wind Data

As we have two measured points of data for the same location we can directly solve for the roughness parameters α and z for the North American and European methods respectively using the expressions below.

$$\alpha = \frac{\log\left(\frac{v}{v_o}\right)}{\log\left(\frac{H}{H_o}\right)}$$

Eq 5-1 : North American frictional parameter expression

$$z = \exp\left[\frac{v_o \ln(H) - v\ln(H_o)}{v_o - v}\right]$$

Eq 5-2 : European roughness co-efficient expression

Solving for the frictional and roughness parameters directly based upon the mean yields the following monthly average wind speeds and scaling co-efficient, Table 5-II.

Albany	**Scaled down to @10m**		**Scaled up to @50m**	
	US method	EU method	US method	EU method
alpha/z	0.298	0.735	0.298	0.735
Jan	4.571	4.571	7.634	7.634
Feb	4.781	4.781	7.455	7.455
Mar	4.503	4.503	6.983	6.983
Apr	4.126	4.126	6.040	6.040
May	4.262	4.262	6.354	6.354
Jun	4.410	4.410	6.287	6.287
Jul	4.515	4.515	7.185	7.185
Aug	4.849	4.849	7.522	7.522
Sep	4.373	4.373	7.949	7.949
Oct	4.398	4.398	8.083	8.083
Nov	4.577	4.577	8.083	8.083
Dec	4.689	4.689	7.814	7.814
Mean	4.505	4.505	7.283	7.283

Table 5-II : Scaled wind speeds using solved scaling parameters

In most cases the wind scaling parameters are predicted using approximate values based upon the tables in chapter two. This assumption is made based upon the local terrain and the likely difference in wind speed at the two heights. A logical prediction based upon readily available site information for the two sites using Google Earth was made, Table 5-II. Albany lies on the south coast where the local environment is low lying scrub and a few undulating hills.

	Predicted	Actual
US method	0.18	0.298
EU method	0.05	0.735

Table 5-III : Realistic assessment of change of height parameters

Table 5-III shows that the US method appears to be more accurate when directly comparing the 10m BoM data and NASA satellite data. However usually the mounting height of a wind turbine is not the same as the height of the measured data. Both sets of data were scaled to a standard mounting height of 18m, using a predicted representation of the scaling variables for the North American and European methods, Table 5-IV.

Albany	**Scaled to @18m** **BoM - US method**		**Bom - EU method**		**NASA - US method**		**NASA - EU method**	
	Predicted	Actual	Predicted	Actual	Predicted	Actual	Predicted	Actual
alpha/z	0.180	0.298	0.050	0.735	0.180	0.298	0.050	0.735
Jan	5.249	5.626	5.246	5.786	6.149	5.450	6.297	5.601
Feb	5.126	5.494	5.123	5.650	6.432	5.701	6.587	5.858
Mar	4.802	5.146	4.799	5.292	6.057	5.369	6.203	5.517
Apr	4.153	4.451	4.151	4.578	5.550	4.919	5.684	5.055
May	4.369	4.683	4.367	4.816	5.733	5.082	5.871	5.222
Jun	4.323	4.633	4.320	4.765	5.932	5.259	6.075	5.404
Jul	4.940	5.295	4.938	5.445	6.074	5.384	6.220	5.532
Aug	5.172	5.543	5.169	5.701	6.523	5.782	6.680	5.942
Sep	5.465	5.858	5.462	6.024	5.882	5.214	6.024	5.358
Oct	5.558	5.957	5.555	6.126	5.916	5.244	6.058	5.388
Nov	5.558	5.957	5.555	6.126	6.157	5.458	6.306	5.608
Dec	5.373	5.759	5.370	5.922	6.307	5.590	6.459	5.745
Mean	5.007	5.367	5.004	5.519	6.059	5.371	6.205	5.519

Table 5-IV : Albany scaled data using predicted and actual parameters

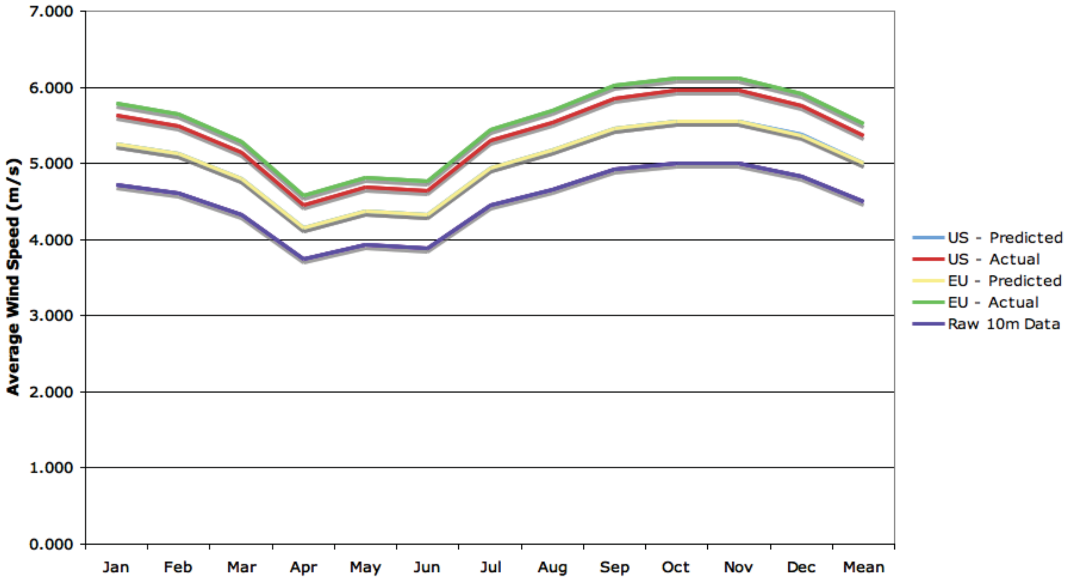

Figure 5-5 : BoM data scaled to 18m

The range of scaled wind speed data for the US method from Figure 5-5 is 0.360m/s or +/-3.467% of the mean. The range of scaled wind speed data for the EU method from Figure 5-5 is 0.515m/s or +/-4.892% of the mean. The initial measurement error is +/-3% and the combination of these errors is represented in Figure 5-7.

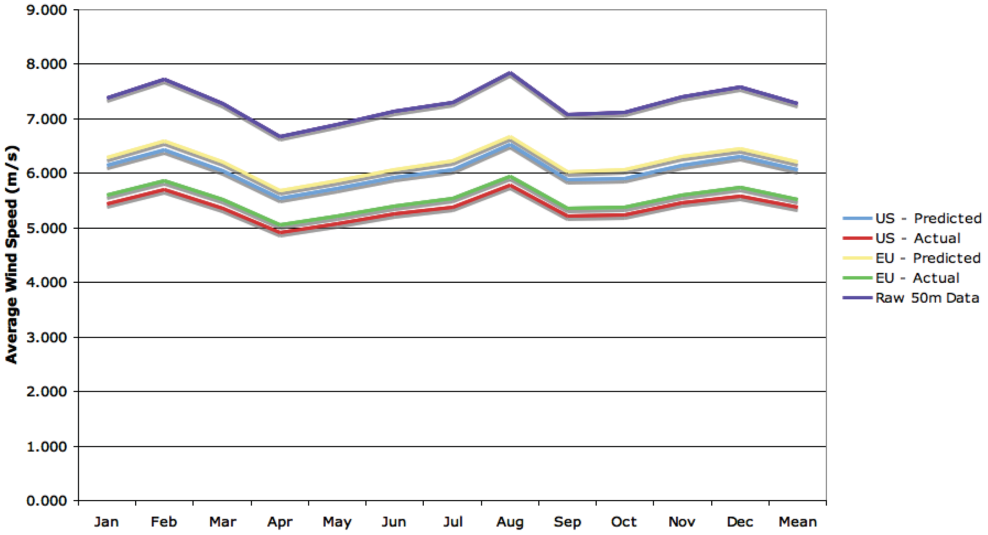

Figure 5-6 : Satellite data scaled to 18m

The range of scaled wind speed data for the US method from Figure 5-6 is 0.688m/s or +/-6.020% of the mean. The range of scaled wind speed data for the EU method from Figure 5-6 is 0.686m/s or +/-5.853% of the mean. The initial measurement error is +/-15% and the combination of these errors is represented in Figure 5-7.

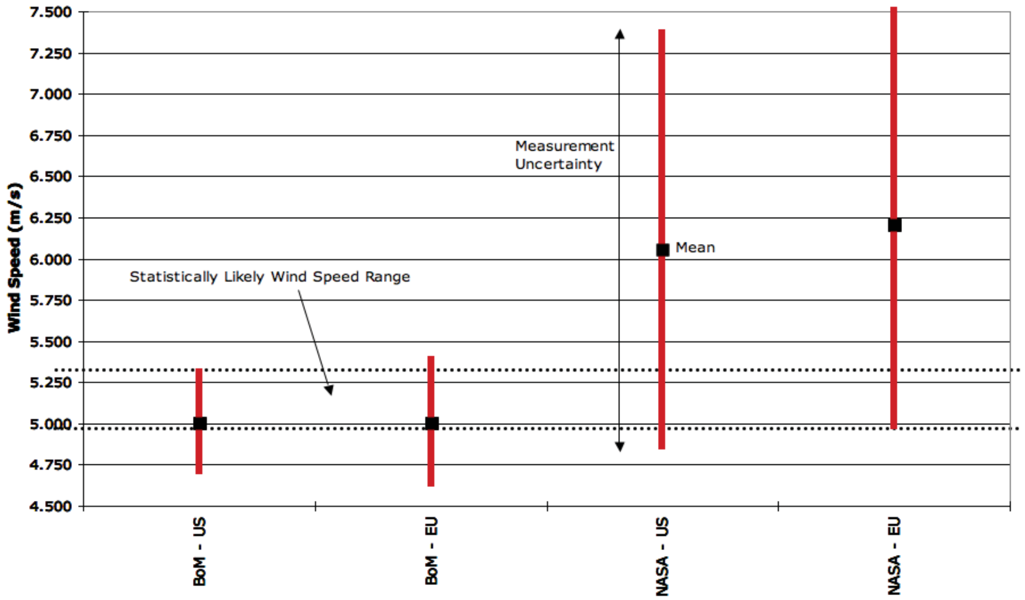

Figure 5-7 : Box and whiskers plots for scaled wind speed at 18m

The box and whiskers plot in Figure 5-7 diagrammatically shows the overlay of the ranges using two different sources of data, BoM and satellite while implementing both commonly used wind scaling methods. A region exists where all methods can be seen to crossover and this represents the most likely average wind speed for the location. The range of the satellite data can be contributed to both the inaccuracy in measurement and required scaling distance, from 50m to 18. If only satellite data is available the results show that large errors are possible when scaling the wind speed that can create very significant errors in predicting the overall yearly energy generation. A full error analysis should be performed and the energy prediction calculation based upon the lower tail wind speed, below the mean.

For most locations some form of official government weather data measured at 10m is available. This data represents the most reliable form of generally available data. Figure 5-7 shows strong correlation between both methods of height scaling with a similar range of possible error. The overall analysis shows that the scaling methods from 10m up to 18m are reliable, however all scaling methods become less reliable based upon the change in height.

5.3. Interpolating Wind Turbine Power Curves

In predicting the annual energy generation of a wind turbine, an accurate representation of its power curve is required before the detailed analysis can be conducted. Throughout this research the author has implemented many methods for creating a table of values from digital images of power curves. Initially simply measuring the data directly from the printed plot, however this becomes a very cumbersome and fairly inaccurate method. Eventually software package called Graph Digitizer [5] was discovered and with help of Microsoft Excel has been successful in recreating complicated power curves.

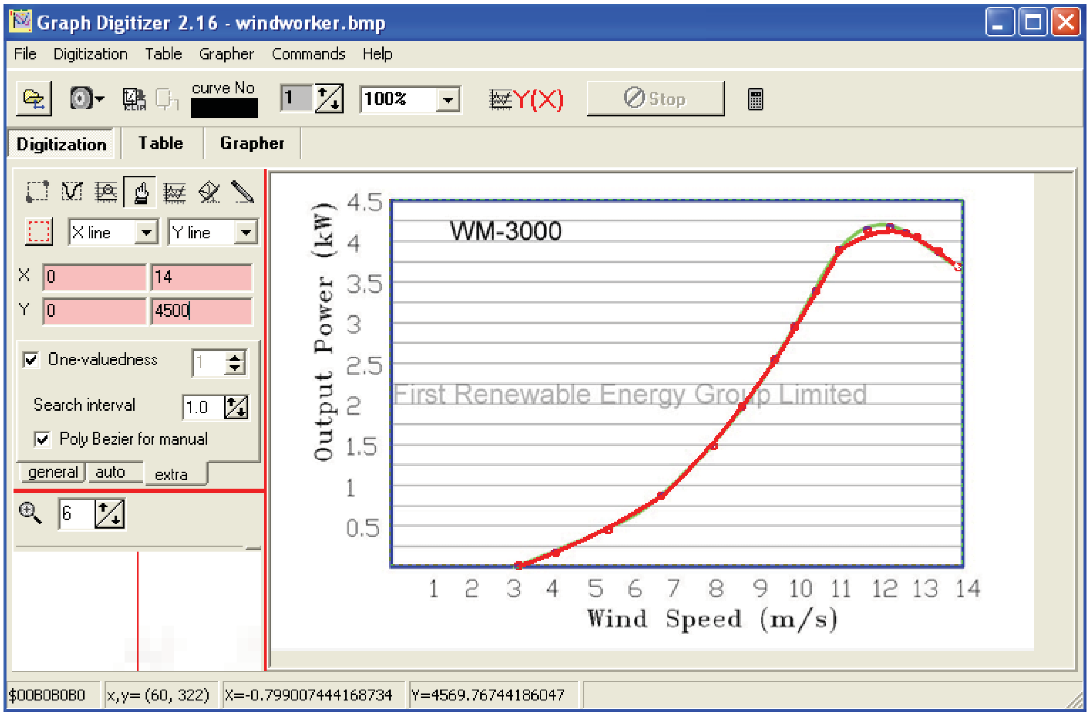

curve No 1

100%

X line

Y line

X 0 14

Y 0 4500

☑ One-valuedness 1

Search interval 1.0

☑ Poly Bezier for manual

6

$00B0B0B0 x,y= (60, 322) X=-0.799007444168734 Y=4569.76744186047

Figure 5-8 : Screenshot of Graph Digitizer

The scaling of the axis allows an accurate representation of the curve in tabulated form. However the increments of the data are based upon the resolution of pixels of the image. This is accurate for redrawing the curve. However to perform energy analysis calculation generally the power at a certain exact wind speed is required. This can be done in excel from the tabulated data by using the LOOKUP function from small incremental data.

5.4. Numerical Methods to Analyse Wind Distributions

In order to calculate the expected energy generated for any wind turbine at any location a dynamic model of the wind must be developed. The two parameters to generate the wind probability distribution are the average and variance of the wind speed. The Rayleigh distribution is a commonly used probability distribution, which makes an assumption on the spread of the wind speed data and is independent of the variance of the data. A more accurate distribution of the wind speed data can be made using a Weibull distribution of the data. However, the Weibull distribution requires the variance of the data to be known, this is generally not published but can be easily calculated from raw wind speed data such as that from the Bureau of Meteorology.

$$f(v) = \frac{2v}{c^2}\exp\left[-\left(\frac{v}{c}\right)^2\right]$$

Eq 5-3 : Rayleigh Probability Distribution Function

$$f(v) = \frac{k}{c}\left(\frac{v}{c}\right)^{k-1}\exp\left[-\left(\frac{v}{c}\right)^k\right]$$

Eq 5-4 : Weibull Probability Distribution Function

The Rayleigh distribution has a direct relationship between the average wind speed and the c parameter, given in Eq 5-5.

$$\bar{v} = \frac{\sqrt{\pi}}{2}c$$

Eq 5-5 : Average Value Expression

An accurate fit of the data to a Weibull distribution requires both the average and statistical variance of the data [6, 7]. The shape, k parameter, can be determined directly from the variance and mean of the height scaled data by Eq 5-6.

$$k = \left(\frac{\sigma}{\bar{v}}\right)^{-1.086}$$

Eq 5-6 : Calculation of k Parameter

The scale parameter, c, can be determined from the shape parameter and use of the gamma function as seen in Eq 5-7.

$$c = \frac{\bar{v}}{\Gamma\left(1 + \frac{1}{k}\right)}$$

Eq 5-7 : Calculation of the c Parameter

Utilising a spreadsheet, a numerical analysis can be carried out to determine the probability that the wind speed will be between two certain values. The author has used bin widths of 0.5m/s so the integral is evaluated between x+0.25 and x-0.25 for the power value estimated at x. The Rayleigh distribution is evaluated through Eq 5-8. The Weibull distribution can be directly evaluated by calculating the integral at the bin width limits and subtracting the interval area through Eq 5-9.

$$P(x - 0.25 < x < x + 0.25) = \frac{\pi}{4}\left(\frac{x}{\bar{v}^2}\right)\exp\left(\frac{-\pi}{4}\left(\frac{x}{\bar{v}}\right)^2\right)$$

Eq 5-8 : Rayleigh Numerical Evaluation

$$P(x - 0.25 < x < x + 0.25) = \int_0^{x+0.25} \frac{k}{c}\left(\frac{x}{c}\right)^{k-1} \exp\left[-\left(\frac{x}{c}\right)^k\right] dx - \int_0^{x-0.25} \frac{k}{c}\left(\frac{x}{c}\right)^{k-1} \exp\left[-\left(\frac{x}{c}\right)^k\right] dx$$

Eq 5-9 : Weibull Numerical Evaluation

This can be evaluated in excel using the following expression:

=WEIBULL(x+0.25,k,c,TRUE)-WEIBULL(x-0.25,k,c,TRUE)

These numerical methods were used on the twice-daily sampled data from the Bureau of Meteorology. This data was scaled from the measured 10m to 18m and then the average and variance was calculated. Using Eq 5-5, Eq 5-6 and Eq 5-7 the Rayleigh and Weibull probability distribution parameters were calculated, as seen in Table 5-V.

Site Data	**Denmark BoM data**		
Mean Wind Speed	Vo	4.4416	m/s
Variance		12.8828	
Height of measurement	Ho	10	m
Turbine Hub Height	H	18	m
Surface Roughness	a	0.14	
Scaled Mean Wind Speed	V	4.8226	m/s
Shape Parameter	k	1.3782	
Scale Parameter	c	5.2779	

Table 5-V : Denmark scaled BoM data

Using the values from Table 5-V and expressions Eq 5-8, Eq 5-9 the data was tabulated. The graphical representation is seen in Figure 5-9. The Rayleigh approximation is shown to unrealistically produce a higher spread of wind probabilities based upon the same data. An energy analysis for this data based upon only a Rayleigh distribution would produce a higher average energy generation for the site. A system designed by this method would not produce enough energy to cover the loads, which would lead to the batteries in the system having an average state of charge lower then the expected, leading to a decrease in battery longevity. Where accurate wind data is available and the data sets variance is known the Weibull distribution creates a more accurate energy analysis.

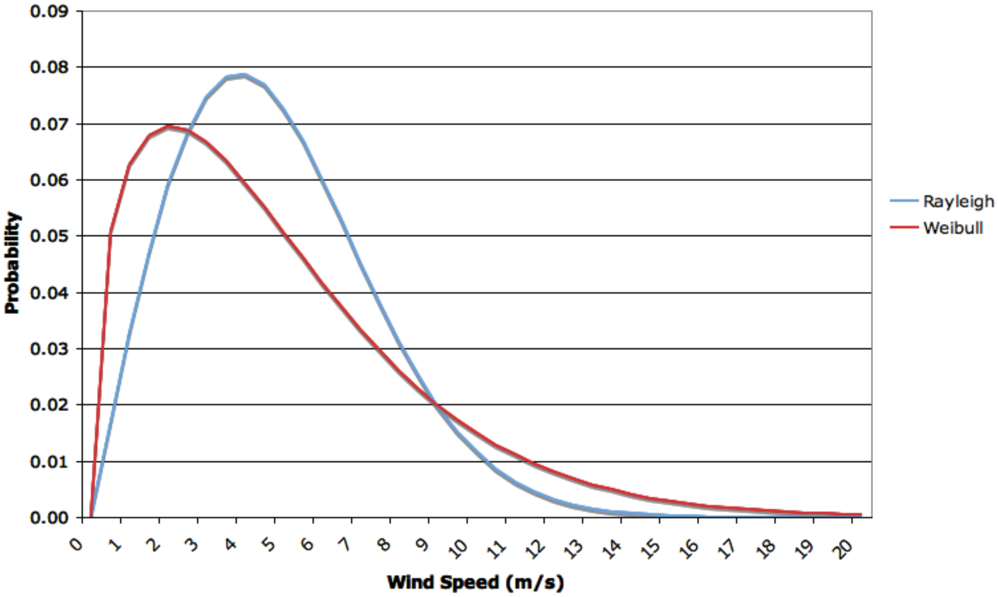

Figure 5-9 : Rayleigh and Weibull distributions based upon the same data

5.5. Methods to Predict the Best Wind Turbine for a Location

Throughout the research required for this dissertation the author has continually experienced confusion with respect to the differing marketing methods used to promote various small wind turbines. This section presents three methods that can be used to verify differing wind turbines based upon reliable data sheet and pricing information. These methods are capacity factor, economic feasibility and conversion efficiency. Capacity Factor is the same definition, which can be found in many textbooks and is readily used in the industry[8], however the method is standardised so that the reference wind speed is the same across differing models, this is set at 10m/s. Economic Feasibility is a direct measure of the cost of the wind turbine with respect to predicted annual energy generation. Conversion Efficiency is the ratio of annual energy generated with respect to wind swept area of the WT.

It should be noted that this section promotes methods that may be used to allow cross comparison of various differing WT's in the market. It is not an exhaustive study and should not be used to give any market advantage to any particular wind turbine.

The design and manufacturing process to engineer the blade of a wind turbine changes the lift and drag characteristics, which ensure that no two companies wind turbine exhibit an identical power curve. The small variations in the power curves create a large difference in annual energy generation. The power curves of 10 common small wind turbines were mapped and are displayed in Figure 5-10. The brands selected provide a comparison of the different types of small wind turbines available in the market. The two Westwind[9] machines are manufactured in Ireland from Australian Technology. The Skystream[10] and Whisper[11] are manufactured in Flagstaff, USA by South West Wind Power. The Swift[12] WT is manufactured in the UK and is specially designed for mounting in urban environments for low noise requirements. The Kestrel[13] is a South African designed and constructed WT and the Windworker a low cost Chinese WT.

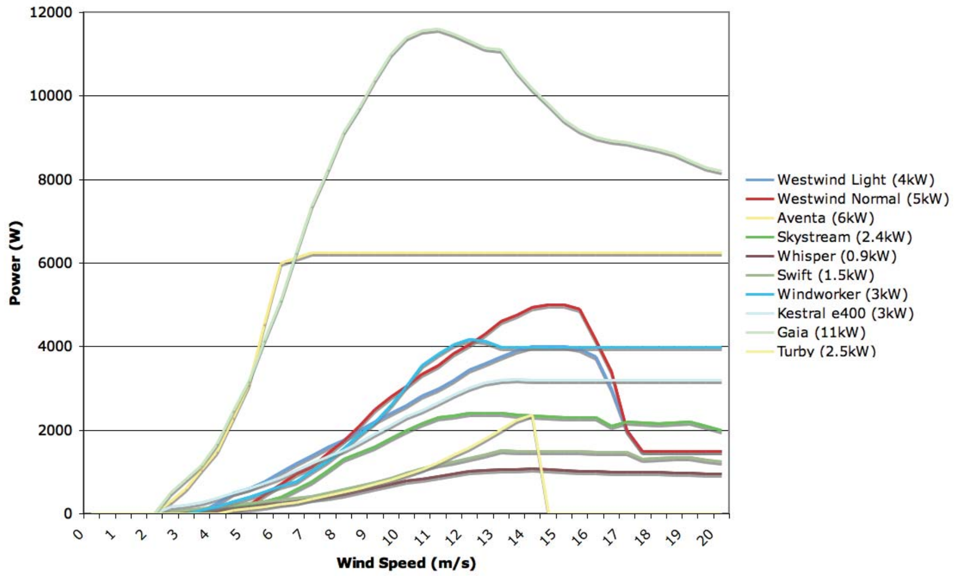

Figure 5-10 : Different Wind Turbine Power Curves

All wind turbines shown are of the horizontal axis variety except the Turby[14], which is a vertical axis type. The Gaia[15] and Aventa[16] wind turbines are of the low wind speed category. The blades are large compared to the generator allowing the machine to generate greater energy at lower wind speeds. Using the site data in Table 5-V and the Weibull model the expected energy output can be generated for different bin wind speeds for the selection of wind turbines, seen in Figure 5-11 and Figure 5-12. The annual energy generated by each wind turbine is the area under each curve. WT's with a larger wind swept area tend to have their peak energy wind speed at lower values then other WT's, which is to be expected.

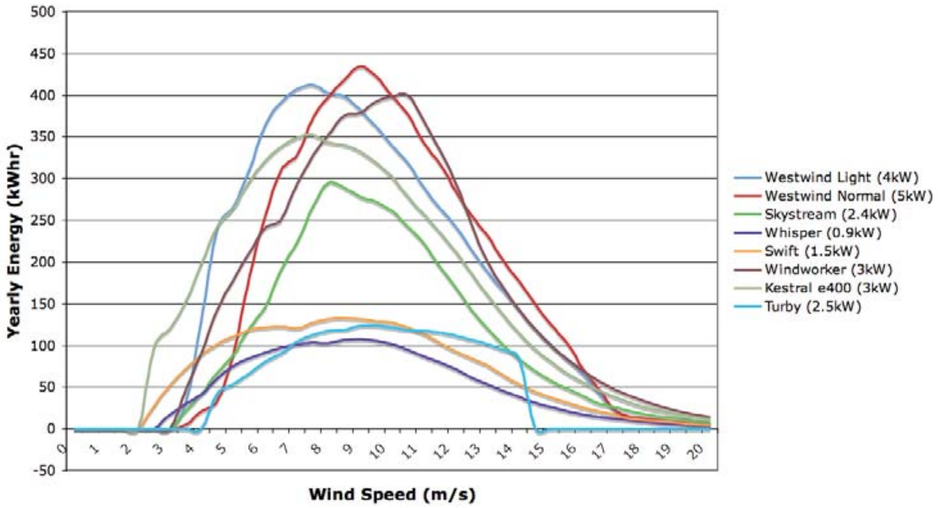

Figure 5-11 : Expected Energy Generation Profile for Selected Wind Turbines

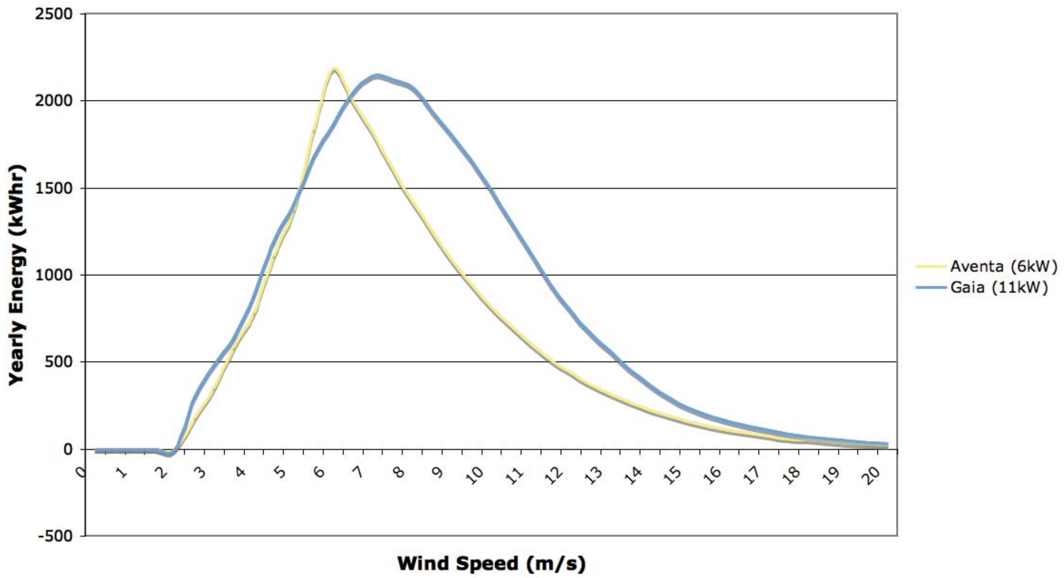

Figure 5-12 : Expected Energy Generation Profile for Selected Low Speed Wind Turbines

Wind Turbine	Type	Speed	Rated Power (kW)	Power@10m/s (kW)	# Blades	Blade Length (m)	Wind Swept Area (m*m)	Cost ($AUD)
Westwind Light	HAWT	Normal	4.00	2.60	3	2.55	20.43	N/A
Westwind Normal	HAWT	Normal	5.00	3.05	3	2.55	20.43	N/A
Aventa	HAWT	Low	6.00	6.25	3	6.45	130.70	N/A
Skystream	HAWT	Normal	2.40	2.00	3	1.86	10.87	$7,100
Whisper	HAWT	Normal	0.90	0.78	3	1.05	3.46	$2,370
Swift	HAWT	Normal	1.50	0.98	5	1	3.14	$4,950
Windworker	HAWT	Normal	3.00	3.05	3	2	12.57	$6,500
Kestral e400	HAWT	Normal	3.00	2.32	3	2	12.57	$10,000
Gaia	HAWT	Low	11.00	11.41	2	6.5	132.73	$59,000
Turby	VAWT	Normal	2.50	0.93	3	N/A	5.30	$2,500

Table 5-VI : Selected Wind Turbine Data

A common method used to determine the best wind turbine for a given location is the capacity factor. This is denoted by the ratio of the annual energy generated over the expected energy generated at rated power. A problem with this approach is the rated power stated by the manufacturer is often stated as the peak power of the machine which is an arbitrary wind speed when compared to other WT's. This degrades the reliance of the CF as a good wind turbine correlation method. To remove the ambiguity of rated power across manufactures this research has developed various methods to standardise the rating and hence suitability of wind turbines for various locations.

$$CF_{\text{Rated}} = \frac{E_{\text{Annual Generated}}}{8760 \text{ x } P_{\text{Rated}}}$$

$$CF_{10\text{m/s}} = \frac{E_{\text{Annual Generated}}}{8760 \text{ x } P_{10\text{m/s}}}$$

Eq 5-10 : Capacity Factor definition

The first approach was to set the machines rated power to a pre-determined wind speed, this was chosen to be 10m/s, this analysed WT's power at this wind speed are seen in Table 5-VI. This wind speed was chosen as it represents a point at which a wind turbine should be outputting a power very close to its peak but is not high enough to be on the declining end of a low wind speed turbines power curve. It also represents a wind speed, which is easily achievable at most locations. The energy generation analysis can also be carried out for either a Rayleigh or Weibull distribution. However the test site data for Albany shows the Rayleigh fit to be rather inaccurate, from Figure 5-9, so the Weibull distribution is used for the following analysis.

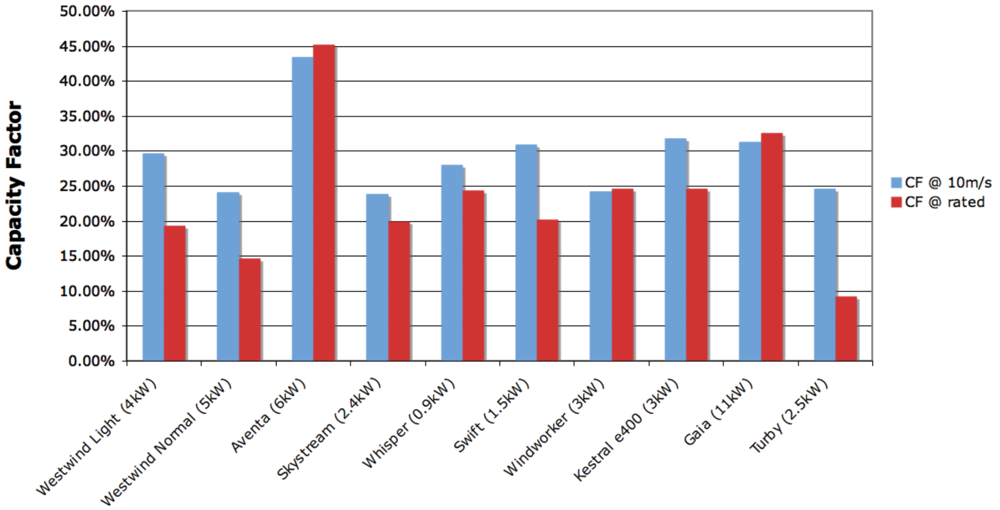

Figure 5-13 : Capacity Factor Analysis using Weibull Distribution

Figure 5-13 shows that majority of wind turbines benefit by having an increased capacity factor when standardising this to the pre-determined wind speed, in this case at 10m/s. Low wind speed turbines are seen to yield higher capacity factors due to their larger blade diameters and consequently larger wind swept area. So by capacity factor analysis alone low wind speed machines are observed generally to be better at energy generation for all but the windiest sites. The drawback to these machines is larger blade size, which ensures taller towers and greater installation expense.

The cost of installing a wind turbine is mainly determined by the site conditions, installing on the top of a mountain will be more cost prohibitive than on a farm, however the incremental cost due to the location is generally a set ratio of the simple install cost. So this does not contribute as a factor to decide between differing wind turbines, the same assumption can be made for the tower height. So the second selection criteria is the ratio of the wind turbine cost with respect to the energy generated by the machine over a year. The costs for each wind turbine were sourced in April 2009 on information gained on their sale into the Australian market. Each WT price is only its component cost when sourced from the various manufactures. Transportation, importation and installation costs are not included as they would add uneven values on the cost. This section is provided as a method approach on how to assess differing wind turbines on an economic basis and should not be used as an exhaustive analysis.

The authors definition of economic feasibility of the system, Eq 5-11, given is dollars per kWh.

$$EF = \frac{\text{Cost}}{E_{\text{Annual Generated}}}$$

Eq 5-11 : Economic Feasibility

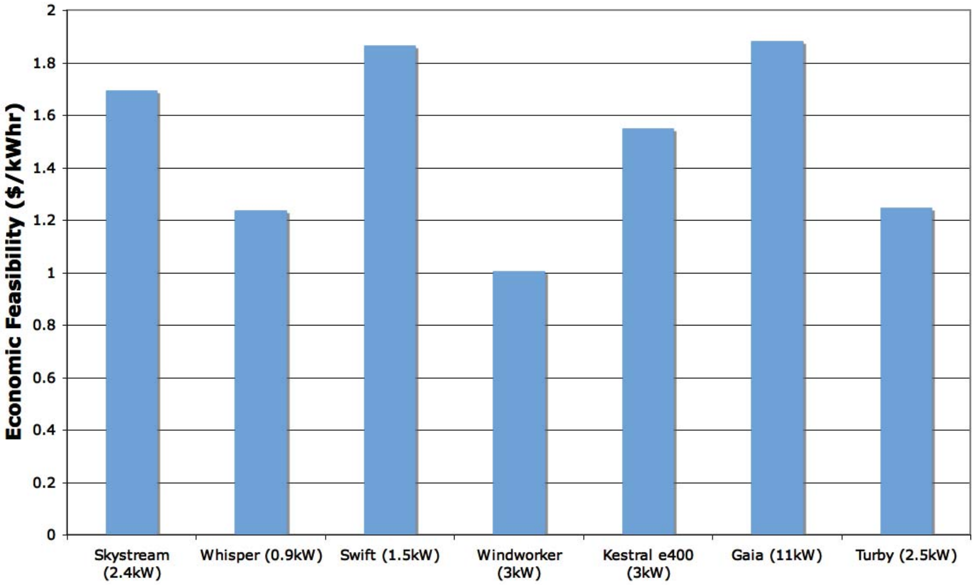

Figure 5-14 : Economic Feasibility for Selected Wind Turbines

The EF data in Figure 5-14 is show for only seven of the ten selected machines. This is due to the two Westwind machines being currently unavailable and the value of the Aventa machine was not readily available. From the EF data alone the Windworker would be the most suitable machine, however this is a low cost machine and quality and warranty would need to be reviewed. The installation costs were not factored into this modelling and should be for an accurate site analysis.

The final comparison method is the conversion efficiency (CE). This is a direct method to determine the performance of the wind turbine in converting wind energy to electrical energy. The CE is defined by the ratio of annual energy generation to the wind swept area of the wind turbine. A higher CE implies a greater ability of the blades to successfully interact with the moving air to develop the torque required to drive the generator. This is also a measure of a higher average power coefficient of the WT across the entire wind regime.

$$CE = \frac{E_{\text{Annual Generated}}}{\pi \mathrm{L}^2_{\text{Blade}}}$$

Eq 5-12 : Conversion Efficiency

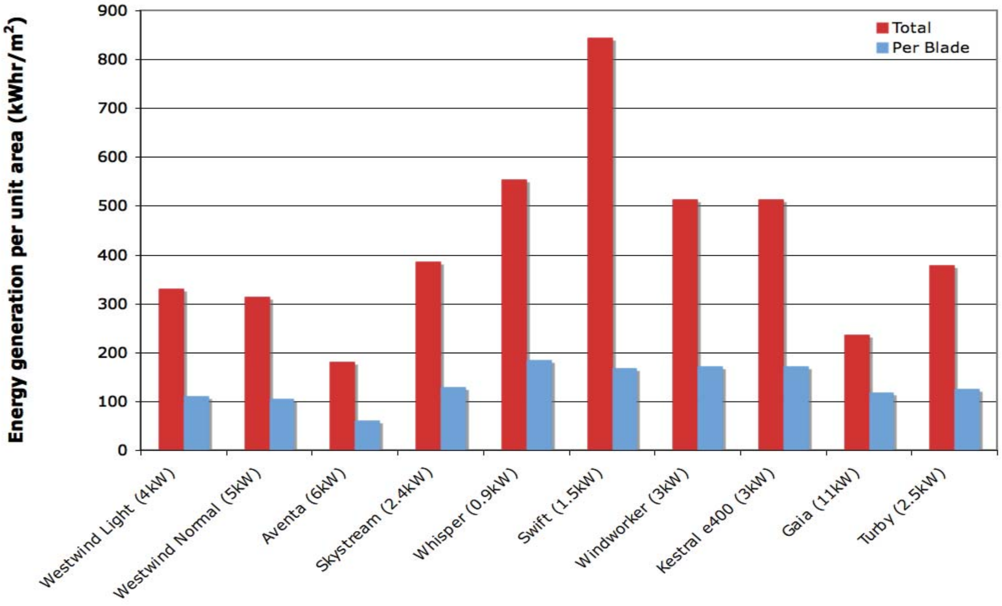

Figure 5-15 : Conversion Efficiency for Selected Wind Turbines

The CE can be misleading due to the number of the wind turbine blades. The Swift machine is a five blade machine, the Gaia is a two bladed turbine and the rest use three blades. From the blade scaled data the Whisper machine exhibits the best CE however its small size, 900W, would be very prohibitive for a larger system and so would only be a good candidate for the smaller battery charging situations. The Kestral, Swift and Windworker all show similar levels of CE. The extra blades on the Swift machine ensures it is a better choice for turbulent wind conditions such as those in close proximity to buildings. The Kestral and Windworker are both good options for a general location.

The wind turbine selection analysis has been carried out for the specific wind speed data for the location of Albany in Western Australia. The three selection criteria of capacity factor, economic feasibility and conversion efficiency should be combined to allow an unbiased judgement for wind turbine selection. The final constraints are the required energy generation for the load and the nature of the surroundings. The location may only have a certain number of possible locations available for wind turbines to be installed. This may limit the wind turbines available for use as the sum of them must produce the desired energy requirements.

5.6. Summary

This chapter presented a method and analysis to determine the most suitable WT for a given location. The accuracy of freely available wind data was also examined with a conclusion, which prefers ground based data from satellite data. The methods of measurement for satellite data generate errors that are too large to allow direct input within a wind energy analysis.

A summary the components of this chapter is seen below:

- Wind data analysis
    - Accessibility of wind data
    - Reliability of wind data
- Interpolation of power curves
- Analysis of wind distributions
    - Capacity factor analysis
    - Economic feasibility
    - Conversion Efficiency

The key research points of this chapter are:

- Application of statistical analysis and representations to wind resources;
- Application of Graph Digitizer to wind turbine power curves;
- Creation of definitions of Economic Feasibility and Conversion Efficiency to assist Capacity Factor to aide the selection of wind turbines;

5.7. References

1. Meteorology, A.G.B.o., *Australian Hourly Wind Data*, in *Australian Government: Bureau of Meteorology*. June 2008, National Climate Centre.
2. Paul W. Stackhouse, J., *Surface meteorology and Solar Energy* in *NASA Earth Science Enterprise*. March 2006, NASA: Atmospheric Science Data Center.
3. McVanInstruments, *Series 706 Heavy Duty Wind Speed and Direction Transmitter* 2001: Victoria, Australia.
4. F. Naderi, M.H.F., and D. G. Long, *Spaceborne Radar Measurement of Wind Velocity Over the Ocean--An Overview of the NSCAT Scatterometer System.* Proceedings of the IEEE, June 1991. **79**(6): p. 850-866.
5. Rodionov, N., *Graph Digitizer*. 2002: St Petersburg.
6. Jangamshetti, S.R., Guruprasada, *Site Matching of Wind Turbine Generators : A Case Study.* IEEE Transactions on Energy Conversion, 1999. **14**(4, December): p. 1538.
7. Yeh, T.-H. and L. Wang, *A Study on Generator Capacity for Wind Turbines Under Various Tower Heights and Rated Wind Speeds Using Weibull Distribution* IEEE Transactions on Energy Conversion, 2008. **23**(2, June): p. 592.
8. Masters, G., *Renewable and Efficient Electric Power Systems*. 2004: Wiley Interscience.
9. Westwind, *Westwind - wind turbines for remote areas*, in *Data Sheet*. 2001: Perth, Western Australia.
10. SWWP, *Skystream 3.7*, in *Data Sheet*. 2008, South West Wind Power: Flagstaff, AZ.
11. SWWP, *Whisper 300*, in *Data Sheet*. 2008, South West Wind Power: Flagstaff, AZ.
12. SWIFT, *Swift Rooftop Wind Energy System*, in *Data Sheet*. 2009, Renewable Devices Swift Turbines Ltd: Edinburgh, UK.
13. Kestrel, *Eveready : Kestrel Wind Turbines - e400i*, in *Data Sheet*. 2007, DC Power Systems.
14. Turby, *Turby : Specification sheet*, in *Data Sheet*. 2006, Core International: Amsterdam, Netherlands.
15. Gaia-Wind, *Gaia-Wind 11kW, Energy Production Data*. 2009.
16. Aventa, *Technical data of Aventa® LoWind Turbine AV-7*. 2008, Aventa Ltd.

“Every reasonable effort has been made to acknowledge the owners of copyright material. I would be pleased to hear from any copyright owner who has been omitted or incorrectly acknowledged.”

6. Design, Control and Energy Management for Hybrid Systems

This chapter presents methods to integrate and operate renewable energy sources with conventional generating equipment to produce stable, reliable and robust electricity supplies. The desolate nature of Australia ensures the need of many independent stand-alone power systems to supply indigenous communities, farming stations, and more recently tourist resorts. Invariably these systems include peak loads well in excess of 100kW. Methods of operating DGs with inverters are examined in this chapter.

This chapter develops the methods and techniques required to design complete power systems and draws on example systems the author has designed and commissioned over the past four years with the industry partner Regen Power. The projects discussed in this chapter each focus on different priorities for the renewable system.

The first example is from a feasibility study to install renewable energy to directly offset diesel consumption in 2008. Details of the design of this system are presented as a guide to design this type of system. The second example is the complete power system for the island of Uligam[1], Kondey[2] and Raimandhoo[3] in the Republic of the Maldives. Each island required a stable electricity supply where the local utility could install and meter each household's consumption. Reliability was the central focus of this systems with the renewable energy proportion designed to offset the total islands energy consumption. DGs were used only when the natural conditions had been unfavourable for energy production. This project included both solar and wind renewable generation sources. The Uligam system is mostly a centralised system as the wind energy component is fed from a designated feeder back to the powerhouse. Uligam islands design is the described in detail in this chapter.

6.1. *Interconnection of Large Hybrid Systems*

Large hybrid systems can roughly be divided into two main types, centralised and distributed. Centralised stand-alone systems are defined where the energy production is constrained to a small locality around the main generation infrastructure and the energy to the loads is transferred in one direction, Figure 6-1. Alternatively, distributed systems have many generating sources interconnected with the loads ensuring power flow is bi-directional within the network, Figure 6-2.

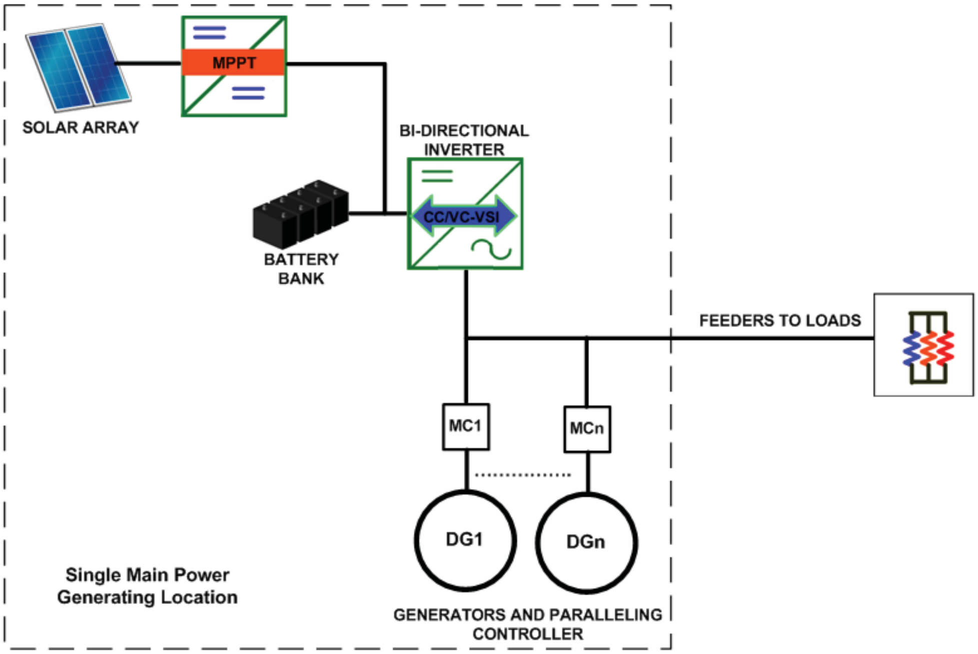

Figure 6-1 : Centralised Hybrid System

Centralised systems are common in Australia for remote towns and communities. Multiple diesel generators within a single powerhouse are used in the majority of these systems. The increasing cost of fuel and difficultly in performing regular maintenance ensures the failure rate of the generators within these systems is high. Also, the regular light loading of the generators also causes cylinder glazing, which can quickly damage the piston rings ultimately shortening the working life of the DGs. The use of a centralised inverter to control the running of the DGs can eliminate the light loading of the DGs while optimising the operating power allowing the fuel efficiency to be maximised. This chapter presents novel methods or controlling these isolated stand alone systems and investigates the sizing of the DGs based upon probability functions based upon the DG loading profiles.

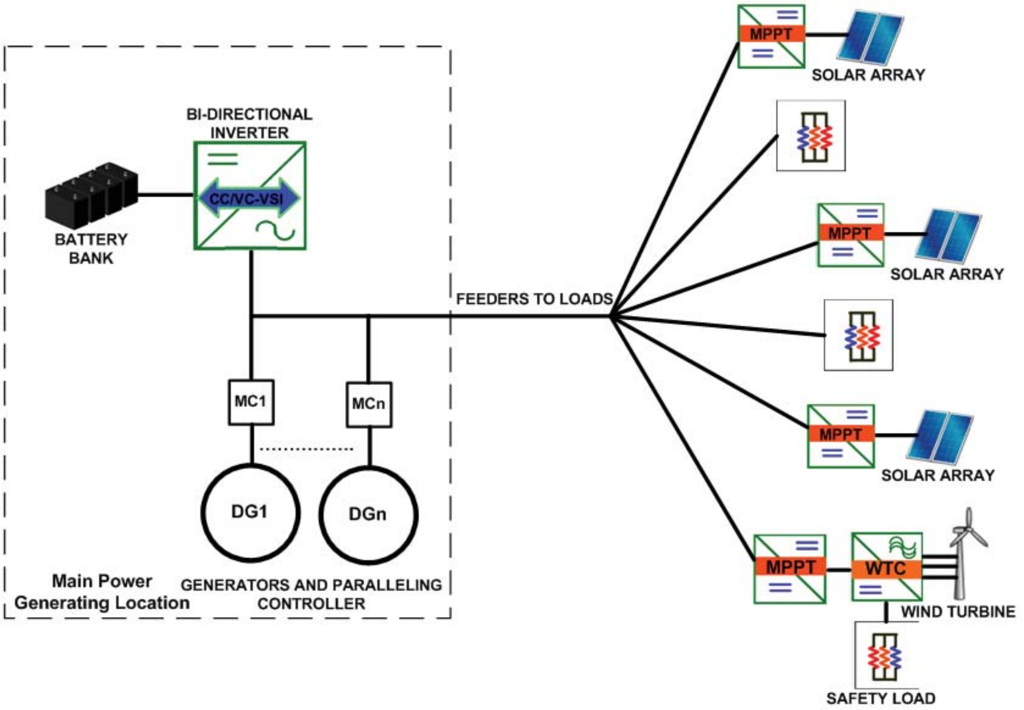

Figure 6-2 – Distributed Hybrid System

Distributed hybrid energy systems usually have the majority of the natural energy resources at the peripherals of the electricity network. This causes a bi-directional power flow from the distribution feeders back to the central power plant. This creates further problems for the systems operation such as the possibility of over charging the battery bank or reverse power to the generators. The concept of frequency shift is developed as a method to control the power from distributed generation equipment instead of simply using a dump load. The ability to automatically control the power output from the field inverters is also investigated as part of the designs.

6.2. *Design methodology for Hybrid Systems*

The theoretical design of a stand-alone hybrid power system requires seven key stages. Each stage follows logically from the previous stage to develop the required technical solution. Economic constraints are then included and may affect the final hybrid system design. These are commonly due to a trade off between system reliability, battery capacity and battery longevity.

1) Development of a daily load profile

A daily load profile is an accurate representation of the load demand throughout a typical day for the power system. This is the starting point of any hybrid system design and can be used to ascertain the optimal generator sizing for the system. The load profile for the island of Uligam in the Republic of the Maldives is seen in Figure 6-3. The load profile can be created by using a current measuring device on a phase of the load bus at the power station. The balancing of the phases and knowledge of the seasonal load variations are also required to determine an accurate load profile. An acceptable load profile should be within +/- 20% of the actual loads for a successful design.

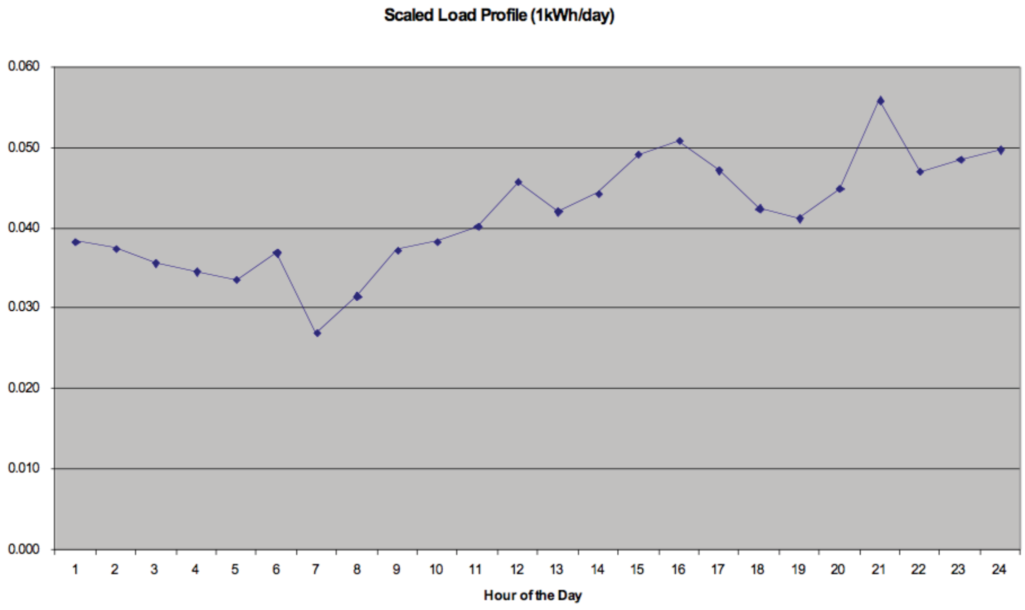

Figure 6-3 : Uligam Load Profile

In some instances a hybrid system design is required for a new location where no previous electricity generation equipment has been installed. In these cases an energy audit for the entire site must be carried out and the total energy consumption of all appliances must be tallied. This approach was carried out for the Eco Beach project and can be seen in Appendix 9.5.

Once the general shape of the load profile is determined, on site knowledge of the larger loads must be acknowledged to ascertain if they will effect any seasonal variations of the net load. For instance, hot water systems are likely to be used more during the colder months so if they contain electric booster these will need to be accounted. Similarly air conditioners in the summer months will create a summer peak in the late afternoon. Using this knowledge the daily load profile may be expanded into an average monthly load profile taking into account the seasonal load variations, Figure 6-4.

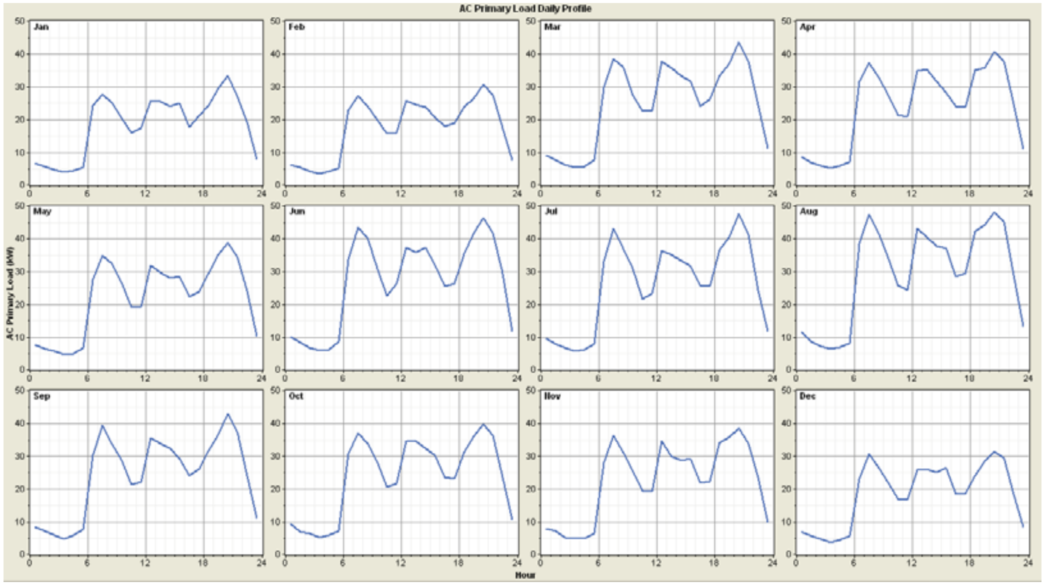

Figure 6-4 : Initial monthly load profiles for Eco Beach Project

2) Maximum power requirement

The maximum power requirement is the absolute peak power ever required by the system. This is determined by the sum of the peak of the highest monthly load profile with any perceived annual average load increase over the lifetime of the system, and the starting current requirement for the largest induction machine at the location. This is the maximum power that the system must be able to cover at anytime.

$$P_{system,peak} = \Delta P_{lifetime,system} \times P_{load,\max} + P_{IM,start}$$

Eq 6-1 : Systems peak power requirement

In most hybrid systems the peak load is usually carried by the single largest generator multiple generators or the inverter with a generator. The single large generator method easily allows the peak load to be matched. However it is likely that this generator usually runs lightly loaded and inefficient most of the time. The multiple generator option assumes that the initially running machine cannot match the load and must call up a second DG. If this DG cannot synchronise quickly enough or the load is too great the system will blackout. This leaves the DG combined with an inverter option. When an increase in load requirement is seen with a single DG running, a CC-VSI can feed in the desired power instantaneously to cover the required peak or assist in the load management until the second DG can be called to take over the load. In the case where the inverter is operating autonomously, VC-VSI, it can often take 20% greater then there rated capacity for up to five minutes, this is ample time for a DG to start, synchronise and share the load, preventing a blackout situation. In this case the DG must synchronise with the VC-VSI.

3) Total average daily energy usage

The area under of the load profile curve is the daily energy usage. Using the average power level each hour, the hourly kWhs can be calculated and then the summation of each hour yields the total average daily energy usage. This approach should be adopted for the various times of the year allowing the seasonal energy variations to be taken into account.

In a DG only system this energy requirement can be directly approximated to the litres of diesel fuel required each year/month to supply the loads. A purely renewable hybrid system must collect enough energy from renewable resources to cover for its total electrical energy expenditure in one day. Many systems are designed with this concept as a goal; however, it is very difficult to realise if the system is required to be reliable. Even though the addition of a battery in the system allows the instantaneous excess renewable energy to be stored and utilised later in the day, at some point in the future renewable resources will be low causing a continuous drain on the battery, ultimately causing a blackout. This requirement generally ensures that some form of DG is required and they are inevitably sized to supply the total system load.

4) System control topology

The method of controlling the hybrid system determines both the size of the renewable energy component and the requirement of a centralised inverter. The possible system topologies in increasing order of sophistication can be summarised as:

- Predominantly DG grid with distributed renewable resources fed through CC-VSIs. A requirement of this system is that the minimum load must be less than the total renewable power generation otherwise a reverse power situation at the DG will occur causing blackout.
- Predominantly DG grid with distributed renewable resources fed through CC-VSIs. With a power limiting method employed to allow a greater renewable portion of energy usage when available.
- Centralised hybrid system as in Figure 6-1. The inverter controller selects the method to power the grid; either inverter or DG. The battery is charged through the bi-directionality of the inverter or the DC coupled PV array.
- Distributed hybrid system, as in Figure 6-2, has many generating resources intermixed within the grid causing power flows to be bi-directional. If the energy generated within the grid is greater than net loads, then the central inverter must use the excess to charge the battery. If the battery is full, the main inverter must signal to the field inverters to decrease their power generation. This is now routinely done through frequency shift control, which takes advantage of the strict operational frequency window as determined by AS4777. The central inverter can also control the start of the DG if the renewable resources and battery is at a low state of charge.

5) Renewable energy availability

A trade-off between the usage of diesel and infrastructure cost of renewable generation equipment are the two deciding factors for the installed amount of renewable energy. A solar energy analysis should be carried out based upon the locations solar irradiation and likely installation angle for a suitably sized PV array, such as 1kW. The similar process should also be carried out for a suitable wind turbine for the location. Once a vague idea of the system topology and possible system components exist the software package HOMER can be utilised to optimise the system further. HOMER allows various combinations of PV, wind, inverter, DG and battery to be iterated over one year to find the overall most cost effective and energy efficient solution.

6) Required storage capability

One of the largest financial components of the system is the battery bank. A correctly and efficiently sized battery bank is essential in renewable energy systems. The longevity of the battery bank is always a concern with any hybrid system. The system optimisation program HOMER can be used to model and summarise the charging and discharging cycles of the battery bank and estimate its lifetime. Correctly sized battery banks operating in rated conditions should operate for more the seven years.

In the majority of hybrid systems the battery bank will be required to power the loads for the time of the day when the renewable energy is low, and be charged when the renewable energy is high. This generally corresponds with one charging cycle per day. The most efficient portion of a battery is between 40% - 85% SOC. This 55% capacity of the battery bank must be utilised to supply the load, usually at night. The net energy during this discharge time, available to the loads given the battery depth available and loop charging (85%) and inverting (95%) efficiency can be used to estimate the battery storage requirements.

$$E_{battery(kWhr)} = \frac{E_{disch\arg e(kWhr)}}{0.55 \times 0.85 \times 0.95}$$

Eq 6-2 : Required battery capacity

7) Generator loading optimisation

All reliable hybrid energy systems require some form of backup conventional generation. If the DGs are required to run for significant periods during each day to supplement the renewable generation or recharge the batteries they will have an optimal efficiency point where they most effectively convert the diesel fuel to electricity. A frequency analysis of the load profile can be used to create a probability density function of the generator loading. This can be used to optimise the sizing of the generators to allow them to operate on average more efficiently.

8) Total System Efficiency

The net efficiency of a hybrid system depends upon the interconnection topology and the method of control. Centralised systems tend to exhibit the greatest efficiency when the renewable generators are DC coupled, as they only undergo one conversion from the generated voltage to the battery voltage, approximately 97% efficient. Decentralised systems are most efficient when the generated energy is consumed at the AC loads nearby the source.

The starting of a DG uses more fuel then its continuous operation so a central inverter that may feed energy to the grid is beneficial in preventing a nuisance DG start on a transient load. If the load is sustained or the battery is low the DG can still be operated at any point in the future.

Knowledge of the likely forthcoming conditions, such as sunrise or an afternoon sea breeze should also be incorporated into any control topology. During the nights the average loads are usually lower and the hybrid system should be run in inverter mode to prevent generator low level loading and lower the battery SOC for the upcoming solar energy generation. A well-balanced system allows the solar generation to supply all loads with the remainder being used to recharge the battery to a SOC that allows flexibility for the usually larger evening loads. This flexibility allows the inverter to operate in either charging or feeding mode keeping the DGs operating at their optimal efficiency point, saving fuel.

These eight points allow the basic design, sizing and most cost effective hybrid system option to be realised. In many instances the required system reliability constrains the possible solutions. Utility grade power requires that a fault at a generator can be allowed for without causing a network interruption. This constraint makes inverter based hybrid systems difficult to implement, as the inverter much be capable to perform a certain level of fault ride through capability.

6.3. Hybrid System Control

6.3.1. Maximising the use of Renewable Energy in Hybrid Systems

The process of adding renewable energy generating devices to an existing power station can disturb and decrease the generation reliability of the plant. A conventional diesel generation system contains at least one generator, which follows the load profile of the community. The community load will continuously vary depending upon the consumers application. If more power is required an additional generator is installed, which together can cover a greater load, while increasing the overall reliability of the generation plant. For parallel operation of generators a station controller is required which allows the generators to synchronise and share the load. This station controller also performs a generator selection function, which ensures that no one generator operates significantly more hours then any other one. This increases the overall time before maintenance is required on the plant and increases the generators longevity.

Selecting the number of generators in a plant is a trade off between operational and maintenance costs and overall system reliability. Large networks generally operate on the premise that the spinning reserve on the system must be greater then the largest operating generator on the network. So if a major fault is to occur on any generator and its ability to supply power ceases the system has enough spare capacity to absorb for the fault. This requirement becomes very expensive in smaller scale systems as the required spinning reserve needs double the generator capacity running or two generators where one is sufficient to cover the load. The generation efficiency is also significantly decreased due to the lower loading of all generators on the network. This strategy is known as N+1.

In terms of generator efficiency and reliability it is better to operate multiple smaller units in parallel. Multiple units allow the spinning reserve capacity to be a lower percentage of the overall generation, which decreases the operational cost to maintain the spinning reserve. However maintenance costs and system complexity increase with multiple units. So a direct trade off exists between operational and maintenance costs and reliability. In smaller systems the ability to have N+1 redundancy becomes financially prohibitive however the system must still meet a certain level of reliability.

Integrating renewable energy, solar and wind generation sources into existing power networks can cause disruptions to the network. Initially this may take the form of fluctuations in the voltage and frequency on the line which may cause flickering due to the rapid increase or decrease in generation at the point of common coupling. These issues can be minimised if the line impedance to the loads is as small as possible. It is recommended that the renewable energy generators be connected through a separate feeder to the main power station switchboard to prevent these effects from a weak grid. Stronger grids such as those around a city or in close location to the generation plant do not exhibit these issues as the line has sufficient capacity to prevent major effects on the voltage magnitude and frequency.

A reliable but conservative approach to introduce renewable power into an existing network is to only allow the peak renewable generation to be the difference between the minimum load and minimum diesel generator loading. This represents the portion of power that prevents light loading of the diesel but also contributes some renewable portion to the system. Longevity of the diesel generator should not be affected as the loading is never below its minimum.

To investigate the level of safe renewable energy penetration on an existing system a load profile was developed which incorporated a daily trend with a randomised element for a 24 hour period. The day was broken into 144 ten minute increments and the load calculated for each. Figure 6-5 shows a sample load profile with upper and lower trend bands. The actual power level is randomly calculated within this band to allow the testing of occasional step load conditions.

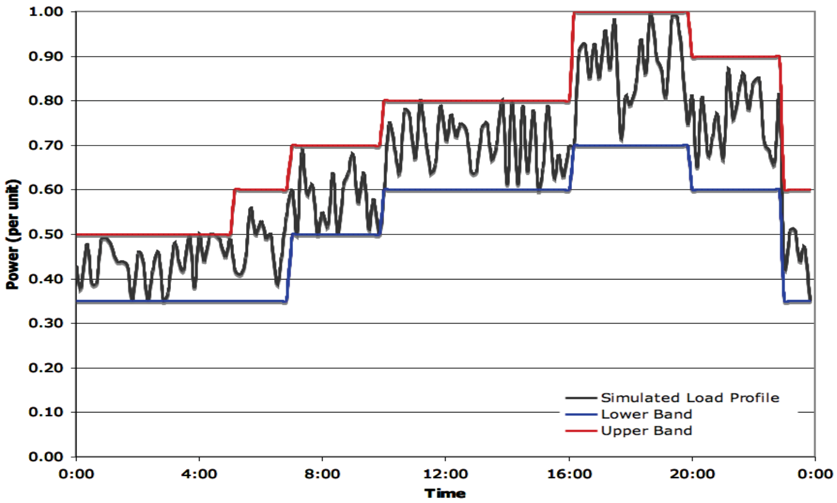

Figure 6-5 : Simulated load profile and bands

Figure 6-6 shows the available level of renewable energy penetration over the simulated day with no chance of loading the DG below 30%. The minimum DG loading is based upon the peak rating of the generator, which is assumed to be 5% greater then its continuous rating for the simulation. This is the most conservative but reliable approach to integrate renewable energy into an existing system. It is not known the exact magnitude of renewable power produced at any instant in time so it must be assumed that maximum installed capacity is generated at any time. Using this design constraint the maximum renewable component may be up to 4% of the per unit generation power.

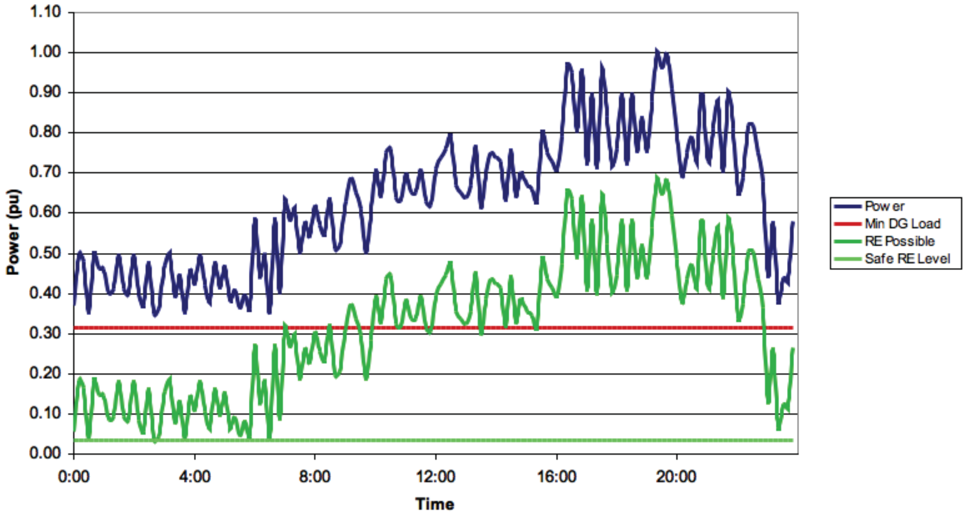

Figure 6-6 ; Single DG operating > 30%

Another approach is to allow the diesel loading to drop below its minimum however not for extended periods of time and never to the extent that a reverse power situation may occur. In this case the DG is allowed to drop as low as 10% of the continuous rating of the DG. As the renewable generation is only generated occasionally the DG will only be lightly loaded rarely. This method allows a much greater level of installed renewable capacity, up to 25%, while maintaining system reliability, however generator life may be shortened. Light loading DGs are available and are applicable to this situation.

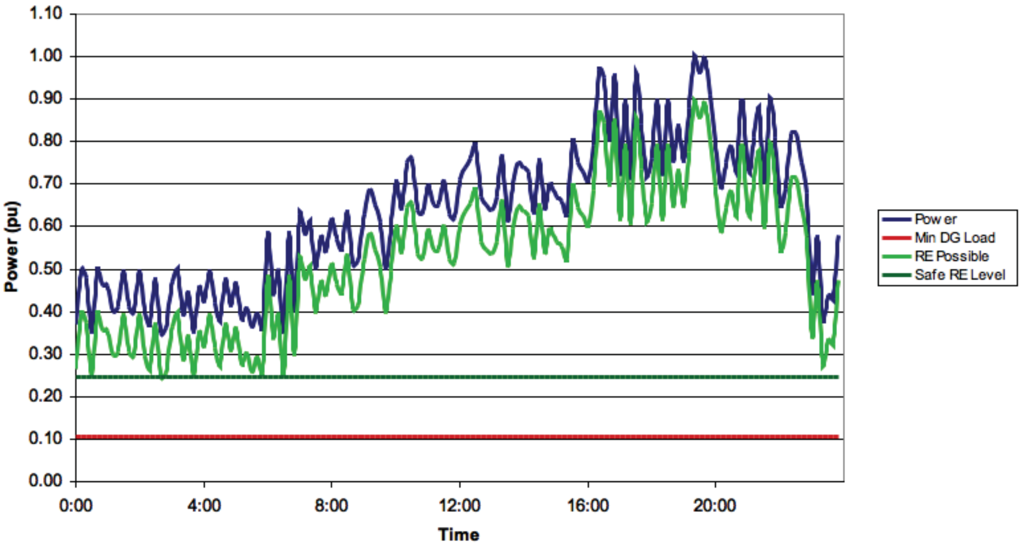

Figure 6-7 : Single DG operating > 10%

The major limitation of renewable integration in small diesel based systems is the amount of renewable penetration before the DG may fail due to a reverse power situation. This is governed by the following conditions.

$$P_{DG} > 0$$
$$P_{DG} = P_{LOAD} - P_{RENEWABLE}$$

Eq 6-3 : Reverse power conditions

Conventionally the renewable component is variable due to local conditions of sun and wind however its maximum power is fixed. This causes a problem as the maximum power can be produced at anytime independent of the load. During times of low load it would be advantageous to limit the amount of power that can be drawn from the renewable generators. This could prevent the possibility of a back feed to the DG, which may cause a black out situation. Some hybrid systems that incorporate a battery bank to allow this excess energy to charge the batteries. This energy can be stored, however at some point the battery may be full so the same excess energy problem results.

The ideal method to control the any excess renewable energy is to limit it being fed into the grid at the inverter. This requires some form of communication and controller between the generator and the inverter. Various inverter manufacturers are looking to utilise this approach and it has potential to greatly increase the renewable energy component of isolated power stations in the future.

A simulation was developed which would allow the renewable energy component to be controlled in increments of 10% per unit of the installed capacity. Voltage and frequency control on this system would still be performed by a DG and its loading would always be held greater then 30%. The amount of renewable energy that may be generated can be calculated as the difference between the simulated load and minimum required DG load. The amount of renewable energy installed was taken to be the statistical mean of this safe renewable energy contribution. For a 30% minimum DG loaded system this was found to be 32% per unit of the DG generation capacity based upon the simulated load profile. Figure 6-8 shows the limit placed upon the renewable energy generation, for almost half of the simulated day all of this energy generated to fed into the system, however at low load times this is strictly limited. This method of control can be implemented through a PLC controller with a communication interface to the field inverters.

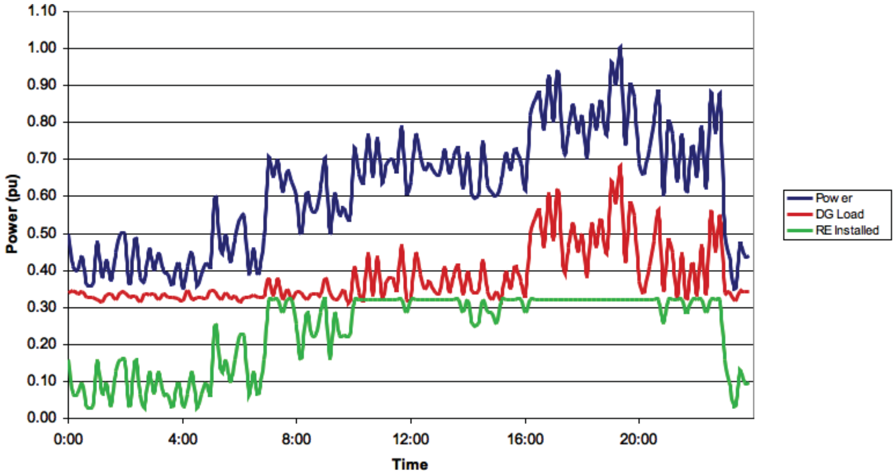

Figure 6-8 : Single DG operating > 30% with power limiter

Further simulations were performed for differing levels of minimum DG operation. Figure 6-9is set with a minimum DG loading of 20% with a renewable energy component of 41% and Figure 6-10 is set with a minimum DG loading of 10% with a renewable energy component of 52%.

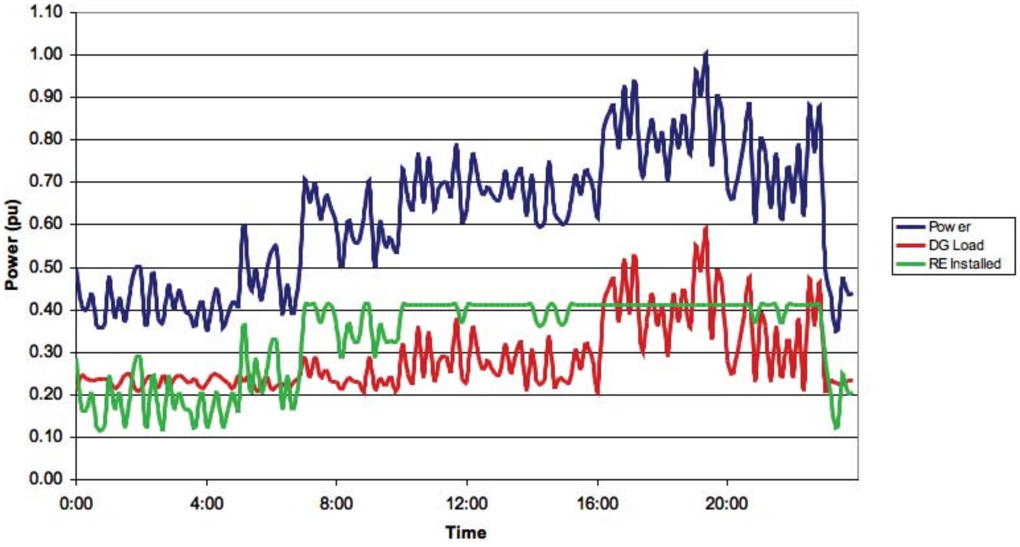

Figure 6-9 : Single DG operating > 20% with power limiter

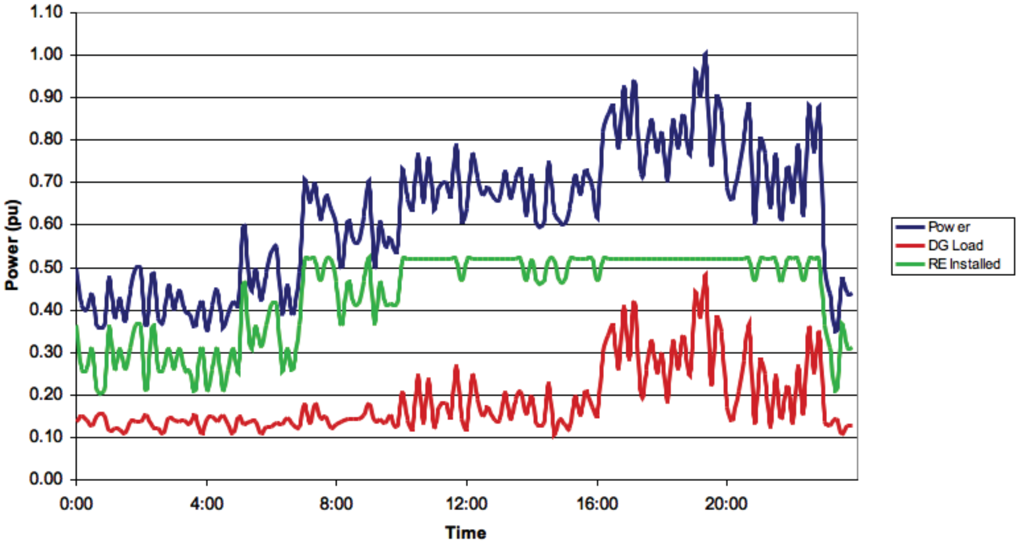

Figure 6-10 : Single DG operating > 10% with power limiter

A linear relationship exists between the magnitude of renewable energy penetration and the set point of minimum load of the DG. This is seen in Figure 6-11. The gradient of this line is dependant upon the differences in the minimum and maximum load on a load profile. However this approach is only valid in a one DG system where reliability is not of greatest concern and critical loads are not apparent in the network. An extension to this work would be to expand the control method to multiple generators with differing sized sets.

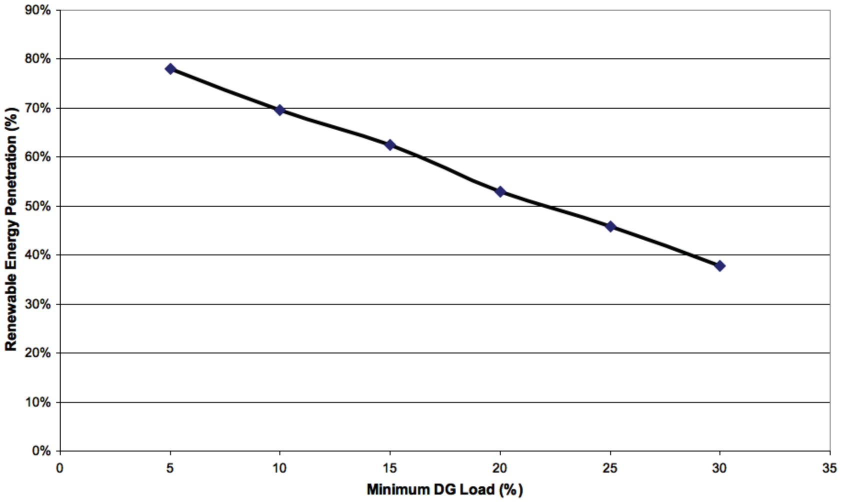

Figure 6-11 : DG load against safe renewable penetration

Where the grid requires a higher level of reliability the use of an inverter with battery bank can provide a spinning reserve without the need of a second generator. An inverter-centralised system can also assist with the penetration of renewable energy in the network as the central inverter can control the field inverters by using the frequency shift control. This method utilises a band of frequency above the grids fundamental, which allows the inverter power to be capped based upon the frequency. For the Eco Beach Project this band was set between 50.5Hz to 51.5Hz. 51.5Hz represented 0% of the inverters power capacity to be injected into the system. A linear extrapolation of this increasing to 50.5Hz was implemented and simulated in chapter seven.

6.3.2. Central Inverter and Diesel Generator Integration Strategies

The transition between a DG grid and inverter grid is a key aspect in any hybrid system. The system must energise the loads continuously throughout the transfer. This is comparable to an uninterrupted power supply, however the transition occurs at a greater power level and with much increased regularity, usually twice a day.

During DG operation the inverter may be in either charging or feeding, CC-VSI modes. At some point defined by the SOC, time of day or the requirement of frequency control, the inverter's controller will determine to change into inverter mode, VC-VSI, where it will control the voltage and frequency on the grid. The current loads from the generators must shift from the DGs to the inverter. This is done by advancing the phase of the inverter so it gradually takes a greater portion of the load. Thus, decreasing in load on the generators. This will inturn cause them to shut down via the DGs paralleling controller until the inverter will send a stop signal. The networks, voltage and frequency is now only controlled by the inverter. Other generation sources connected through CC-VSI's can now be controlled using frequency shift to prevent overcharging of the battery or voltage rise across the network. Frequency shift control cannot be used when the generators are controlling the networks voltage and frequency as the mechanical speed of the engine controls the frequency. Slight variations in frequency between paralleled generators is utilised to perform load sharing, so all conventional station controllers currently do not exhibit features to allow frequency shift to control the distributed inverters.

The DG's can operate in two modes of operation isochronous or droop mode. The term isochronous refers to a method of control for generators whereby they are governed either mechanically or electrically to achieve a steady state speed error of zero. In electrical terms this implies the frequency of the generation is set to constant such as 50Hz in Australia. This is a form of integral control which is best suited to a single generator plant or in a master-slave arrangement where the master is operating in isochroous mode and the slave are operating in droop. Droop mode allows small changes in frequency to control the power output of the generator. A drooping frequency implies the load has increased allowing more power to be produced by the generator, a swell implies excess generation is available and power may be reduced.

The VC-VSI is analogous to a diesel generator where the frequency is fixed from the mechanical speed and an electronic governor controls the voltage. A conventional multiple DG power station has a central controller that chooses one generator to be the master and the other DGs follow the voltage, frequency and phase. These other generators are termed slaves. A VC-VSI operates like a master DG as it controls the voltage, frequency and phase of the local grid and allows other inverters operating under a current controlled mode and DGs to synchronise with it. The transition from VC-VSI mode to DGs running the grid is started by a signal for the inverter controller to start the DGs. Depending upon the switchboard configuration the DG through the station controller will synchronise with the inverter or the first DG online. The split bus topology, Figure 6-12, is currently the most commonly implemented strategy. A main contactor (MC1) is located between the inverter and the feeders and is controlled by the inverter. To allow load transfer to the DG the inverter sends an DG start command which is required to start enough DG to cover the loads. The DG will start and synchronise with each other on the separate generator bus. When enough DGs are ready to take the load the inverter will phase shift the grids phase to be the same as the DGs. Once synchronised the central inverter will close MC1 and load will be transferred to the DGs. The inverter can the change its control to CC-VSI to charge or support the load to optimise the fuel usage. For this approach to be realised a central MC1 or bus coupler is required to be designed into the switchboard with current and voltage sensors on both sides of this device. The main drawback of the split bus approach is that it cannot be integrated into an existing switchboard. The bus coupler is generally a large withdrawable circuit breaker with open/close contacts and some operational state feedback. An error in the control of the bus coupler could cause major damage to the switchboard so feedback to ensure its correct state is required.

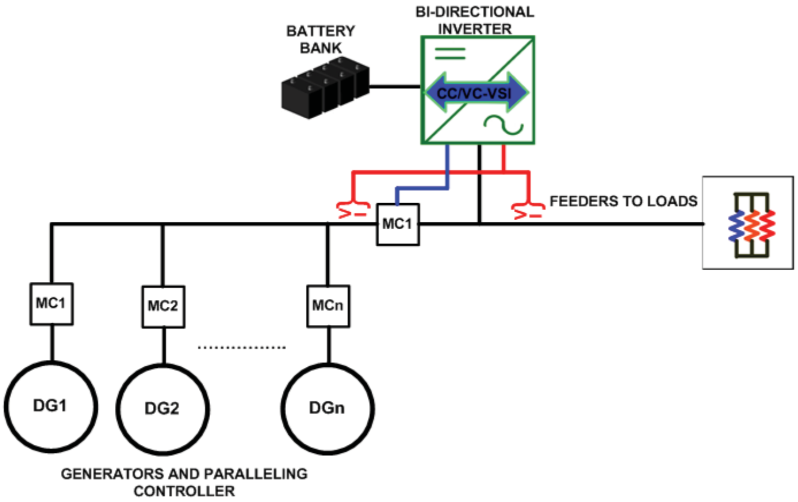

Figure 6-12 : Split bus topology

Another method to implement the central inverter design is the common bus approach. This topology allows an inverter hybrid system to be interconnected to an existing power station. Instead of using a central controllable bus coupler each DG has its own main contactor, which is controlled by the inverter. To transfer the load to the DG the central inverter will cease any frequency shift and send a start signal to the required generators to start. Each DG will be set to start in isochronous mode where it maintains 50Hz operation regardless of loading. Once synchronised it will communicate to the inverter that it is ready to take load. The inverter will then close the DGs main contactor to the main bus and delay its phase to allow more load to be taken by the DGs. The inverter must then disconnect and allow the generators to take the load. One will then become the master and control the voltage and frequency on the bus and load sharing between generators can occur. This situation is synonymous to the a fault on the master generator and another taking over the control. Problems with this approach are the communication between the inverter and the station controller is required to be at level that is currently difficult to achieve. For this method to be successful further research must be carried on the transfer interface and feedback. A likely scenario is that the inverter controller will actually become the station controller for the generators. However commercially this approach has not yet been demonstrated.

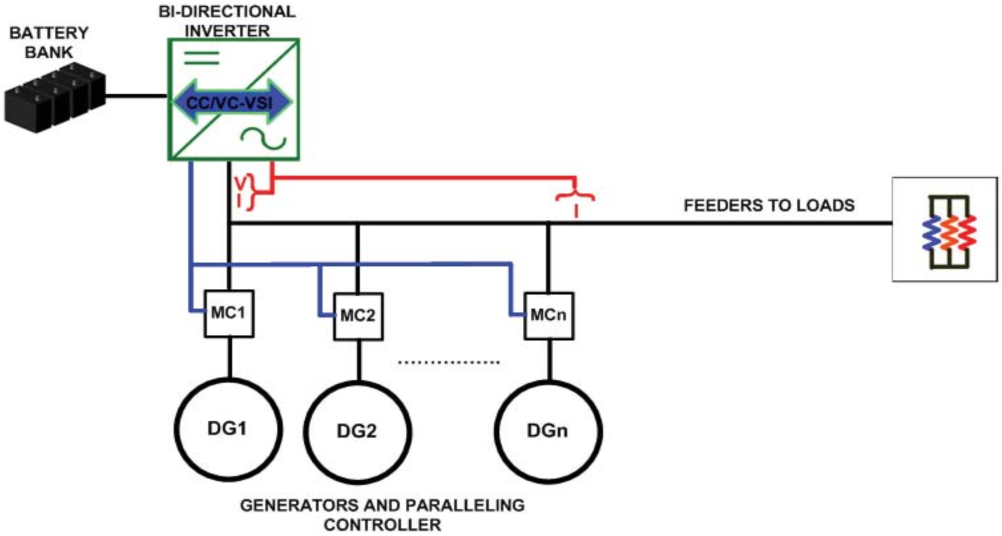

Figure 6-13 : Common bus topology

6.4. Design Example for a Typical Renewable System to Offset Diesel Consumption – Turf Farm

In many remote areas of Australia, DGs are used to produce power for agricultural, refrigeration or military requirements. The main aim for the renewable system is to offset diesel fuel consumption and cost. An economic analysis of the current fuel usage, future fuel cost and possible saving in installing renewable energy generating equipment is required look to offset this capital expenditure. This example is from a feasibility study[4] the author carried out for a turf farm in Western Australia. Any fuel offset saving must be used to recoup the capital of a loan required over the period of in this case 15 years. Various options of solar/diesel, wind/diesel and solar/wind/diesel are optimised in HOMER to produce the cost comparisons for each option.

A load profile for the site was developed based upon an audit of the site loads. This was not difficult as the major loads were water pumps, which operated when watering was required during the year. A house load is also added to the profile which includes a higher random component. An expansion of load in the near future was also simulated to predict future fuel savings.

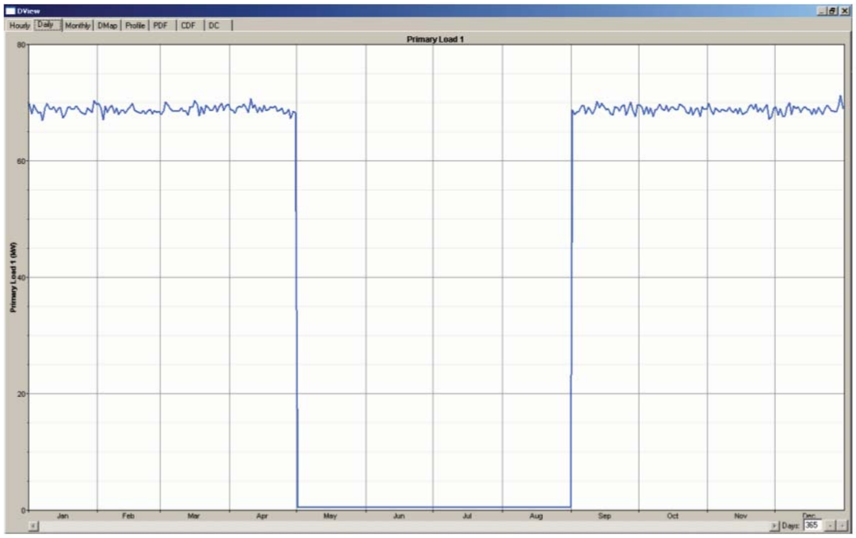

Figure 6-14 : Water pumping load A at turf farm

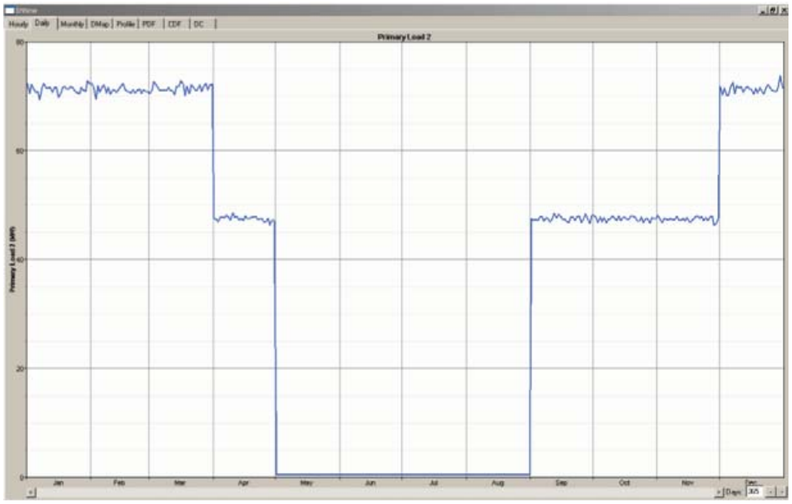

Figure 6-15 : Water pumping load B at turf farm

The maximum power requirement at the site was 160kW and induction motor peak loads were not considered an issue as the predominant load was IM so the load would be low when they were starting. The daily energy usage was 3.48MWhs in the period December to March, 2.9MWhs September to November and April and only 16kWh May to August. The control methodology for this system was only to offset diesel consumption, one generator would always be operational and no energy storage would be implemented.

The nearest wind measuring location was found as a department of agriculture site at East Lancelin. This data is presented as Table 6-I and was entered into HOMER as Figure 6-16.

	Jan	Feb	Mar	Apr	May	Jun	Jul	Aug	Sep	Oct	Nov	Dec
Average	6.78	6.33	5.74	4.93	4.56	4.81	4.89	5.1	5.17	5.81	6.22	6.67

Table 6-I : Average monthly wind speed for Lancelin East at 10 metres

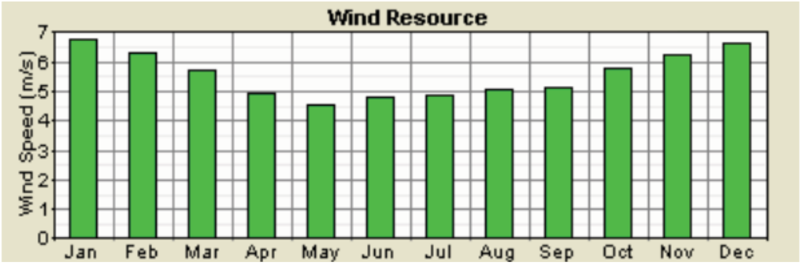

Figure 6-16 : Chart of average monthly wind speed for Lancelin East

The closest BoM recording site was found at Mimegarra, the incident solar energy was collected for this site and is presented in Table 6-II and Figure 6-17.

	Jan	Feb	Mar	Apr	May	Jun	Jul	Aug	Sep	Oct	Nov	Dec
kWh/m^2	8.35	7.3	5.69	4.2	2.99	2.57	2.82	3.49	4.88	6.22	7.48	8.25

Table 6-II : Average daily irradiation for Mimegarra

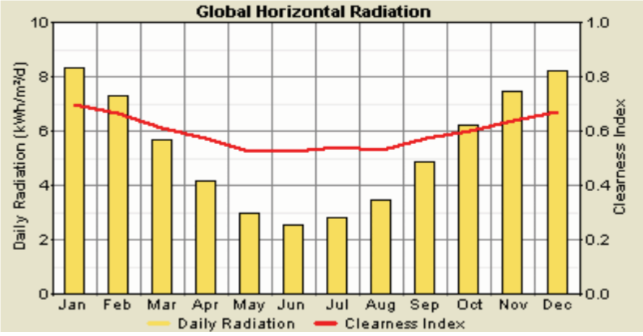

Figure 6-17 : Chart of average daily irradiation for Lancelin East

The basic system design shows an AC coupled PV and wind system. The wind turbines included in the feasibility were the 1.8kW SkyStream with polycrystalline photovoltaic panels. At the time of the feasibility study these were the only available wind turbines. Larger machines would have allowed a lower cost per kWh generated. The generator loading is determined by the renewable penetration into the system as no central inverter can perform DG loading optimisation. No power limiting was required as the loads were predictable and the renewable penetration was low.

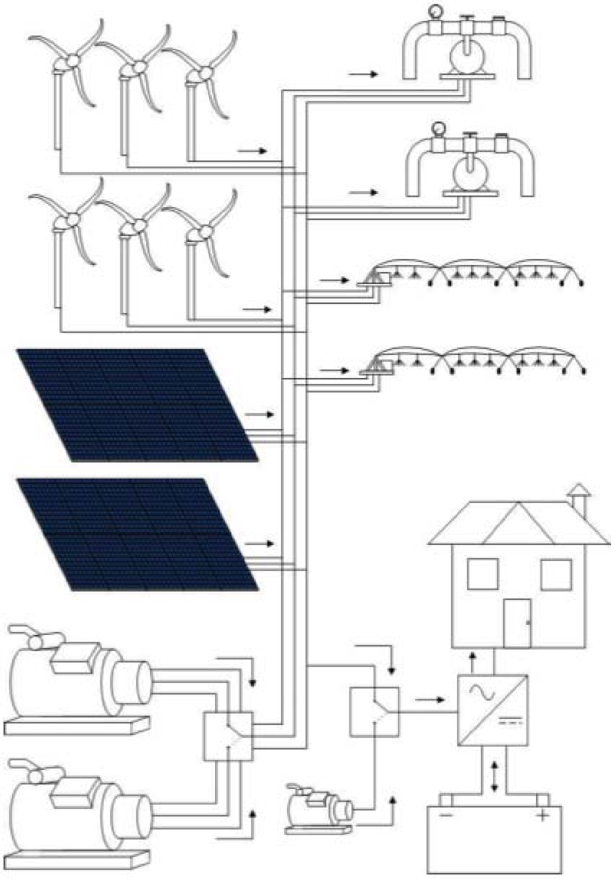

Figure 6-18 : Turf farm system sketch

HOMER[5] was used to simulate each combination of resources based upon the load, solar and wind profiles and loan requirements. Figure 6-19 shows a screen capture of the solar/wind/diesel optimisation. This option was optimal based upon the diesel fuel minimising strategy with 60kW of PV and 18 SkyStream[6] wind turbines. The wind/diesel option recommended 39 Skystream wind turbines and the PV/diesel only system predicted 120kW of PV to be optimal.

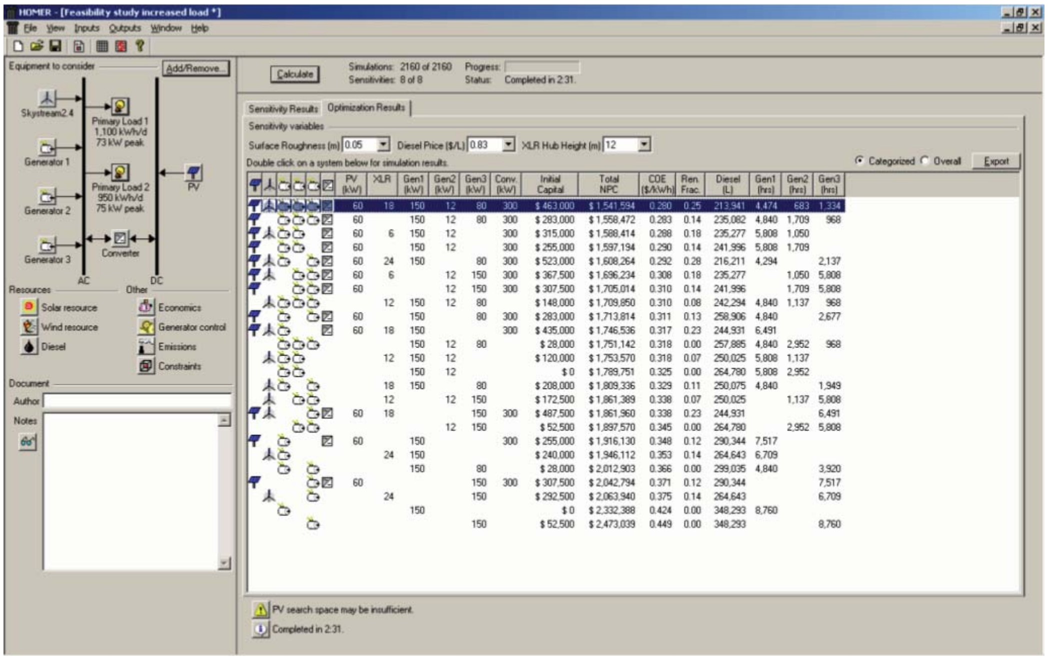

Simulations: 2160 of 2160 Progress:
Sensitivities: 8 of 8 Status: Completed in 2:31.

Surface Roughness (m) 0.05 Diesel Price ($/L) 0.83 XLR Hub Height (m) 12

Double click on a system below for simulation results.

PV (kW)	XLR	Gen1 (kW)	Gen2 (kW)	Gen3 (kW)	Conv. (kW)	Initial Capital	Total NPC	COE ($/kWh)	Ren. Frac.	Diesel (L)	Gen1 (hrs)	Gen2 (hrs)	Gen3 (hrs)
60	18	150	12	80	300	$ 463,000	$ 1,541,594	0.280	0.25	213,941	4,474	683	1,334
60		150	12	80	300	$ 283,000	$ 1,558,472	0.283	0.14	235,082	4,840	1,709	968
60	6	150	12		300	$ 315,000	$ 1,588,414	0.288	0.18	235,277	5,808	1,050	
60		150	12		300	$ 255,000	$ 1,597,194	0.290	0.14	241,996	5,808	1,709	
60	24	150		80	300	$ 523,000	$ 1,608,264	0.292	0.28	216,211	4,294		2,137
60	6		12	150	300	$ 367,500	$ 1,696,234	0.308	0.18	235,277		1,050	5,808
60			12	150	300	$ 307,500	$ 1,705,014	0.310	0.14	241,996		1,709	5,808
	12	150	12	80		$ 148,000	$ 1,709,850	0.310	0.08	242,294	4,840	1,137	968
60		150		80	300	$ 283,000	$ 1,713,814	0.311	0.13	258,906	4,840		2,677
60	18	150			300	$ 435,000	$ 1,746,536	0.317	0.23	244,931	6,491		
		150	12	80		$ 28,000	$ 1,751,142	0.318	0.00	257,885	4,840	2,952	968
	12	150	12			$ 120,000	$ 1,753,570	0.318	0.07	250,025	5,808	1,137	
		150	12			$ 0	$ 1,789,751	0.325	0.00	264,780	5,808	2,952	
	18	150		80		$ 208,000	$ 1,809,336	0.329	0.11	250,075	4,840		1,949
	12		12	150		$ 172,500	$ 1,861,389	0.338	0.07	250,025		1,137	5,808
60	18			150	300	$ 487,500	$ 1,861,960	0.338	0.23	244,931			6,491
			12	150		$ 52,500	$ 1,897,570	0.345	0.00	264,780		2,952	5,808
60		150			300	$ 255,000	$ 1,916,130	0.348	0.12	290,344	7,517		
	24	150				$ 240,000	$ 1,946,112	0.353	0.14	264,643	6,709		
		150		80		$ 28,000	$ 2,012,903	0.366	0.00	299,035	4,840		3,920
60				150	300	$ 307,500	$ 2,042,794	0.371	0.12	290,344			7,517
	24			150		$ 292,500	$ 2,063,940	0.375	0.14	264,643			6,709
		150				$ 0	$ 2,332,388	0.424	0.00	348,293	8,760		
				150		$ 52,500	$ 2,473,039	0.449	0.00	348,293			8,760

PV search space may be insufficient.

Completed in 2:31.

Figure 6-19 : Turf farm HOMER economic analysis

SOLAR/DIESEL	
Number of payments to loan per year (after 3 months)	26
Time to pay off loan (in years)	10
Interest Rate:	8%
Bank Loan:	$1,020,000.00
Loan value including Interest in first three months	$1,039,815.08
Rebate amount	$510,000.00
RECS amount	$105,032.00
Value to be repayed after RECs and Rebate	$424,783.08
Periodic Loan payment	-$2,375.90

Table 6-III : PV/Diesel option outcome

Each case was then compared against the diesel only baseline option. Further to the economic model government rebates, renewable energy certificates and tax breaks were also included. A loan for the capital requirement was then factored in with an assumed interest rate. The entire process was then duplicated for future loads. For the selected wind turbine the analysis showed that the PV only option was the most economic, Table 6-III. The complete financial modelling is not relevant to this dissertation however this project shows the methodology one would use to assess the implementation of a diesel offset type hybrid system.

The turf farm project did not go ahead mainly due to the large variations in diesel price during 2008 and the inability to secure a more ideal wind turbine. The construction cost per wind turbine was very high for such a small machine. The wind resource at the site was high enough to justify a wind/diesel system as the most applicable however the price point of wind turbines in Australia makes it difficult for them to be included in many systems. More recently wind turbines from China have reached Australia, some which were analysed in chapter five. If the client was to carry out a new analysis today it would likely show a more favourable outcome however the current cost of diesel is still low.

6.5. Design Example for a combined PV and Wind Hybrid System – Uligam Island, Maldives

In 2006 Regen Power was contracted to produce a feasibility study for the development and deployment of three hybrid wind solar power systems for islands in the Maldives. Only one of these systems, Uligam [1], in which the author was most involved will be presented in this section, these systems were commissioned in 2007.

Uligam is the most northern located of the three islands for which power systems were designed. The original power system was diesel only and often operated at low loads. The new power system was to produce 24hr power at a magnitude, which was attainable and affordable to the island while taking into account the maximum penetration of renewable energy sources.

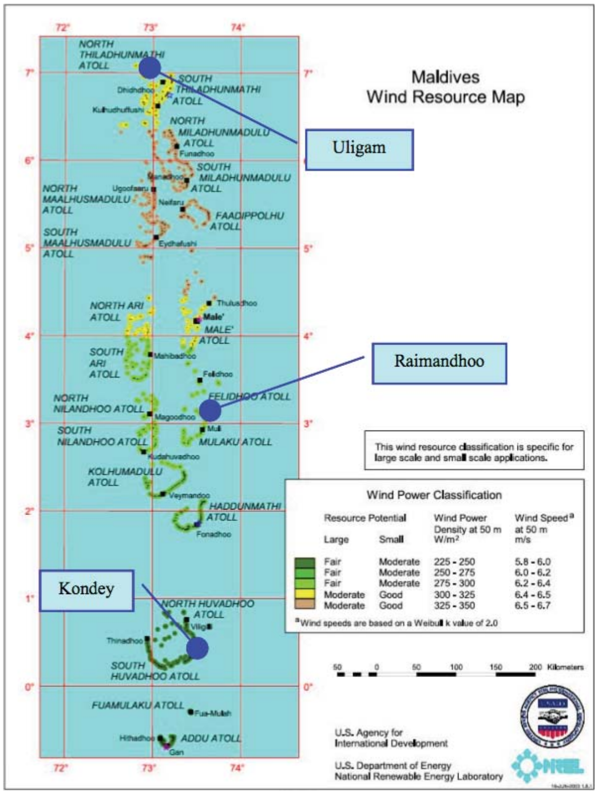

Figure 6-20 : NREL wind map for Maldives[7]

A load profile, Figure 6-21, was developed with the application of a current data logger on a single phase of the generator at the powerhouse. In this example the profile was scaled to a combined use of 1kWh per day, the peak load can be seen to be approximately 55kW and minimum load to be 27kW. The load profile is relatively flat and does not show any significant features that would allow PV generation to be naturally favoured as during high solar irradiation levels the loads are not apparently larger. If convenient water pumping and filtration may be used to demand side manage based upon times with excess renewable energy generation.

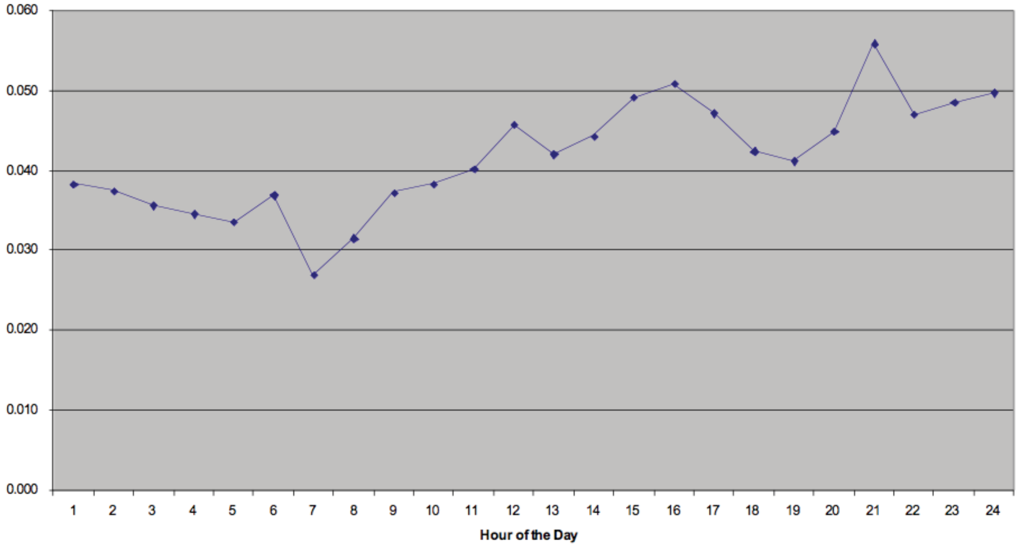

Figure 6-21 : Typical scaled Uligam load profile

The monthly energy usage is seen in Table 6-VI, this was determined by the previous systems billing services. A strong increasing trend can be seen in daily energy consumption on the island. This is due to an increasing use in the residential sector so a future load increase must be factored into the design. This sector without seasonal variations gained 50% in it energy use, likely from the residents purchasing new equipment in their homes. Increasing predicted energy consumption forces the system designer to guess a level at which the load may increase in the future, this is difficult as the raw data may show increases which could be transient. For Uligam the base level set was 300kWh per day. Increasing energy usage does allow the more efficient use to renewable energy as less is available to be stored. However, once the renewable component is installed any shift in energy consumption must be taken up by the conventional source of diesel generation. Any battery bank must also be cycled to a minimum SOC that for increasing loads means the DG is used to charge the battery, which is the least efficient energy pathway.

Month	School	Health Clinic	Guest House	Port Services	Island Office	Mobile Phone Tower	Sub total commercial	Residential and other	Total	Daily Consumption
Jan	119	161	368	612	217	1255	2732	2303	5035	162.4
Feb	215	192	311	574	383	1212	2887	2164	5051	180.4
Mar	268	214	386	594	226	1359	3047	2751	5798	187.0
Apr	140	305	500	538	232	1346	3061	2851	5912	197.1
May	313	428	468	622	245	1753	3829	2713	6542	211.0
Jun	297	595	410	710	196	1729	3937	2523	6460	215.3
Jul	152	780	503	585	189	1602	3811	3017	6828	220.3
Aug	256	657	502	568	226	1706	3915	3142	7057	227.6
Sep	278	701	418	528	249	1699	3873	3013	6886	229.5
Oct	254	821	438	584	265	1631	3993	3871	7864	253.7
Nov	129	818	301	709	279	1681	3917	3270	7187	239.6
Dec	124	894	383	634	274	1686	3995	3873	7868	253.8

Table 6-IV : Uligam energy consumption (kWh) by location for 2006

To determine the power rating of the inverter and DG the logging equipment is required to measure the instantaneous power requirements of the existing system. Figure 6-22shows one day of data, many short duration peaks can be seen which was caused by the inrush current at the starting of each households water pump. This transient spike must not exceed the inverter or DG rating. The highest spike in Figure 6-22 is approximately 45A, which corresponds to 32.4kW. To allow for future system expansion a 45kW three phase central inverter was chosen was chosen for this system.

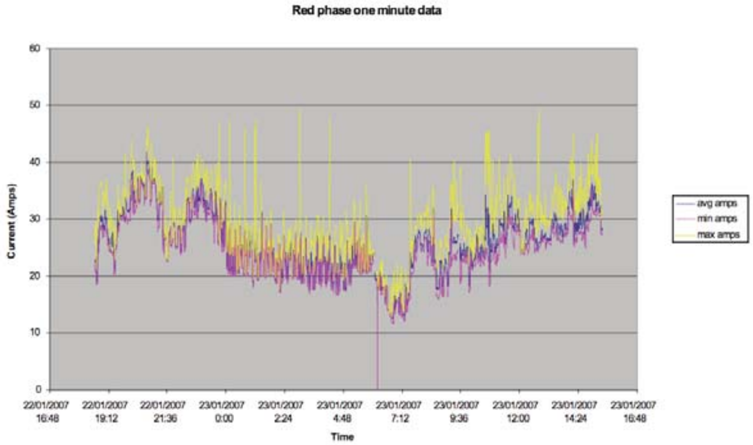

Figure 6-22 : Instantaneous single phase current profile

The solar irradiation levels were acquired from NASA satellite information of the area and is shown in Table 6-V. Wind data was available from an NREL report looking at Maldives as a suitable wing site. Table 6-VIis taken from this report and shows that Uligam is a favourable wind site [8].

	Jan	Feb	Mar	Apr	May	Jun	Jul	Aug	Sep	Oct	Nov	Dec
kWhr/m^2	5.36	6.01	6.21	5.82	5.17	4.73	4.94	4.79	5.25	5.43	5.23	5.06

Table 6-V : Solar data for Uligam

	Jan	Feb	Mar	Apr	May	Jun	Jul	Aug	Sep	Oct	Nov	Dec
Region 9	3.9	3.75	3.3	3.9	6	8	7.6	7	5.9	5.2	3.7	3.9
Region 8	4.55	4.1	3.4	3.9	6.1	7.6	7.1	6.6	5.9	5.5	4	4.5
Average	4.225	3.925	3.35	3.9	6.05	7.8	7.35	6.8	5.9	5.35	3.85	4.2

Table 6-VI : Average monthly wind speeds across Uligam

A distributed hybrid system design was used as it allows the highest level of renewable energy penetration while ensuring a reliable service. The required loads are only moderate so a central inverter can easy cover the complete island load. This methodology does lead to a slight decrease in reliability but a few outtakes a year would be tolerated by the community. Australian utility grade SAIDI and SAIFI levels are not expected in remote island communities which allows for a degree of flexibility in the design.

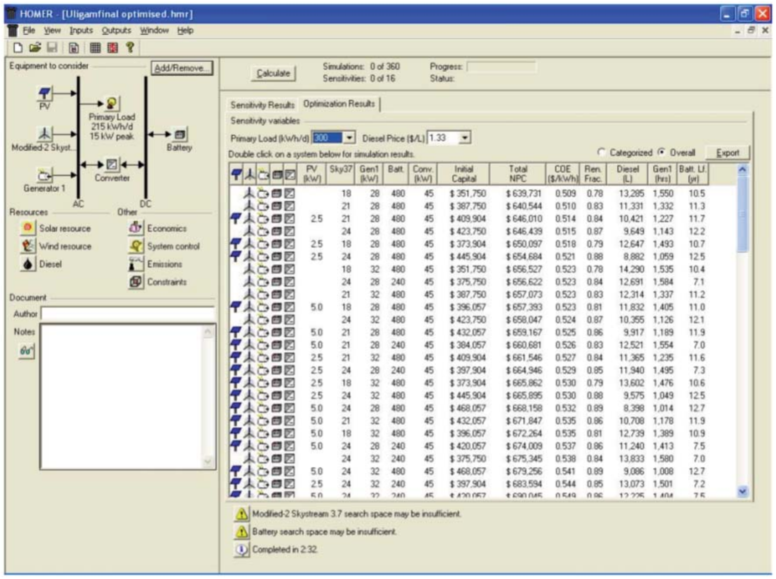

Simulations: 0 of 360
Sensitivities: 0 of 16

Primary Load (kWh/d) 300
Diesel Price ($/L) 1.33

Double click on a system below for simulation results.

PV (kW)	Sky37	Gen1 (kW)	Batt.	Conv. (kW)	Initial Capital	Total NPC	COE ($/kWh)	Ren. Frac.	Diesel (L)	Gen1 (hrs)	Batt. Lf. (yr)
	18	28	480	45	$ 351,750	$ 639,731	0.509	0.78	13,285	1,550	10.5
	21	28	480	45	$ 387,750	$ 640,544	0.510	0.83	11,331	1,332	11.3
2.5	21	28	480	45	$ 409,904	$ 646,010	0.514	0.84	10,421	1,227	11.7
	24	28	480	45	$ 423,750	$ 646,439	0.515	0.87	9,649	1,143	12.2
2.5	18	28	480	45	$ 373,904	$ 650,097	0.518	0.79	12,647	1,493	10.7
2.5	24	28	480	45	$ 445,904	$ 654,684	0.521	0.88	8,882	1,059	12.5
	18	32	480	45	$ 351,750	$ 656,527	0.523	0.78	14,290	1,535	10.4
	24	28	240	45	$ 375,750	$ 656,622	0.523	0.84	12,691	1,584	7.1
	21	32	480	45	$ 387,750	$ 657,073	0.523	0.83	12,314	1,337	11.2
5.0	18	28	480	45	$ 396,057	$ 657,393	0.523	0.81	11,832	1,405	11.0
	24	32	480	45	$ 423,750	$ 658,047	0.524	0.87	10,355	1,126	12.1
5.0	21	28	480	45	$ 432,057	$ 659,167	0.525	0.86	9,917	1,189	11.9
5.0	21	28	240	45	$ 384,057	$ 660,681	0.526	0.83	12,521	1,554	7.0
2.5	21	32	480	45	$ 409,904	$ 661,546	0.527	0.84	11,365	1,235	11.6
2.5	24	28	240	45	$ 397,904	$ 664,946	0.529	0.85	11,940	1,495	7.3
2.5	18	32	480	45	$ 373,904	$ 665,862	0.530	0.79	13,602	1,476	10.6
2.5	24	32	480	45	$ 445,904	$ 665,895	0.530	0.88	9,575	1,049	12.5
5.0	24	28	480	45	$ 468,057	$ 668,158	0.532	0.89	8,398	1,014	12.7
5.0	21	32	480	45	$ 432,057	$ 671,847	0.535	0.86	10,708	1,178	11.9
5.0	18	32	480	45	$ 396,057	$ 672,264	0.535	0.81	12,739	1,389	10.9
5.0	24	28	240	45	$ 420,057	$ 674,009	0.537	0.86	11,240	1,413	7.5
	24	32	240	45	$ 375,750	$ 675,345	0.538	0.84	13,833	1,580	7.0
5.0	24	32	480	45	$ 468,057	$ 679,256	0.541	0.89	9,086	1,008	12.7
2.5	24	32	240	45	$ 397,904	$ 683,594	0.544	0.85	13,073	1,501	7.2
5.0	24	32	240	45	$ 420,057	$ 690,045	0.549	0.86	12,225	1,404	7.5

Modified-2 Skystream 3.7 search space may be insufficient.

Battery search space may be insufficient.

Completed in 2:32.

Figure 6-23 : HOMER system design optimisation and sensitivity results

HOMER was used to assess the possible configurations of renewable energy components after a wind turbine type and location was selected and a PV installation area was assessed. Skystream wind turbine options from 15 to 24 were considered and PV installations of 2.5 – 5kW could be accommodated. A sensitivity analysis on the likely future load and price of diesel were also incorporated into the analysis. Figure

6-23 shows the results of this analysis. Based upon energy availability and cost, wind turbines were favoured to PV at this site. 24 Skystream wind turbines were incorporated into the final design and 2.5kW of PV. An inclusion of PV was justified as the sites solar irradiation was high however lower then expected due to atmospheric particulates from northern countries.

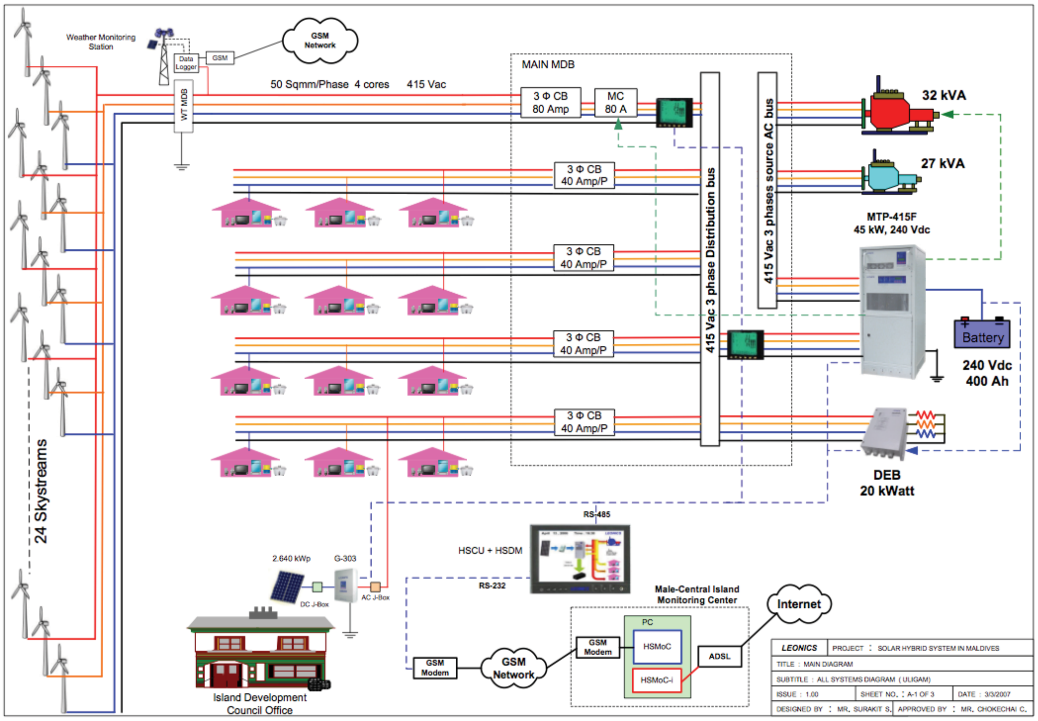

Figure 6-24 : Uligam electrical design

Figure 6-24 shows the final single line drawing for the Uligam electrical system. A central inverter system was chosen with distributed solar and wind resources. A 240V, 400Ahr battery bank was used as the energy storage device and the existing generators were integrated into the system to provide diesel support. The renewable energy components consisted of a single 2.64kW PV array located on the school roof, which was connected through a typical CC-VSI. The wind farm utilises twenty-four 1.8kW Skystream wind turbine. These were selected due to their integrated power electronics, marine environment enclosure rating and small foundation base. Each Skystream inverter was single phase so the interconnection across the farm was alternated to ensure each phase was balanced. It is quite conceivable that the wind may come through at one end of the farm causing phase imbalance. Also a quantity of 24 allows them to be evenly spread across each phase. The main wind farm was laid out on and 6 x 3 grid with 25m spacing, a further eight wind turbines were placed along the road back to the power house. Figure 6-25 was the authors' sketch of the wind turbine layout from the design report.

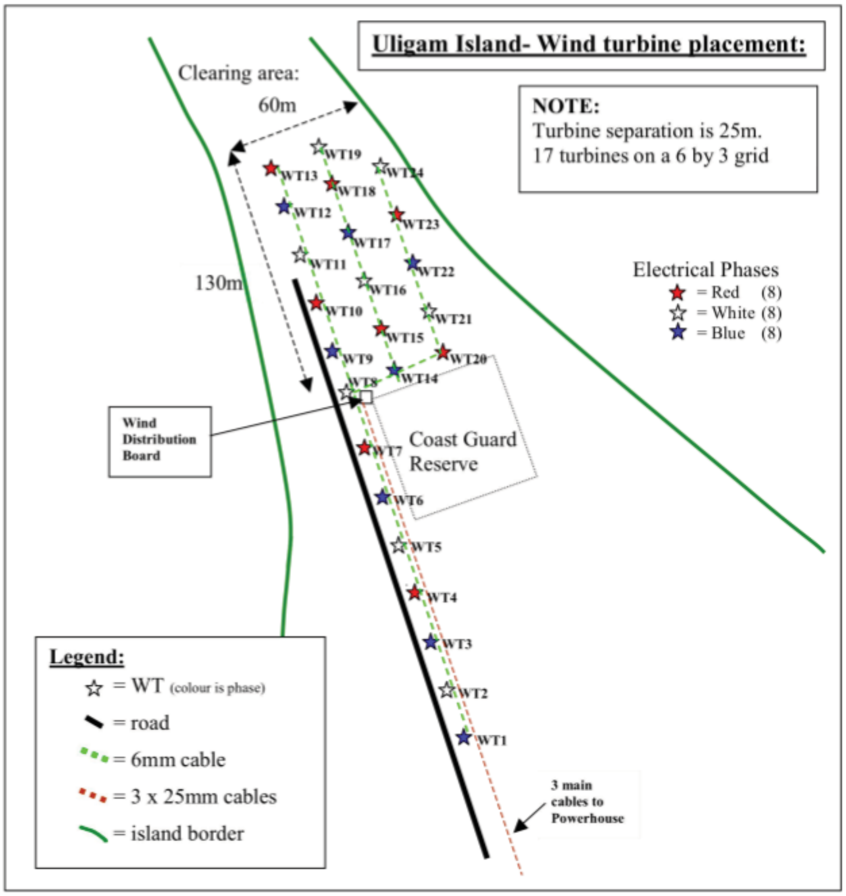

Figure 6-25 : Uligam wind turbine placement map

Simulations in HOMER were carried out to assess the expected wind and solar energy generation levels, diesel usage, battery cycling and battery longevity. A renewable energy penetration level of around 75% was expected for 300kWh loads. Figure 6-26 shows the expected battery cycling and longevity results from HOMER. The expected battery bank to be installed were Hoppecke[9] and these showed an expected life of 7.28 years at this site with a yearly throughput of 22.4MWh/yr. Final financial constraints caused a different battery manufacturer, Exide[10], to be installed, however the battery longevity is assumed to be the same.

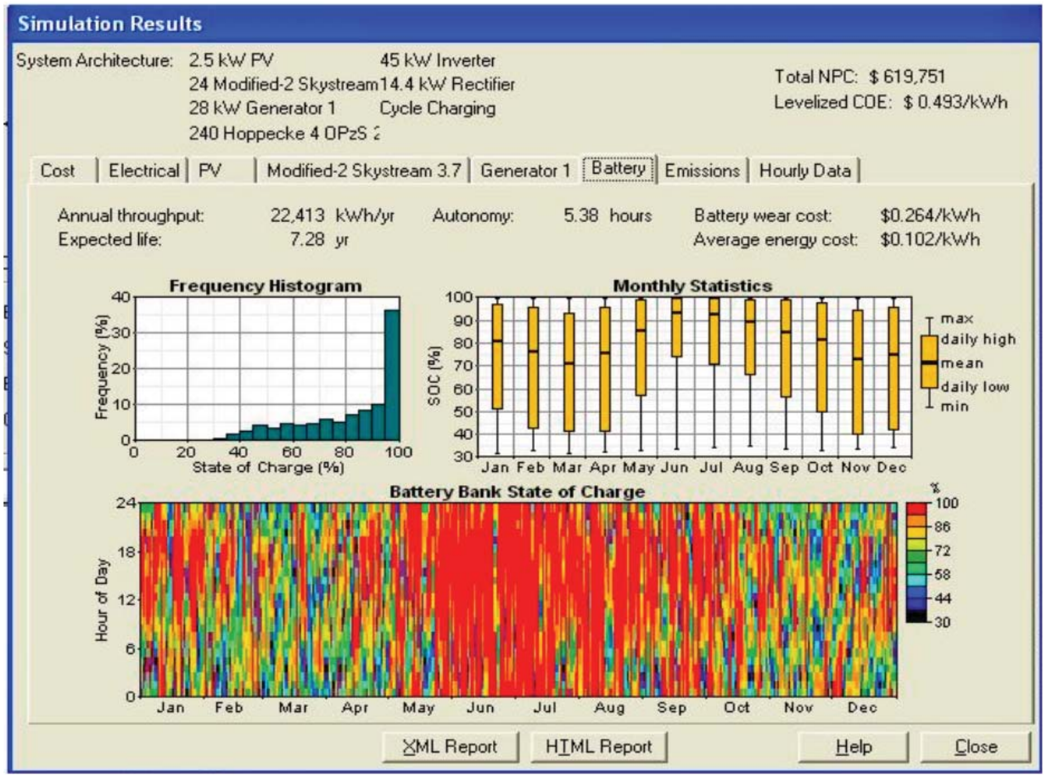

Simulation Results

System Architecture: 2.5 kW PV
24 Modified-2 Skystream
28 kW Generator 1
240 Hoppecke 4 OPzS 2
45 kW Inverter
14.4 kW Rectifier
Cycle Charging

Total NPC: $ 619,751
Levelized COE: $ 0.493/kWh

Annual throughput: 22,413 kWh/yr
Expected life: 7.28 yr
Autonomy: 5.38 hours
Battery wear cost: $0.264/kWh
Average energy cost: $0.102/kWh

Figure 6-26 : Simulation with an average 300kWh daily load

On the 7th of January 2008 the Hybrid Renewable Energy Pilot Project was officially opened on the island of Uligam, Maldives. The simulation and designs were exonerated and the power system now provides 24 hour power to the islands residents. The feasibility study carried out by the author and colleagues was shown to be accurate and will energise the island for many years to come.

6.6. Summary

This chapter combines the previously developed power electronic blocks into a complete control methodology for medium to large scale hybrid power systems, with the goal of increasing the renewable energy penetration and minimising fuel usage. The requirements of diesel generators are now included from a control and interconnection points of view. The inverter control requirements for these differing modes of operation are described and simulated.

A summary of this chapters key section is below

- Large scale hybrid system interconnection methods
- Design methodology for a hybrid system
- Increasing the penetration of renewable energy in large systems
- Integration with DG
- Design example – Turf Farm
- Design example – Maldives Island, Uligam

The key research points of this chapter are:

- Development of a hybrid system design methodology;
- Creation of methods to achieve higher renewable energy penetration levels using inverter control.

6.7. References

1. Nayar, C., M. Dymond, and J. Darbyshire, *Hybrid Power System Design for Uligam Island, Maldives.* March 2007, Regen Power: Perth, Australia.
2. Nayar, C., M. Dymond, and J. Darbyshire, *Hybrid Power System Design for Kondey Island, Maldives.* March 2007, Regen Power: Perth, Australia.
3. Nayar, C., M. Dymond, and J. Darbyshire, *Hybrid Power System Design for Raimandhoo Island, Maldives.* March 2007, Regen Power: Perth, Australia.
4. Nayar, C., et al., *Feasibility Study for Renewable Energy Integration into Turf Farms (WA) site at Mimegarra*. April 2007, Regen Power & Solar Matrix.
5. Lambert, T., *HOMER: the micro-power optimisation model*. 2008, NREL.
6. SWWP, *Skystream 3.7*, in *Data Sheet*. 2008, South West Wind Power: Flagstaff, AZ.
7. Nayar, C.V., M. Tang, and W. Suponthana. *An AC Coupled PV/Wind/Diesel Microgrid System Implemented in a Remote Island in the Republic of Maldives*. in *AUPEC 2007*. 2007. Curtin University of Technology.
8. Chem Nayar, M.T., Wuthipong Suponthana. *An AC Coupled PV/Wind/Diesel Microgrid System Implemented in a Remote Island in the Republic of Maldives*. in *AUPEC 2007*. 2007. Curtin University of Technology.
9. Hoppecke, *OPzV Valve regulated lead-acid battery*, in *Hoppecke: Power from innovation*. 2007, Hoppecke: Brion, Germany.
10. Tubular, E., *Data Sheet: Product Features for Exide Tubular Lead-acid Batteris*. May 2007, Exide.

"Every reasonable effort has been made to acknowledge the owners of copyright material. I would be pleased to hear from any copyright owner who has been omitted or incorrectly acknowledged."

7. Design, Control and Energy Management for Hybrid Systems

This final chapter presents the complete system design, control and implementation of the Eco Wilderness Resort project[1], from which the author was the design engineer and electrical project manager for Regen Power. The project encompasses a large decentralised electrical system with 24 2kW PV arrays and a 120kW three phase central inverter with integrated generator control. This is the largest and only system of its type in Australia. The system operates using frequency control to shed excess distributed renewable energy sources. This method of control is modelled and simulated in PSIM[3]. The different modes of control are shown and the methodology imposed to store excess renewable energy for operation during the night is shown. A key concern of the client was the silent operation of the system through out the night allowing guests to hear the natural surroundings.

7.1. Design Example for a Large De-centralised RAPS System

7.1.1. Eco Beach Project Overview

Eco Beach Wilderness resort is the first large scale, over 100kW, fully hybrid renewable power system in Western Australia. In June 2008 Regen Power[4] were approached to create a feasibility study for the site. This study was completed and an application was submitted to the Sustainable Energy and Development Office for $500,000 of the $1.2M project. After 12 weeks the application was approved and Regen Power was contracted to design, install and commission the power system for the resort. This was completed in late April 2009.

The final power system consisted of 24 x 2kW PV arrays, a 120kW central bi-directional inverter with a 360V, 1500Ahr battery bank and 4 x 50kW diesel generators. Each villa had a power monitoring device installed which tracked the renewable energy generated and the actual energy used in the villa, this allowed energy conscious guests to audit their usage during their occupancy.

Figure 7-1 : Eco Beach Layout

Figure 7-1 shows an aerial layout of the entire site. The villa's are seen on the right near the coast and also further inland, with tin roofs. Each villa had a 2kW PV array installed on it most northern facing roof. The power station is tin roof building on the left inland, the largest load Jack's Bar is in the centre by the coast. The system was designed with two main design principles, minimise the use of diesel fuel as it was an eco tourist resort and run diesel off at night time to allow the natural sounds be heard throughout the night. These two requirements ensured that an inverter based system would be required with maximum solar penetration and a large battery bank to carry the load throughout the night.

As Eco Beach was a greenfields site the power level and energy consumption were unknown. A detailed energy audit of the system was carried out, APPENDIX A5, and the system loads were predicted to be as seen in Table 7-I. From this analysis an absolute peak load of 120kW was expected with a surge not greater then 150kW and an energy requirement of up to 600kWh per day. Scaling values based upon resort occupancy were factored in to create seasonal and monthly load profiles. These were entered into HOMER and can be seen in Figure 7-2.

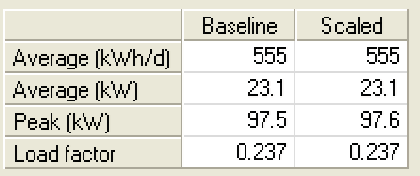

	Baseline	Scaled
Average (kWh/d)	555	555
Average (kW)	23.1	23.1
Peak (kW)	97.5	97.6
Load factor	0.237	0.237

Table 7-I: Eco System Loads

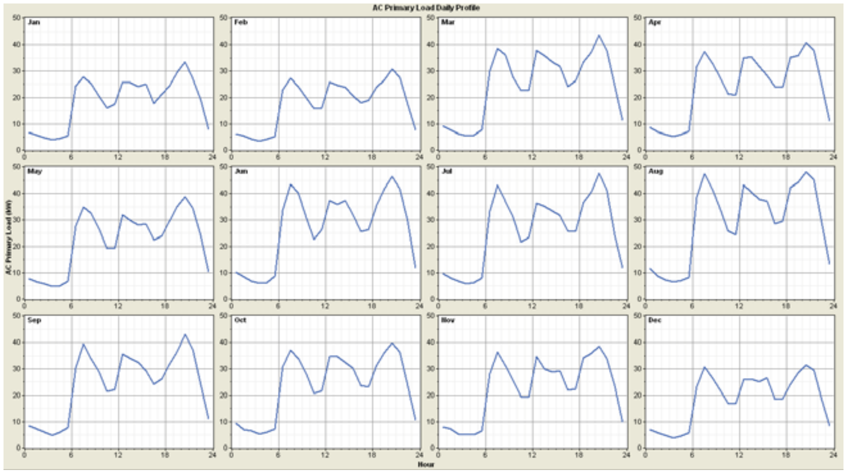

Figure 7-2 : Predicted daily load profile per month

A frequency analysis of the load profile was carried out over a year in HOMER[5]. This approach allows the sizing of generators to be optimised as the system loading may be expressed as probability distribution, Figure 7-3. Eco beach, due to the no night noise requirement, had to use a bi-directional central inverter, which allows the system to operate in VC-VSI and CC-VSI modes. This CC-VSI feeding functionality allows the inverter to cover the small scale changes in load profile and attempt to hold the DGs at a constant optimal load, in this case 80%. This ability ensures the generators are never lightly loaded or transiently overloaded extending their operational lifetime. Figure 7-3 shows that for the majority of the systems operation the load is below 50kW, the inverter control can be adjusted to allow inverter only operation below 30kW load, one DG with battery charging for loads between 30 – 45kW holding the DG at 40 - 45kW and inverter feeding operation for loads greater then 45kW. Each mode of operation requires a feedback control based upon the battery SOC to enable the operation. For this design four 50kVA DG were selected which would allow optimised single engine operation for a large proportion of the day and two engine operation in the evening to power higher kitchen loads and top up the battery for the night time requirement.

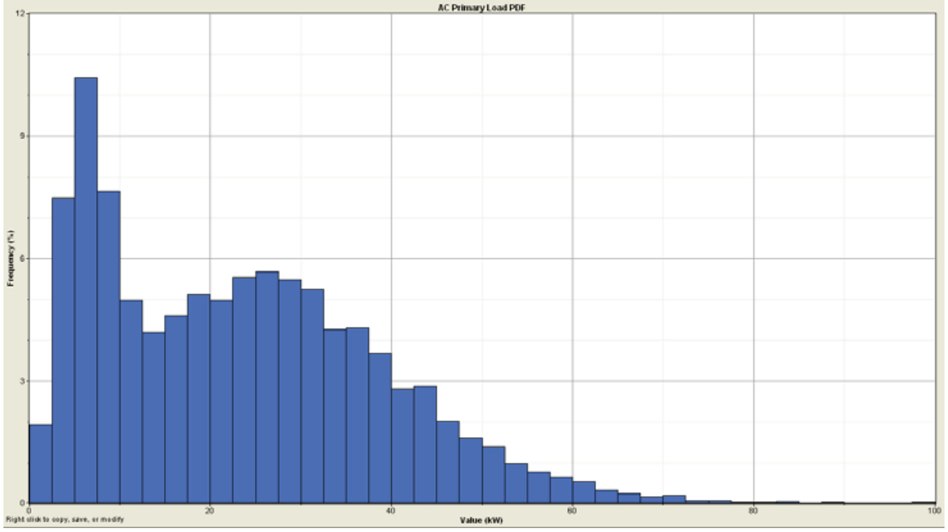

Figure 7-3 : System load frequency distribution

Four Hino 50kVA generators were selected with ComAp Intelligen[6] paralleling controllers. The maximum ever required by the system should be three so one is allowed to be in maintenance without any adverse effect on the system operation. The inverter control system does not directly communicate with the Intelligen system. Controlling the power extracted from the DG bus carries out the signalling to start or stop a DG. If another DG is required the inverter decreases the power it is feeding to the load, subsequently increasing the load on the DGs. When the DG load reaches 90% the paralleling controller automatically calls for another engine to come online and synchronises, the inverter receives a status signal to show this generator is now online. The inverter can now switch and draw a current to charge the batteries, again optimising the load on the DGs.

The amount of renewable energy that can be implemented into the system was primarily selected from financial requirements. A SEDO rebate of $500,00 was available for a $1M system. The owner wished to financially optimise this rebate so the renewable energy system was limited to this value. Initially the engineering design requested a total solar component of 78kW of PV and three 3kW wind turbines. This was later reduced due to the large decrease in the value of the Australian dollar in the latter part of 2008. The final system could only financially facilitate 24 x 2kW solar arrays on the villas. It is hoped in future a 20kW DC coupled PV array may be installed on the powerhouse roof.

The solar irradiation information was collected from BoM[7] ground irradiation data at Broome Airport, some 80km away. This monthly information was entered into HOMER to create the expected monthly variations in energy yield. This information is shown in Table 7-II and Figure 7-4.

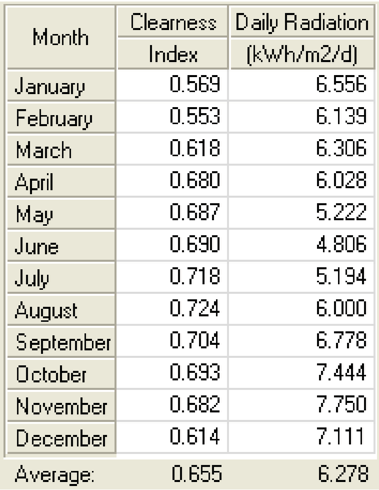

Month	Clearness Index	Daily Radiation (kWh/m2/d)
January	0.569	6.556
February	0.553	6.139
March	0.618	6.306
April	0.680	6.028
May	0.687	5.222
June	0.690	4.806
July	0.718	5.194
August	0.724	6.000
September	0.704	6.778
October	0.693	7.444
November	0.682	7.750
December	0.614	7.111
Average:	0.655	6.278

Table 7-II: Broome monthly solar data

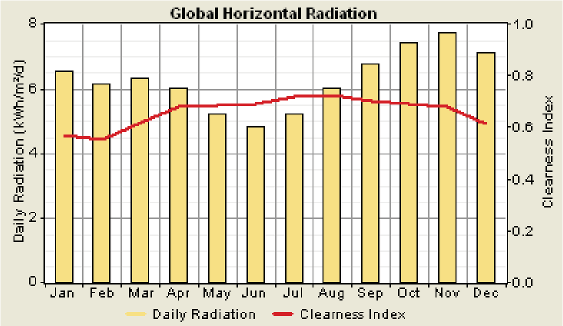

Figure 7-4 : Eco HOMER solar plot

An energy analysis was created from the load profile, solar profile and system schematic. This showed that the final system should achieve a renewable energy penetration of 32.7% with a PV generation of 92,251kWh/yr. The expected wasted energy was only 0.63% of the predicted total 282,530kWh/yr load. These results are shown below in Figure 7-5.

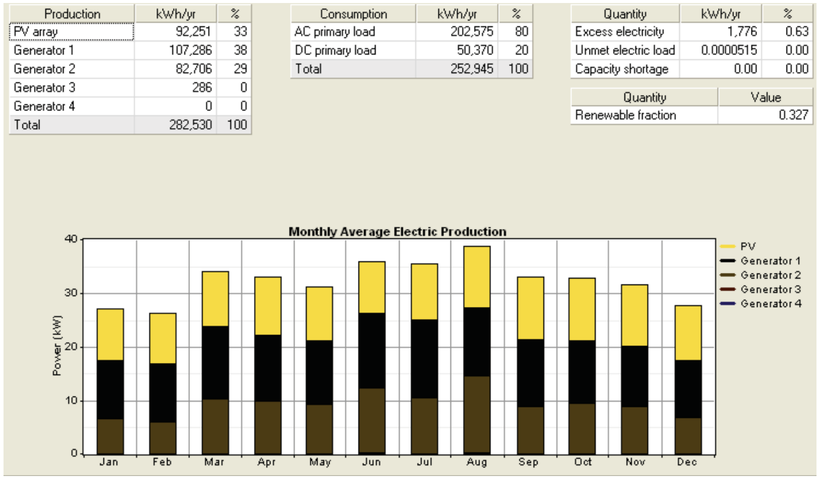

Production	kWh/yr	%
PV array	92,251	33
Generator 1	107,286	38
Generator 2	82,706	29
Generator 3	286	0
Generator 4	0	0
Total	282,530	100

Consumption	kWh/yr	%
AC primary load	202,575	80
DC primary load	50,370	20
Total	252,945	100

Quantity	kWh/yr	%
Excess electricity	1,776	0.63
Unmet electric load	0.0000515	0.00
Capacity shortage	0.00	0.00

Quantity	Value
Renewable fraction	0.327

Figure 7-5 : HOMER Electrical load components

A 120kW central inverter and hybrid controller was selected as the main power and control source for the system. This inverter is nominally operated from a 360V battery bank, which reduces the overall DC cable losses. The capacity of the battery bank was selected based upon the expected cycling requirements, minimal depth of discharge and minimum longevity of the battery bank. A model for the battery used in the system is available from the Hoppecke[8] website and was imported to HOMER for simulation. Details of this battery system is seen in Figure 7-6.

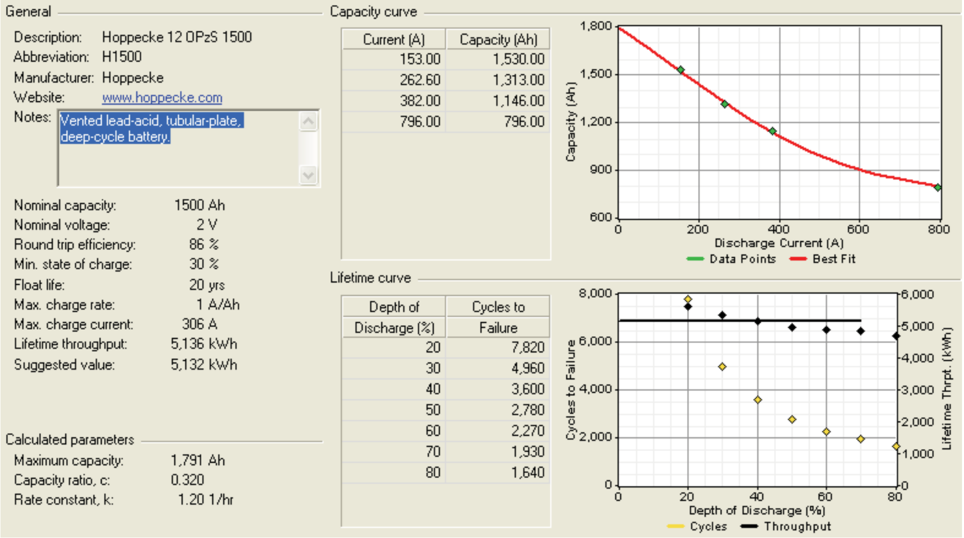

General

Description: Hoppecke 12 OPzS 1500
Abbreviation: H1500
Manufacturer: Hoppecke
Website: www.hoppecke.com
Notes: Vented lead-acid, tubular-plate, deep-cycle battery.

Nominal capacity:	1500 Ah
Nominal voltage:	2 V
Round trip efficiency:	86 %
Min. state of charge:	30 %
Float life:	20 yrs
Max. charge rate:	1 A/Ah
Max. charge current:	306 A
Lifetime throughput:	5,136 kWh
Suggested value:	5,132 kWh

Calculated parameters

Maximum capacity:	1,791 Ah
Capacity ratio, c:	0.320
Rate constant, k:	1.20 1/hr

Capacity curve

Current (A)	Capacity (Ah)
153.00	1,530.00
262.60	1,313.00
382.00	1,146.00
796.00	796.00

Lifetime curve

Depth of Discharge (%)	Cycles to Failure
20	7,820
30	4,960
40	3,600
50	2,780
60	2,270
70	1,930
80	1,640

Figure 7-6 : Hoppecke battery bank profile

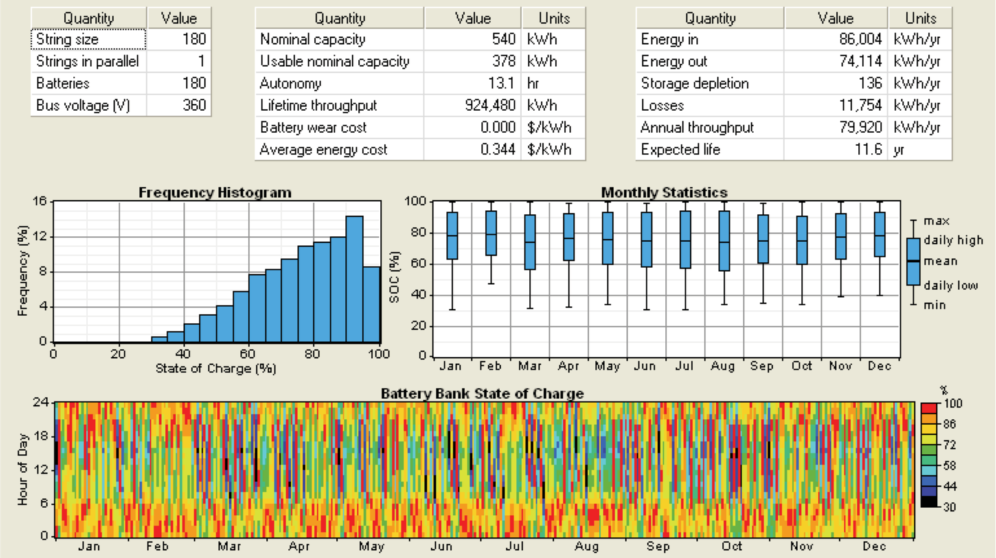

Quantity	Value
String size	180
Strings in parallel	1
Batteries	180
Bus voltage (V)	360

Quantity	Value	Units
Nominal capacity	540	kWh
Usable nominal capacity	378	kWh
Autonomy	13.1	hr
Lifetime throughput	924,480	kWh
Battery wear cost	0.000	$/kWh
Average energy cost	0.344	$/kWh

Quantity	Value	Units
Energy in	86,004	kWh/yr
Energy out	74,114	kWh/yr
Storage depletion	136	kWh/yr
Losses	11,754	kWh/yr
Annual throughput	79,920	kWh/yr
Expected life	11.6	yr

Figure 7-7 : HOMER battery cycle analysis

HOMER allows an annual battery cycling analysis to be easily simulated, Figure 7-7. The expected battery lifetime is 11.6 years with an annual battery throughput of 80MWh. The battery SOC should never fall below 30 with it nominally operating between 60 and 95%. The lowest annual SOC is expected in the middle of the year June to August when the occupancy and loads are the highest and the solar irradiation levels are low.

7.1.2. Frequency Shift Power Control

A major concern for decentralised hybrid systems is the excess generation of renewable energy, which cannot be absorbed by either the loads or battery bank[9]. Traditionally dump loads have been included into the design to allow for this over generation. Maldives project from the previous chapter use a “dynamic energy balancer” which allows excess energy to be sunk when the system is overloaded [10-13]. Many systems such as Rottnest Island use the thermal component of this energy to warm the generators, slightly increasing their efficiency. However with all of these methods electric energy is wasted in the form of heat to protect the power system.

The Eco Beach Wilderness Resort design with 24 decentralised PV arrays did not easily allow the utilisation of a dump load, which would have increased the overall project cost. Direct communications to the inverters was considered but did not offer the reliability as required for this system protective function. Finally frequency shift power control was considered and implemented.

Frequency shift power control implements a linear frequency band between 50.5 and 52 Hz that is detected by the decentralised inverters and enacts a power limitation. The central inverter will begin to change the system frequency once the battery is above a SOC of 80% and is in a VC-VSI mode. The charging efficiency of the VRLA battery is lessened at SOC’s greater than 80%, allowing the battery to remain around this charge state, thus optimising the energy storage device.

The Sunny Island product from SMA utilises a similar control technique however it is designed to work with only a few distributed resources and its exact operational methods are held as SMA intellectual property [14, 15]. Other references to proposed systems using the SMA approach has been presented at the World Climate & Energy Event in 2009[16], Studer Innotec a Swiss power electronics company have some literature on the concept and appear to be using a similar method to SMA[17, 18].

The differences between the SMA frequency shift power control and the one proposed in this dissertation are:

- The number of controlled devices on this mini-grid is twenty four, this is greater then any project using the SMA technique found by the author.
- The frequency shift is also used to optimise the energy efficiency of the battery and not only as a safety function.
- The power and battery voltage levels are significantly higher then that applied by the SMA device. The central inverter is 120 kW at 360 Vdc whereas the SMA operates at 5 kW at 48 Vdc.
- The distance area responsive to the frequency shift control is much larger then that used with any SMA project found by the author.

7.1.3. Eco Beach System Control

The control topology for Eco Beach required the switchboard to be designed with a split bus topology, Figure 7-12. This method allows the inverter controller to call for DGs, which will synchronise on a separate bus before allowing them to feed power to the loads. The interconnection between the load bus and DG bus is controlled through a large controllable motorised circuit breaker, known as a bus coupler. This topology allows the inverter full and constant control over the load bus. In an emergency situation the inverter control can be disengaged and main inverter CB opened and the bus coupler manually closed allowing conventional DG plant type operation.

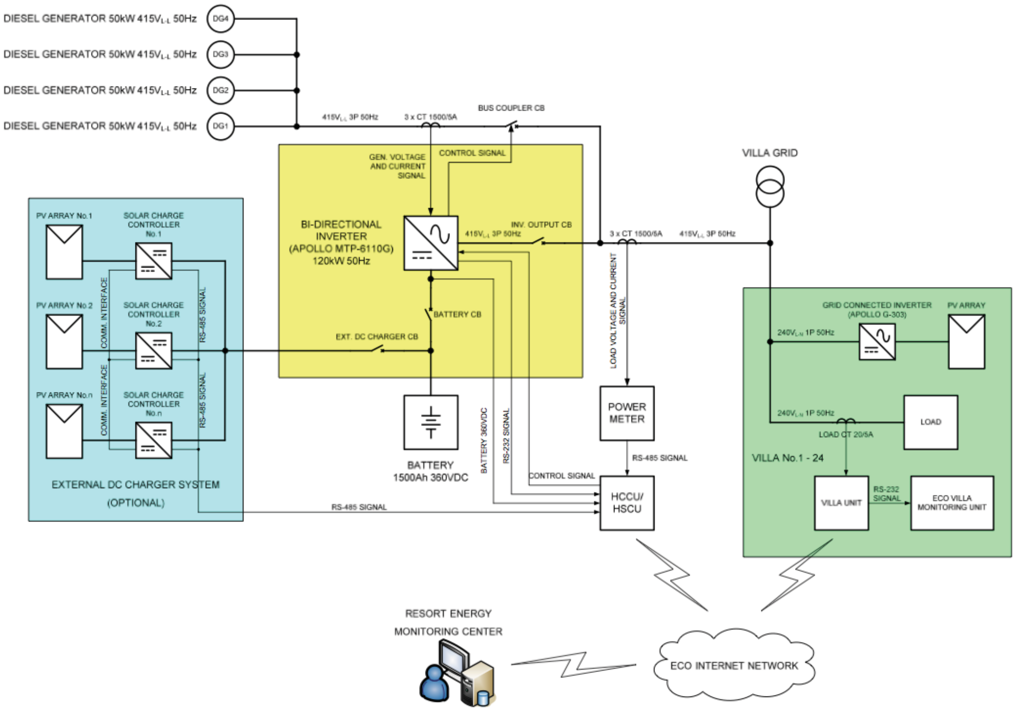

Figure 7-8 : Eco system topology

Figure 7-8 shows this connection topology in the form of a single line diagram. The main loads are seen by the villa grid, which represents the main system feeders. The distributed 24 x 2kW PV arrays and field inverters are seen in the green box with their remote wireless monitoring interface back to the central resort energy monitoring centre. At the power house the central inverter is directly connected to the villa grid and the DGs form a separate grid and its interconnection is formed through the bus coupler controlled by the inverter. CT's and voltage sensors are seen for both the DG bus and net feeder load. The HCCU monitors these the main system parameters, battery SOC, net load, DG load and inverter load as well as time of day for likely future energy requirements and communicates the optimal mode for which the inverter should operate.

The central inverter can operate in four different basic modes; inverter, charging, feeding and standby. During inverter only mode, VC-VSI, Figure 7-9, the central inverter controls the voltage frequency on the grid. All DG are off and any excess energy generated by the distributed PV CC-VSI's can be used to charge the battery. This system can operate in VC-VSI mode with a negative charging current. If the battery is full frequency variation is adopted to allow the central inverter to vary the power generated by the distributed field inverters. This technique was developed collaboratively with the manufacturer to prevent overcharging of the battery bank and this is the first application of this technology within Australia. A frequency band between 50.5Hz and 52Hz is used by the central inverter and monitored by the field inverters. A linear power shedding regime is used within this frequency band so that at 52Hz the power from the field inverters is down to 0%. To the authors knowledge at the installation date this is the largest deployment of this control method in the world. A simulation of the system in the following sub chapter shows the implementation of this type of controller.

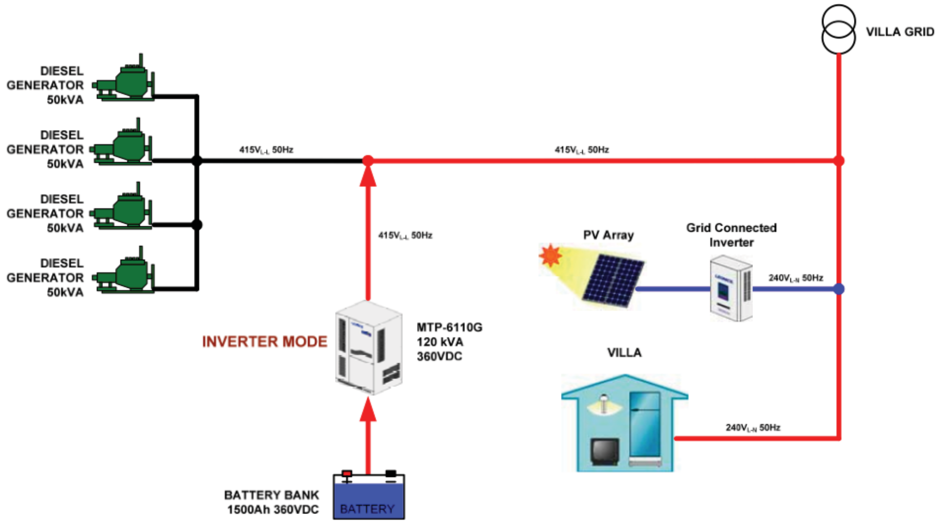

Figure 7-9 : Inverter mode

The charging mode is used when the battery bank has a reduced SOC, and the DGs require to be optimised by drawing extra current, and the battery has some spare capacity or the battery SOC needs to be increased to allow night time operation. The power flows during this mode are seen in Figure 7-10.

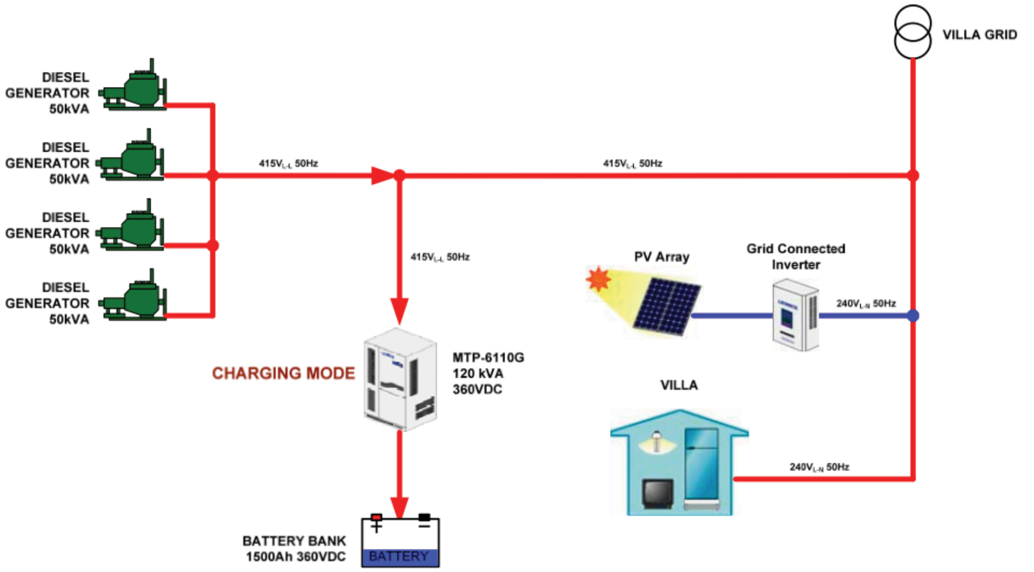

Figure 7-10 : Charging mode

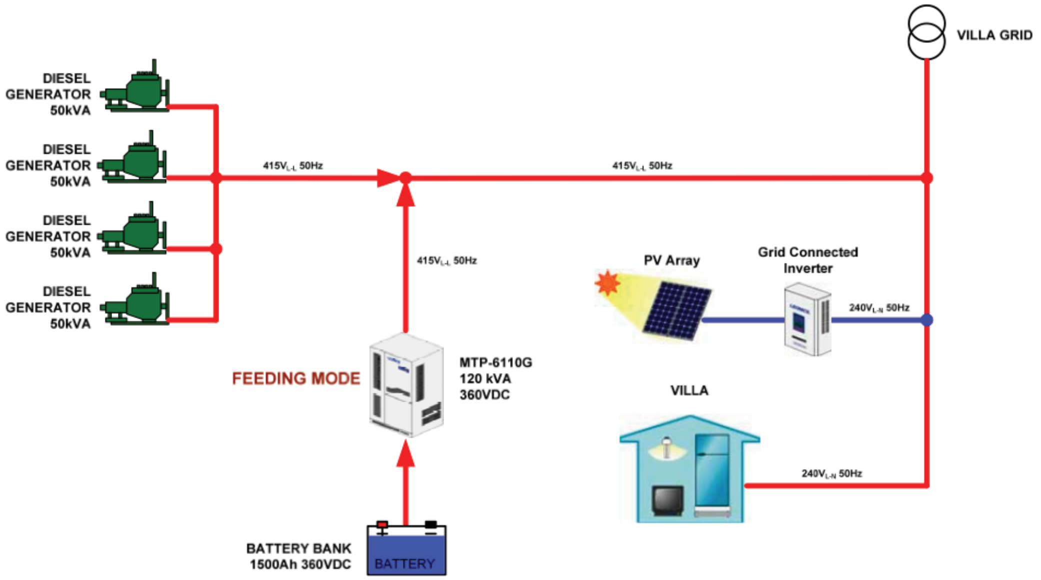

Figure 7-11 : Feeding mode

Feeding mode operation, Figure 7-11, is used when the battery is at a high SOC and the DGs are operating at a high level. The inverter will operate as a CC-VSI and feed power to optimise the loading of the DG or prevent another DG from starting from a transient load such as a fridge compressor or finally, allow an additional DG to shut down as the load is at an inefficient level between one and two generators.

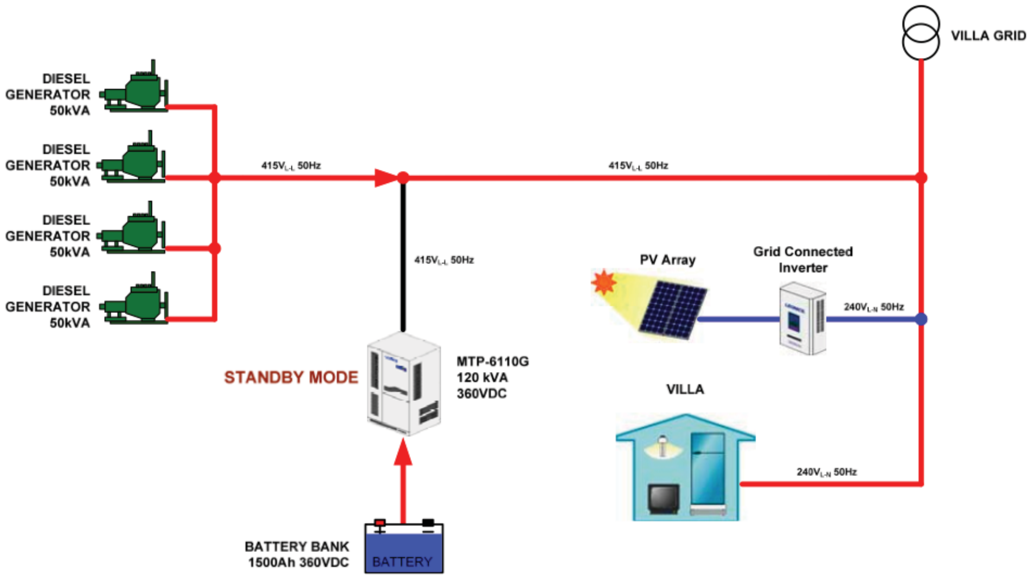

Figure 7-12 : Standby mode

Standby operation is selected when the battery is at a high enough SOC for the general time based variables and the DG are naturally operating at a power level which is quite efficient. This is a UPS type operation where if for some reason a DG fault occurred the inverter could quickly pick up the load and either prevent or only cause a momentary blackout. The difference between blackout and momentary blackout is determined by the instantaneous load, this transient power must be sourced quickly by the DC bus capacitor storage. If the load is too great the inverter's internal capacity cannot cover the energy and must start slowly to carry the load and prevent damaging current transients within the inverter.

7.2. Eco Beach Control Simulation

7.2.1. System and frequency control model

To simulate the Eco Beach system the large central inverter was modelled in PSIM [3], it could operate in either VC-VSI or CC-VSI, only a single phase of the system was modelled. The VC-VSI operated with voltage feedback control and CC-VSI using the hysteresis current control method. The central inverter was rated to 40kW, a third or single phase of the full system, and was based around the H-bridge topology as seen in Figure 7-13. To allow implementation of the frequency shift control the central inverter required the ability to shift its frequency based upon the state of charge of the battery, this control is implemented in the FunctionGenerator.dll dynamic link library compiled C code.

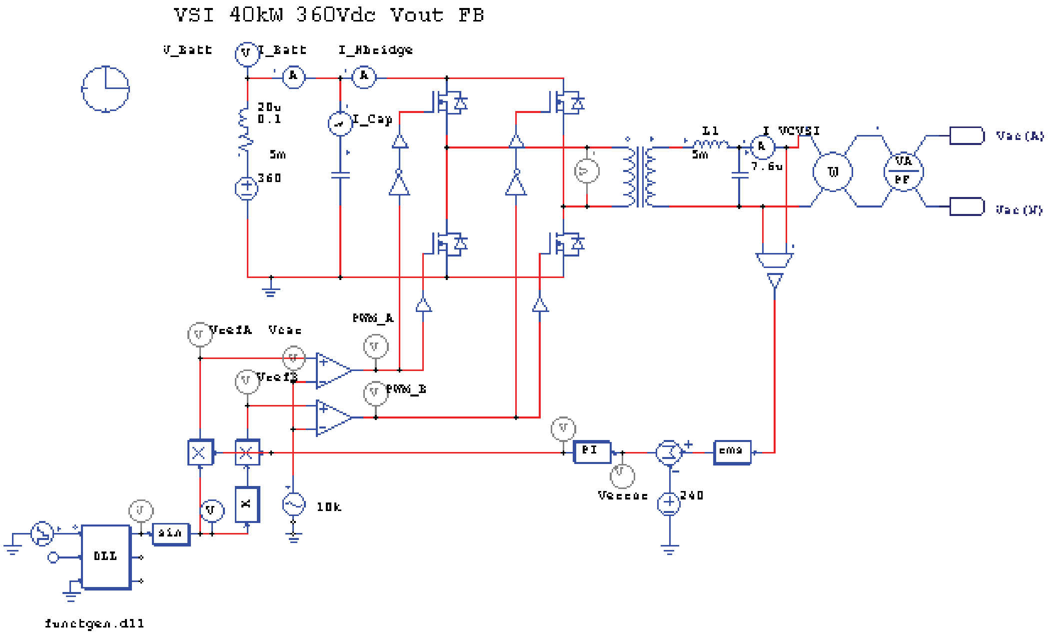

Figure 7-13 : Central inverter PSIM model

The central inverter output frequency is determined by the SOC of the battery. A linear frequency band between 50.5Hz and 52Hz is generated once the battery SOC is greater than 80%. This prevents the possibility of a back feed of current, which could overcharge the battery or damage the dc bus capacitors. The expression used to define the system frequency is seen in Eq 7-1.

$$
\begin{aligned}
f &= f_{base} + \Delta f \\
f_{base} &= 50 \\
\Delta f &= 7.895(SOC - 389.145) \\
\therefore f &= 7.895(SOC + 5.596) : \mathrm{SOC} \geq 0.8
\end{aligned}
$$

Eq 7-1 : Frequency shift control expressions

```
//FunctionGenerator.dll

//James Darbyshire
//Copyright 2009

#include <math.h>
__declspec(dllexport) void simuser (t, delt, in, out)
double t, delt;
double *in, *out;
{
        double SOC, timer;
        static double count, freq, value_x, value_y; //Make sure u use a static double for counters!
//INPUTS
        SOC = in[0];
        timer = in[2];
//CODE
//frequency load shedding
        if(SOC >= 0.8)
        {
                freq = (1/0.1266667)*(SOC + 5.5966667);
        }
        else
        {
                freq = 50.0;
        }

//function generator
if(value_y >= 360)
{
        value_y = 0;
        count = 0;
}
else
{
count++;
value_x = timer*count;
value_y = 360*freq*value_x;

if(value_y >= 360)
{
value_y = 360;
}
}

//OUTPUT
out[0]     = value_y;
out[2]     = SOC;
out[2] = freq;
}
```

Once the system frequency is known this is used to create a ramp, which can be fed to the sine block and converted to a sinusoid of the required frequency. The ramp counts up from 0 to 360 degrees while the counting width is varied proportionally with both the internal PSIM counter and the desired frequency.

The distributed CC-VSI which model the roof top PV arrays are combined into a single system with a maximum output of 16kW, a single phase of the total 48kW system. To decrease computational time the CC-VSI is modelled as a battery type CC-VSI where the current is limited based upon the PV output to 65A. The standard H-bridge topology is used with a hysteresis current controller. The current limitation is based upon the power limiter circuit which, updates the maximum inverter current, Figure 7-14. A standard implementation of the current controller and phase lock loop are utilised, Figure 7-15.

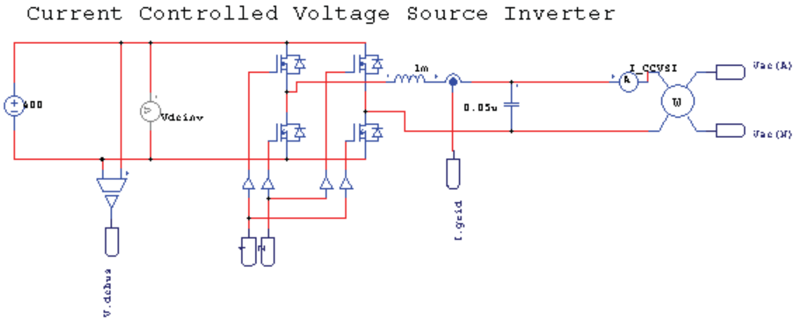

Figure 7-14 : Eco combined CC-VSI

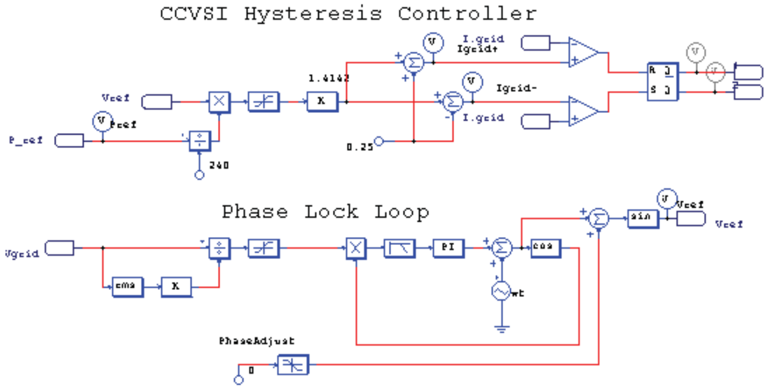

Figure 7-15 : Hysteresis current controller and PLL

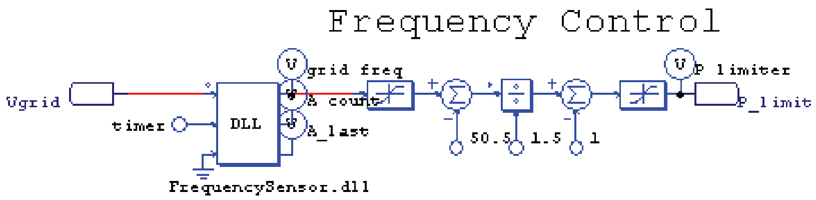

Figure 7-16 : Frequency shift control

The CC-VSI previously modelled has not been required to sense the grid frequency, in order to implement frequency shift control a PSIM frequency sensor block was developed. This block was created as a dynamic link library, compiled C code below.

```
//FrequencySensor.dll

//James Darbyshire
//Copyright 2009

#include <math.h>
__declspec(dllexport) void simuser (t, delt, in, out)
double t, delt;
double *in, *out;
{
        double V_source, timer;
        static double A_count, A_last, freq, freq4, freq3, freq2, freq1, freqave; //Make sure u use a static
double for counters!!!

//INPUTS
        V_source = in[0];
        timer = in[2];

//CODE
        if(V_source > 0)
        {
        A_count++;
        }
        if(V_source < 0)
        {
                A_last = A_count;
                A_count = 0;
        }
        if(A_last > 0 && 1/(2*A_last*timer) < 60 )
        {
        freq = 1/(2*A_last*timer);
        freq4 = freq3;
        freq3 = freq2;
        freq2 = freq1;
        freq1 = freq;
        freqave = 0.25*(freq1 + freq2 + freq3 + freq4);
        }

//OUTPUT
out[0]  = freqave;
out[2]  = A_count;
out[2]  = A_last;
}
```

The frequency sensor block monitors the ac voltage waveform and starts a counter at a zero crossing. At the next zero crossing the counter is compared with the internal PSIM simulation increment timer and the system frequency is calculated. A four point moving average was used to prevent any rapid frequency shift which caused PI controller hysteresis, the frequency is also expected to be less than 60Hz, this band was used to prevent zero crossing distortion from adversely affecting the simulation. Once the grid frequency has been accurately determined the corresponding power limit of the CC-VSI is determined by Eq 7-2.

$$P_{\text{limit}} = 1 - \left(\frac{f_{grid} - 50.5}{\Delta f} \right)$$

Eq 7-2 : CC-VSI power limit

Finally the power controller block dynamic link library compares the CC-VSI power limit with the actual operating power. If the operating power is too great the actual output is reduced to the power limit. The control block passes the new limit to the inverter current control algorithm, as seen in Figure 7-17.

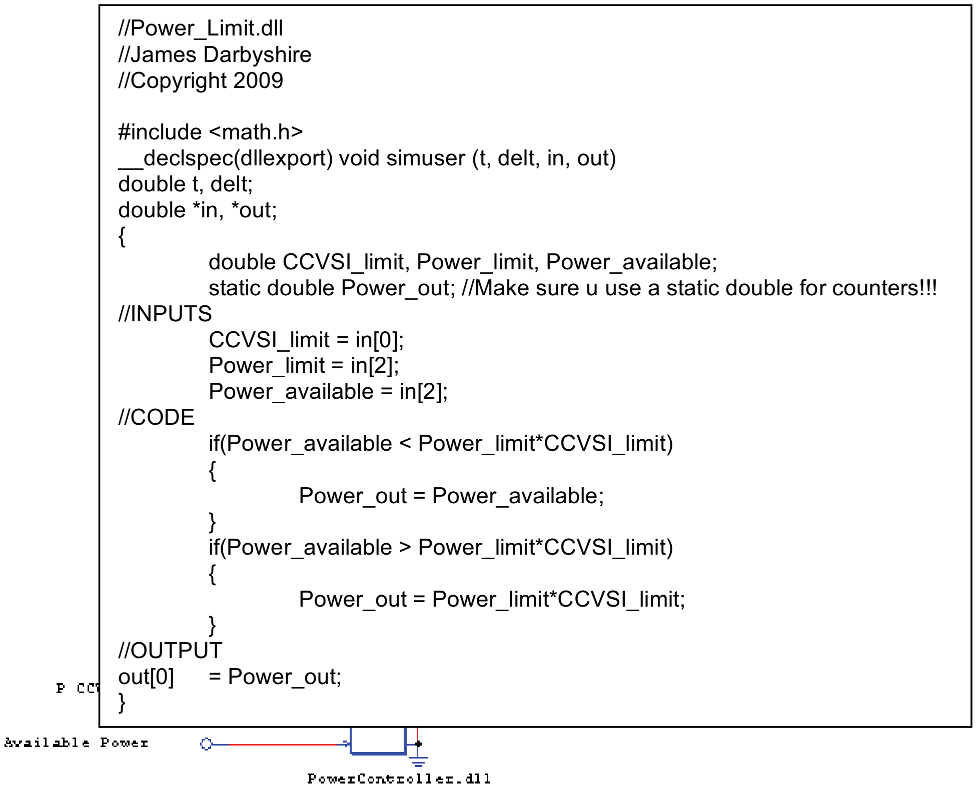

```
//Power_Limit.dll
//James Darbyshire
//Copyright 2009

#include <math.h>
__declspec(dllexport) void simuser (t, delt, in, out)
double t, delt;
double *in, *out;
{
            double CCVSI_limit, Power_limit, Power_available;
            static double Power_out; //Make sure u use a static double for counters!!!
//INPUTS
            CCVSI_limit = in[0];
            Power_limit = in[2];
            Power_available = in[2];
//CODE
            if(Power_available < Power_limit*CCVSI_limit)
            {
                        Power_out = Power_available;
            }
            if(Power_available > Power_limit*CCVSI_limit)
            {
                        Power_out = Power_limit*CCVSI_limit;
            }
//OUTPUT
out[0]      = Power_out;
}
```

Figure 7-17 : CC-VSI power controller block

The load was controlled as a single impedance which was linked between the CC-VSI and VC-VSI. The component values could be changed in a time based method to model the load profile.

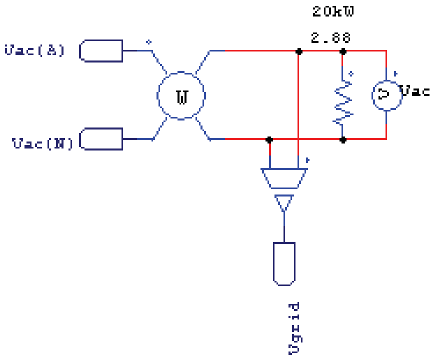

Figure 7-18 : Load simulation

7.2.2. Simulation of a changing load

Switching 10kW loads onto the system at 0.2s increments simulates a changing load, this is synonymous with a load bank test however the speed of the transition is faster then likely in the experimental test. The load set up is seen in Figure 7-19. The available solar irradiance is assumed to be 1kW/m^2 corresponding to 16kW of generated power.

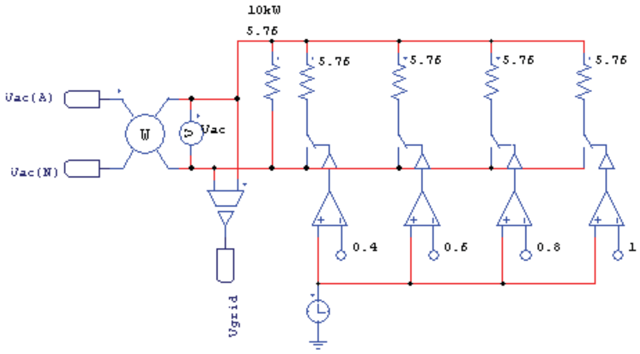

Figure 7-19 : 10kW to 50kW load changes

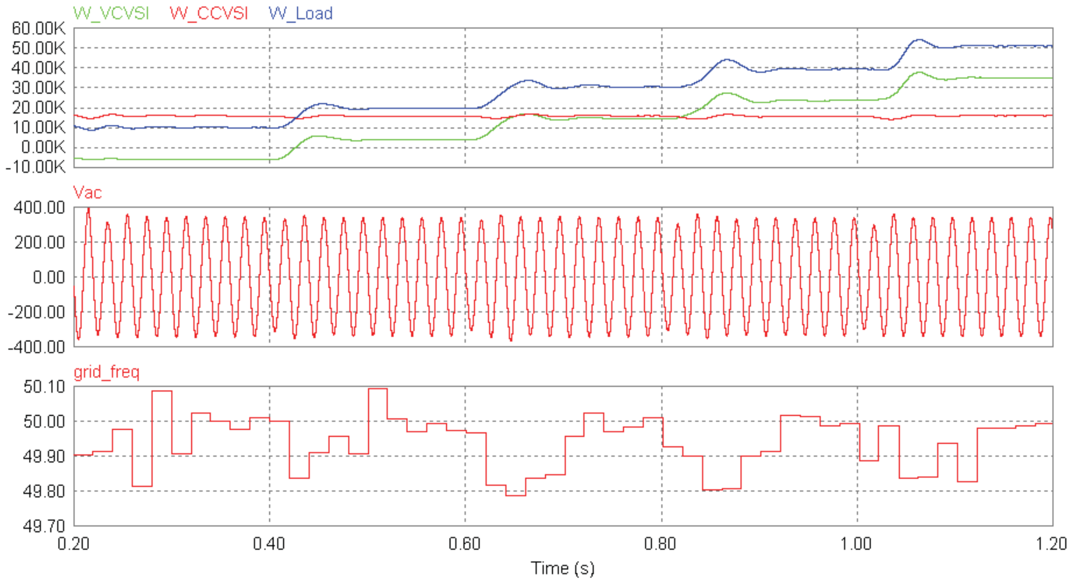

Figure 7-20 : Eco load test simulation

Figure 7-20 shows the changing power, voltage and frequency from the step load tests. An initial grid load of 10kW is entirely carried by the CC-VSI with the remaining 6kW flowing to the battery via the bi-directional VC-VSI. As the grid load increases in steps the VC-VSI supplies all the required power. During each step load the frequency on the ac bus is seen to droop in both voltage and frequency. The PI controller of the VC-VSI quickly brings these parameters back to the desired 240V, 50Hz within a few cycles. The frequency sensors averaging function causes the waveform to look slightly more delayed then the system would actually represent.

7.2.3. Simulation of changing solar irradiation

The changing solar irradiation simulates a cloud event occurring over the resort. As the cloud passes over the CC-VSI output will rapidly fall, this is usually no faster than one second. The simulation quickly ramps the CC-VSI power output from 16kW to 0kW. Figure 7-21 shows the CC-VSI quickly decreasing and the VC-VSI correspondingly picking up the load. The decrease in CC-VSI is seen as an extra load to the VC-VSI but the smooth decrease prevents a significant frequency droop occurrence.

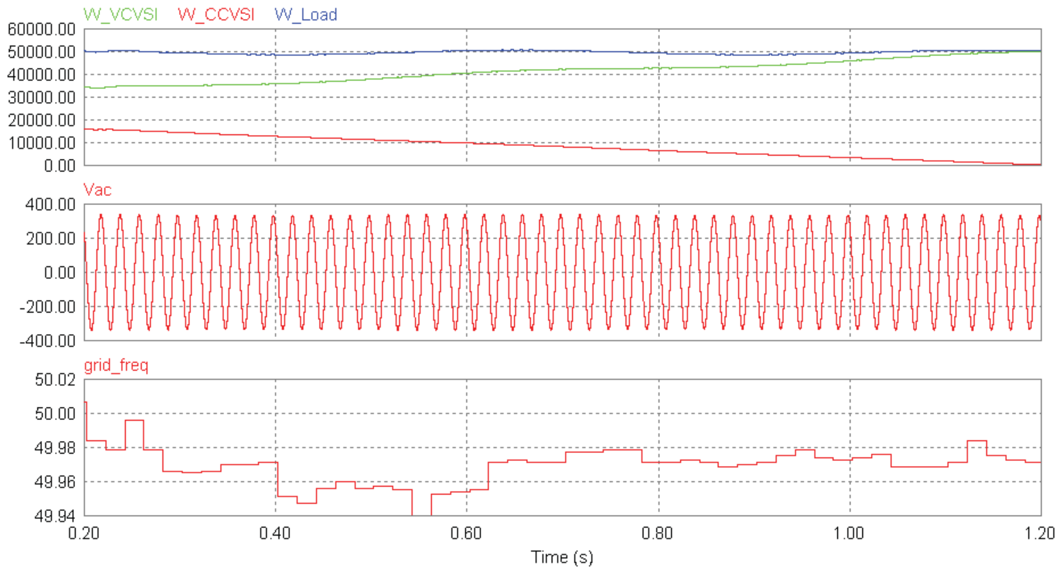

Figure 7-21 : Cloud event simulation

7.2.4. Simulation of changing load and solar irradiation

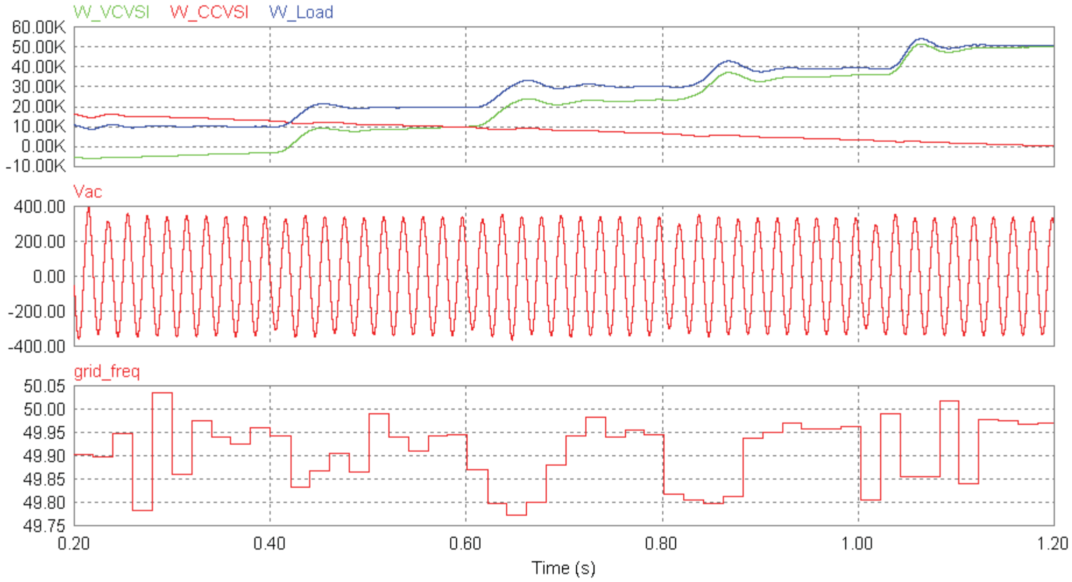

Figure 7-22 : Eco PV decrease and load test simulation

The simulation above, Figure 7-22, shows the combination of 10kW step load changes and solar irradiance dropping from 1kW/m^2 to 0kW/m^2 over 1s. As the solar irradiance decreases the CC-VSI output also decreases proportionally. The VC-VSI increases its power to keep the load current at its required level. The step load still causes frequency droop, however the VC-VSI is faster in recovering the frequency, when it is the only source on the grid, as seen towards the end of the simulation.

7.2.5. Simulation of frequency shift controller

To simulate the frequency shift control the battery SOC was set as a variable changing from 80% to 100% over one second. The load was set at 50kW and the solar contribution was set at 16kW. As the battery SOC changed the VC-VSI adjusted the grid frequency in accordance to Eq 7-1. The CC-VSI monitored this change in frequency and adjusted its power limit accordingly by Eq 7-2. Figure 7-23 shows the smooth transition of limiting the CC-VSI power as the grid frequency increases, within one second the power has decreased from 100 to 0%.

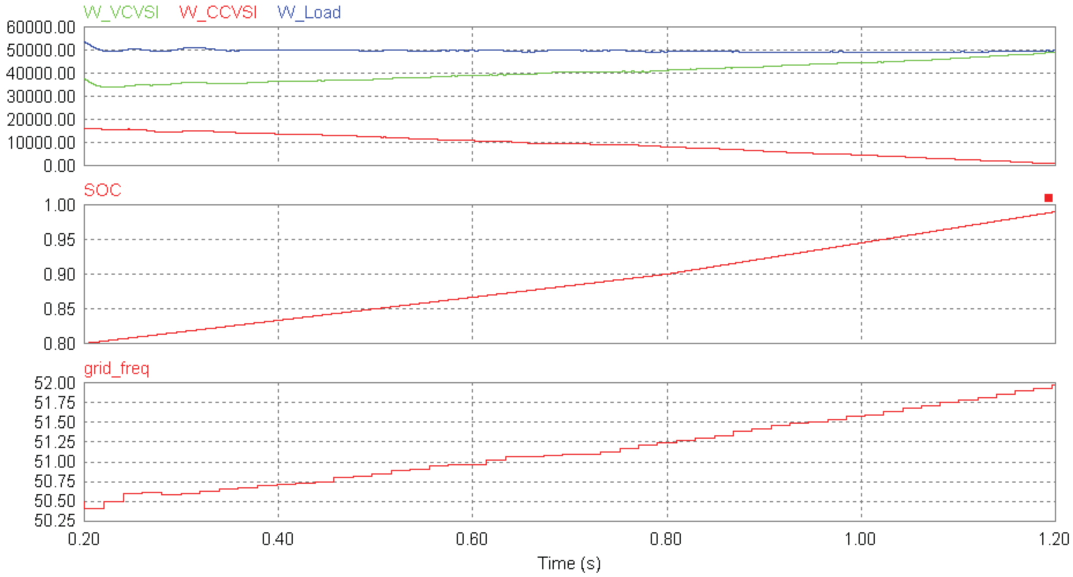

Figure 7-23 : Simulation of frequency shift controller

The concept can be applied to any mini grid where the central source is an inverter. The combination of this control method with current generating paralleling methods using frequency droop control is an area for future research.

7.3. Eco Beach Installation and Commissioning

This section presents the key components of the electrical system at Eco Beach. The author was the project engineer and manager and was onsite to oversee the installation and commissioning procedure. Brett Donald a local electrician from Broome and his apprentices carried out the actual electrical work to the project managers' specifications. This was carried out at the end of April 2009.

Figure 7-24 : 360V 540kWh battery room installation

The battery room, Figure 7-24, consisted of 180 2V 1500Ah Hoppecke VRLA cells forming a 360V series connected bank. Each battery was connected through two 90mm^2 cables directly bolted to the battery terminals. The bank was subdivided into 120V ELV segments by four manual disconnects, the middle two containing bar links. The battery bank electrical protection was provided through two sets of parallelled 400A DC fuses located at the bank positive and negative disconnects. This set up provided double 800A fused protection for the battery bank. Further to this a 630A circuit breaker was installed on the inverter side of the battery bank that would allow fast safe isolation in an emergency. These double safety provisions were adopted, as this was the first 360V battery bank to be deployed in Australia. The circuit breaker is a standard AC circuit breaker where the positive is looped through each phase allowing for it to be used for DC applications. Finally a window from the inverter control room to the battery room allows a person to see if there is any issue and isolate immediately if a problem is apparent.

Figure 7-25 : Jack's bar and coastal villas

Figure 7-25 shows a side profile of Jack's Bar during commissioning, five 2kW PV arrays can be seen on the coastal villas in the background. One of two of the main data receiving antenna's[19] from the villas can be seen on the pinnacle of the roof of Jack's Bar. Figure 7-26 shows the author and Eco Beach's owner discussing the installation of the inverter, DC PV circuit breaker and villa energy monitoring equipment installed inside one villa.

Figure 7-26 : Distributed Villa Inverters

Figure 7-27 : Central inverter and controller

Figure 7-27 shows the author checking set points on the central inverter in the powerhouse. The HCCU is the cabinet on the left with the central inverter installed in the two right cabinets. On the opposite side of the room is the main switchboard, Figure 7-28, the four generators interconnect to the left side from behind the switchboard. The upper central compartment contains the bus coupler and the inverter connects to the lower central compartment. The feeders are seen as the four right side components. A cable tray runs across the room to the inverter and up to its circuit breaker.

Figure 7-28 : Powerhouse main switchboard

Figure 7-29 : 4 x 50kVA Hino diesel generation plant

The four DG were installed in a room some 10m away from the main switchboard, fuel systems were outside and away from the building. Maximum sound proofing was used around the generators to ensure operational noise was kept to a minimum.

Figure 7-30 : Lightening protection at main switchboard

Lightening was considered a major problem in the area and protection was provided on every villa, at the powerhouse and on all antenna's throughout the system. The main system was protected with three 20kA surge arrestors located at the powerhouse attached across the main feeder bus, each was connected between L-N, N-E, L-E for each phase. Each villa had two 6kA surge arrestors these were connected across L-E and N-E and the MEN link was provided at the close by distribution panels. The wireless villa anntenna’s operated using PoE technology and a surge arrestor was installed between the antenna and each villa’s SMU.

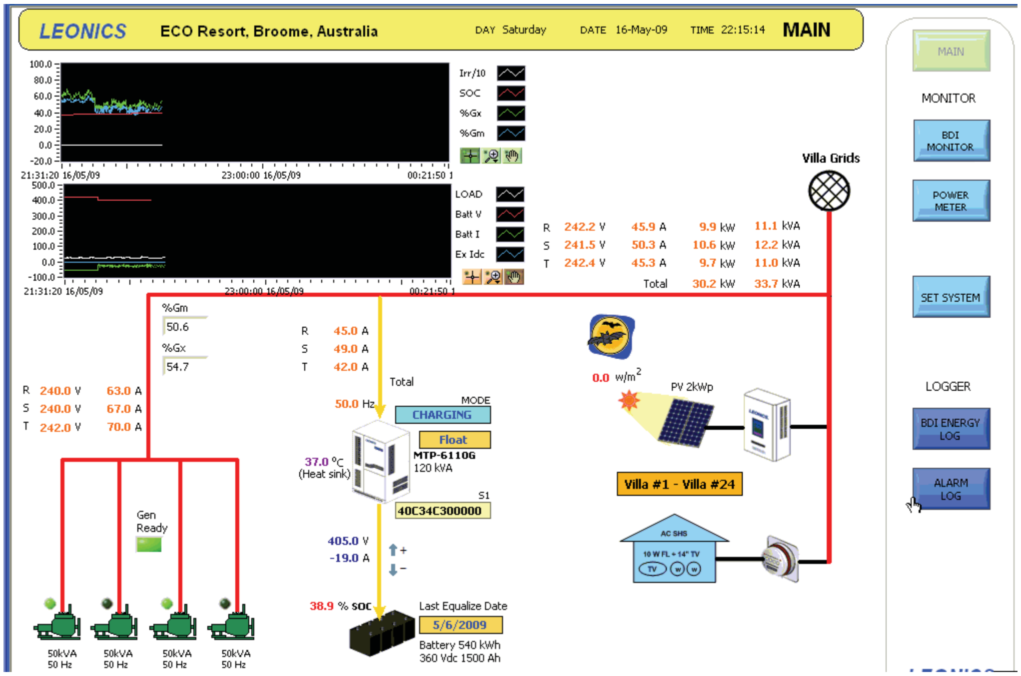

Figure 7-31 : Eco power system monitoring interface

The power monitoring system can be accessed at the powerhouse or Jack’ Bar at the central monitoring computer. This computer also acts as a web server and is the remote portal for the entire system. Figure 7-31 shows the main graphical user interface for the Eco resort system. All system parameters are recorded indefinitely and the previous six hours operation are provided as part of the main display. Instantaneous current, voltage and frequency parameters are provided for each phase. The systems operational mode, status of the generators and battery SOC are all visualised. The status of every villa is also seen through the web based GUI on the resorts intranet.

7.4. Eco Beach System Operations

The Eco Beach power system was commissioned in late April 2009. It was quickly discovered that some of the batteries supplied for the project were faulty. Extensive tests were carried out on the battery cells and it was discovered that during manufacture some contaminate had entered the process, which caused the adverse effect of greatly reducing the capacity of the cell. A warranty claim was made and a replacement set of batteries was installed in December 2009.

The following screen shots represent the operation of the system for the week of 16th to the 22nd of January 2010. Most days the generators are operated twice to three times a day and their operation is determined by the time of day and the SOC of the battery. Once the generator is started it is run at a level to both cover the load and charge the batteries to a predetermined set point of 80%. The plots show the daily solar irradiation in blue. At times of high solar irradiation the total AC power requirement on the inverter is seen to be negative, allowing excess solar energy to be stored in the battery. This is the most efficient use of the renewable energy as it is directly covering the local AC loads which is subsequently not seen as a load at the power house. The plots show the AC load at the power house bus in red, inverter/charger load in green and the generator loading the black. The battery SOC is seen in yellow.

Almost everyday in the period shown the solar PV energy is seen to cover all local AC loads and be used to charge the battery. This is a requirement of the design to store excess renewable energy to be utilised at later times. However the addition of extra load to the system from the initial design and removal of PV has caused an increase in generator runtime. This could be offset with the addition of more PV to the system.

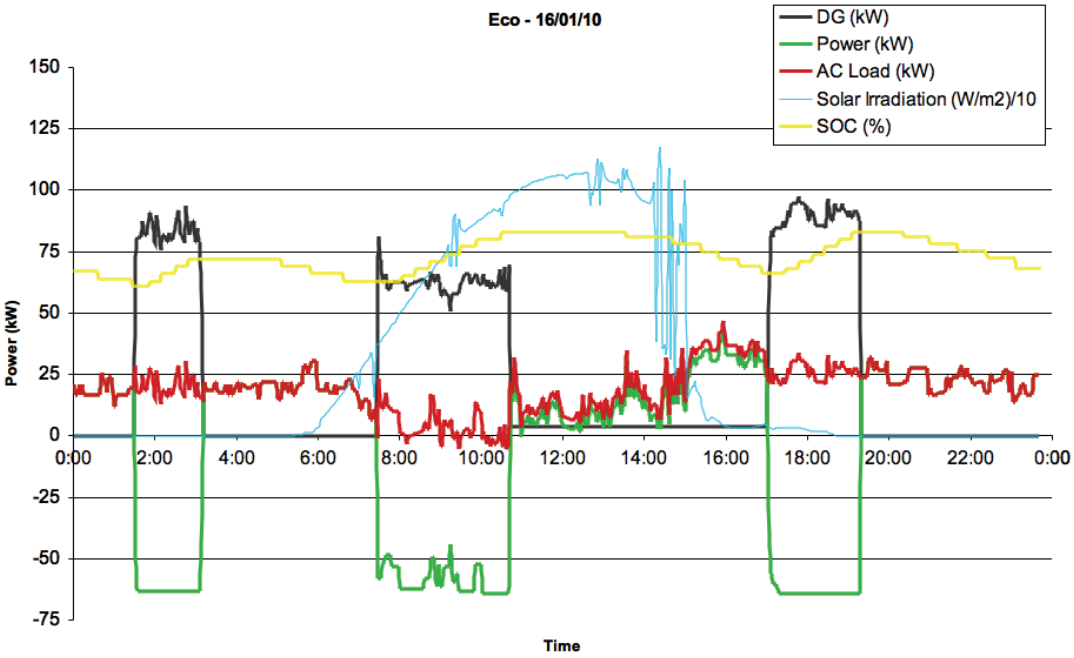

Figure 7-32 : Eco Beach Power System Operation 16/01/10

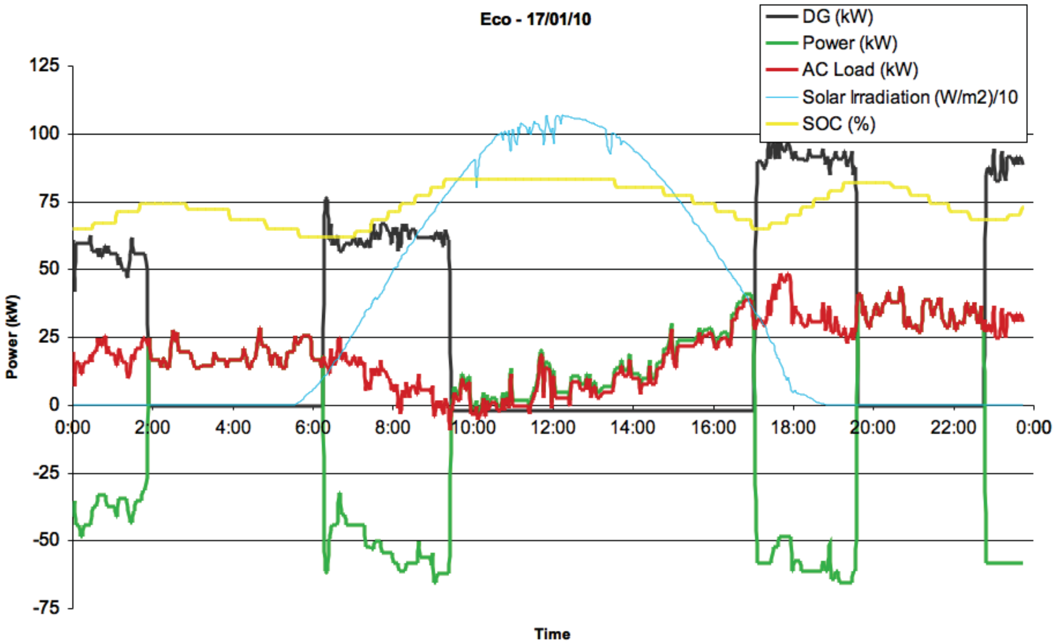

Figure 7-33 : Eco Beach Power System Operation 17/01/10

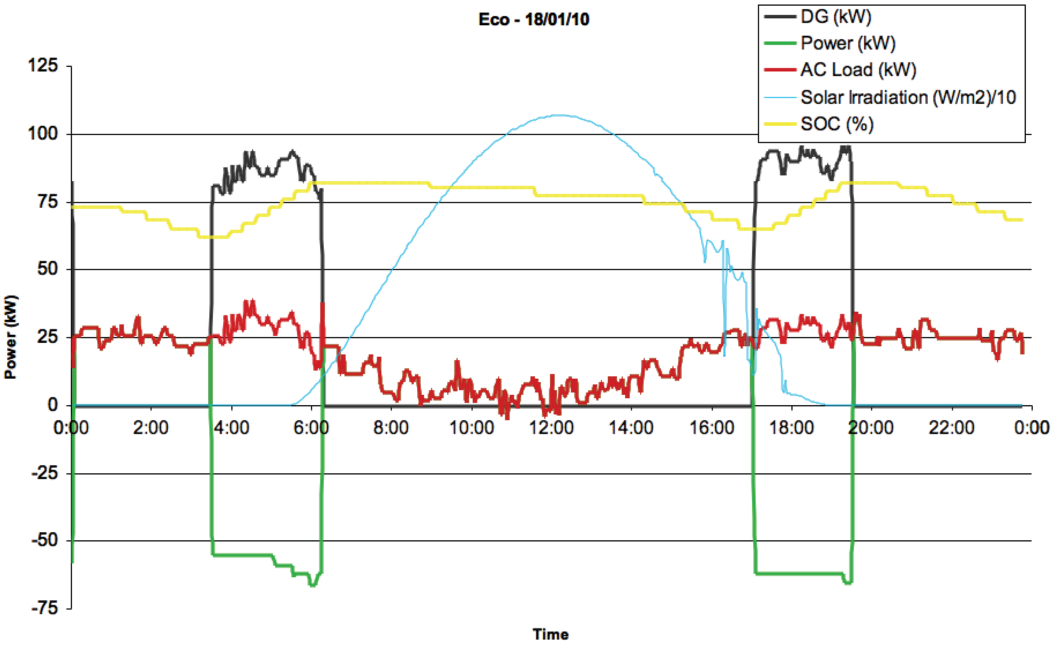

Figure 7-34 : Eco Beach Power System Operation 18/01/10

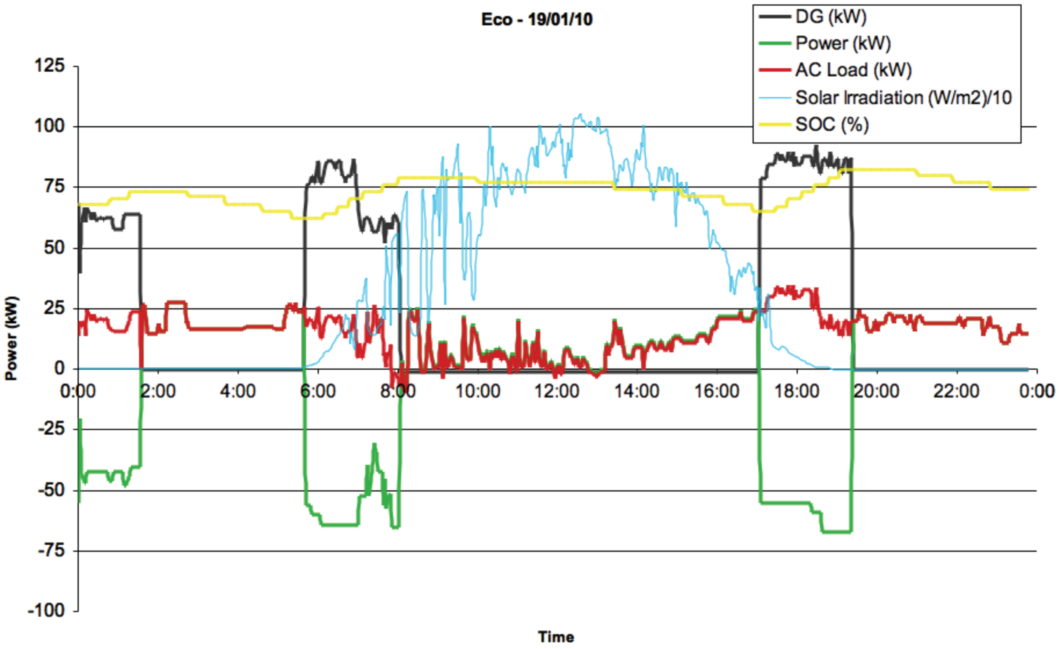

Figure 7-35 : Eco Beach Power System Operation 19/01/10

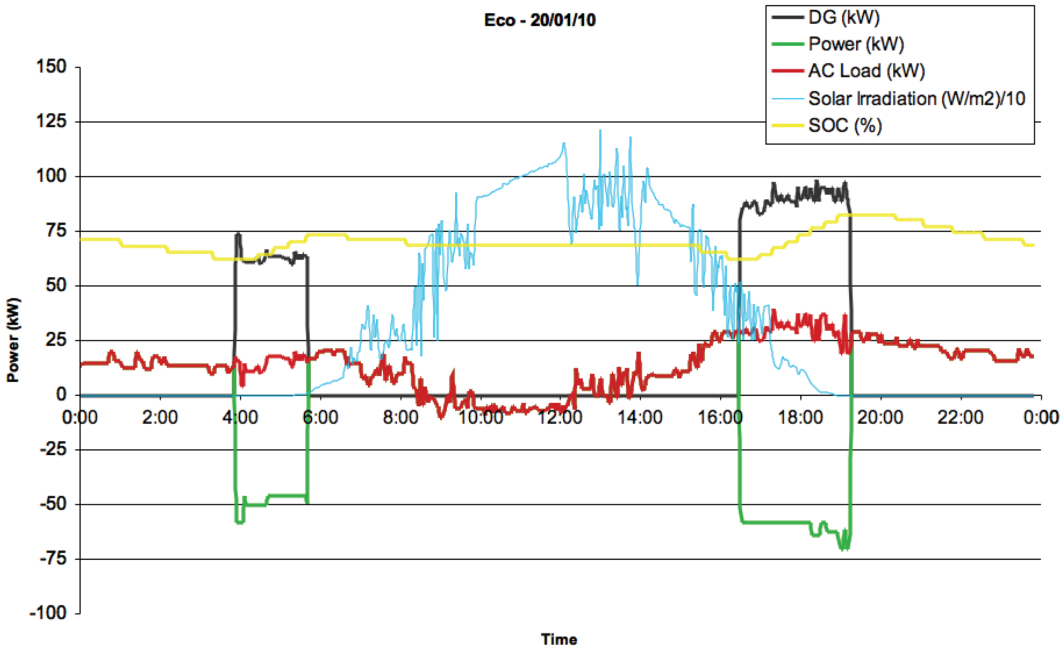

Figure 7-36 : Eco Beach Power System Operation 20/01/10

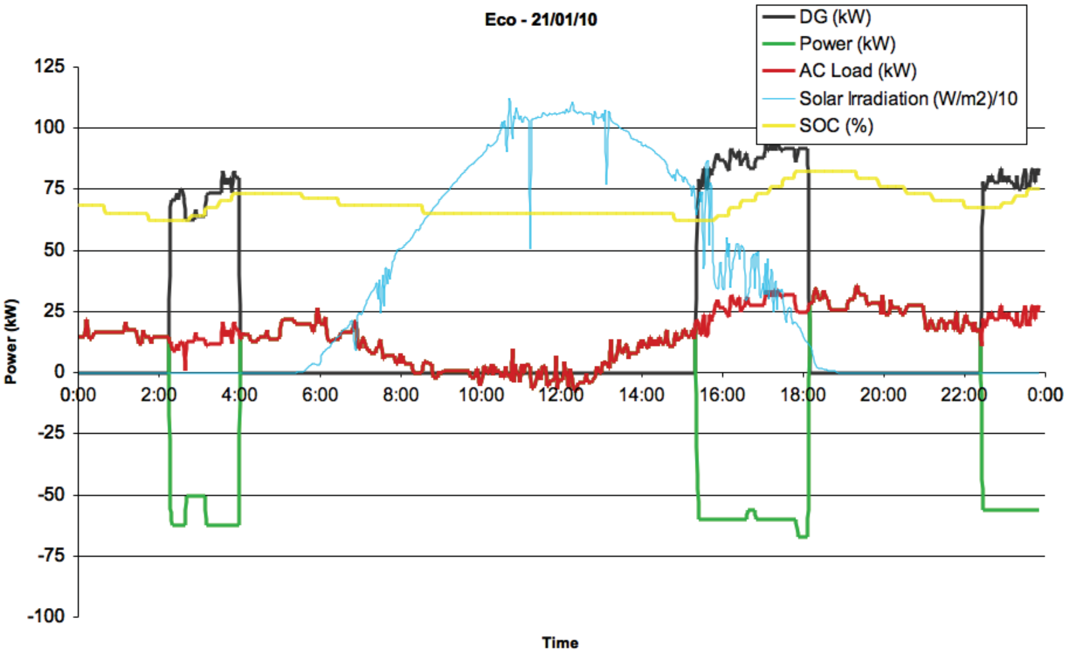

Figure 7-37 : Eco Beach Power System Operation 21/01/10

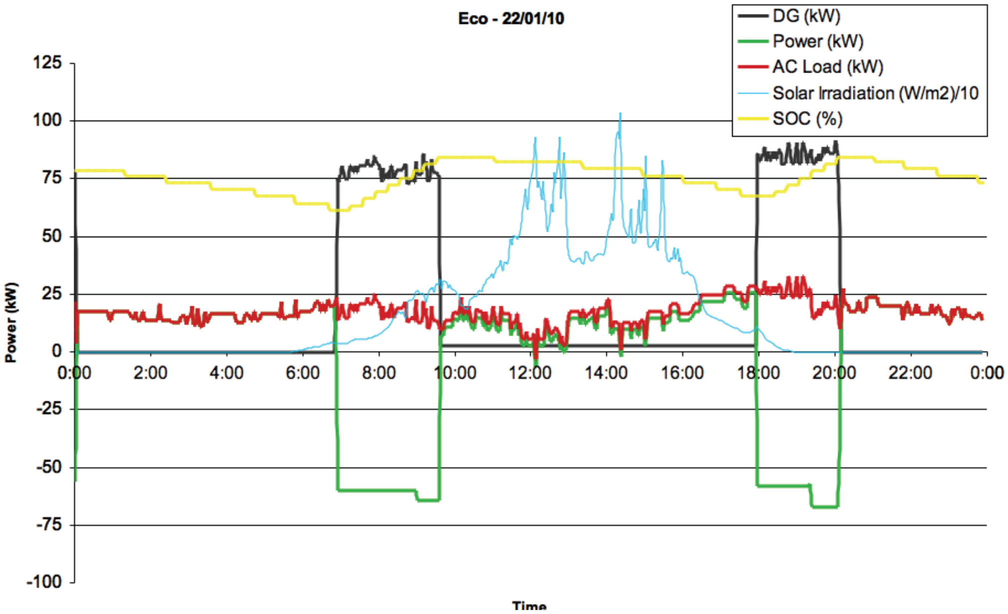

Figure 7-38 : Eco Beach Power System Operation 22/01/10

Figure 7-39 shows the power system operations for the 26th of December 2009, very high loads in excess of 110kW are seen at the power station bus. It is not recommended to have the load increase beyond 120kW with out changes to the system control as the inverter capacity is 120kW.

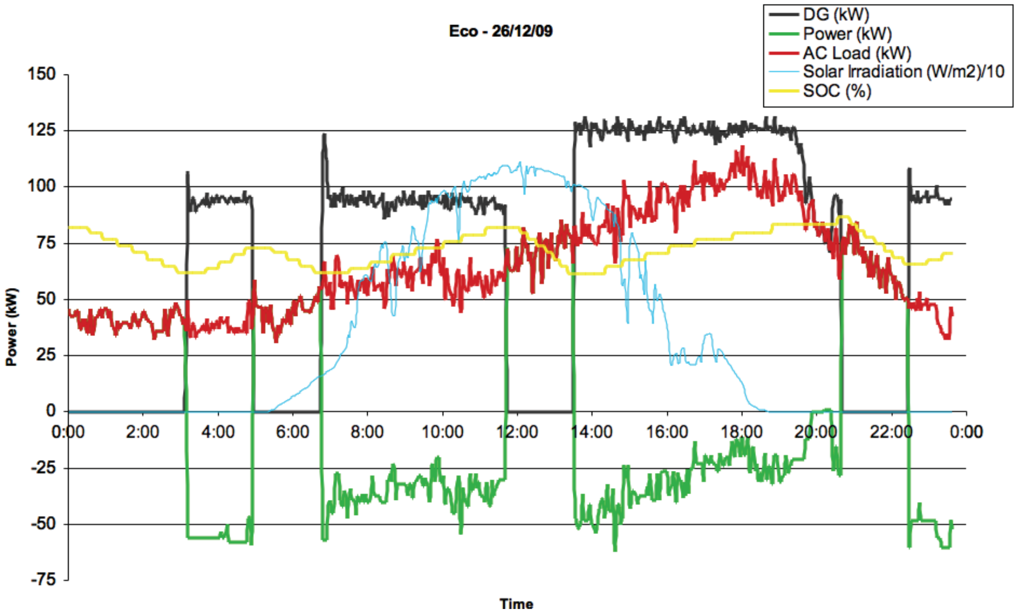

Figure 7-39 : Eco Beach Power System Operation 26/12/09

The solar irradiation levels at Broome are excellent for the PV systems. A web based interface is available on site to monitor the output from the PV arrays. This is via a wireless communication system that is centrally linked to the web server in Jack's Bar, Figure 7-40. Since installation the 48kW of PV installed has generated 58.3MWh of energy over 10 months, which represents a diesel fuel saving of approximately 19.5kL.

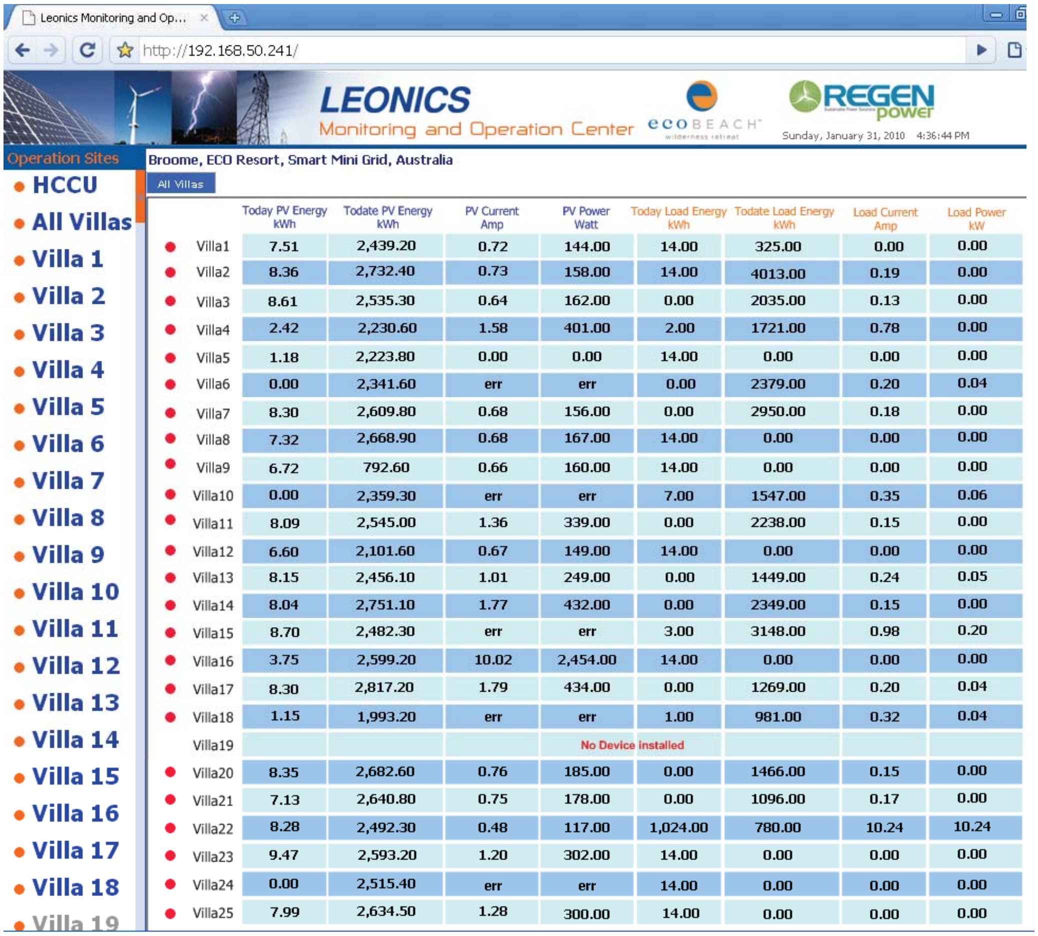

Broome, ECO Resort, Smart Mini Grid, Australia

	Today PV Energy kWh	Todate PV Energy kWh	PV Current Amp	PV Power Watt	Today Load Energy kWh	Todate Load Energy kWh	Load Current Amp	Load Power kW
● Villa1	7.51	2,439.20	0.72	144.00	14.00	325.00	0.00	0.00
● Villa2	8.36	2,732.40	0.73	158.00	14.00	4013.00	0.19	0.00
● Villa3	8.61	2,535.30	0.64	162.00	0.00	2035.00	0.13	0.00
● Villa4	2.42	2,230.60	1.58	401.00	2.00	1721.00	0.78	0.00
● Villa5	1.18	2,223.80	0.00	0.00	14.00	0.00	0.00	0.00
● Villa6	0.00	2,341.60	err	err	0.00	2379.00	0.20	0.04
● Villa7	8.30	2,609.80	0.68	156.00	0.00	2950.00	0.18	0.00
● Villa8	7.32	2,668.90	0.68	167.00	14.00	0.00	0.00	0.00
● Villa9	6.72	792.60	0.66	160.00	14.00	0.00	0.00	0.00
● Villa10	0.00	2,359.30	err	err	7.00	1547.00	0.35	0.06
● Villa11	8.09	2,545.00	1.36	339.00	0.00	2238.00	0.15	0.00
● Villa12	6.60	2,101.60	0.67	149.00	14.00	0.00	0.00	0.00
● Villa13	8.15	2,456.10	1.01	249.00	0.00	1449.00	0.24	0.05
● Villa14	8.04	2,751.10	1.77	432.00	0.00	2349.00	0.15	0.00
● Villa15	8.70	2,482.30	err	err	3.00	3148.00	0.98	0.20
● Villa16	3.75	2,599.20	10.02	2,454.00	14.00	0.00	0.00	0.00
● Villa17	8.30	2,817.20	1.79	434.00	0.00	1269.00	0.20	0.04
● Villa18	1.15	1,993.20	err	err	1.00	981.00	0.32	0.04
Villa19				No Device installed				
● Villa20	8.35	2,682.60	0.76	185.00	0.00	1466.00	0.15	0.00
● Villa21	7.13	2,640.80	0.75	178.00	0.00	1096.00	0.17	0.00
● Villa22	8.28	2,492.30	0.48	117.00	1,024.00	780.00	10.24	10.24
● Villa23	9.47	2,593.20	1.20	302.00	14.00	0.00	0.00	0.00
● Villa24	0.00	2,515.40	err	err	14.00	0.00	0.00	0.00
● Villa25	7.99	2,634.50	1.28	300.00	14.00	0.00	0.00	0.00

Figure 7-40 : PV array interface web page

The feasibility report recommended an extra 20kW of PV to be DC coupled on the power house roof. Due to the financial crisis this was not installed, also the total loads on the system have increased by approximately 20kW average and 50kW peak during high occupancy periods. However the overall system is operating as expected under these conditions. It is recommended that the owner install 20-30 kW DC coupled on the power house roof and a further 20 kW AC coupled and distributed on other building. This would greatly reduce the fuel requirements from the system by preventing extra generator starts. The original design only required the generators to run for approximately 6 hrs per day during the high evening cooking and air conditioning load times. At low occupancy periods such as Figure 7-38 the generators are running for 5 hours per day, however in high load times such as Figure 7-39 they are running up to 15 hours.

Overall the power system for Eco Beach resort is operating as expected for the changing load requirements. However, it would greatly benefit with the addition of another 30 – 40kW of PV to compensate for the increased energy usage. With the global cost of PV reducing dramatically since construction the author hopes this will be realised and the complete ecologically sustainable Eco Beach Resort can be fully realised. Eco Beach Resort, as of the January 2010 represents the most technically challenging hybrid system constructed in Australia.

7.5. Summary

This chapter presents the complete design, simulation and implementation of a large hybrid power system into a real operating system. A method of limiting the power from remote renewable energy sources using frequency shift is simulated and implemented. Methods to control the use of the renewable energy are investigated, with a controller using the predictable nature of the Sun to determine the battery charging states. A weeks operational data is presented to assess the design and implementation. As with many renewable projects the initial design is curtailed due to financial constraints. Eco Beach operates very well given the increased loads and the reduction PV installed. The simulated system closely matches the implemented and commissioned one, given these changing factors. The author hopes additional PV will be added to the system to allow a maximum penetration of renewable energy given the new loads.

A summary of this chapters key section is below

- Design example – Eco Beach Wilderness Resort Broome;
- Complete simulation model of medium to large scale hybrid system with frequency control implementation;
- Implementation of system design into operating plant.

The key research points of this chapter are:

- Development of frequency shift control in decentralised distributed renewable systems;
- Creation of simulation method in PSIM to simulate a combination VC-VSI and CC-VSI inverter controlled system;
- Development of controller for the largest decentralised multi function renewable power system in Western Australia.

7.6. References

1. Plunkett, K. *Eco Beach Broome Resort*. 2009 [cited 2009 22 Dec]; Available from: www.ecobeach.com.au.
2. Durisch, W. and D. Ti1le, *Testing Of Small Sinusoidal-Inverters For Photovoltaic Stand-Alone Systems.* Applied Energy, 1998. **64**.
3. *PSIM Version 7.0*. 2006, Powersim Inc. (www.powersimtech.com): Woburn, MA.
4. Darbyshire, J., et al., *Preliminary Study for Renewable Energy Integration into the Eco Beach Resort Power Supply*. June 2008, Regen Power & Solar Matrix: Perth.
5. Lambert, T., *HOMER: the micro-power optimisation model*. 2008, NREL.
6. Greenbird, *Intelligen ComAp NT Datasheet*. 2008, Greenbird Technologies.
7. Meteorology, A.G.B.o. *Average Daily Sunshine*. 2008 [cited 2008 19/08/2008]; Available from: http://www.bom.gov.au/.
8. Hoppecke, *OPzV Valve regulated lead-acid battery*, in *Hoppecke: Power from innovation*. 2007, Hoppecke: Brion, Germany.
9. Ph. Strauss, A.E., *AC COUPLED PV HYBRID SYSTEMS AND MICRO GRIDS - STATE OF THE ART AND FUTURE TRENDS*, in *3rd World Conference on Photovoltaic Energy Conversion*. 2003: OsakA, Japan.
10. Nayar, C., M. Dymond, and J. Darbyshire, *Hybrid Power System Design for Uligam Island, Maldives.* March 2007, Regen Power: Perth, Australia.
11. Nayar, C., M. Dymond, and J. Darbyshire, *Hybrid Power System Design for Raimandhoo Island, Maldives.* March 2007, Regen Power: Perth, Australia.
12. Nayar, C., M. Dymond, and J. Darbyshire, *Hybrid Power System Design for Kondey Island, Maldives.* March 2007, Regen Power: Perth, Australia.
13. Nayar, C.V., M. Tang, and W. Suponthana. *An AC Coupled PV/Wind/Diesel Microgrid System Implemented in a Remote Island in the Republic of Maldives*. in *AUPEC 2007*. 2007. Curtin University of Technology.
14. SMA, *Sunny Island 5048 - Installation & Instruction Manual*, in *SMA Technical*. 2008, SMA Technologie AG: Niestetal.
15. SMA, *TechnologyCompendium 2: Solar Stand-Alone Power and Backup Power Supply*, in *SMA TechnologyCompendium*. 2009, SMA Technologie AG: Niestetal. p. 44.
16. Stratis Tapanlis, M.W. *Advanced Active And Reactive Power Control For Mini Grids*. in *RIO 9 - World Climate & Energy Event*. March 2009. Rio de Janeiro, Brazil.
17. MOIX, P.-O., *New Trends in Hybrid Systems with Battery Inverter*, in *Technical Brief*. 2009, Studer Innotec: Sion, Switzerland. p. 6.
18. Moix, P.-O. *Current Assistance Inverter: Opening New Possibilities in Hybrid Systems and Minigrids*. in *4th EUROPEAN CONFERENCE PV-HYBRID and MINI-GRID*. 2008. Athens, Greece: Studer Innotec.
19. D-LINK, *D-Link ANT24-1400 : Outdoor Directional Panel Antenna*, in *ANT24-Series*. 2008.

"Every reasonable effort has been made to acknowledge the owners of copyright material. I would be pleased to hear from any copyright owner who has been omitted or incorrectly acknowledged."

8. Conclusions and Further Recommendations

8.1. Summary of Work

The authors' work is summarised below. The terms invention, creation, development and application are used to describe the originality of each section of work. The term invention describes a new concept that has come out of the research conducted for this dissertation and is directly correlated to the authors work. The term creation defines a new piece of work that has stemmed from the research and has been used to prove a concept. The term development is used where the author has transcribed or converted a previous concept into a new model or simulation. The term application has been used where the author has applied a known method to a new situation.

Chapter two created the basic power electronic building blocks, which would be required to allow complete hybrid power systems to be developed. The control methods for VSI's were created as well as the generic inverter model. The software suites of PSIM and Visual Studio C++ were used to create the algorithms required for the controllers. Each model was robustly tested before being utilised in further work.

- Development of PSIM model of VC-VSI using PI voltage feedback controller;
- Development of PSIM model of CC-VSI using PI current controller;
- Development of PSIM model of CC-VSI using hysteresis current controller through SR flip flop;
- Development of PSIM model of a PLL.

Chapter three began modelling the MPPT algorithms for solar and wind systems, culminating in a novel IC wind algorithm. PSIM and Visual Studio C++ were used to develop and refine these algorithms with a testing and verification method applied.

- Creation of PSIM model and C++ code for PV model array based upon commonly available data sheet values utilising the Newton-Raphson algorithm;
- Development of a MPPT P&O PV model;
- Development of a MPPT IC PV model;

- Application of MPPT IC PV algorithm to create a wind MPPT algorithm;
- Development of PSIM wind turbine and inverter model;
- Creation and testing method for wind IC MPPT algorithm.

Chapter four presents the differing possible interconnection methods for small or large renewable based hybrid power systems. The review of the currently existing approaches leads to the complimentary hybrid system. This new system is modelled and shown to be advantageous for some locations. Mathematical analysis and simulations were presented for each of the systems. The complimentary system is demonstrated as part of the Denmark project.

- Invention of the complimentary hybrid system;
- Development of edge of grid hybrid system topologies;
- Creation of crossover loss definition;
- Creation of mathematical analysis for complimentary hybrid systems.

Throughout this research there has been a need for a methodology to compare differing wind turbines to find the best suited for a location. This work required careful analysis of the power curve with respect to the wind resource model. In chapter five, two new comparison methods were derived to supplement the notional capacity factor definition; these were termed economic efficiency and conversion efficiency.

- Application of statistical analysis and representations to wind resources;
- Application of Graph Digitizer to wind turbine power curves;
- Creation of definitions of Economic Feasibility and Conversion Efficiency to assist Capacity Factor to aide the selection of wind turbines.

Chapter six combines the previously developed power electronic blocks into a complete control methodology for medium to large scale hybrid power systems, with the goal of increasing the renewable energy penetration and minimising fuel usage. The requirements of diesel generators are now included from a control and interconnection points of view. The inverter control requirements for these differing modes of operation are described and simulated.

- Development of a hybrid system design methodology;
- Creation of methods to achieve higher renewable energy penetration levels using inverter control.

Chapter seven presents the complete design, simulation and implementation of a large hybrid power system into a real operating system. A method of limiting the power from remote renewable energy sources using frequency shift is simulated and implemented. Methods to control the use of the renewable energy are investigated, with a controller using the predictable nature of the Sun to determine the battery charging states.

- Development of frequency shift control in decentralised distributed renewable systems;
- Creation of simulation method in PSIM to simulate a combination VC-VSI and CC-VSI inverter controlled system;
- Development of controller for the largest decentralised multi function renewable power system in Western Australia.

Twenty-two distinct pieces of work stem from the research conducted and are presented in this dissertation. Of these one is an invention, seven are creation of new work, eleven are continuous development on previous work and three are application of new methods to previous work.

The work carried out in this dissertation resulted in the design of the largest stand alone inverter based renewable hybrid power system in Australia. Significant aspects of this research with the help of the industry partner Regen Power allowed for this system to be developed. It is the hope of the author that the Eco Beach system will be the starting point for many small to medium scale remote renewable hybrid power systems in the future.

8.2. Conclusions

This dissertation is a culmination of four years of successful research under the guidance of Professor C.V. Nayar. The author was delighted to have the research lead to a practical conclusion in the form of the system designed, developed and implemented at Eco Beach Wilderness Resort in Broome, Western Australia.

The author believes the key aspects of this research were the development, modelling and demonstration of the complimentary hybrid system. This combination of solar and wind resources allows a hybrid system to increase its energy output and inverter utilisation. Mathematically modelling was carried out to show exactly where this type of system is advantageous over conventional power electronic topologies. The system was developed for both the stand alone and grid connected configurations. The demonstration Denmark project ratified the complementary system as an appropriate approach for some locations. Sites with intermediate solar and wind resources are best suited with a complementary type solution. The solution vastly increases energy output however the system must also be shown to be cost effective.

The second aspect of this research was the modelling and development of a novel MPPT algorithm for small wind turbines. This algorithm was derived from the application of the IC solar algorithm and developed for use with a wind system. A detailed wind turbine model was created in PSIM to allow accurate analysis of the algorithm. This model is more appropriate in rapidly changing wind conditions as it can determine the direction it must track automatically.

The final key aspect of the research comes from the control and configuration of larger hybrid power systems. These systems use a compartmentalised approach to allow solar of wind systems to be AC coupled to the distribution network. A central inverter and controller are used as the brain for the system and this determines generator runtimes and energy storage requirements based upon likely future free energy availability. The interconnection methods and controls between the generations and inverters are a key requirement for the reliability of the overall system. This research represents the multi-functional aspect of the dissertation. The larger system design methodology presented allows the most ideal system to be designed through a logical process. The Maldives, turf farm and Eco Beach projects were developed using these methods, culminating in successful designs. The Maldives and Eco Beach projects were constructed and are now in operation.

8.3. Further Areas of Research

The author hopes that this thesis represents advancement in the area of hybrid power systems and control for remote area applications. However, much work is still to be carried out on the optimal balance between renewable energy extraction, the storage of this energy and increasing the reliability of the overall system.

It is suggested by the author that future research is focused on the following areas based upon the conclusions of this dissertation:

- Application of the IC wind algorithm on a variety of PMSG wind turbines;
- Side by side demonstration of complimentary hybrid system against conventional to verify some of the findings of this research.
- Development of transition of VC-VSI to CC-VSI without the requirement of opening the interface contactor;
- Development of better and more accurate battery SOC algorithms

The central failure point for remote hybrid power systems is the energy storage aspect; specifically the battery bank. High temperatures, faulty interconnects, prolonged and cyclic discharge levels and deep discharge states all reduce the life expectancy of the cells. Various new technologies such as Zinc Bromide flow type batteries do not experience these affects, however have other unique charging requirements. Lithium ion batteries have high energy densities but are strongly effected by temperature variations and are not currently economically justifiable. With increasing development of electric car battery technology, the cost of Lithium ion cells may reduce to a point where they could be used in stand alone and edge of grid situations.

Diesel engine technology is being driven to a more fuel efficient future due to the global economic downturn and increases fuel prices. Common rail diesel injection and the ability to turn off cylinders is allowing the larger engines to operate at lower loads for longer periods of time. This ultimately allows the renewable energy penetration to be increased.

The combination of development in battery technology, increasing diesel engine efficiency and novel short term energy storage using new super capacitors may lead to a revolution in area of renewable hybrid power systems.

8.4. Power Electronics An Exciting and Invaluable Area to Research

Australia, like many locations across the globe will have an ongoing requirement to bring electricity to remote and isolated locations. The research presented in this dissertation draws on the energy sources of solar and wind with conventional diesel systems to provide reliable electricity. The enabling technology with allows this to be possible is power electronics. This area of research is likely to be undergo a revolution in the next few years as switching devices change from being Silicon based to Silicon Carbide. This new material will vastly decrease switching losses allowing higher power and faster switching devices allowing a new level of efficiency for power electronics.

The power electronics technology is the heart of any new hybrid power system. As novel battery, super-capacitor and diesel technologies evolve the power electronic control must develop to manage and regulate the flow of power. As electricity is transferred from source to storage to load, power electronic devices remain the mechanism by which this conversion takes place. This area of research is of immense importance if we are to transform humanity from its dependency on fossil fuels for our energy needs.

9. Appendices

9.1. Theory and Proof of Betz Limit

The Betz limit can be described by the actuator disc concept. This theory proposes that the mass flow rate at any point along the stream tube must be constant and the actuator disc is modelled as a wind turbine with and infinite number of blades.

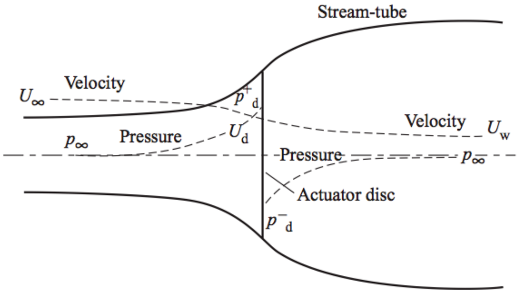

Figure 9-1 : Actuator Disc Model

From Figure 9-1, U_∞ and p_∞ represent the air velocity and pressure at a point far enough upstream not to be effected by the presence of the wind turbine. U_W is the air velocity in the wake of the wind turbine and p_d^+, p_d^- are the air pressure either side of the actuator disc.

The mass flow rate along the air stream tube can be described by;

$$\rho A_\infty U_\infty = \rho A_d U_d = \rho A_W U_W$$

Eq 9-1 : Mass Flow Balance

The air velocity through the turbine is decreased by a ratio of the upwind airspeed, denoted by a.

$$U_d = U_\infty (1 - a)$$

Eq 9-2 : Ratio of Air Speed Loss

The pressure difference across the actuator disc causes a change in force and so a change in momentum of the air.

$$\Delta P = (U_\infty - U_W)\rho A_d U_d$$

Eq 9-3 : Pressure Differential Across the Stream Tube

The change in force at the actuator disc can be described as the change in pressure over the cross sectional area of the disc.

$$\Delta F = (p_d^+ - p_d^-)A_d = (U_\infty - U_W)\rho A_d U_\infty (1-a)$$

Eq 9-4 : Force Differential

The total energy in the stream tube comprises of three components, the airs kinetic energy, the static pressure and the gravitational potential energy. This energy is not the same upstream as down stream with the difference being the maximum energy that can be utilised by the wind turbine. The net energy at a point far from the front of the turbine must equal the net energy at the front interface of the turbine. This can be represented below.

$$E_{Upstream} = \frac{1}{2}\rho_\infty U_\infty^2 + \rho_\infty g h_\infty = \frac{1}{2}\rho_d U_d^2 + p_d^+ + \rho_d g h_d$$

Eq 9-5 : Energy Available Upstream

Assuming the height is fixed and the flow is incompressible.

$$\begin{aligned} E_{Upstream} &= \frac{1}{2}\rho U_\infty^2 + \rho_\infty = \frac{1}{2}\rho U_d^2 + p_d^+ \\ E_{Downstream} &= \frac{1}{2}\rho U_w^2 + \rho_\infty = \frac{1}{2}\rho U_d^2 + p_d^- \\ \therefore E_{Upstream} - E_{Downstream} &= (p_d^+ - p_d^-) = \frac{1}{2}\rho(U_\infty^2 - U_w^2) \end{aligned}$$

Eq 9-6 : Balance of Upstream and Downstream Airflow

Substituting back into Eq 9-4.

$$\begin{aligned} \frac{1}{2}\rho(U_\infty^2 - U_w^2)A_d &= (U_\infty - U_w)\rho A_d U_\infty (1-a) \\ (U_\infty - U_w)(U_\infty + U_w) &= 2(U_\infty - U_w)U_\infty (1-a) \\ U_w &= 2U_\infty - 2aU_\infty - U_\infty \\ \therefore U_w &= U_\infty (1-2a) \end{aligned}$$

Eq 9-7 : Conservation of Energy

The power available at the actuator disc is the force on the disc multiplied wind velocity through the disc.

$$\begin{aligned} F &= (U_\infty - (U_\infty(1-2a))\rho A_d U_\infty (1-a) \\ &= 2\rho A_d U_\infty^2 a(1-a) \end{aligned}$$

$$\begin{aligned} P_{Disc} &= FU_d = 2\rho A_d U_\infty^2 a(1-a) U_\infty (1-a) \\ &= 2\rho A_d U_\infty^3 a(1-a)^2 \end{aligned}$$

Eq 9-8 : Power Expression

The power co-efficient is defined as the ratio between the power extracted by the turbine and the power in the wind.

$$C_P = \frac{P_R}{P_W} = \frac{2\rho A_d U_\infty^3 a(1-a)^2}{\frac{1}{2} C_P \rho A_d U_\infty^3} = 4a(1-a)^2$$

$$\therefore \max C_P \Rightarrow \frac{dC_P}{da} = 4(1-a)(1-3a) = 0$$

$$C_{P,\max} = \frac{16}{27} = 0.593$$

Eq 9-9 : Betz Limit Proof

9.2. Bipolar Pulse Width Modulation

The bipolar PWM concept switches each opposite gate in alternately; Figure 9-2 shows the carrier waveform called "$v_{control}$" being compared to the triangular switching waveform. The frequency of the triangular waveform is known as the switching frequency. Parts (b) and (c) show the times at which the opposite switches are on and off. When one set of switches is on it connects the DC bus to the load this is known as V_{an} and has the magnitude of the DC supply or V_d. The same can be said for V_{bn} however it is of opposite polarity with respect to the load.

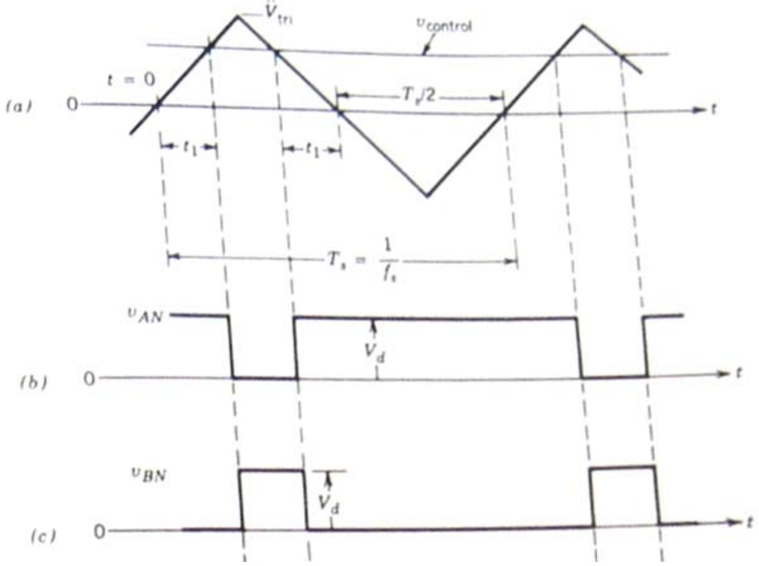

Figure 9-2 - Creating a PWM

Describing the top waveform (a) in terms of mathematics.

$$v_{tri} = \frac{\hat{V}_{tri}}{T/4} t \qquad @t_1 = \frac{v_{control}}{\hat{V}_{tri}} \frac{T}{4}$$

The proportion at which $v_{control}$ is less than v_{tri} is:

$$\mathrm{t_{on}} = 2t_1 + \frac{T}{2}$$

Conduction to the load through V_{AN} occurs whenever $v_{control} > v_{tri}$, and conduction through V_{BN} occurs when $v_{control} < v_{tri}$. The duty ratio is defined as the ratio that a rectangular wave is on with respect to the switching period.

$$D = \frac{t_{on}}{T}$$

Substituting:

$$\mathrm{D_A} = \frac{1}{T}\left(2t_1 + \frac{T}{2}\right) \Rightarrow \frac{1}{T}\left(2\left(\frac{v_{control}}{\hat{V}_{tri}}\frac{T}{4}\right) + \frac{T}{2}\right) = \frac{1}{2}\left(\frac{v_{control}}{\hat{V}_{tri}} + 1\right)$$

also

$$\mathrm{D_B} = 1 - \mathrm{D_A} = \frac{1}{2}\left(1 - \frac{v_{control}}{\hat{V}_{tri}}\right)$$

The output of waveform is given by the subtraction of the V_{AN} and V_{BN} waveforms.

$$V_{0,ave} = V_{AN} - V_{BN} = \mathrm{D_A} V_D - \mathrm{D_B} V_D = V_D\left(2\mathrm{D_A} - 1\right)$$

Substituting

$$V_{0,ave} = V_D\left(2\frac{1}{2}\left(\frac{v_{control}}{\hat{V}_{tri}} + 1\right) - 1\right) = V_D\frac{v_{control}}{\hat{V}_{tri}}$$

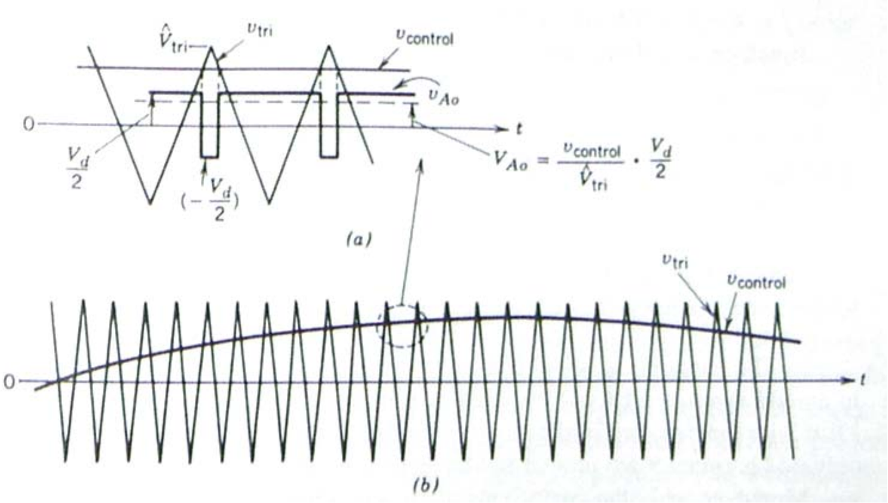

Figure 9-3 – Zoomed in switching period

If we assume the switching frequency is much greater then the control frequency we can conclude the following, and introduce the term modulation index as the ratio of $V_{control}$ to V_{tri}.

$$\text{For } f_{sw} >> f_{control}$$

$$\frac{v_{control}}{\hat{V}_{tri}} \approx \frac{\hat{V}_{control}}{\hat{V}_{tri}} = m_a$$

$$\therefore V_{0,ave} = V_D m_a$$

The waveform $v_{control}$ has a relationship described by;

$$v_{control} = \hat{V}_{control}\sin(\omega t)$$

The peak of our output waveform is:

$$\hat{V}_{O,peak} = V_D\frac{\hat{V}_{control}}{\hat{V}_{tri}} = V_D m_a$$

So the output fundalmental sinusoid can be given as:

$$V_{O1} = V_D m_a \sin(\omega t)$$

The rms of this is simply:

$$V_{O1,rms} = \frac{V_D m_a}{\sqrt{2}}$$

To calculate the RMS value of the bipolar square wave which switches from $+V_{BN}$ to $-V_D$ at any instant between 0 and T, the ratio of T at which it switches is given by α.

$$V_{O,rms} = \sqrt{\frac{1}{T}\int_0^T v(t)^2\,dt}$$

$$V_{O,rms} = \sqrt{\frac{1}{T}\left(\int_0^{\frac{T}{\alpha}}(V_D)^2\,dt + \int_{\frac{T}{\alpha}}^{T}(-V_D)^2\,dt\right)} = \sqrt{\frac{1}{T}\left(V_D^{\,2}\left(\frac{T}{\alpha}-0\right)+V_D^{\,2}\left(T-\frac{T}{\alpha}\right)\right)} = \sqrt{\frac{1}{T}\left(V_D^{\,2}T\right)} = V_D$$

The total harmonic distortion (THD) of a bipolar switching scheme can be calculated by:

$$THD = \sqrt{\frac{V_{O,rms}^{\,2} - V_{O1,rms}^{\,2}}{V_{O1,rms}^{\,2}}}$$

$$THD = \sqrt{\frac{V_D^{\,2}\left(1-\frac{m_a^{\,2}}{2}\right)}{\frac{V_D^{\,2}m_a^{\,2}}{2}}} = \sqrt{\frac{2-m_a^{\,2}}{m_a^{\,2}}}$$

The output ripple of the waveform can be given by:

$$V_{ORIP,rms} = \sqrt{V_{O,rms}^{\,2} - V_{O1,rms}^{\,2}}$$

$$V_{ORIP,rms} = \sqrt{V_D^{\,2} - \frac{V_D^{\,2}m_a^{\,2}}{2}} = V_D\sqrt{1-\frac{m_a^{\,2}}{2}}$$

Figure 9-4 shows the waveforms of voltages and currents in a standard H bridge using bipolar PWM generation methods, in this case the switching frequency is 9 times the carrier. Part a) shows the generation technique, b) and c) show the gating signals, d) shows the output voltage waveform, e) the FFT of the output voltage, f) the output current waveform, g) and h) show the dc current and its FFT, i) shows the switch current and j) the diode current.

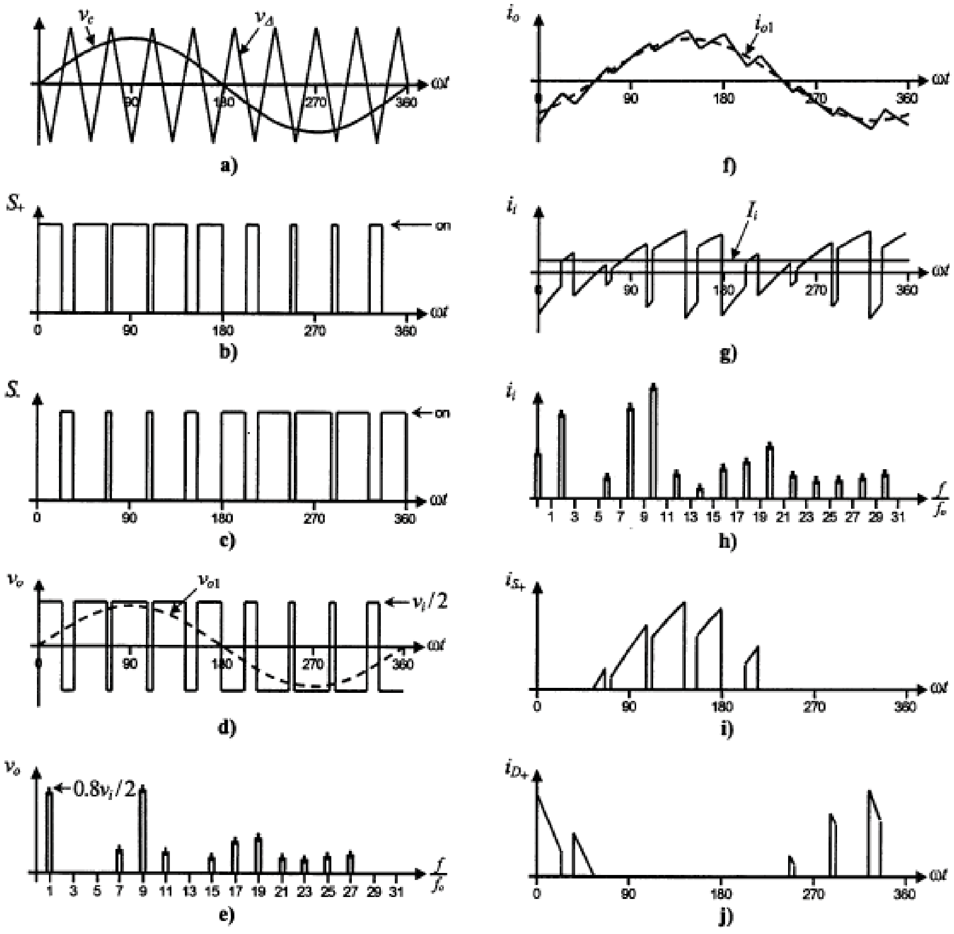

Figure 9-4 - Bipolar waveforms

9.3. Unipolar Pulse Width Modulation

Unipolar switching is very similar to bipolar techniques but has the advantage of fewer low frequency harmonics then bipolar, allowing a simpler design for an output filter. Unipolar uses two reference or control sinusoids that create two contrary PWM waveforms. For each waveform the mathematics of the description on the waves are identical to bipolar. The main difference is that unipolar waveforms only switch between $+V_D$ and 0 for the positive half cycle and $-V_D$ and 0 for the negative half cycle. Figure 9-5 shows the unipolar PWM generation method. The two contrary PWM signals are applied to the full bridge legs independently, they are not simply the inverse of each other as for bipolar.

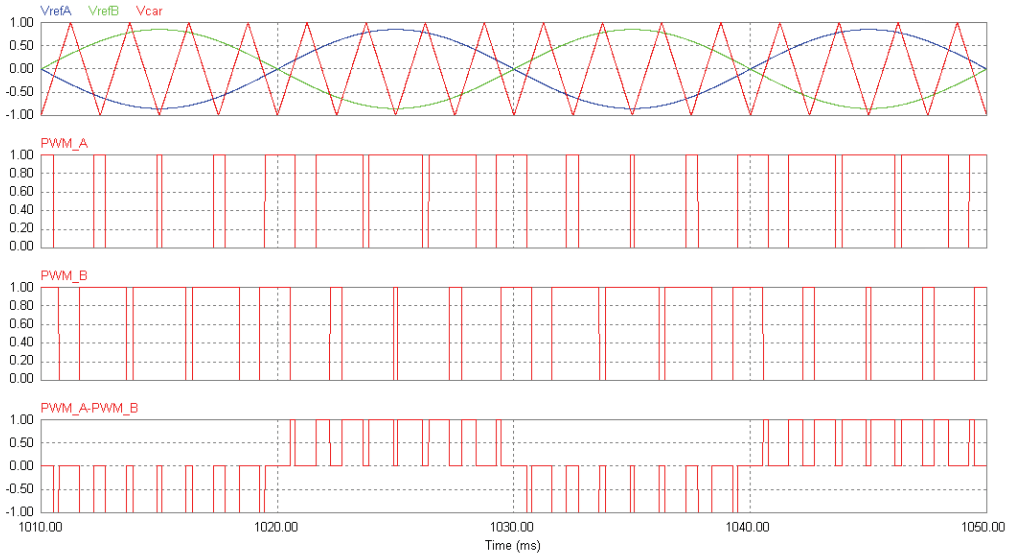

Figure 9-5 - Unipolar Switching Technique

As a single control sinusoid is identical to the bipolar technique the average output voltage is the same.

$$\mathrm{D_A} = \frac{1}{2}\left(\frac{v_{control}}{\hat{V}_{tri}} + 1\right)$$

$$V_{0,ave} = V_{AN} - V_{BN} = \mathrm{D_A}V_D - \mathrm{D_B}V_D = V_D\left(2\mathrm{D_A} - 1\right)$$

$$V_{0,ave} = V_D\frac{v_{control}}{\hat{V}_{tri}} = m_a V_D$$

The fundamental component of the output waveform is also identical to bipolar technique.

$$V_{O1,rms} = \frac{V_D m_a}{\sqrt{2}}$$

The rms value of the output waveform is dependant on the duty cycle of the waveform due to the unipolar output waveform. For bipolar all switching existed between +V$_D$ and -V$_D$ causing the rms value to be independent of the duty cycle, as seen for bipolar. In order to calculate the rms value for a unipolar signal we must make an assumption about the duty cycle. This is that for the positive half cycle the switches conduct for the same amount of time as the average value of the positive segment of a sinusoid.

To calculate the average value of the half sinusoid:

$$V_{ave} = \frac{1}{T}\int_0^T v(t)\,dt = \frac{1}{T}\int_0^{T/2} \sin\theta d\theta = \frac{1}{2\pi}\int_0^{\pi} \sin\theta d\theta = \frac{1}{2\pi}\left[(-\cos\pi) - (-\cos 0)\right] = \frac{1}{\pi}$$

So the ratio that gives the half the duty cycle for half the sinusoid is:

$$Ratio \approx \frac{V_{ave}}{V_D} = \frac{\frac{V_D m_a}{\pi}}{V_D} = \frac{m_a}{\pi}$$

$$\therefore D = \frac{2m_a}{\pi}$$

Finally the rms value of a rectangular waveform is given by:

$$V_{O,rms} = \sqrt{\frac{1}{T}\int_0^T v(t)^2\,dt} = \hat{V}\sqrt{D}$$

$$V_{O,rms} = V_D\sqrt{\frac{2m_a}{\pi}}$$

The total harmonic distortion (THD) of a unipolar switching scheme can be calculated by:

$$THD = \sqrt{\frac{{V_{O,rms}}^2 - {V_{O1,rms}}^2}{{V_{O1,rms}}^2}}$$

$$THD = \sqrt{\frac{m_a\left(\frac{2}{\pi} - \frac{m_a}{2}\right)}{\frac{{m_a}^2}{2}}} = \sqrt{\frac{4}{m_a\pi} - 1}$$

The output ripple of the waveform can be given by:

$$V_{ORIP,rms} = \sqrt{{V_{O,rms}}^2 - {V_{O1,rms}}^2}$$

$$V_{ORIP,rms} = \sqrt{{V_D}^2 \frac{2m_a}{\pi} - \frac{{V_D}^2 {m_a}^2}{2}} = V_D\sqrt{m_a\left(\frac{2}{\pi} - \frac{m_a}{2}\right)}$$

Figure 9-6 shows the waveforms of voltages and currents in a standard H bridge using bipolar PWM generation methods, in this case the switching frequency is 9 times the carrier. Part a) shows the generation technique, b) and c) show the gating signals, d) shows the output voltage waveform, e) the FFT of the output voltage, f) the output current waveform, g) and h) show the dc current and its FFT, i) shows the switch current and j) the diode current.

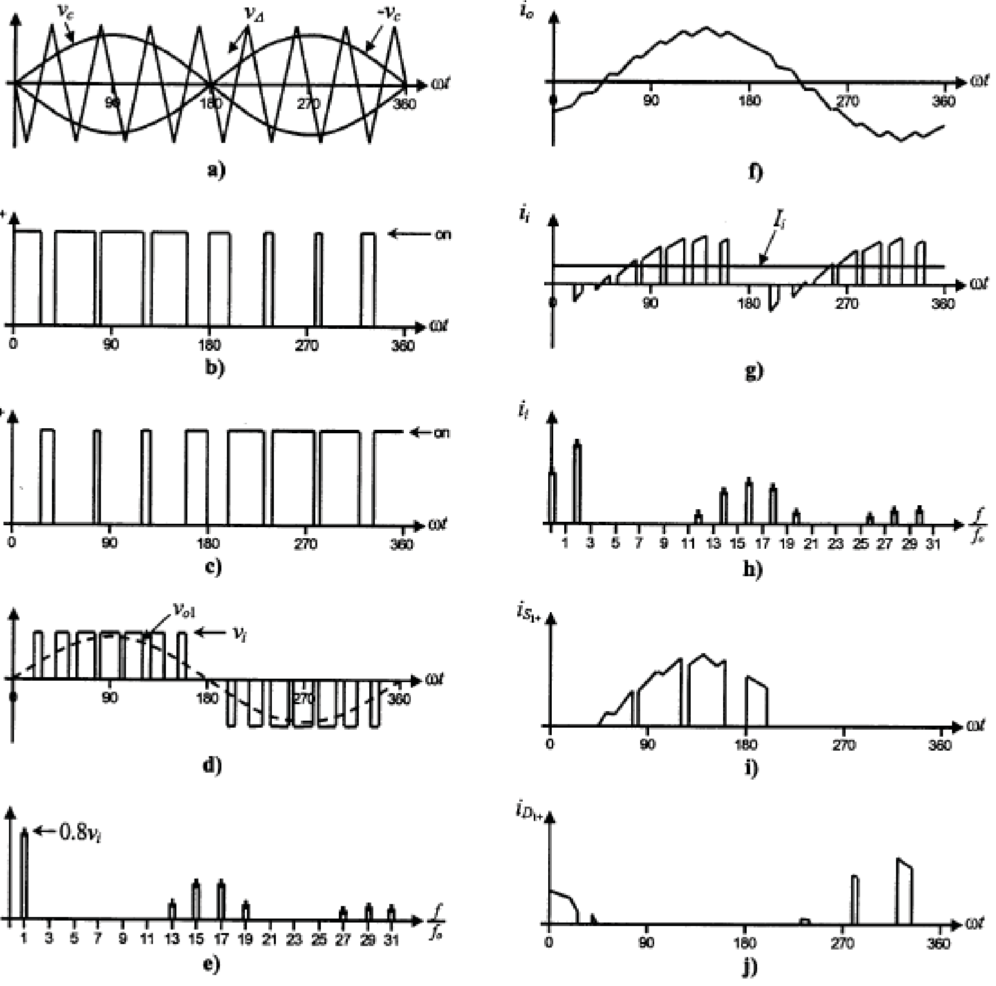

Figure 9-6 - Unipolar Switching Technique

9.4. Additional Wind MPPT Simulations

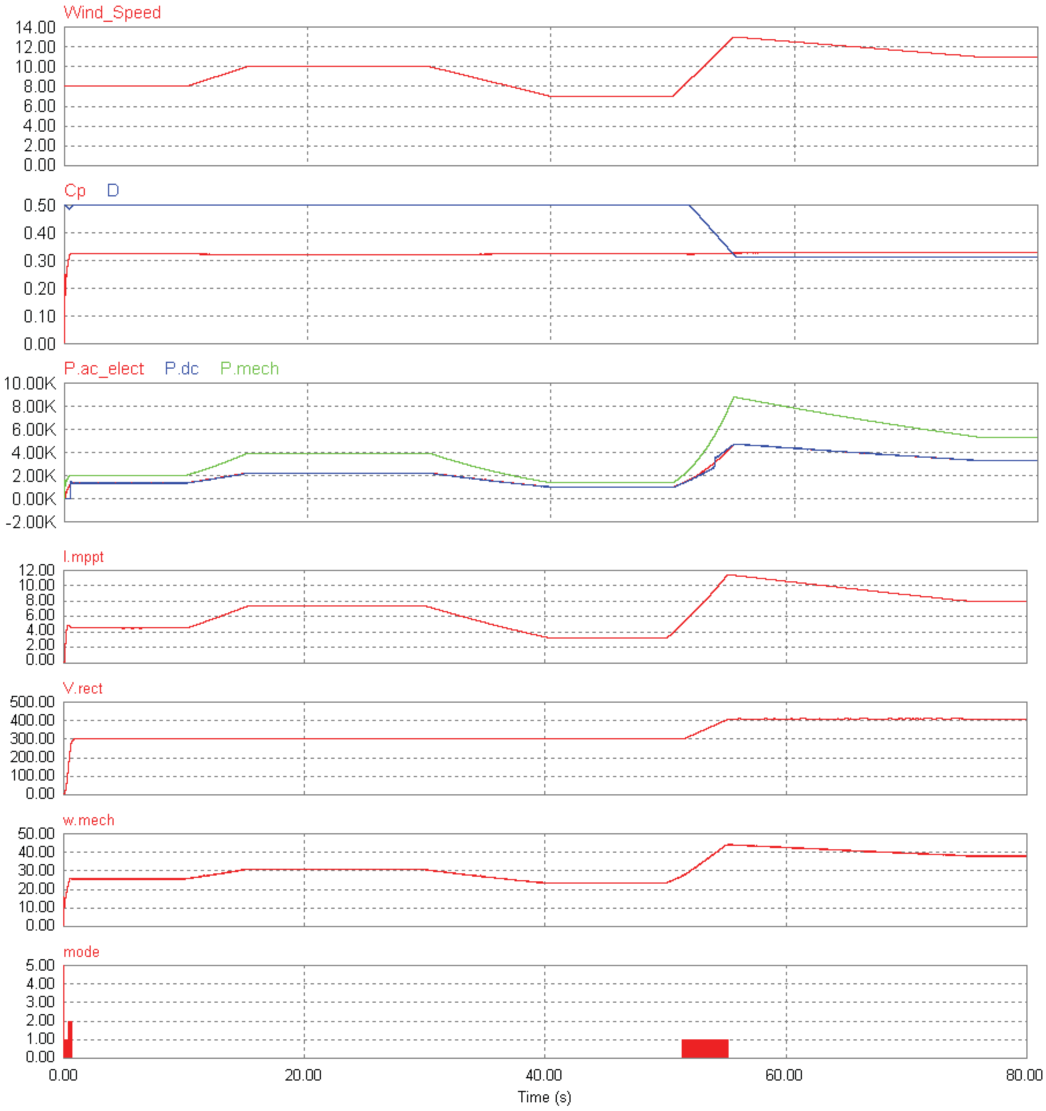

Figure 9-7 : MPPT simulation with cycle = 100; ΔP = 0.05, E = 9.046Wh

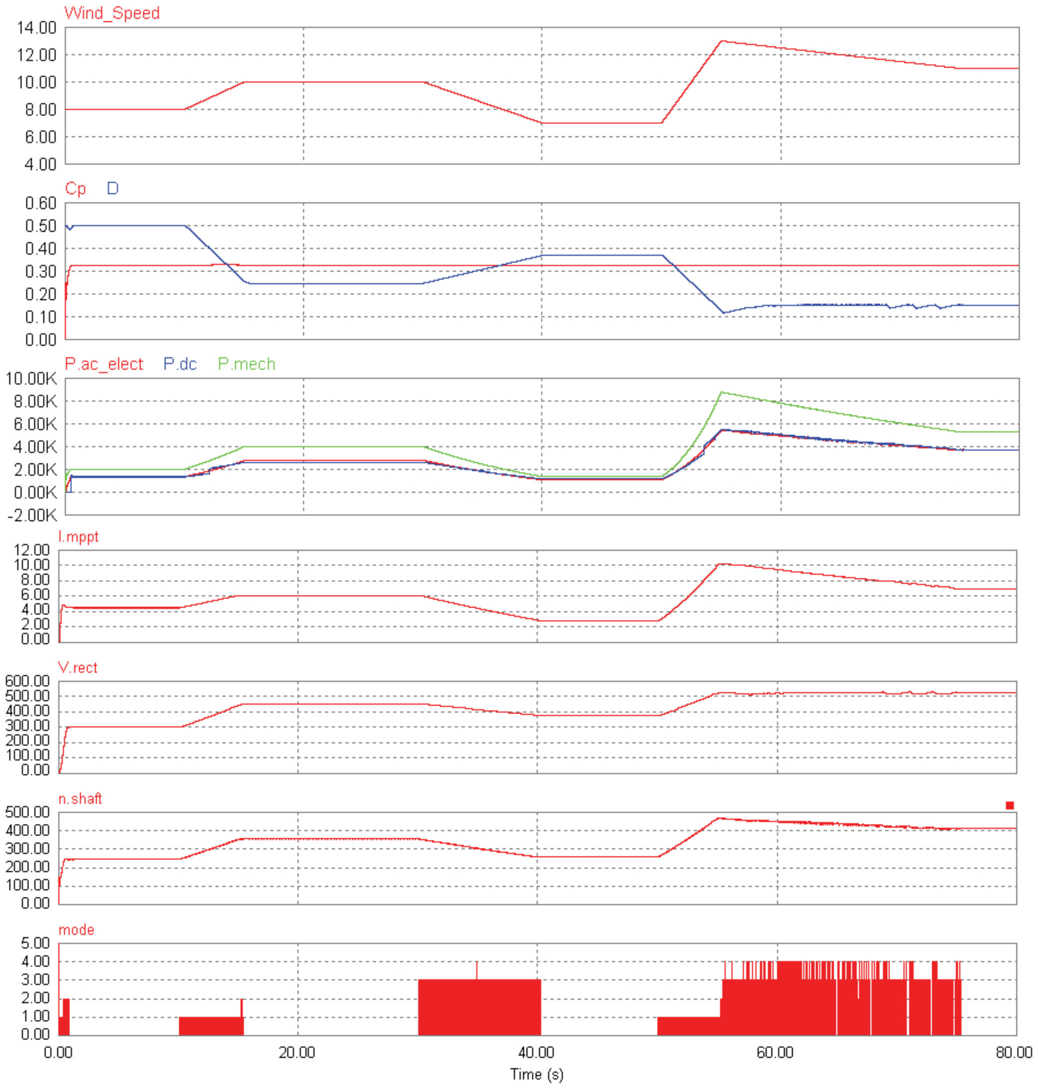

Figure 9-8 : MPPT simulation with cycle = 100; ΔP = 0.005; E = 9.121 Wh

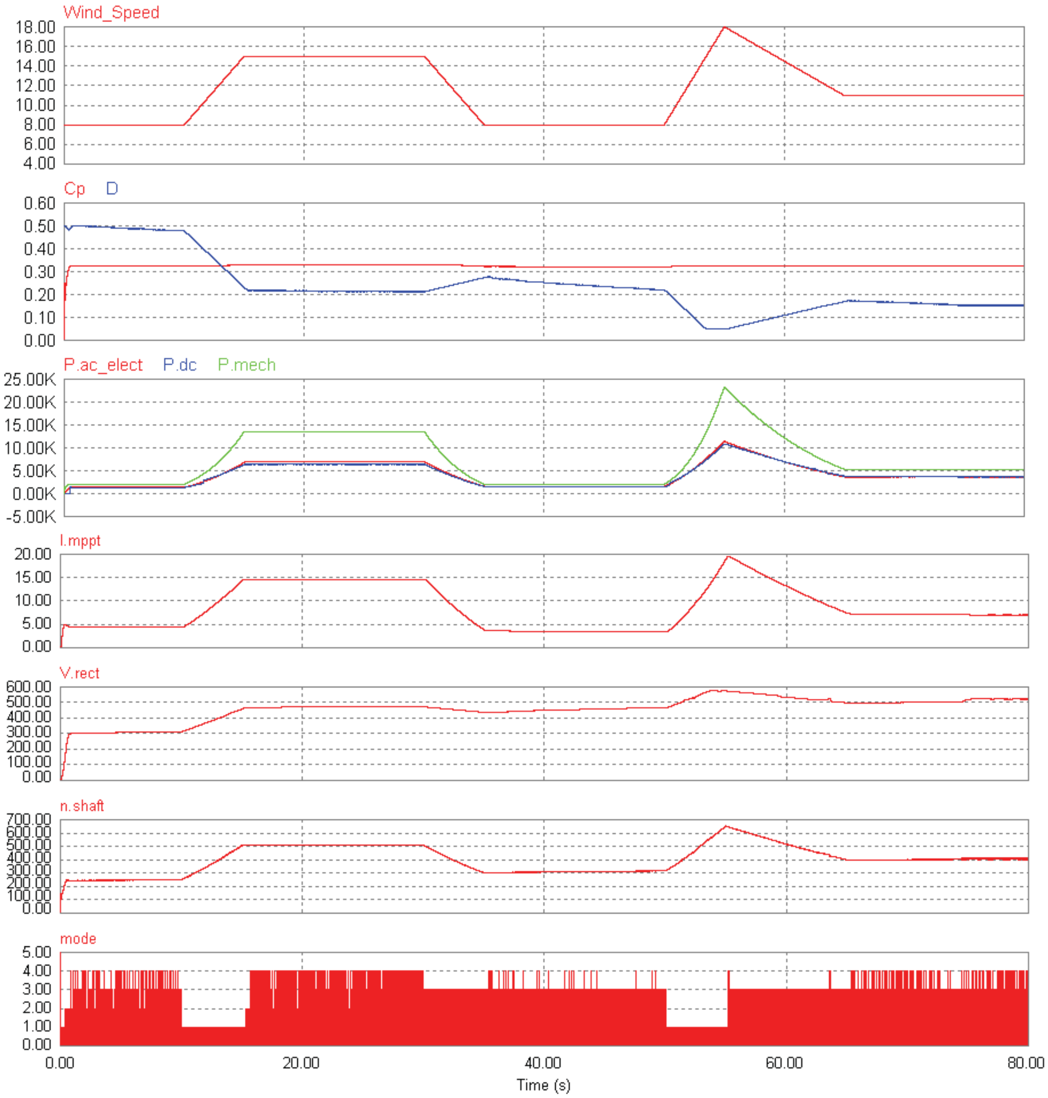

Figure 9-9: MPPT simulation with cycle = 100; ΔP = 0.0005; P = 9.262

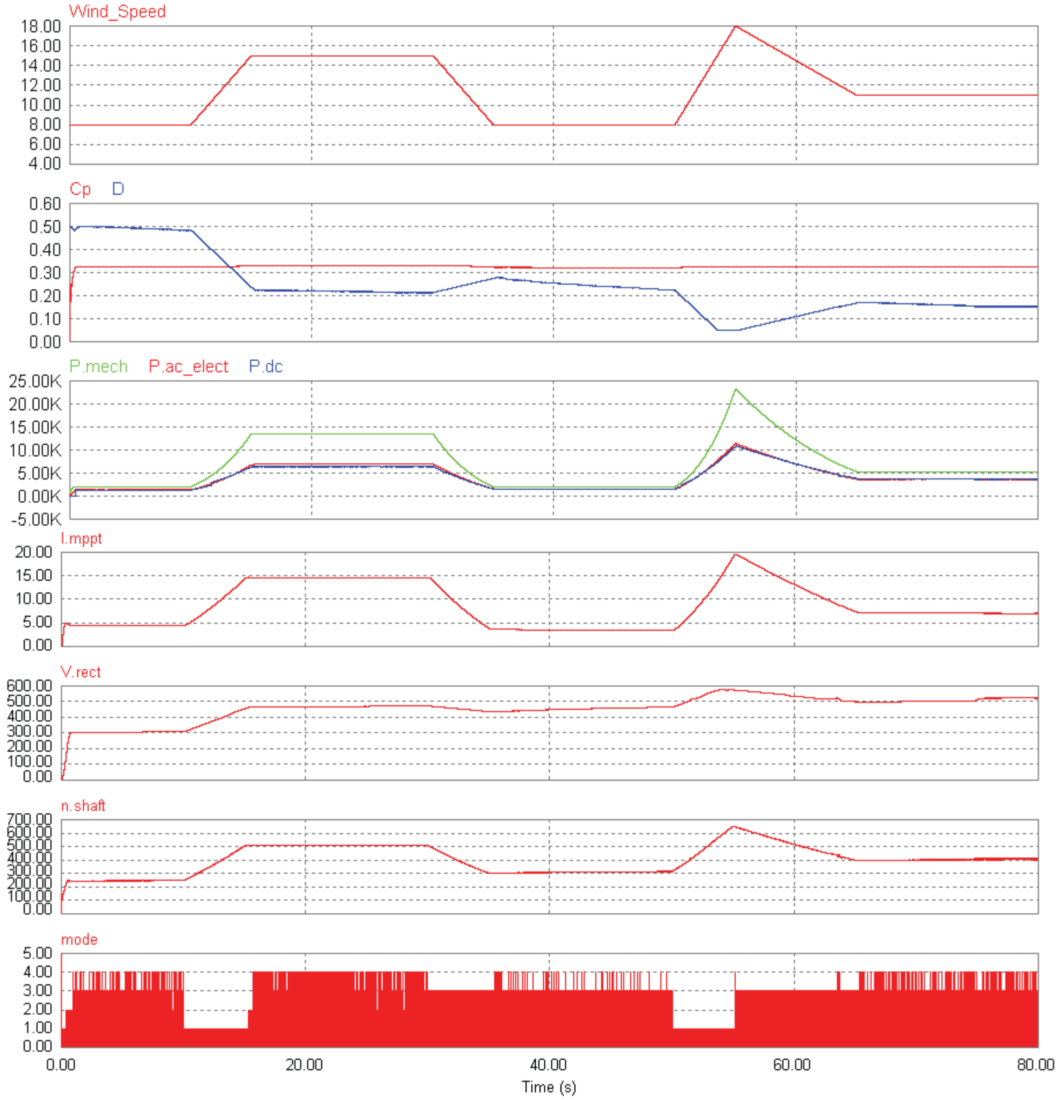

Figure 9-10 : MPPT simulation with cycle = 100; ΔP = 0.00005, E = 9.2497Wh

9.5. Eco Beach Load Data

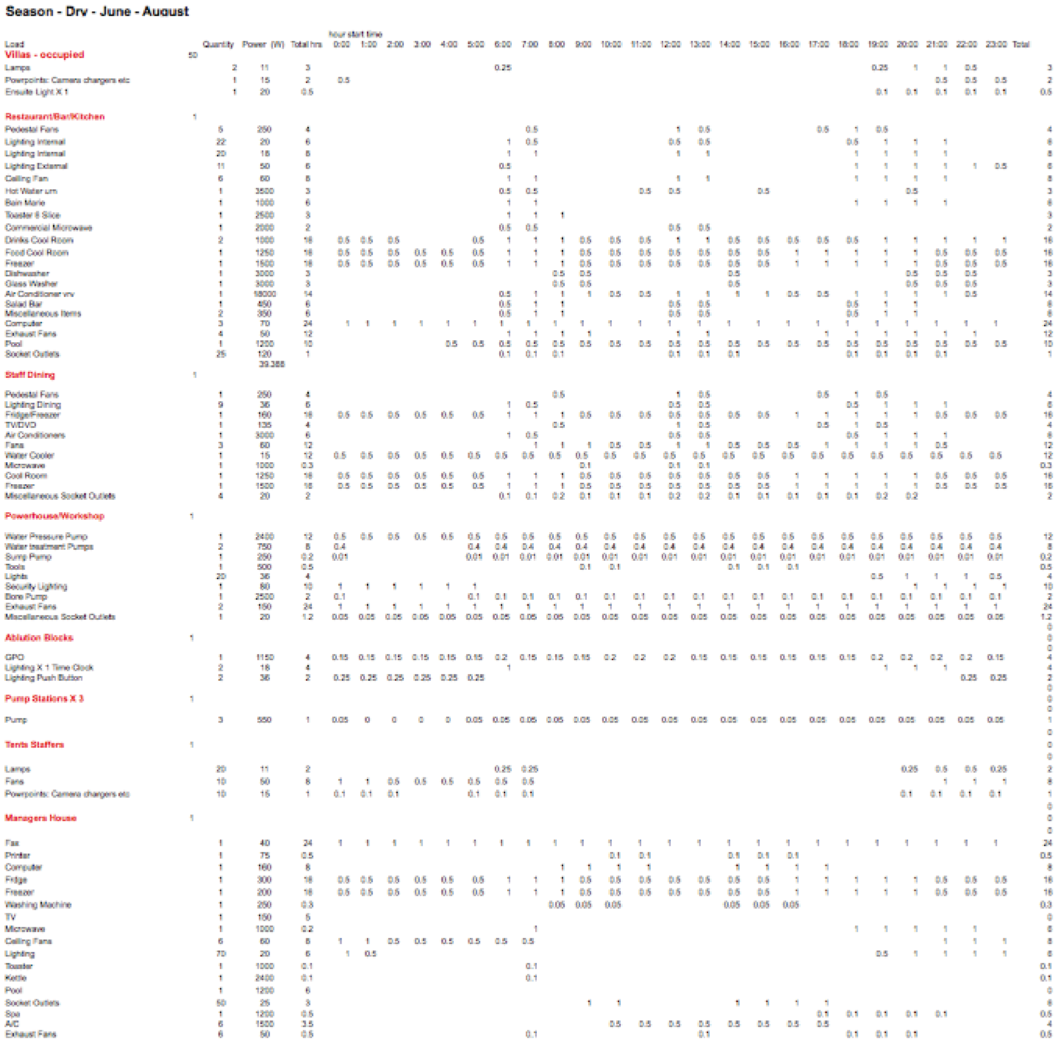

Season - Dry - June - August

					hour start time																								
Load		Quantity	Power (W)	Total hrs	0:00	1:00	2:00	3:00	4:00	5:00	6:00	7:00	8:00	9:00	10:00	11:00	12:00	13:00	14:00	15:00	16:00	17:00	18:00	19:00	20:00	21:00	22:00	23:00	Total
Villas - occupied	50																												
Lamps		2	11	3							0.25													0.25	1	1	0.5		3
Powerpoints: Camera chargers etc		1	15	2	0.5																					0.5	0.5	0.5	2
Ensuite Light X 1		1	20	0.5																				0.1	0.1	0.1	0.1	0.1	0.5
Restaurant/Bar/Kitchen	1																												
Pedestal Fans		5	250	4								0.5					1	0.5				0.5	1	0.5					4
Lighting Internal		22	20	6							1	0.5					0.5	0.5					0.5	1	1	1			6
Lighting Internal		20	18	8							1	1					1	1					1	1	1	1			8
Lighting External		11	50	6							0.5												1	1	1	1	1	0.5	6
Ceiling Fan		6	60	8							1	1					1	1					1	1	1	1			8
Hot Water urn		1	3500	3							0.5	0.5				0.5	0.5			0.5					0.5				3
Bain Marie		1	1000	6							1	1											1	1	1	1			6
Toaster 6 Slice		1	2500	3							1	1	1																3
Commercial Microwave		1	2000	2							0.5	0.5					0.5	0.5											2
Drinks Cool Room		2	1000	16	0.5	0.5	0.5			0.5	1	1	1	0.5	0.5	0.5	1	1	0.5	0.5	0.5	0.5	0.5	1	1	1	1	1	16
Food Cool Room		1	1250	16	0.5	0.5	0.5	0.5	0.5	0.5	1	1	1	0.5	0.5	0.5	0.5	0.5	0.5	0.5	1	1	1	1	1	0.5	0.5	0.5	16
Freezer		1	1500	16	0.5	0.5	0.5	0.5	0.5	0.5	1	1	1	0.5	0.5	0.5	0.5	0.5	0.5	0.5	1	1	1	1	1	0.5	0.5	0.5	16
Dishwasher		1	3000	3									0.5	0.5					0.5						0.5	0.5	0.5		3
Glass Washer		1	3000	3									0.5	0.5					0.5						0.5	0.5	0.5		3
Air Conditioner vrv		1	18000	14							0.5	1	1	1	0.5	0.5	1	1	1	1	0.5	0.5	1	1	1	1	0.5		14
Salad Bar		1	450	6							0.5	1	1				0.5	0.5					0.5	1	1				6
Miscellaneous Items		2	350	6							0.5	1	1				0.5	0.5					0.5	1	1				6
Computer		3	70	24	1	1	1	1	1	1	1	1	1	1	1	1	1	1	1	1	1	1	1	1	1	1	1	1	24
Exhaust Fans		4	60	12							1	1	1	1			1	1				1	1	1	1	1	1		12
Pool		1	1200	10					0.5	0.5	0.5	0.5	0.5	0.5	0.5	0.5	0.5	0.5	0.5	0.5	0.5	0.5	0.5	0.5	0.5	0.5	0.5	0.5	10
Socket Outlets		25	120	1							0.1	0.1	0.1				0.1	0.1	0.1				0.1	0.1	0.1	0.1			1
			39.388																										
Staff Dining	1																												
Pedestal Fans		1	250	4									0.5				1	0.5				0.5	1	0.5					4
Lighting Dining		9	36	6							1	0.5					0.5	0.5					0.5	1	1	1			6
Fridge/Freezer		1	160	16	0.5	0.5	0.5	0.5	0.5	0.5	1	1	1	0.5	0.5	0.5	0.5	0.5	0.5	0.5	1	1	1	1	1	0.5	0.5	0.5	16
TV/DVD		1	135	4									0.5				1	0.5				0.5	1	0.5					4
Air Conditioners		1	3000	6							1	0.5					0.5	0.5					0.5	1	1	1			6
Fans		3	60	12								1	1	1	0.5	0.5	1	1	0.5	0.5	0.5	1	1	1	1	0.5			12
Water Cooler		1	15	12	0.5	0.5	0.5	0.5	0.5	0.5	0.5	0.5	0.5	0.5	0.5	0.5	0.5	0.5	0.5	0.5	0.5	0.5	0.5	0.5	0.5	0.5	0.5	0.5	12
Microwave		1	1000	0.3										0.1			0.1	0.1											0.3
Cool Room		1	1250	16	0.5	0.5	0.5	0.5	0.5	0.5	1	1	1	0.5	0.5	0.5	0.5	0.5	0.5	0.5	1	1	1	1	1	0.5	0.5	0.5	16
Freezer		1	1500	16	0.5	0.5	0.5	0.5	0.5	0.5	1	1	1	0.5	0.5	0.5	0.5	0.5	0.5	0.5	1	1	1	1	1	0.5	0.5	0.5	16
Miscellaneous Socket Outlets		4	20	2							0.1	0.1	0.2	0.1	0.1	0.1	0.2	0.2	0.1	0.1	0.1	0.1	0.1	0.2	0.2				2
Powerhouse/Workshop	1																												
Water Pressure Pump		1	2400	12	0.5	0.5	0.5	0.5	0.5	0.5	0.5	0.5	0.5	0.5	0.5	0.5	0.5	0.5	0.5	0.5	0.5	0.5	0.5	0.5	0.5	0.5	0.5	0.5	12
Water treatment Pumps		2	750	8	0.4					0.4	0.4	0.4	0.4	0.4	0.4	0.4	0.4	0.4	0.4	0.4	0.4	0.4	0.4	0.4	0.4	0.4	0.4	0.4	8
Sump Pump		1	250	0.2	0.01					0.01	0.01	0.01	0.01	0.01	0.01	0.01	0.01	0.01	0.01	0.01	0.01	0.01	0.01	0.01	0.01	0.01	0.01	0.01	0.2
Tools		1	500	0.5										0.1	0.1				0.1	0.1	0.1								0.5
Lights		20	36	4																				0.5	1	1	1	0.5	4
Security Lighting		1	60	10	1	1	1	1	1	1															1	1	1	1	10
Bore Pump		1	2500	2	0.1					0.1	0.1	0.1	0.1	0.1	0.1	0.1	0.1	0.1	0.1	0.1	0.1	0.1	0.1	0.1	0.1	0.1	0.1	0.1	2
Exhaust Fans		2	150	24	1	1	1	1	1	1	1	1	1	1	1	1	1	1	1	1	1	1	1	1	1	1	1	1	24
Miscellaneous Socket Outlets		1	20	1.2	0.05	0.05	0.05	0.05	0.05	0.05	0.05	0.05	0.05	0.05	0.05	0.05	0.05	0.05	0.05	0.05	0.05	0.05	0.05	0.05	0.05	0.05	0.05	0.05	1.2
																													0
Ablution Blocks	1																												0
																													0
GPO		1	1150	4	0.15	0.15	0.15	0.15	0.15	0.15	0.2	0.15	0.15	0.15	0.2	0.2	0.2	0.15	0.15	0.15	0.15	0.15	0.15	0.2	0.2	0.2	0.2	0.15	4
Lighting X 1 Time Clock		2	18	4							1													1	1	1			4
Lighting Push Button		2	36	2	0.25	0.25	0.25	0.25	0.25	0.25																	0.25	0.25	2
																													0
Pump Stations X 3	1																												0
																													0
Pump		3	550	1	0.05	0	0	0	0	0.05	0.05	0.05	0.05	0.05	0.05	0.05	0.05	0.05	0.05	0.05	0.05	0.05	0.05	0.05	0.05	0.05	0.05	0.05	1
																													0
Tents Staffers	1																												0
																													0
Lamps		20	11	2							0.25	0.25													0.25	0.5	0.5	0.25	2
Fans		10	60	8	1	1	0.5	0.5	0.5	0.5	0.5	0.5														1	1	1	8
Powerpoints: Camera chargers etc		10	15	1	0.1	0.1	0.1			0.1	0.1	0.1													0.1	0.1	0.1	0.1	1
																													0
Managers House	1																												0
																													0
Fax		1	40	24	1	1	1	1	1	1	1	1	1	1	1	1	1	1	1	1	1	1	1	1	1	1	1	1	24
Printer		1	75	0.5											0.1	0.1			0.1	0.1	0.1								0.5
Computer		1	160	8									1	1	1	1			1	1	1	1							8
Fridge		1	300	16	0.5	0.5	0.5	0.5	0.5	0.5	1	1	1	0.5	0.5	0.5	0.5	0.5	0.5	0.5	1	1	1	1	1	0.5	0.5	0.5	16
Freezer		1	200	16	0.5	0.5	0.5	0.5	0.5	0.5	1	1	1	0.5	0.5	0.5	0.5	0.5	0.5	0.5	1	1	1	1	1	0.5	0.5	0.5	16
Washing Machine		1	250	0.3									0.05	0.05	0.05				0.05	0.05	0.05								0.3
TV		1	150	5																									0
Microwave		1	1000	0.2								1											1	1	1	1			5
Ceiling Fans		6	60	8	1	1	0.5	0.5	0.5	0.5	0.5	0.5														1	1	1	8
Lighting		70	20	6	1	0.5																		0.5	1	1	1	1	6
Toaster		1	1000	0.1								0.1																	0.1
Kettle		1	2400	0.1								0.1																	0.1
Pool		1	1200	6																									0
Socket Outlets		50	25	3										1	1				1	1	1	1							6
Spa		1	1200	0.5																		0.1	0.1	0.1	0.1	0.1			0.5
A/C		6	1500	3.5											0.5	0.5	0.5	0.5	0.5	0.5	0.5	0.5							4
Exhaust Fans		6	60	0.5								0.1						0.1					0.1	0.1	0.1				0.5

Figure 9-11 : June to August

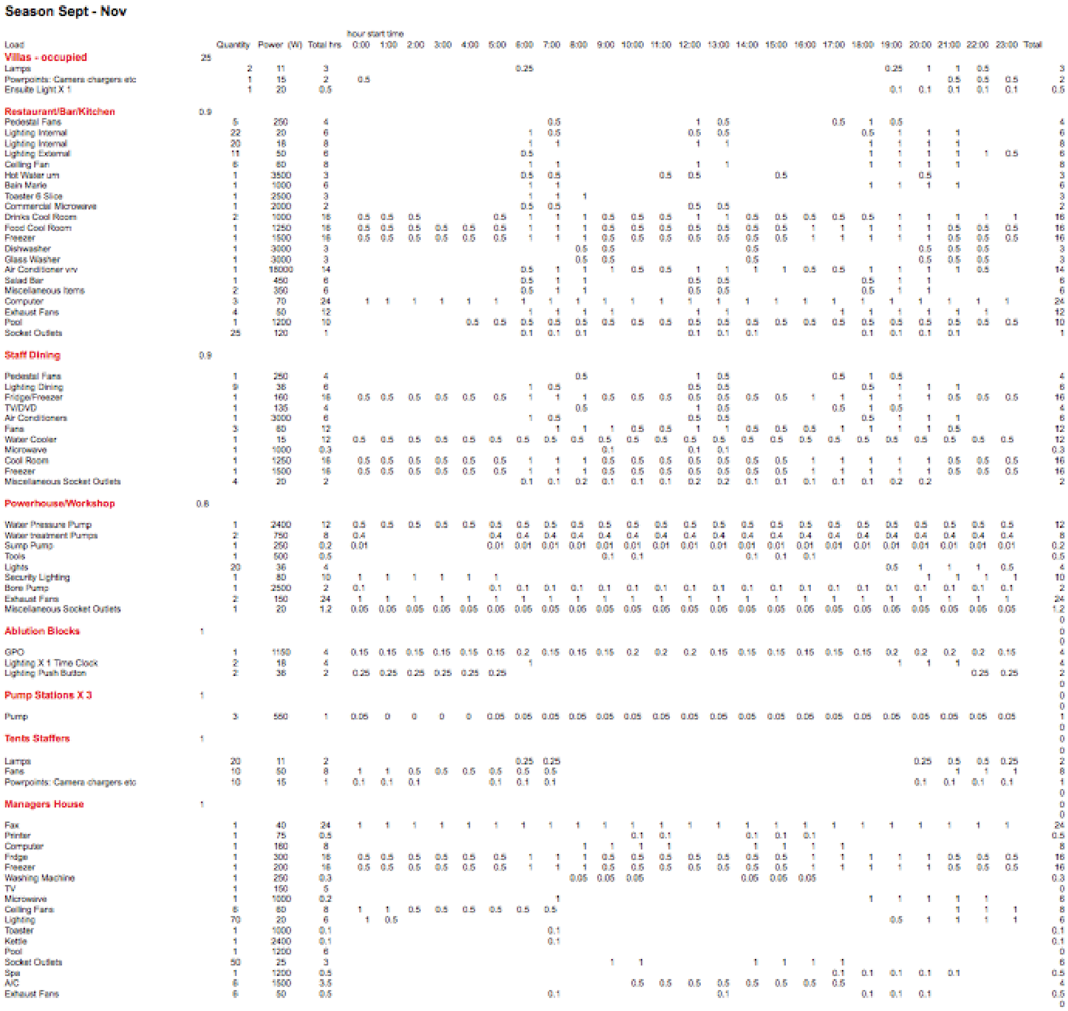

Season Sept - Nov

					hour start time																								
Load		Quantity	Power (W)	Total hrs	0:00	1:00	2:00	3:00	4:00	5:00	6:00	7:00	8:00	9:00	10:00	11:00	12:00	13:00	14:00	15:00	16:00	17:00	18:00	19:00	20:00	21:00	22:00	23:00	Total
Villas - occupied	25																												
Lamps		2	11	3							0.25													0.25	1	1	0.5		3
Powerpoints: Camera chargers etc		1	15	2	0.5																					0.5	0.5	0.5	2
Ensuite Light X 1		1	20	0.5																				0.1	0.1	0.1	0.1	0.1	0.5
Restaurant/Bar/Kitchen	0.9																												
Pedestal Fans		5	250	4								0.5					1	0.5				0.5	1	0.5					4
Lighting Internal		22	20	6							1	0.5					0.5	0.5					0.5	1	1	1			6
Lighting Internal		20	18	8							1	1					1	1					1	1	1	1			8
Lighting External		11	50	6							0.5												1	1	1	1	1	0.5	6
Ceiling Fan		6	60	8							1	1					1	1					1	1	1	1			8
Hot Water urn		1	3500	3							0.5	0.5				0.5	0.5			0.5					0.5				3
Bain Marie		1	1000	6							1	1											1	1	1	1			6
Toaster 6 Slice		1	2500	3							1	1	1																3
Commercial Microwave		1	2000	2							0.5	0.5					0.5	0.5											2
Drinks Cool Room		2	1000	16	0.5	0.5	0.5			0.5	1	1	1	0.5	0.5	0.5	1	1	0.5	0.5	0.5	0.5	0.5	1	1	1	1	1	16
Food Cool Room		1	1250	16	0.5	0.5	0.5	0.5	0.5	0.5	1	1	1	0.5	0.5	0.5	0.5	0.5	0.5	0.5	1	1	1	1	1	0.5	0.5	0.5	16
Freezer		1	1500	16	0.5	0.5	0.5	0.5	0.5	0.5	1	1	1	0.5	0.5	0.5	0.5	0.5	0.5	0.5	1	1	1	1	1	0.5	0.5	0.5	16
Dishwasher		1	3000	3									0.5	0.5					0.5						0.5	0.5	0.5		3
Glass Washer		1	3000	3									0.5	0.5					0.5						0.5	0.5	0.5		3
Air Conditioner vrv		1	18000	14							0.5	1	1	1	0.5	0.5	1	1	1	1	0.5	0.5	1	1	1	1	0.5		14
Salad Bar		1	450	6							0.5	1	1				0.5	0.5					0.5	1	1				6
Miscellaneous Items		2	350	6							0.5	1	1				0.5	0.5					0.5	1	1				6
Computer		3	70	24	1	1	1	1	1	1	1	1	1	1	1	1	1	1	1	1	1	1	1	1	1	1	1	1	24
Exhaust Fans		4	50	12							1	1	1	1			1	1				1	1	1	1	1	1		12
Pool		1	1200	10					0.5	0.5	0.5	0.5	0.5	0.5	0.5	0.5	0.5	0.5	0.5	0.5	0.5	0.5	0.5	0.5	0.5	0.5	0.5	0.5	10
Socket Outlets		25	120	1							0.1	0.1	0.1				0.1	0.1	0.1				0.1	0.1	0.1	0.1			1
Staff Dining	0.9																												
Pedestal Fans		1	250	4									0.5				1	0.5				0.5	1	0.5					4
Lighting Dining		9	36	6							1	0.5					0.5	0.5					0.5	1	1	1			6
Fridge/Freezer		1	160	16	0.5	0.5	0.5	0.5	0.5	0.5	1	1	1	0.5	0.5	0.5	0.5	0.5	0.5	0.5	1	1	1	1	1	0.5	0.5	0.5	16
TV/DVD		1	135	4									0.5				1	0.5				0.5	1	0.5					4
Air Conditioners		1	3000	6							1	0.5					0.5	0.5					0.5	1	1	1			6
Fans		3	60	12								1	1	1	0.5	0.5	1	1	0.5	0.5	0.5	1	1	1	1	0.5			12
Water Cooler		1	15	12	0.5	0.5	0.5	0.5	0.5	0.5	0.5	0.5	0.5	0.5	0.5	0.5	0.5	0.5	0.5	0.5	0.5	0.5	0.5	0.5	0.5	0.5	0.5	0.5	12
Microwave		1	1000	0.3										0.1			0.1	0.1											0.3
Cool Room		1	1250	16	0.5	0.5	0.5	0.5	0.5	0.5	1	1	1	0.5	0.5	0.5	0.5	0.5	0.5	0.5	1	1	1	1	1	0.5	0.5	0.5	16
Freezer		1	1500	16	0.5	0.5	0.5	0.5	0.5	0.5	1	1	1	0.5	0.5	0.5	0.5	0.5	0.5	0.5	1	1	1	1	1	0.5	0.5	0.5	16
Miscellaneous Socket Outlets		4	20	2							0.1	0.1	0.2	0.1	0.1	0.1	0.2	0.2	0.1	0.1	0.1	0.1	0.1	0.2	0.2				2
Powerhouse/Workshop	0.8																												
Water Pressure Pump		1	2400	12	0.5	0.5	0.5	0.5	0.5	0.5	0.5	0.5	0.5	0.5	0.5	0.5	0.5	0.5	0.5	0.5	0.5	0.5	0.5	0.5	0.5	0.5	0.5	0.5	12
Water treatment Pumps		2	750	8	0.4					0.4	0.4	0.4	0.4	0.4	0.4	0.4	0.4	0.4	0.4	0.4	0.4	0.4	0.4	0.4	0.4	0.4	0.4	0.4	8
Sump Pump		1	250	0.2	0.01					0.01	0.01	0.01	0.01	0.01	0.01	0.01	0.01	0.01	0.01	0.01	0.01	0.01	0.01	0.01	0.01	0.01	0.01	0.01	0.2
Tools		1	500	0.5										0.1	0.1				0.1	0.1	0.1								0.5
Lights		20	36	4																				0.5	1	1	1	0.5	4
Security Lighting		1	80	10	1	1	1	1	1	1															1	1	1	1	10
Bore Pump		1	2500	2	0.1					0.1	0.1	0.1	0.1	0.1	0.1	0.1	0.1	0.1	0.1	0.1	0.1	0.1	0.1	0.1	0.1	0.1	0.1	0.1	2
Exhaust Fans		2	150	24	1	1	1	1	1	1	1	1	1	1	1	1	1	1	1	1	1	1	1	1	1	1	1	1	24
Miscellaneous Socket Outlets		1	20	1.2	0.05	0.05	0.05	0.05	0.05	0.05	0.05	0.05	0.05	0.05	0.05	0.05	0.05	0.05	0.05	0.05	0.05	0.05	0.05	0.05	0.05	0.05	0.05	0.05	1.2
																													0
Ablution Blocks	1																												0
																													0
GPO		1	1150	4	0.15	0.15	0.15	0.15	0.15	0.15	0.2	0.15	0.15	0.15	0.2	0.2	0.2	0.15	0.15	0.15	0.15	0.15	0.15	0.2	0.2	0.2	0.2	0.15	4
Lighting X 1 Time Clock		2	18	4							1													1	1	1			4
Lighting Push Button		2	36	2	0.25	0.25	0.25	0.25	0.25	0.25																	0.25	0.25	2
																													0
Pump Stations X 3	1																												0
																													0
Pump		3	550	1	0.05	0	0	0	0	0.05	0.05	0.05	0.05	0.05	0.05	0.05	0.05	0.05	0.05	0.05	0.05	0.05	0.05	0.05	0.05	0.05	0.05	0.05	1
																													0
Tents Staffers	1																												0
																													0
Lamps		20	11	2							0.25	0.25													0.25	0.5	0.5	0.25	2
Fans		10	50	8	1	1	0.5	0.5	0.5	0.5	0.5	0.5														1	1	1	8
Powerpoints: Camera chargers etc		10	15	1	0.1	0.1	0.1			0.1	0.1	0.1													0.1	0.1	0.1	0.1	1
																													0
Managers House	1																												0
																													0
Fax		1	40	24	1	1	1	1	1	1	1	1	1	1	1	1	1	1	1	1	1	1	1	1	1	1	1	1	24
Printer		1	75	0.5											0.1	0.1			0.1	0.1	0.1								0.5
Computer		1	160	8									1	1	1	1			1	1	1	1							8
Fridge		1	300	16	0.5	0.5	0.5	0.5	0.5	0.5	1	1	1	0.5	0.5	0.5	0.5	0.5	0.5	0.5	1	1	1	1	1	0.5	0.5	0.5	16
Freezer		1	200	16	0.5	0.5	0.5	0.5	0.5	0.5	1	1	1	0.5	0.5	0.5	0.5	0.5	0.5	0.5	1	1	1	1	1	0.5	0.5	0.5	16
Washing Machine		1	250	0.3									0.05	0.05	0.05				0.05	0.05	0.05								0.3
TV		1	150	5																									0
Microwave		1	1000	0.2								1											1	1	1	1	1		6
Ceiling Fans		6	60	8	1	1	0.5	0.5	0.5	0.5	0.5	0.5														1	1	1	8
Lighting		70	20	6	1	0.5																		0.5	1	1	1	1	6
Toaster		1	1000	0.1								0.1																	0.1
Kettle		1	2400	0.1								0.1																	0.1
Pool		1	1200	6																									0
Socket Outlets		50	25	3										1	1				1	1	1	1							6
Spa		1	1200	0.5																		0.1	0.1	0.1	0.1	0.1			0.5
A/C		6	1500	3.5											0.5	0.5	0.5	0.5	0.5	0.5	0.5	0.5							4
Exhaust Fans		6	50	0.5								0.1						0.1					0.1	0.1	0.1				0.5
																													0

Figure 9-12 : September - November

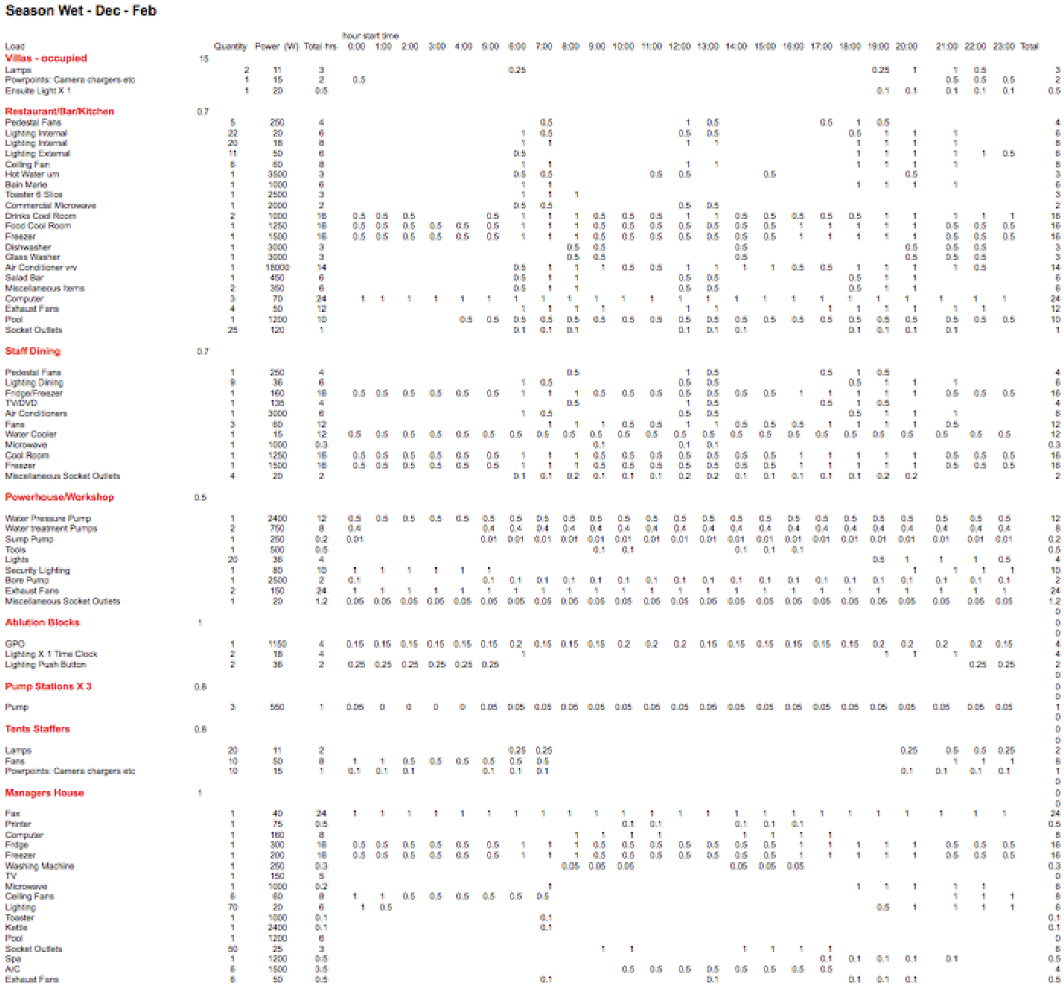

Season Wet - Dec - Feb

					hour start time																								
Load		Quantity	Power (W)	Total hrs	0:00	1:00	2:00	3:00	4:00	5:00	6:00	7:00	8:00	9:00	10:00	11:00	12:00	13:00	14:00	15:00	16:00	17:00	18:00	19:00	20:00	21:00	22:00	23:00	Total
Villas - occupied	15																												
Lamps		2	11	3							0.25													0.25	1	1	0.5		3
Powpoints: Camera chargers etc		1	15	2	0.5																					0.5	0.5	0.5	2
Ensuite Light X 1		1	20	0.5																				0.1	0.1	0.1	0.1	0.1	0.5
Restaurant/Bar/Kitchen	0.7																												
Pedestal Fans		5	250	4								0.5					1	0.5				0.5	1	0.5					4
Lighting Internal		22	20	6							1	0.5					0.5	0.5					0.5	1	1	1			6
Lighting Internal		20	18	8							1	1					1	1					1	1	1	1			8
Lighting External		11	50	6							0.5												1	1	1	1	1	0.5	6
Ceiling Fan		6	60	8							1	1					1	1					1	1	1	1			8
Hot Water urn		1	3500	3							0.5	0.5				0.5	0.5			0.5					0.5				3
Bain Marie		1	1000	6							1	1											1	1	1	1			6
Toaster 6 Slice		1	2500	3							1	1	1																3
Commercial Microwave		1	2000	2							0.5	0.5					0.5	0.5											2
Drinks Cool Room		2	1000	16	0.5	0.5	0.5			0.5	1	1	1	0.5	0.5	0.5	1	1	0.5	0.5	0.5	0.5	0.5	1	1	1	1	1	16
Food Cool Room		1	1250	16	0.5	0.5	0.5	0.5	0.5	0.5	1	1	1	0.5	0.5	0.5	0.5	0.5	0.5	0.5	1	1	1	1	1	0.5	0.5	0.5	16
Freezer		1	1500	16	0.5	0.5	0.5	0.5	0.5	0.5	1	1	1	0.5	0.5	0.5	0.5	0.5	0.5	0.5	1	1	1	1	1	0.5	0.5	0.5	16
Dishwasher		1	3000	3									0.5	0.5					0.5						0.5	0.5	0.5		3
Glass Washer		1	3000	3									0.5	0.5					0.5						0.5	0.5	0.5		3
Air Conditioner vrv		1	18000	14							0.5	1	1	1	0.5	0.5	1	1	1	1	0.5	0.5	1	1	1	1	0.5		14
Salad Bar		1	450	6							0.5	1	1				0.5	0.5					0.5	1	1				6
Miscellaneous Items		2	350	6							0.5	1	1				0.5	0.5					0.5	1	1				6
Computer		3	70	24	1	1	1	1	1	1	1	1	1	1	1	1	1	1	1	1	1	1	1	1	1	1	1	1	24
Exhaust Fans		4	50	12							1	1	1	1			1	1				1	1	1	1	1	1		12
Pool		1	1200	10					0.5	0.5	0.5	0.5	0.5	0.5	0.5	0.5	0.5	0.5	0.5	0.5	0.5	0.5	0.5	0.5	0.5	0.5	0.5	0.5	10
Socket Outlets		25	120	1							0.1	0.1	0.1				0.1	0.1	0.1				0.1	0.1	0.1	0.1			1
Staff Dining	0.7																												
Pedestal Fans		1	250	4									0.5				1	0.5				0.5	1	0.5					4
Lighting Dining		9	36	6							1	0.5					0.5	0.5					0.5	1	1	1			6
Fridge/Freezer		1	160	16	0.5	0.5	0.5	0.5	0.5	0.5	1	1	1	0.5	0.5	0.5	0.5	0.5	0.5	0.5	1	1	1	1	1	0.5	0.5	0.5	16
TV/DVD		1	135	4									0.5				1	0.5				0.5	1	0.5					4
Air Conditioners		1	3000	6							1	0.5					0.5	0.5					0.5	1	1	1			6
Fans		3	60	12								1	1	1	0.5	0.5	1	1	0.5	0.5	0.5	1	1	1	1	0.5			12
Water Cooler		1	15	12	0.5	0.5	0.5	0.5	0.5	0.5	0.5	0.5	0.5	0.5	0.5	0.5	0.5	0.5	0.5	0.5	0.5	0.5	0.5	0.5	0.5	0.5	0.5	0.5	12
Microwave		1	1000	0.3										0.1			0.1	0.1											0.3
Cool Room		1	1250	16	0.5	0.5	0.5	0.5	0.5	0.5	1	1	1	0.5	0.5	0.5	0.5	0.5	0.5	0.5	1	1	1	1	1	0.5	0.5	0.5	16
Freezer		1	1500	16	0.5	0.5	0.5	0.5	0.5	0.5	1	1	1	0.5	0.5	0.5	0.5	0.5	0.5	0.5	1	1	1	1	1	0.5	0.5	0.5	16
Miscellaneous Socket Outlets		4	20	2							0.1	0.1	0.2	0.1	0.1	0.1	0.2	0.2	0.1	0.1	0.1	0.1	0.1	0.2	0.2				2
Powerhouse/Workshop	0.5																												
Water Pressure Pump		1	2400	12	0.5	0.5	0.5	0.5	0.5	0.5	0.5	0.5	0.5	0.5	0.5	0.5	0.5	0.5	0.5	0.5	0.5	0.5	0.5	0.5	0.5	0.5	0.5	0.5	12
Water treatment Pumps		2	750	8	0.4					0.4	0.4	0.4	0.4	0.4	0.4	0.4	0.4	0.4	0.4	0.4	0.4	0.4	0.4	0.4	0.4	0.4	0.4	0.4	8
Sump Pump		1	250	0.2	0.01					0.01	0.01	0.01	0.01	0.01	0.01	0.01	0.01	0.01	0.01	0.01	0.01	0.01	0.01	0.01	0.01	0.01	0.01	0.01	0.2
Tools		1	500	0.5										0.1	0.1				0.1	0.1	0.1								0.5
Lights		20	36	4																				0.5	1	1	1	0.5	4
Security Lighting		1	80	10	1	1	1	1	1	1															1	1	1	1	10
Bore Pump		1	2500	2	0.1					0.1	0.1	0.1	0.1	0.1	0.1	0.1	0.1	0.1	0.1	0.1	0.1	0.1	0.1	0.1	0.1	0.1	0.1	0.1	2
Exhaust Fans		2	150	24	1	1	1	1	1	1	1	1	1	1	1	1	1	1	1	1	1	1	1	1	1	1	1	1	24
Miscellaneous Socket Outlets		1	20	1.2	0.05	0.05	0.05	0.05	0.05	0.05	0.05	0.05	0.05	0.05	0.05	0.05	0.05	0.05	0.05	0.05	0.05	0.05	0.05	0.05	0.05	0.05	0.05	0.05	1.2
																													0
Ablution Blocks	1																												0
																													0
GPO		1	1150	4	0.15	0.15	0.15	0.15	0.15	0.15	0.2	0.15	0.15	0.15	0.2	0.2	0.2	0.15	0.15	0.15	0.15	0.15	0.15	0.2	0.2	0.2	0.2	0.15	4
Lighting X 1 Time Clock		2	18	4							1													1	1	1			4
Lighting Push Button		2	36	2	0.25	0.25	0.25	0.25	0.25	0.25																	0.25	0.25	2
																													0
Pump Stations X 3	0.8																												0
																													0
Pump		3	550	1	0.05	0	0	0	0	0.05	0.05	0.05	0.05	0.05	0.05	0.05	0.05	0.05	0.05	0.05	0.05	0.05	0.05	0.05	0.05	0.05	0.05	0.05	1
																													0
Tents Staffers	0.8																												0
																													0
Lamps		20	11	2							0.25	0.25													0.25	0.5	0.5	0.25	2
Fans		10	60	8	1	1	0.5	0.5	0.5	0.5	0.5	0.5														1	1	1	8
Powpoints: Camera chargers etc		10	15	1	0.1	0.1	0.1			0.1	0.1	0.1													0.1	0.1	0.1	0.1	1
																													0
Managers House	1																												0
																													0
Fax		1	40	24	1	1	1	1	1	1	1	1	1	1	1	1	1	1	1	1	1	1	1	1	1	1	1	1	24
Printer		1	75	0.5											0.1	0.1			0.1	0.1	0.1								0.5
Computer		1	160	8									1	1	1	1			1	1	1	1							8
Fridge		1	300	16	0.5	0.5	0.5	0.5	0.5	0.5	1	1	1	0.5	0.5	0.5	0.5	0.5	0.5	0.5	1	1	1	1	1	0.5	0.5	0.5	16
Freezer		1	200	16	0.5	0.5	0.5	0.5	0.5	0.5	1	1	1	0.5	0.5	0.5	0.5	0.5	0.5	0.5	1	1	1	1	1	0.5	0.5	0.5	16
Washing Machine		1	250	0.3									0.05	0.05	0.05				0.05	0.05	0.05								0.3
TV		1	150	5																									0
Microwave		1	1000	0.2								1											1	1	1	1	1		6
Ceiling Fans		6	60	8	1	1	0.5	0.5	0.5	0.5	0.5	0.5														1	1	1	8
Lighting		70	20	6	1	0.5																		0.5	1	1	1	1	6
Toaster		1	1000	0.1								0.1																	0.1
Kettle		1	2400	0.1								0.1																	0.1
Pool		1	1200	6																									0
Socket Outlets		50	25	3										1	1				1	1	1	1							6
Spa		1	1200	0.5																		0.1	0.1	0.1	0.1	0.1			0.5
A/C		6	1500	3.5											0.5	0.5	0.5	0.5	0.5	0.5	0.5	0.5							4
Exhaust Fans		6	50	0.5								0.1						0.1					0.1	0.1	0.1				0.5

Figure 9-13 : December to February

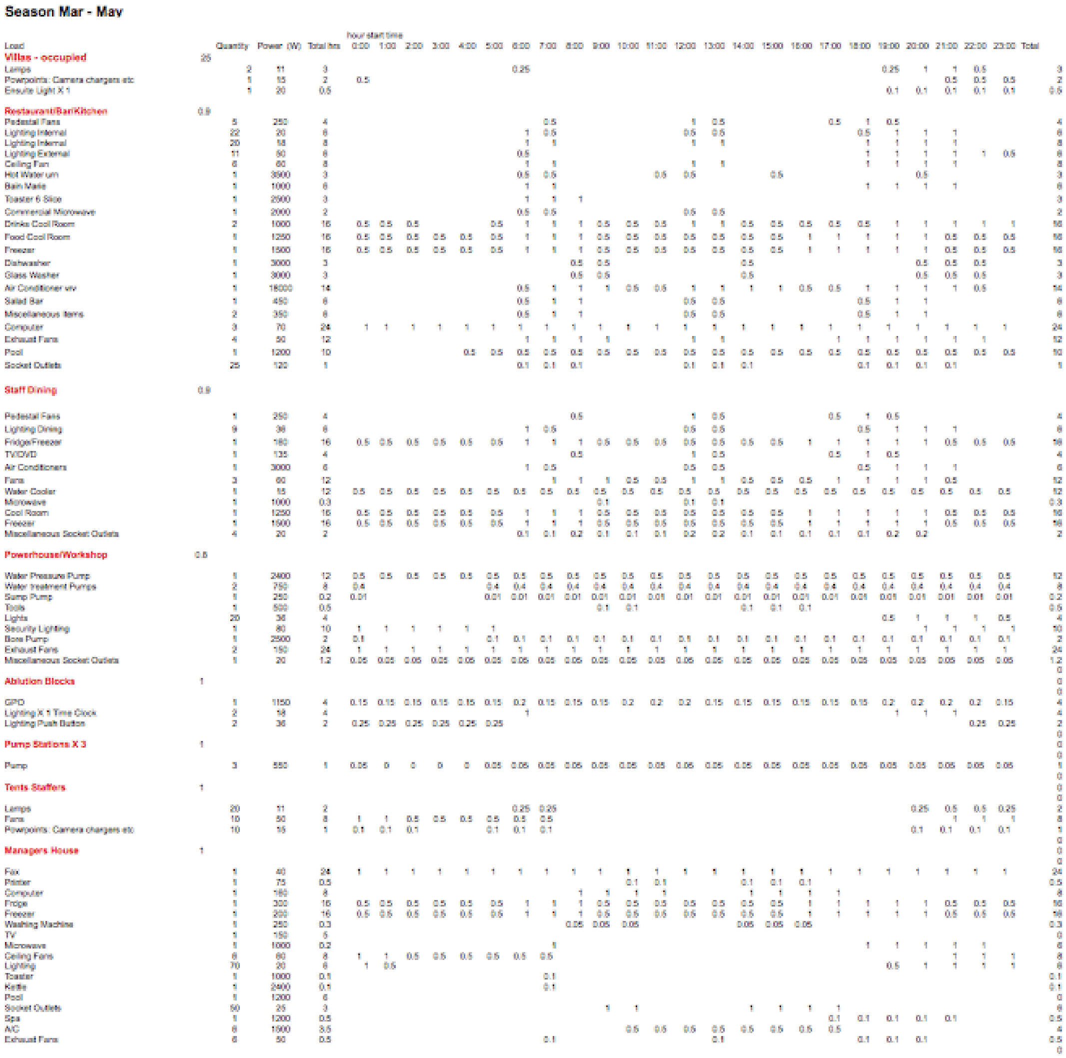

Season Mar - May

					hour start time																								
Load		Quantity	Power (W)	Total hrs	0:00	1:00	2:00	3:00	4:00	5:00	6:00	7:00	8:00	9:00	10:00	11:00	12:00	13:00	14:00	15:00	16:00	17:00	18:00	19:00	20:00	21:00	22:00	23:00	Total
Villas - occupied	25																												
Lamps		2	11	3							0.25													0.25	1	1	0.5		3
Powerpoints: Camera chargers etc		1	15	2	0.5																					0.5	0.5	0.5	2
Ensuite Light X 1		1	20	0.5																				0.1	0.1	0.1	0.1	0.1	0.5
Restaurant/Bar/Kitchen	0.9																												
Pedestal Fans		5	250	4								0.5					1	0.5				0.5	1	0.5					4
Lighting Internal		22	20	6							1	0.5					0.5	0.5					0.5	1	1	1			6
Lighting Internal		20	58	8							1	1					1	1					1	1	1	1			8
Lighting External		11	50	6							0.5												1	1	1	1	1	0.5	6
Ceiling Fan		6	60	8							1	1					1	1					1	1	1	1			8
Hot Water urn		1	3500	3							0.5	0.5				0.5	0.5			0.5					0.5				3
Bain Marie		1	1000	6							1	1											1	1	1	1			6
Toaster 6 Slice		1	2500	3							1	1	1																3
Commercial Microwave		1	2000	2							0.5	0.5					0.5	0.5											2
Drinks Cool Room		2	1000	16	0.5	0.5	0.5			0.5	1	1	1	0.5	0.5	0.5	1	1	0.5	0.5	0.5	0.5	0.5	1	1	1	1	1	16
Food Cool Room		1	1250	16	0.5	0.5	0.5	0.5	0.5	0.5	1	1	1	0.5	0.5	0.5	0.5	0.5	0.5	0.5	1	1	1	1	1	0.5	0.5	0.5	16
Freezer		1	1500	16	0.5	0.5	0.5	0.5	0.5	0.5	1	1	1	0.5	0.5	0.5	0.5	0.5	0.5	0.5	1	1	1	1	1	0.5	0.5	0.5	16
Dishwasher		1	3000	3									0.5	0.5					0.5						0.5	0.5	0.5		3
Glass Washer		1	3000	3									0.5	0.5					0.5						0.5	0.5	0.5		3
Air Conditioner vrv		1	18000	14							0.5	1	1	1	0.5	0.5	1	1	1	1	0.5	0.5	1	1	1	1	0.5		14
Salad Bar		1	450	6							0.5	1	1				0.5	0.5					0.5	1	1				6
Miscellaneous Items		2	350	6							0.5	1	1				0.5	0.5					0.5	1	1				6
Computer		3	70	24	1	1	1	1	1	1	1	1	1	1	1	1	1	1	1	1	1	1	1	1	1	1	1	1	24
Exhaust Fans		4	50	12							1	1	1	1			1	1				1	1	1	1	1	1		12
Pool		1	1200	10					0.5	0.5	0.5	0.5	0.5	0.5	0.5	0.5	0.5	0.5	0.5	0.5	0.5	0.5	0.5	0.5	0.5	0.5	0.5	0.5	10
Socket Outlets		25	120	1							0.1	0.1	0.1				0.1	0.1	0.1				0.1	0.1	0.1	0.1			1
Staff Dining	0.9																												
Pedestal Fans		1	250	4									0.5				1	0.5				0.5	1	0.5					4
Lighting Dining		9	36	6							1	0.5					0.5	0.5					0.5	1	1	1			6
Fridge/Freezer		1	180	16	0.5	0.5	0.5	0.5	0.5	0.5	1	1	1	0.5	0.5	0.5	0.5	0.5	0.5	0.5	1	1	1	1	1	0.5	0.5	0.5	16
TV/DVD		1	135	4									0.5				1	0.5				0.5	1	0.5					4
Air Conditioners		1	3000	6							1	0.5					0.5	0.5					0.5	1	1	1			6
Fans		3	60	12								1	1	1	0.5	0.5	1	1	0.5	0.5	0.5	1	1	1	1	0.5			12
Water Cooler		1	15	12	0.5	0.5	0.5	0.5	0.5	0.5	0.5	0.5	0.5	0.5	0.5	0.5	0.5	0.5	0.5	0.5	0.5	0.5	0.5	0.5	0.5	0.5	0.5	0.5	12
Microwave		1	1000	0.3										0.1			0.1	0.1											0.3
Cool Room		1	1250	16	0.5	0.5	0.5	0.5	0.5	0.5	1	1	1	0.5	0.5	0.5	0.5	0.5	0.5	0.5	1	1	1	1	1	0.5	0.5	0.5	16
Freezer		1	1500	16	0.5	0.5	0.5	0.5	0.5	0.5	1	1	1	0.5	0.5	0.5	0.5	0.5	0.5	0.5	1	1	1	1	1	0.5	0.5	0.5	16
Miscellaneous Socket Outlets		4	20	2							0.1	0.1	0.2	0.1	0.1	0.1	0.2	0.2	0.1	0.1	0.1	0.1	0.1	0.2	0.2				2
Powerhouse/Workshop	0.8																												
Water Pressure Pump		1	2400	12	0.5	0.5	0.5	0.5	0.5	0.5	0.5	0.5	0.5	0.5	0.5	0.5	0.5	0.5	0.5	0.5	0.5	0.5	0.5	0.5	0.5	0.5	0.5	0.5	12
Water treatment Pumps		2	750	8	0.4					0.4	0.4	0.4	0.4	0.4	0.4	0.4	0.4	0.4	0.4	0.4	0.4	0.4	0.4	0.4	0.4	0.4	0.4	0.4	8
Sump Pump		1	250	0.2	0.01					0.01	0.01	0.01	0.01	0.01	0.01	0.01	0.01	0.01	0.01	0.01	0.01	0.01	0.01	0.01	0.01	0.01	0.01	0.01	0.2
Tools		1	500	0.5										0.1	0.1				0.1	0.1	0.1								0.5
Lights		20	36	4																				0.5	1	1	1	0.5	4
Security Lighting		1	80	10	1	1	1	1	1	1															1	1	1	1	10
Bore Pump		1	2500	2	0.1					0.1	0.1	0.1	0.1	0.1	0.1	0.1	0.1	0.1	0.1	0.1	0.1	0.1	0.1	0.1	0.1	0.1	0.1	0.1	2
Exhaust Fans		2	150	24	1	1	1	1	1	1	1	1	1	1	1	1	1	1	1	1	1	1	1	1	1	1	1	1	24
Miscellaneous Socket Outlets		1	20	1.2	0.05	0.05	0.05	0.05	0.05	0.05	0.05	0.05	0.05	0.05	0.05	0.05	0.05	0.05	0.05	0.05	0.05	0.05	0.05	0.05	0.05	0.05	0.05	0.05	1.2
																													0
Ablution Blocks	1																												0
																													0
GPO		1	1150	4	0.15	0.15	0.15	0.15	0.15	0.15	0.2	0.15	0.15	0.15	0.2	0.2	0.2	0.15	0.15	0.15	0.15	0.15	0.15	0.2	0.2	0.2	0.2	0.15	4
Lighting X 1 Time Clock		2	18	4							1													1	1	1			4
Lighting Push Button		2	36	2	0.25	0.25	0.25	0.25	0.25	0.25																	0.25	0.25	2
																													0
Pump Stations X 3	1																												0
																													0
Pump		3	550	1	0.05	0	0	0	0	0.05	0.05	0.05	0.05	0.05	0.05	0.05	0.05	0.05	0.05	0.05	0.05	0.05	0.05	0.05	0.05	0.05	0.05	0.05	1
																													0
Tents Staffers	1																												0
																													0
Lamps		20	11	2							0.25	0.25													0.25	0.5	0.5	0.25	2
Fans		10	50	8	1	1	0.5	0.5	0.5	0.5	0.5	0.5														1	1	1	8
Powerpoints: Camera chargers etc		10	15	1	0.1	0.1	0.1			0.1	0.1	0.1													0.1	0.1	0.1	0.1	1
																													0
Managers House	1																												0
																													0
Fax		1	40	24	1	1	1	1	1	1	1	1	1	1	1	1	1	1	1	1	1	1	1	1	1	1	1	1	24
Printer		1	75	0.5											0.1	0.1			0.1	0.1	0.1								0.5
Computer		1	180	8									1	1	1	1			1	1	1	1							8
Fridge		1	300	16	0.5	0.5	0.5	0.5	0.5	0.5	1	1	1	0.5	0.5	0.5	0.5	0.5	0.5	0.5	1	1	1	1	1	0.5	0.5	0.5	16
Freezer		1	200	16	0.5	0.5	0.5	0.5	0.5	0.5	1	1	1	0.5	0.5	0.5	0.5	0.5	0.5	0.5	1	1	1	1	1	0.5	0.5	0.5	16
Washing Machine		1	250	0.3									0.05	0.05	0.05				0.05	0.05	0.05								0.3
TV		1	150	5																									0
Microwave		1	1000	0.2								1											1	1	1	1	1		6
Ceiling Fans		6	60	8	1	1	0.5	0.5	0.5	0.5	0.5	0.5														1	1	1	8
Lighting		70	20	6	1	0.5																		0.5	1	1	1	1	6
Toaster		1	1000	0.1								0.1																	0.1
Kettle		1	2400	0.1								0.1																	0.1
Pool		1	1200	6																									0
Socket Outlets		50	25	3										1	1				1	1	1	1							6
Spa		1	1200	0.5																		0.1	0.1	0.1	0.1	0.1			0.5
A/C		8	1600	3.5											0.5	0.5	0.5	0.5	0.5	0.5	0.5	0.5							4
Exhaust Fans		6	50	0.5								0.1						0.1					0.1	0.1	0.1				0.5
																													0

Figure 9-14 : March to May